NSF ATM-9616818
NOAA/CIRA NA67RJ0152

INSTRUMENT WETTING ERRORS IN HURRICANES AND A RE-EXAMINATION OF INNER-CORE THERMODYNAMICS

by Matthew D. Eastin

P.I.–William M. Gray

Colorado State University

DEPARTMENT OF ATMOSPHERIC SCIENCE

PAPER NO. 683

INSTRUMENT WETTING ERRORS IN HURRICANES AND A RE-EXAMINATION OF INNER-CORE THERMODYNAMICS

By
Matthew D. Eastin

Department of Atmospheric Science
Colorado State University
Fort Collins, CO 80523

August 1999

P.I. - William M. Gray
Special Advisor - Peter G. Black (NOAA/HRD)

ABSTRACT

Thermodynamic errors caused by instrument wetting are thoroughly examined and are accurately removed from 579 radial legs of aircraft flight-level data in 27 hurricanes. Similar to previous studies, a radiometer is used to provide accurate temperatures in clouds and precipitation where immersion thermometers and cooled-mirror hygrometers typically experience large errors induced by instrument wetting. Theoretical temperature errors caused by the presence of hydrometeors in the sampled air are reviewed and discussed for each instrument. A correction method is developed to remove a time-dependent bias from the radiometer temperatures using data in clear air and adjust supersaturated dew points to the equivalent of 99 percent relative humidity. In contrast to previous studies, clear air is defined using dew point depression and aircraft roll rather than the absence of liquid water. The resulting radiometer temperatures and adjusted dew points are shown to be free of instrument wetting errors and accurate.

Instrument wetting locations (IWL) are identified in roughly 50 percent of the radial legs, but are more frequent in intense (Category 3, 4, and 5) hurricanes than in minimal (Category 1 and 2) hurricanes, and were comprised of larger temperature errors. The maximum temperature error, liquid water content, and radial extent of each IWL is highly variable, but the majority of IWL are located in cloudy updrafts associated with eyewall and rainband convection, and extend less than 15 km radially. Theoretical temperature errors are rarely achieved, however, average IWL temperature errors are significant and range with height from 1.0 to 4.5°C. The temperature errors, combined with average specific humidity (q) errors ranging from 1.0 to 2.0 g kg^{-1}, result in virtual temperature (T_v) errors ranging from 1.5 to 5.0°C and equivalent potential temperature (θ_e) errors ranging from 5 to 11 K. In the eyewall average temperature and specific humidity errors range with height from 0.5 - 2.0°C and 0.5 - 1.0 g kg^{-1} respectively. Errors of such magnitudes can have a significant effect upon thermodynamic calculations in an near convection.

Various aspects of hurricane thermodynamics are thus re-examined. Radial composites about the eyewall Radius of Maximum Updraft (RMU) indicate that after instrument wetting errors are removed: the eyewall temperature is equivalent to 50-70 percent of the total anomaly observed from the environment; specific humidity maxima are located in the eyewall but are nearly equivalent to values in the eye; and eyewall θ_e is 0-5 K lower than values in the eye. The composite eyewall is shown to be moist-adiabatic with height to a *first approximation*, and better represented by pseudo-adiabatic, rather than reversible, ascent. Average eyewall θ_e for minimal and intense hurricanes are 351 K and 360 K respectively, with maximum values near 385 K. Instrument wetting errors are shown to significantly affect calculations of thermal wind balance. Finally, surface temperatures and pressures are estimated beneath the eyewall. The ratio of eyewall surface pressure to minimum central pressure is 1.02 on average. The estimated average air-sea temperature difference (SST-T_a) beneath nearly-saturated eyewalls is 2°C with maximum values near 5°C. However, the air-sea temperature difference tends to decrease toward 1°C as hurricane intensity increases.

TABLE OF CONTENTS

LIST OF SYMBOLS AND ACRONYMS

AOC: Aircraft Operations Center

ASC: Air-Sea Contrast (SST-T_a)

B: Baroclinicity

B_{ex}: Baroclinicity excess

B_o: Planck function

CAPE: Convective Available Potential Energy

c_p: Specific heat of dry air at constant pressure

c_w: Specific heat of water

CIRA: Cooperative Institute for Research of the Atmosphere

CWC: Cloud Liquid Water Content

D: Diffusion coefficient of water vapor in air

DIV: Radial divergence

EOF: Empirical orthogonal function

e_o: Vapor pressure of the free air stream

e_s: Saturation vapor pressure

ϵ: Ratio of molecular weights of water to air

f: Coriolis parameter

f_o: Non-dimensional ventilation factor

FSSP: Forward Scattering Spectrometer Probe

GPS: Global Positioning System

γ: Ratio of specific heats

GATE: Global Atmospheric Research Program Atlantic Tropical Experiment

h: Convective heat transfer coefficient

h_w: Mass transfer coefficient

HRD: Hurricane Research Division

INE: Inertial Navigation Equipment

IWL: Instrument Wetting Location

JW: Johnson-Williams cloud water instrument

K: Thermal conductivity of air

L_v: Latent heat of vaporization

λ: Slope of the eyewall

LED: Light Emitting Diode

LW: Liquid Water

m_v: Mass flow rate of water vapor

M: Mach number

MPI: Maximum Potential Intensity

ν: Wavelength

N: Observed radiance

NCAR: National Center for Atmospheric Research

NHC: National Hurricane Center

NHRP: National Hurricane Research Project

NOAA: National Oceanographic and Atmospheric Administration

ORT: Ophir Radiometric Thermometer

ω: Angular velocity

P_{cen}: Minimum central pressure

P_{diff}: Differential pressure

P_o: Static air pressure

P_r: Prantl number

P_s: Total pressure at the surface of the sensor

P_{sfc}: Surface pressure beneath the eyewall

PMS: Particle Measuring Systems

PRT-5: CO_2 Precision Radiometer Thermometer Model PRT-5

q: Specific humidity of the free air stream

q_l: Liquid water content

q_s: Specific humidity at the surface of the sensor

r: Radius

r_e: Effective recovery factor of a sensing element

ρ: Density of air

ρ_w: Density of water

R: Gas constant for dry air

RH: Relative humidity

RMTE: Radius of Maximum Temperature Error

RMU: Radius of Maximum Updraft

RMW: Radius of Maximum tangential Wind

ROSE: Rosemount temperature sensor

ROSECORR: Rosemount thermometer temperatures corrected

S: Vertical wind shear

S_a: Subsaturation of an air parcel

S_c: Schmidt number

S_s: Surface area of the sensor

SR: CO_2 Side-looking Radiometer

SR-ROSE: Side-looking Radiometer and Rosemount thermometer temperature difference

SPD: Hurricane translation speed

τ_ν: Transmittance

t_r: Relaxation time of a freely falling water drop

T: Temperature

T_a: Surface air temperature

T_d: Dew point temperature

T_e: Temperature recovery error

T_o: Static air temperature

T_r: Recovery temperature at the surface of a sensing element

T_t: Total temperature

T_v: Virtual temperature

T_{wb}: Wet-bulb temperature

ΔT_{env}: Temperature anomaly from the local environment

ΔT_{JM}: Temperature anomaly from the mean hurricane season sounding taken from Jordan (1958)

θ: Potential temperature

θ_e: Pseudo-adiabatic equivalent potential temperature

θ_{er}: Reversible equivalent potential temperature

θ_{es}: Saturated pseudo-adiabatic equivalent potential temperature

θ_v: Virtual potential temperature

TC: Tropical Cyclone

TDD: Dew point Depression

TOGA COARE: Tropical Ocean Global Atmosphere Coupled Ocean-Atmosphere Response Experiment

TPC: Tropical Prediction Center

U_o: True airspeed of an aircraft

V_{max}: Maximum surface wind speed

V_r: Radial velocity

V_θ: Tangential velocity

w: Vertical velocity

W: Inertial parameter

z: Pressure surface height

ζ: Relative vorticity

Chapter 1

INTRODUCTION

The measurement of air temperature from an aircraft has traditionally been accomplished by immersing a temperature sensitive element into the air stream. These "immersion" thermometers measure air temperature and the effects of dynamic heating as air slows to near stagnation during its approach to the sensing element. The dynamic heating component can be easily and accurately removed either by instrument design or with knowledge of the aircraft's true airspeed. If the sensor becomes wet the thermometer will measure the effects of evaporational cooling in addition to the dynamic heating of the air. Lenschow and Pennell (1974) and Lawson and Cooper (1990) argued that a *completely* wet sensor measures the wet-bulb temperature of the dynamically heated air, which at true airspeeds of 130 m s^{-1} can be 4-5°C cooler than the heated air. However, the effects of evaporative cooling on a *partially* wetted sensor are difficult to determine without knowledge of how much of the sensor is wet. For this reason analytic correction of temperatures from wetted sensors have been impossible.

The difficulty in measuring thermodynamic quantities in cumulus clouds with an immersion thermometer susceptible to possible instrument wetting errors have been addressed by Heymsfield et al. (1979), LeMone (1980), Blyth et al. (1988), and Lawson and Cooper (1990). The net effect of wetting errors is to underestimate thermodynamic quantities in clouds and precipitation. The determination of large-scale and mesoscale thermodynamic structure in hurricanes rely heavily on accurate thermodynamic measurements in and out of air containing liquid water. However, the majority of studies investigating hurricane thermodynamics have utilized immersion thermometers, and thus, the results may be in error due to instrument wetting. In recent years the development of

radiometric thermometers have provided an alternative indirect measurement of air temperature without the direct effects of instrument wetting. The purpose of this study is to use a radiometer to correct for instrument wetting errors in a large hurricane database and then to re-examine aspects of hurricane thermodynamics.

1.1 Historical Background

Wetting of temperature sensors has been known to occur since the first research flights through convective clouds. During the Thunderstorm Project (Byers and Braham 1949) a reverse-flow thermometer was used, and despite the design of the instrument to prevent drop impingement upon the sensor, wetting was observed. During penetrations of tradewind-cumuli clouds Malkus (1954) noted a drop of the dry-bulb temperature below the wet-bulb temperature and attributed the error to wetting of the dry-bulb. Flights through tropical cyclones were not an exception. In 1944 routine aircraft reconnaissance of tropical cyclones began primarily to obtain center "fixes". Detailed research missions were rarely flown until the inception of the National Hurricane Research Project (NHRP) in 1956. However, one such documented pre-NHRP mission into the eye of Typhoon Marge of 1951 (Simpson 1952) is worth noting. Simpson describes the final exit of Marge's eye on August 15, 1951:

> With fuel growing short, the plane upon completing the second ascent in the eye departed for home at an elevation of 17,000 feet. As the wall of the eye were reached, moderate turbulence was felt, somewhat greater and more continuous than had been felt when entering the eye through the same quadrant at 9,000 to 10,00 feet. At the same time, it was noted that the temperature began to fall more rapidly as the plane entered the wall of clouds surrounding the eye. It was not long before ice began forming on the cockpit windshield and other parts of the plane as the thermometer leveled off at -5°C. *In a lapse*

of several minutes and a distance of 60 miles the temperature had dropped a total of 21.6° C![1]

The temperature drop was later corrected to 18°C due to an aircraft elevation change caused by the eyewall updraft, however, Simpson made no comment about instrument wetting. While the measured temperature drop could be real, two factors support the argument that the drop was partially due to instrument wetting. First, ice was forming on the cockpit windshield and other parts of the aircraft from supercooled water drops, indicating that ice could also be collecting on the temperature sensor. Thus, sublimational cooling would lower the measured temperature as the ice is evaporated from the sensor. Secondly, the mean temperature of the 700-500 mb layer, calculated 40-70 miles from the storm center from the aircraft temperature traces (Figure 2 of Simpson 1952, not shown), is more than 5 °C cooler than the mean synoptic temperatures over the same layer calculated from sounding data near Marge. One would not expect such cool temperatures so close to the center of a strong warm core vortex. This data may be the first documented instance of instrument wetting in a hurricane, although not directly stated.

While the effects of instrument wetting may not have been known by Simpson in 1952, possible errors from the wetting of immersion thermometers were known at the start of the NHRP (Hilleary and Christensen 1957). The onset of the NHRP marked the beginning of frequent research aircraft penetrations of hurricanes, and the foundation for the inner-core (radii up to 150 km from the center) thermal structure of the hurricane. Thus, a brief historical review of observed instrument wetting, and the resulting perception of tropical cyclone thermodynamics is warranted. Shown in Table 1.1 is a summary of notable studies of hurricane thermodynamics and their respective treatment of instrument wetting errors.

After two hurricane disasters along the US East Coast in 1954 and 1955, the NHRP was established in 1956 to accelerate research on the hurricane prediction problem (Staff NHRP, 1956). The goals of the project were to investigate genesis, structure, motion, in-

---

[1] Italics were originally used in Simpson (1952)

teraction with its environment, and the feasibility of human modification. Reconnaissance aircraft were selected (along with rawindsondes) as a primary observational platform for the project, and were instrumented with the most advanced meteorological equipment of the time, including vortex, stagnation, and reverse-flow immersion thermometers and a infrared hydrometer to measure humidity. All three thermometers were selected to ensure the continuous measurement of temperature, capitalize on the advantages of each instrument, and allow for comparison when one instrument is believed to be in error. Further information on each instrument is provided by Hilleary and Christensen (1957). The NHRP observational period was originally planned for a 30 month period. However, the project continued for the next 10 years, and in essence, is presently ongoing with similar goals as the annual Hurricane Field Program conducted by NOAA's Hurricane Research Division (HRD) and Aircraft Operations Center (AOC). Over the years the planes and instrumentation have changed. In the 1970's the P-3 became the workhorse aircraft behind the field program, and continues to be at present. The switch to the P-3's was accompanied by a switch in temperature sensors to a stagnation immersion thermometer designed to minimize wetting by inertial separation of drops from the air, and a switch in dew point sensors to a chilled-mirror hygrometer. The P-3 thermodynamic sensors are used in this study and will be discussed in detail later.

By 1958 the first NHRP observations of hurricane thermal structure were published. Jordan (1958a) reported on the horizontal thermal structure of the eye and eyewall of Hurricane Carrie of 1957. Using two miles averages, Jordan found a similar drop in temperature as Simpson (1952) while the aircraft penetrated the eyewall from the eye. Furthermore, Jordan found a cool minimum in the azimuthal average of the eyewall on both days the storm was observed, which he attributed to evaporative cooling of the ambient air by rain. Colon (1964) investigated the thermal structure of Hurricane Helene of (1958) using data from the vortex thermometer. He noted regions of cool temperatures, up to 2°C below normal, in rain areas. He attributed these cool regions to the evaporative cooling of the air by rain and the adiabatic cooling of air spiraling inward toward the

center of the hurricane. Colon noted during the penetration of one rainband that the temperature decreased, while during the penetration of another the temperature increased. He concluded the difference was the latter was sampled during the growing stage, and thus positively buoyant, while the former was sampled during the rainout stage and was negatively buoyant. Furthermore, Colon found temperature discrepancies on the order of 3-4°C between inbound and outbound passages through the inner edge of the eyewall. He attributed the discrepancies to a time lag of the thermometer during passage through the strong temperature gradient found near the eyewall. While the conclusions by Jordan (1958a) and Colon (1964) are viable, the cool minimums reported near the eyewall cloud and in rainbands may partially attributable to instrument wetting. The temperature discrepancies between inbound and outbound passages of the eye edge may be the result of a wet temperature sensor compared with a yet to be wetted sensor producing errors at different locations along the temperature gradient.

Riehl and Malkus (1961) investigated heat and moisture budgets of Hurricane Daisy (1958) using multi-level aircraft data averaged over 20 mile increments. The storm was first interrogated via aircraft on August 25 and for several days after. They noted temperatures 1-3°C cooler than expected during passage through clouds and precipitation, during which supersaturated dew points were also observed. They attributed these observations to instrument wetting and attempted to correct for the errors by occasionally lifting temperature 1-2°C and disregarding supersaturated dew points.

A set of three papers on the structure and dynamics of hurricanes were published by LaSeur and Hawkins (1963), Hawkins and Rubsam (1968), and Hawkins and Imbembo (1976) on a weak hurricane (Cleo, 1958), a average hurricane (Hilda, 1964) and a small intense hurricane (Inez, 1966). LaSeur and Hawkins (1963), using NHRP vortex-thermometer data, noted temperatures consistently 1°C low in the eyewall and rain areas of Cleo. The low anomalies were attributed to evaporational cooling from entrainment and instrument wetting. Dew points were frequently observed to be supersaturated in the same areas, which they concluded was a result of the infrared hygrometer being calibrated

Table 1.1: Treatment of aircraft instrument wetting errors in notable studies of hurricanes.

Study	Primary Temp. Sensor	Cool Temp. Noted in Convection?	Attributed to Instrument Wetting?	Correction Method	Type of Study
Simpson (1952)	Not Given	No	-	-	Case
Jordan (1958b)	Not Given	Yes	No	None	Case
Riehl and Malkus (1960)	Not Given	Yes	Yes	Objectively adjusted to fit soundings	Case
LaSeur and Hawkins (1963)	Vortex	Yes	Yes	None	Case
Colon (1964)	Vortex	Yes	No	None	Case
Hawkins and Rubsam (1968)	Vortex	Yes	Yes	None	Case
Shea and Gray (1973)	Vortex	No	-	-	Composite
Hawkins and Imbembo (1976)	Vortex	No	-	-	Case
Barnes et al. (1983)	Rosemount	Yes	Yes	Zipser et al. (1981)	Case
Jorgenson (1984a,b)	Rosemount	Yes	Yes	Zipser et al. (1981)	Case/ Composite
Frank (1984)	Rosemount	Yes	Yes	None	Case
Barnes and Stossmeister (1981)	Rosemount	Yes	Yes	Zipser et al. (1981)	Case
Powell (1990)	Rosemount	Yes	Yes	Zipser et al. (1981)	Case/ Composite
Barnes et al. (1991)	Radiometer	Yes	Yes	Jorgenson and LeMone (1989)	Case
Ryan et al. (1992)	Radiometer	Yes	Yes	Jorgenson and LeMone (1989)	Case
Barnes and Powell (1995)	Radiometer	Yes	Yes	Jorgenson and LeMone (1989)	Case

at sea-level, and thus not calibrated for aircraft use. The dew points were adjusted to saturation, but no adjustments were made to the temperatures. Hawkins and Rubsam (1968) used NHRP vortex-thermometer data for Hilda, and also noted anomalously cool temperatures in the eyewall and rain areas of 1.5-2.0°C, which they attributed to instrument wetting. After data analysis Hawkins and Rubsam concluded that there was no systematic way to correct for these errors since the thermal structure was "apparently improved" in some situations, while in other cases corrections made the thermal structure "less acceptable". Thus, no corrections were made.

Hawkins and Imbembo (1976) did not mention instrument wetting of either of the temperature or dew point data used in their analysis of Inez. However, in Figure (1.1) (Figure 9 of Hawkins and Imbembo 1976) a band of cool temperatures were observed in the eyewall to the northeast of the storm center, and in Figure (1.2) (Figure 14 of Hawkins and Imbembo 1976) several cool temperature anomalies were observed at the lowest three flight levels radially out from the eyewall. Relative humidities shown in Figure (1.3) (Figure 12 of Hawkins and Imbembo 1976) reach 105% in the eyewall region, well above typical supersaturations believed to exist in clouds. A radial-height cross section of equivalent potential temperature (θ_e) (Figure 1.4, or Figure 16 of Hawkins and Imbembo 1976) through Inez indicates that θ_e increases on average with decreasing radius, however within and outside the eyewall are pockets of low θ_e air. While the cool anomalies may be real, they may also be the erroneous result of instrument wetting. The data presented in several figures by Hawkins and Imbembo (1976) agree with the locations of similar temperature anomalies that LaSeur and Hawkins (1963) and Hawkins and Rubsam (1968) attributed to instrument wetting errors.

Shea and Gray (1973) utilized vortex-thermometer data from 21 hurricanes observed over the 13 year period of 1957-1969 for a composite study of the inner-core structure. They noted the possiblity of instrument wetting errors of 1-2°C through cumulus clouds, but none were "explicitly detected". They presented the argument that the possible errors would not effect portrayed composite temperature gradients because, first, the large

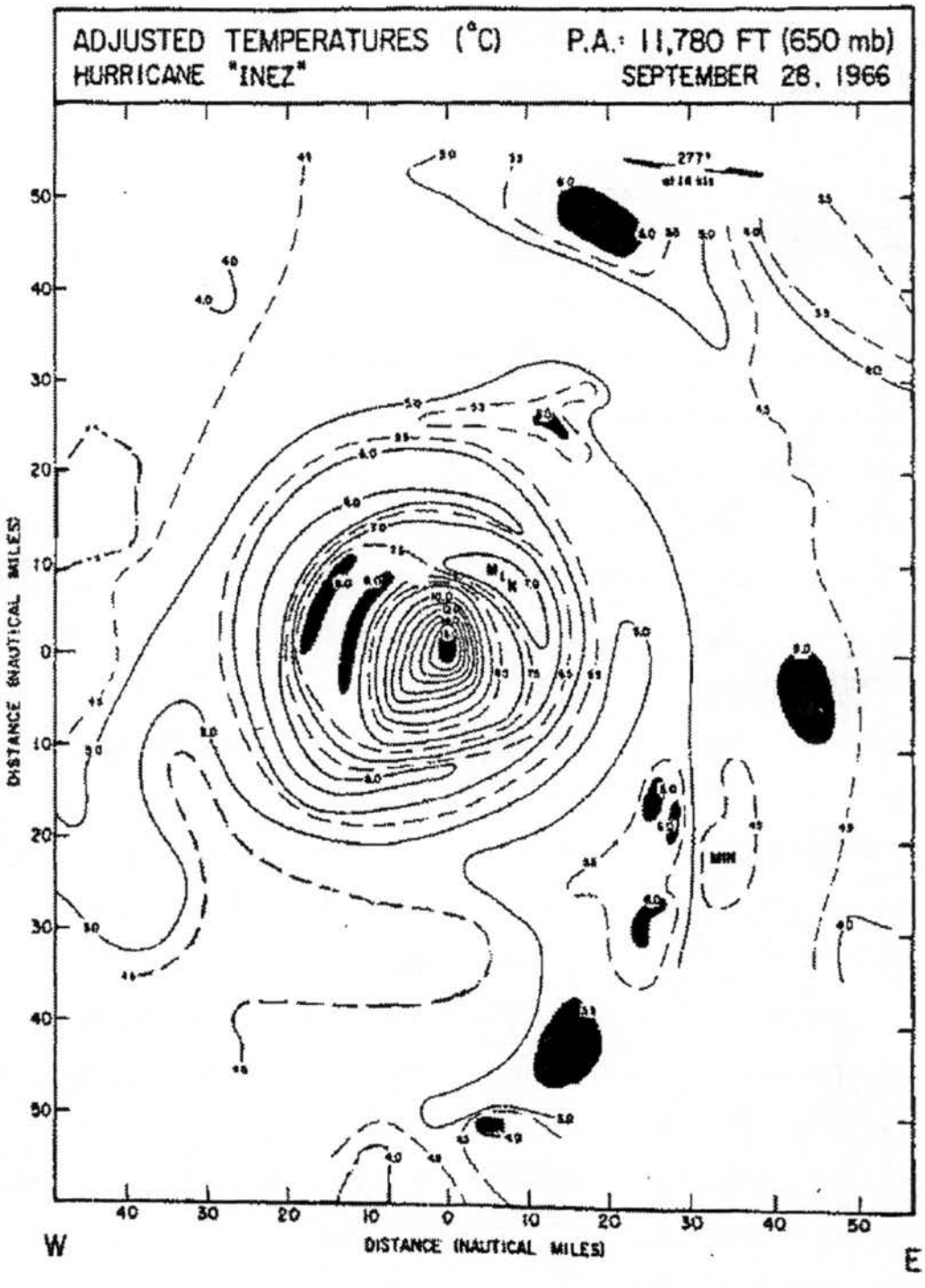

Figure 1.1: Adjusted temperatures at 650 mb in Hurricane Inez (1966) on 28 September. From Hawkins and Imbembo (1976).

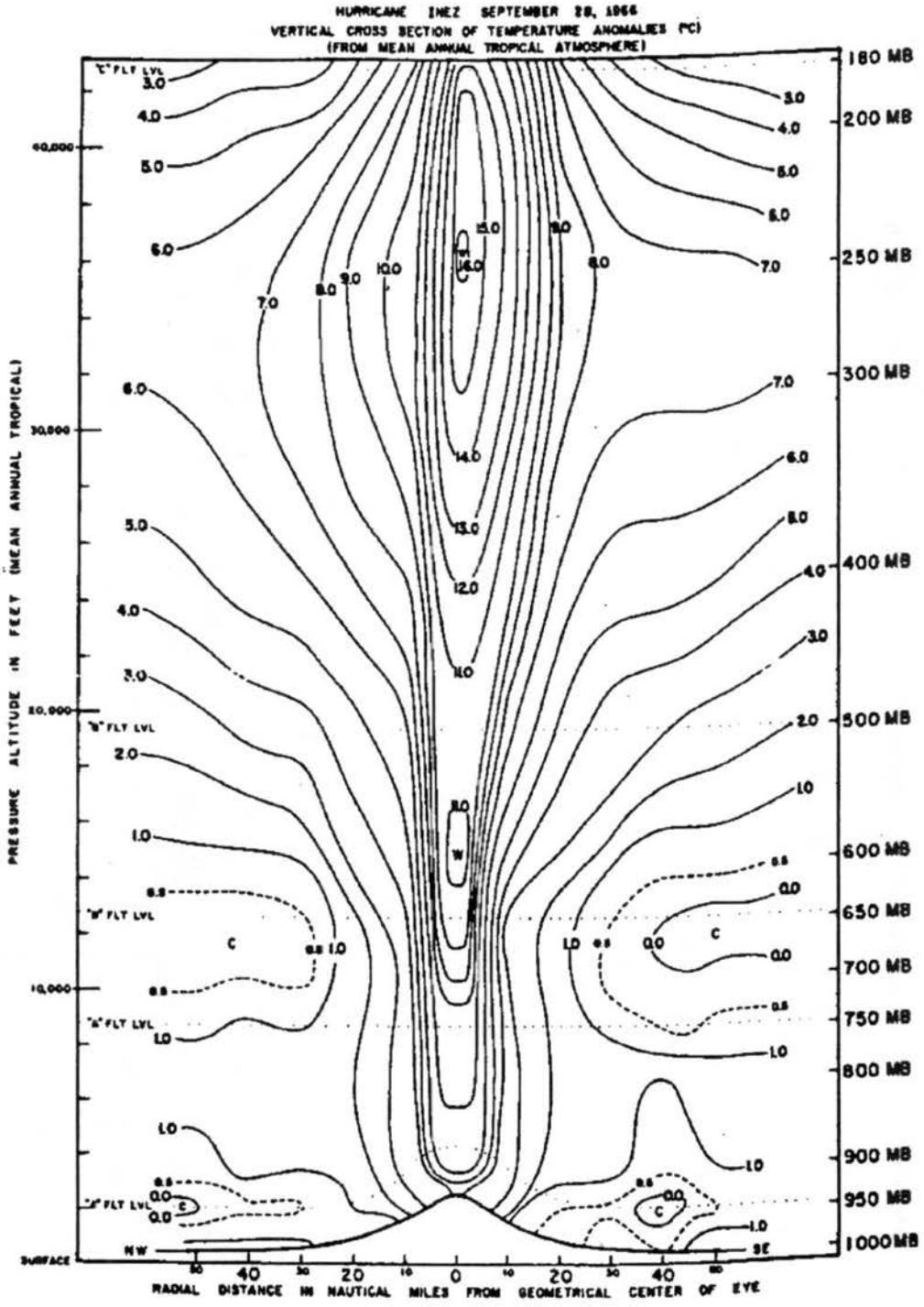

Figure 1.2: Vertical cross-section of temperature anomalies from the mean annual tropical atomosphere (Jordan 1958b) for Hurricane Inez (1966) on 28 September. From Hawkins and Imbembo (1976).

sample of data would produce a statistically insignificant effect. Secondly, the temperature gradients shown are over a scale larger than individual cumulus clouds. Third, the existence of a close statistical agreement between pressure thickness derived from D-values and observed temperature gradients. Fourth, flights into and out of the eye do not always encounter an eyewall cloud with large liquid water contents, and finally, no statistical significance was found for temperature differences between inbound and outbound radial legs as indicated by Colon (1964).

The switch to the P-3 aircraft in the 1970s resulted in improved instrumentation and data recording over shorter time scales ($\sim$1 Hz), and thus spatial scales. The switch was accompanied by studies of the mesoscale and convective-scale thermodynamic structure and interaction between the eyewall, rainbands, and the boundary layer in a hurricane. Thus, a greater need for more accurate thermodynamic measurements arose. Near the same time the first attempt to systematically correct for instrument errors was attempted by Zipser et al. (1981) for an analysis of mesoscale convection observed during the Global Atmospheric Research Program Atlantic Tropical Experiment (GATE). The simple correction method was used by numerous subsequent studies and will be described and evaluated further in Chapters 4 and 5.

Jorgenson (1984a) studied the composite mesoscale features of Hurricanes Anita (1977), David (1979), Frederic (1979), and Allen (1980). Instrument wetting errors were observed and temperatures were corrected using a slightly modified version of the method proposed by Zipser et al. (1981). Jorgenson (1984b) concentrated on the structure of Allen. Individual and composite radial-height cross-sections were constructed from simultaneous multi-level passes on two separate days. Maximum θ_e was observed in the eye, while minimum θ_e was observed in the mid-troposphere outside the eyewall. Cross sections of individual passes on the first day indicated a local maximum of θ_e associated with the eyewall, while a local minumum was located just inside the eyewall along the inner edge of the eye. However, composited cross sections of the second day depicts a steady rise θ_e across the eyewall and into the eye. While the large increase of θ_e with decreasing radius

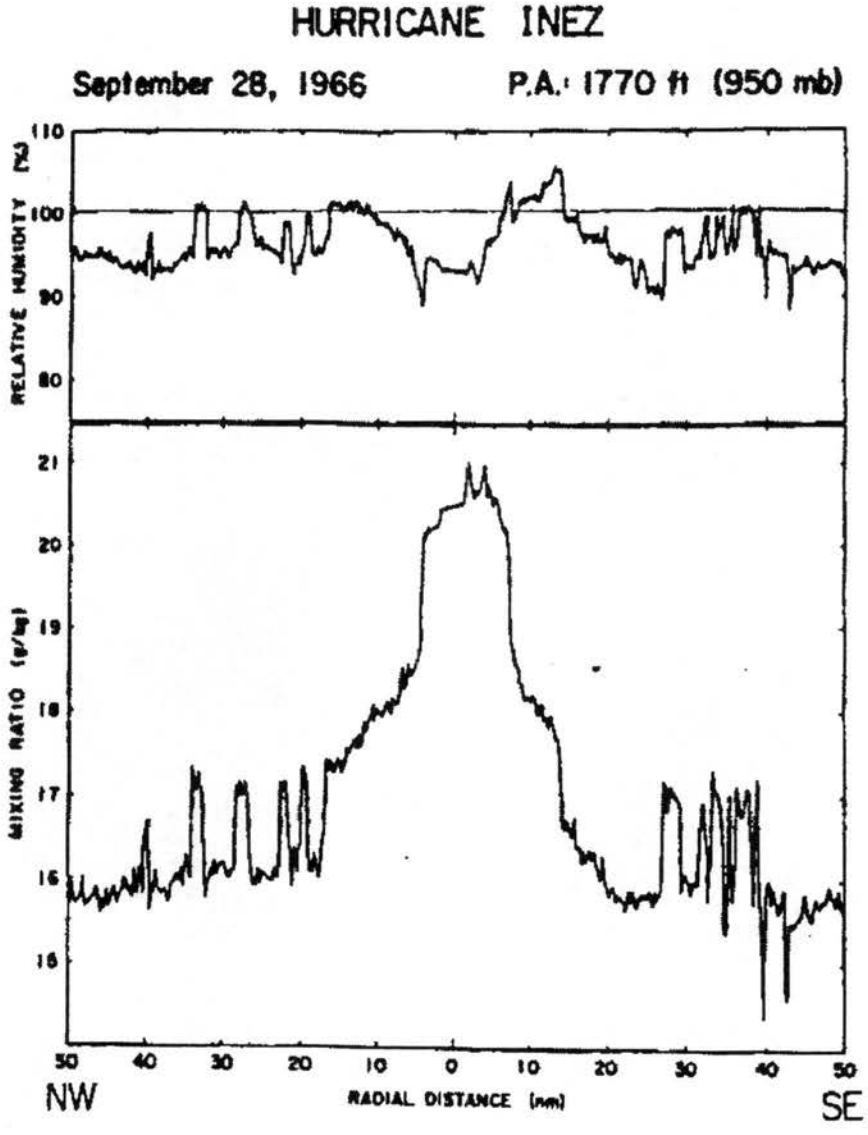

Figure 1.3: Relative humidity and mixing ratio at 950 mb through the eye and eyewall of Hurricane Inez (1966) on 28 September. From Hawkins and Imbembo (1976).

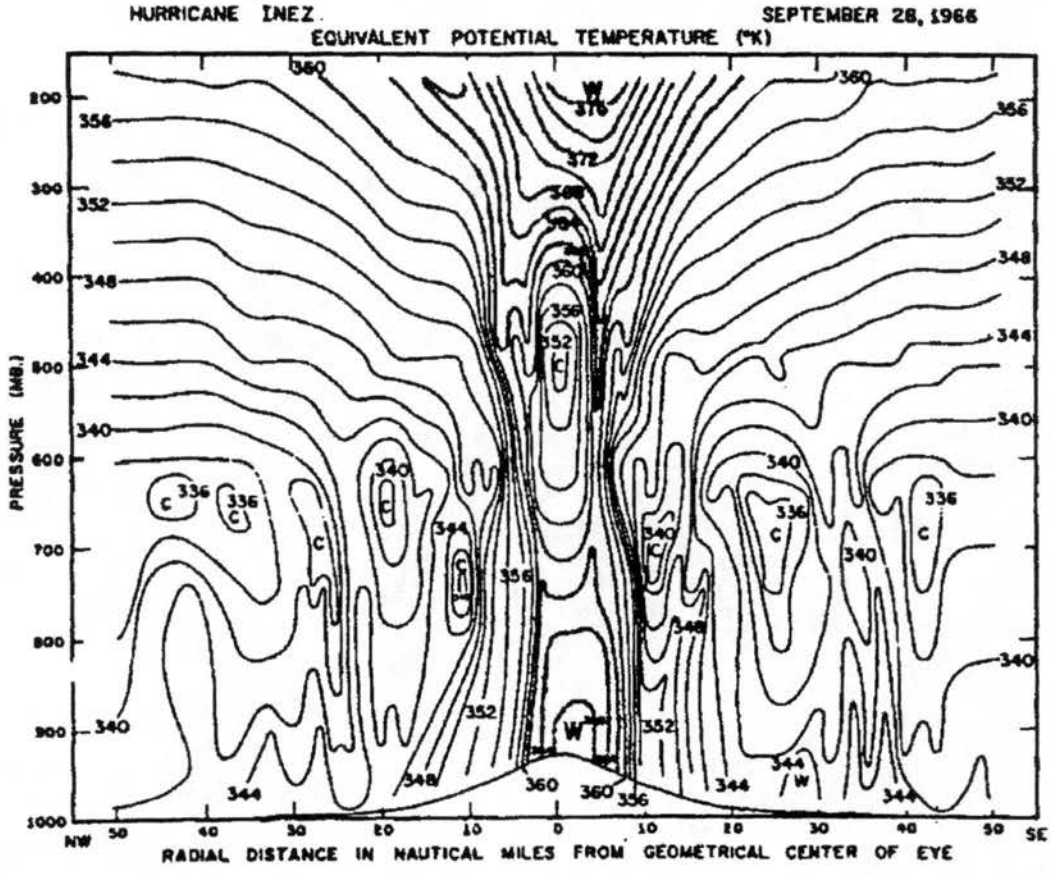

Figure 1.4: Vertical cross-section of θ_e through the eye and eyewall of Hurricane Inez (1966) on 28 September. From Hawkins and Imbembo (1976).

agrees with previous studies, the mesoscale θ_e structure near the eyewall is in contrast to the θ_e presented by Hawkins and Imbembo (1976) in the eyewall of Inez. Are the differences simply an example of the variation found in hurricanes over their lifetime, or are the contrasting results due to the *effective* removal of instrument wetting errors using the method proposed by Zipser et al. (1981)?

Barnes et al. (1983) investigated the mesoscale structure of a rainband in Hurricane Floyd (1981) while Powell (1990) investigated the structure of rainbands in Hurricanes Josephine (1984) and Earl (1986). Each study corrected temperatures using the Zipser et al. (1981) method. Resulting equivalent potential temperatures were believed to be $\pm 2.0K$ of their actual values due to the temperature correction. A significant inward radial decrease in θ_e was observed in the boundary layer across each rainband. This thermodynamic structure could not be explained from the mesoscale motion field, and thus, the drop in θ_e was hypothesized to be a result of convective subgrid-scale downdrafts transporting low θ_e air from aloft during cellular convection within the rainband. The convective scale aircraft data indicated local minima of θ_e associated with both updrafts and downdrafs within each rainband. One would expect from parcel theory that active convective updrafts contain local maxima of θ_e.

In the early 1980's a radiometric thermometer was added to the P-3 instrument package. Jorgenson and LeMone (1989) first utilized the radiometer during a study of oceanic convection of Taiwan. Severe instrument wetting of the immersion thermometer was observed during cloud penetrations, but the radiometer performed well indicating the expected warm anomaly associated with active convection. Several subsequent studies using the radiometer in hurricane's followed (e.g. Barnes et al. 1991; Ryan et al. 1992; Black et al. 1994; and Barnes and Powell 1995). Each was a mesoscale case study. Ryan et al. (1992) and Barnes and Powell (1995) investigated rainband structure and noted locally elevated temperatures and equivalent potential temperatures in convective-scale updrafts. Could the local minima be due to the *ineffective* removal of instrument wetting errors using the method proposed by Zipser et al. (1981)?

1.2 Objectives

The accurate determination of thermodynamic quantities in the hurricane inner core is crucial to understanding hurricane structure and intensity changes. It seems plausible, and contrasting results from previous studies suggest, that instrument wetting errors may substantially alter observed thermodynamics, leading to erroneous conclusions and conceptual understanding of hurricane structure. Since the radiometric thermometer has recently been show to perform well in clouds and precipitation, instrument wetting errors and uncertainties in thermodynamic structure can finally be directly addressed. The opportunity presents several questions that are to be answered in this study. How frequent and of what magnitudes are instrument wetting errors found in hurricanes. Over what spatial scales are wetting errors most significant? Is the temperature correction method proposed by Zipser et al. (1981) effective in removing wetting errors? To what extent could instrument wetting errors effect these previous results and the hurricane thermodynamic structure?

The objective of this study is to use the radiometric thermometer to correct for instrument wetting errors in a large hurricane radial leg database, determine the frequency and magnitude of instrument wetting errors within hurricanes, and then to re-examine hurricane thermodynamics. The results from this study provide the most accurate and reliable values of thermodynamics quantities that have been in question since the onset of the NHRP. Chapter 2 contains a theoretical discussion of possible temperature and dew point instrument errors caused by hydrometeors. Chapter 3 contains a description of the data used in the study. Chapter 4 describes the temperature profile reconstruction methodology and an evaluation of the method. Chapter 5 addresses the magnitude and frequency of wetting errors within the database, along with the resulting errors in thermodynamic variables due to the wetting. The effectiveness of applying the wetting correction method proposed by Zipser et al. (1981) is also evaluated. Chapter 6 re-examines aspects of hurricane thermodynamic structure and theories. The conclusions and ideas for future work are given in Chapter 7.

Chapter 2

THEORETICAL DISCUSSION OF AIRCRAFT THERMODYNAMIC SENSOR ERRORS

2.1 Immersion thermometers

The accurate measurement of static air temperature, or the temperature of the undisturbed air, is desired for many meteorological field studies over horizontally small spatial scales. Traditionally the aircraft observing platform has been used and flight-level temperatures have been obtained with thermometers mounted to the outer fuselage of the aircraft, resulting in the sensing element being immersed within the air. These "immersion thermometers" directly measure the air temperature through thermal relaxation of a platinum resistance sensor. Due to their physical design, immersion thermometers do not measure the static air temperature, but rather the effective temperature at the surface of the sensor, or recovery temperature. The recovery temperature is a result of dynamic heating, or the compressional and viscous heating of the air as it enters the instrument housing and decelerates from the free stream airspeed (U_o) to some fraction (a) of that airspeed, approaching stagnation at the sensor surface. This adiabatic energy conversion warms the air such that the recovery temperature of the element is described by,

$$T_r = T_o + r_e \frac{{U_o}^2}{2c_p} \tag{2.1}$$

where T_r is the recovery temperature at the surface of the sensing element, T_o is the static air temperature, U_o is the true airspeed of the aircraft, c_p is the specific heat of air at constant pressure, and r_e is the effective recovery factor of the instrument. Thus, the static air temperature can be easily obtained by knowing the aircraft true airspeed and the recovery factor of the instrument. The recovery factor is defined as,

$$r_e = \frac{T_r - T_o}{T_t - T_o} = 1 - a^2 \tag{2.2}$$

with T_t being the total temperature, or the temperature resulting from 100% conversion of the free stream kinetic energy. A high recovery factor indicates that a is very low (such that aU_o is near zero) and the effective recovery temperature is close to the total temperature under adiabatic processes. Assuming a recovery factor near unity, the compressional and viscous warming above the static air temperature is about 8°C. A more complete form of (2.2) that takes into account the recovery factor of the instrument housing and the sensing element separately is provided by Lawson and Cooper (1990). A single recovery factor is presented here since the the recovery factors of the platinum wire sensor and the housing are not well known separately. Furthermore, the majority of recovery factors provided in the manufacturer's specifications are for the instrument as a whole.

A Rosemount 102a deiced immersion thermometer (the instrument mounted to the WP-3D aircraft and utilized in this study) uses a modified, but equivalent, expression to (2.1) to recover the static air temperature from the measured air temperature in flight,

$$T_o = \frac{T_t}{1 + \frac{\gamma - 1}{2} M^2} + T_e \tag{2.3}$$

where γ is the ratio of specific heats, M is the Mach number, and T_e is the recovery error. All temperatures are expressed in absolute units. T_e is a correction that compensates for a recovery factor less than unity. The Rosemount 102a has a variable instrument recovery factor that is slightly dependent upon Mach number at sub sonic speeds. Thus, the probe recovery error is calculated for each data point during flight using,

$$T_e = \frac{0.00109 {P_{diff}}^2}{\sqrt{P_o}} \tag{2.4}$$

where P_{diff} and P_o are the differential pressure and static pressure, respectively, in millibars. The average recovery factor in this study for aircraft speeds of 120-145 m s^{-1} and altitudes of 1-8 km is 0.975.

The calculation of static air temperature using (2.1) and (2.3) assumes the recovery temperature at the surface of the sensor is strictly a result of dry adiabatic processes, yet this condition is rarely achieved in field operations. Immersion platinum resistance thermometers experience self-heating (caused by electrical flow through the resistor used to make the measurement), conductive heating from the housing to the sensor, heating of the air by the housing, and radiative heat transfer. Stickney et al. (1990) and Lawson (1988) argue the combination of these errors are negligibly small ($< 0.1°C$) in well-designed temperature probes at typical aircraft speeds (further discussion of these errors and errors from a deicing heater is provided in Appendix A), and immersion thermometers have been shown to perform very well in clear air (Lawson and Cooper 1990). More significant errors can occur in clouds or precipitation if the sensor becomes wet. The air inside the housing, and particularly at the sensor, is always subsaturated due to the large compressional warming of the ambient air. The warming occurs in less than a millisecond, however, the response time of liquid water drops in the air to adjust to this temperature change is on the order of a second (LeMone 1980; Politovich and Cooper 1988). Thus, water drops will not significantly evaporate before reaching the sensor, and drop impingment upon the sensing element can occur. If the sensing element unknowingly becomes wet due to contact with water drops, evaporational cooling ensues, and the sensor may acquire the wet-bulb temperature of the interior environment of the housing.

Lenschow and Pennell (1974) combined the effects of dry convective heat transfer for flow around a cylindrical element and wet-bulb psychometry to argue that the error caused when the sensor becomes wet is the difference between the equilibrium wet-bulb temperature of the sensor and the recovery temperature. Thus, the error of a completely wetted sensor can be calculated. Assuming that the heat lost from a completely wetted sensor by evaporation balances the heat gained by the sensor from forced convection, the first law of thermodynamics can be used to show,

$$m_v L_v = h S_s (T_r - T_{wb}) \tag{2.5}$$

where m_v is the mass flow rate of water vapor required to produce cooling through evaporation that balances the heating of forced convection, L_v is the latent heat of vaporization, h is the convective heat transfer coefficient, S_s is the surface area of the sensor, and $T_r - T_{wb}$ is the difference between the recovery temperature and the temperature of the sensor. A second relationship was determined that balances the mass flow rate of water vapor with the mass at the the surface of the sensor,

$$\frac{m_v}{S_s} = h_w \frac{q_s - q}{1 - q_s} \tag{2.6}$$

where h_w is the mass transfer coefficient, q is the free air stream specific humidity, and q_s is the specific humidity at the surface of the sensor. Using the fact that

$$q_s = \frac{\epsilon e_s(T_{wb})}{P_s} \tag{2.7}$$

where ϵ is the ratio of molecular weights of water to air, $e_s(T_{wb})$ is the saturation vapor pressure at the sensor temperature, and P_s is the total pressure at the sensor surface, equation (2.6) can be written as

$$\frac{m_v}{S_s} = \frac{h_w \epsilon}{P_s} \frac{e_s(T_{wb}) - \frac{P_s}{P_o} e_o}{1 - \frac{\epsilon e_s(T_{wb})}{P_s}} \tag{2.8}$$

where P_o and e_o are the total pressure and water vapor pressure in the free air stream respectively. Lawson and Cooper (1990), following the same argument as Lenschow and Pennell (1974) up to this point, accounted for air density changes due to adiabatic compression. Thus, Equation (2.8) can be inserted into (2.5) along with the relationship for the heat-to-mass transfer coefficients from Bedingfield and Drew (1950) to obtain the equation of the temperature error due to a completely wetted sensor

$$T_{wb} - T_r = \frac{1}{AP_s} \left(\frac{P_s}{P_o} e_o - e_s(T_{wb}) \right) \tag{2.9}$$

where $T_{wb} - T_r$ is the error caused by sensor wetting, and A is the psychometric parameter for a cylindrical sensor given by,

$$A = \frac{C_p}{\epsilon L_v}\left(\frac{S_c}{P_r}\right)^{0.56}\left(1 - \frac{\epsilon e_s(T_{wb})}{P_o}\right) \tag{2.10}$$

where S_c is the Schmidt number (the ratio of kinematic viscosity to the diffusion coefficient), and P_r is the Prandtl (the ratio of kinematic viscosity to the thermal diffusivity). Equation (2.9) indicates the magnitude of the error due to wetting of the sensor is a function of true air speed, temperature, pressure, ambient relative humidity, and recovery factor. Shown in Figure (2.1) are sensor errors at various flight levels as a function of true airspeed calculated from (2.9). A recovery factor of unity (r = 1.0) was assumed along with saturated ambient air and typical temperatures for the mean tropical atmosphere at each level. With typical true airspeeds for tropical cyclone penetrations ranging between 120-145 m s^{-1}, errors from complete sensor wetting can theoretically be as large as 4-6°C. If the air is subsaturated prior to entering the instrument housing and the sensor becomes, or still is, completely wetted, the errors will be higher. Shown in Figure (2.2) are sensor errors calculated with the same assumptions used to produce Figure (2.1) except with an ambient relative humidity of 90%. Resulting errors are 0.5-1.0°C higher than for saturated ambient conditions. Total errors may be even larger due to liquid water on the inner housing surfaces evaporating and cooling the air. In such cases, the expected warming from compressional heating would not be realized, resulting in an additionally cool error up to 1.0°C. Thus, immersion thermometer temperature errors in and near warm clouds or precipitation can be as large as 5-7°C.

At flight levels that encounter cold cloud conditions, supercooled water drops can form ice upon the sensor if the adiabatic warming does not raise the recovery temperature above freezing. In such a case, ice can collect on the sensor. The additional cooling from the sublimation process would result in an error larger than predicted by (2.9). This additional temperature error can be approximated using (2.9) by substituting the latent heat of sublimation for vaporization, along with the saturation vapor pressure and temperature at the surface sensor to their respective values for ice. Shown in Figure (2.3)

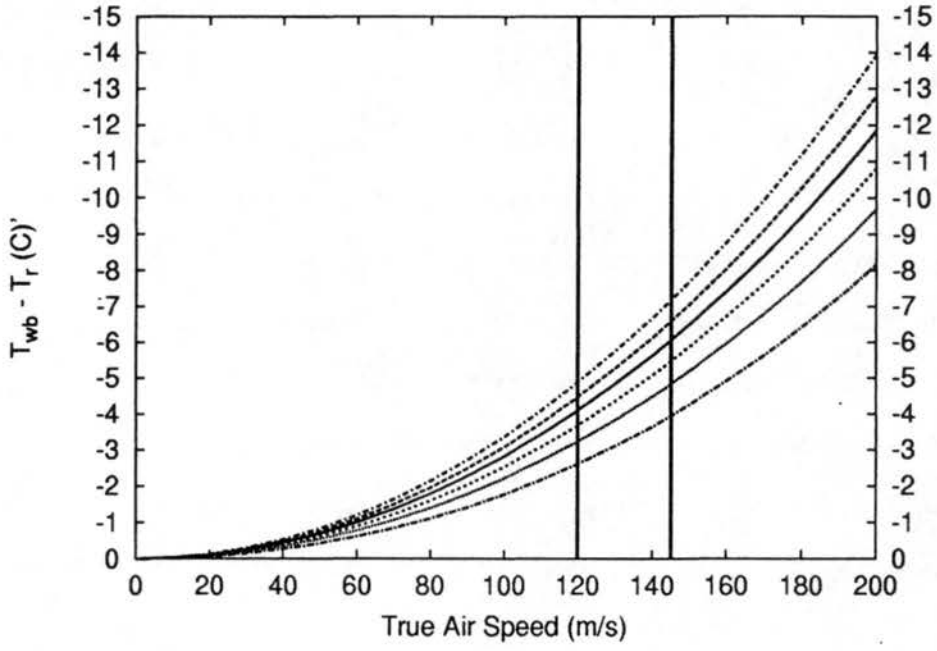

Figure 2.1: Theoretical temperature errors (T_{wb} - T_r) calculated from (2.9) for a completely wetted sensor assuming a recovery factor of unity (r = 1.0), saturated ambient air, and temperatures from the mean tropical atmosphere at 900 mb (dot/short dash), 850 mb (long dash), 700 mb (solid), 600 mb (short dash), 500 mb (dotted), and 400mb (dot/long dash). Vertical solid lines represent the range of typical true air speeds for hurricane penetrations.

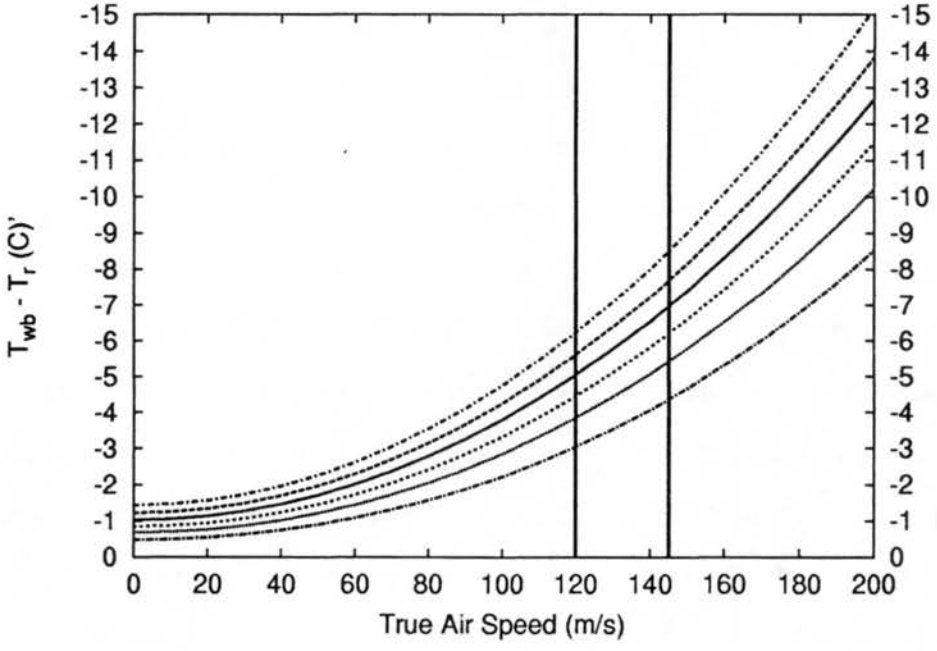

Figure 2.2: Same as Figure 2.2 except for 90% ambient relative humidity.

are the errors for a completely ice covered sensor at 500 mb in saturated and 90% relative humidity ambient air.

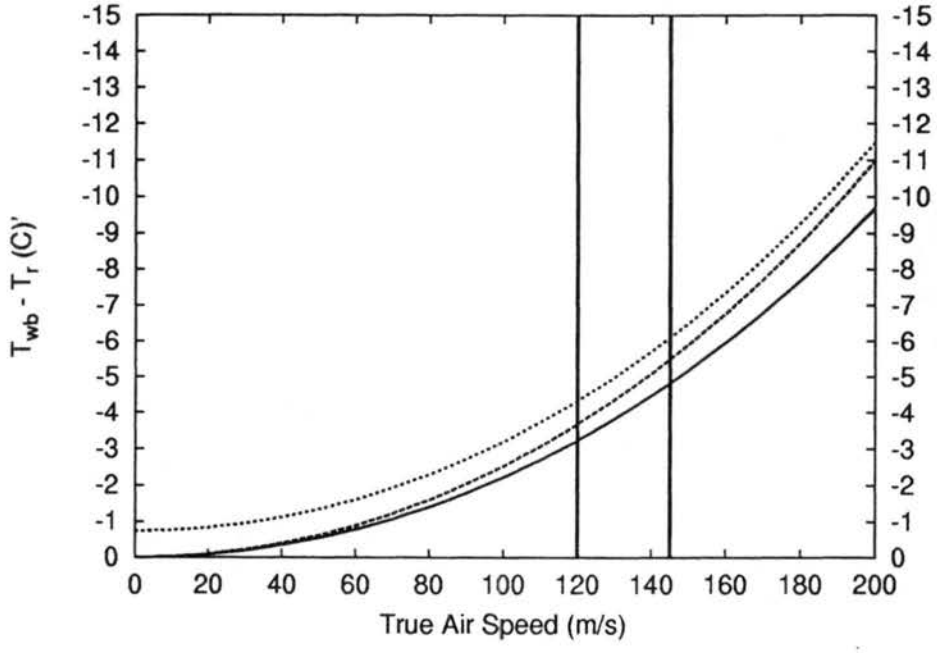

Figure 2.3: Theoretical temperature errors (T_{wb} - T_r) calculated from (2.9) for a completely ice covered sensor at 500 mb assuming a recovery factor of unity (r = 1.0) and temperatures from the mean tropical atmosphere for saturated ambient air (long dash) and 90% ambient relative humidity (short dash). Included for comparison is the theoretical error at 500mb for a completely wetted sensor assuming saturated ambient air (solid).

Resulting errors are 0.5-0.75°C larger for an ice covered sensor, with an additional 0.5-0.75°C error for subsaturated conditions of 90% relative humidity. Thus, theoretical instrument errors can be 5-7°C due to an ice covered sensing element. Furthermore, supercooled water drops can form ice along the leading edges and inside the housing. While a deiced thermometer is designed to prevent this, in regions of high water contents the deicing heater may be insufficient to maintain ice-free conditions. Icing on the housing can have two effects. First, an ice build-up at the entrance and exit ports of the housing can produce a low internal mass flow through the instrument. An expansion of the heated housing boundary layer (an effect of a deicing heater which is normally suppressed during high internal mass flow) toward the sensing element will ensue, resulting in an erroneously warm temperature. Secondly, ice build-up within the housing must melt and evaporate,

resulting in a cooling of the air passing through the housing. The expected warming from compressional heating would not be realized, resulting in an additional cool error up to 1-2°C. Hence, immersion sensor temperature errors on the order of 10°C can occur in and near cold clouds or precipitation.

2.2 Radiometric thermometers

The use of infrared radiometers to indirectly measure air temperature eliminates direct contact with the air, and thus the air being sampled is not disturbed. Furthermore, liquid water does not effect the physical operation of the radiometer. The theoretical basis for measuring air temperatures with a radiometer assumes the measured radiance in a given direction is proportional to a weighted average of the temperature in that direction. Thus following Albrecht et al. (1979), the radiance observed within the conical field of view of the instrument is given by,

$$N(\nu) = \int_0^\infty B_o(\nu, T) \frac{\partial \tau_\nu}{\partial l} dl \tag{2.11}$$

where $N(\nu)$ is the observed radiance, $B_o(\nu, T)$ is the Planck function, and τ_ν is the transmittance of the material along the pathlength, dl, being observed. If the temperature is assumed to be uniform along the observed path length, the Planck function becomes independent of pathlength. By confining observations to a spectral band in which,

$$N(\nu) = \int_0^\infty \frac{\partial \tau_\nu}{\partial l} dl \rightarrow 1.0 \tag{2.12}$$

the observed radiance becomes equal to the Planck function, and the temperature can be directly determined from the observed radiance using Planck's Law. In order to determine local flight-level temperatures, the conical volume observed and the spectral band over which the air is observed is restricted. The AOC modified Barnes PRT-5 radiometers aboard the P-3 aircraft point horizontal to the ground and utilizes a 2° conical field of view. (Further discussion of the radiometer operation is provided in Appendix A). The

small field of view minimizes variations in temperature due to the background lapse rate when the instrument is pointing horizontally.

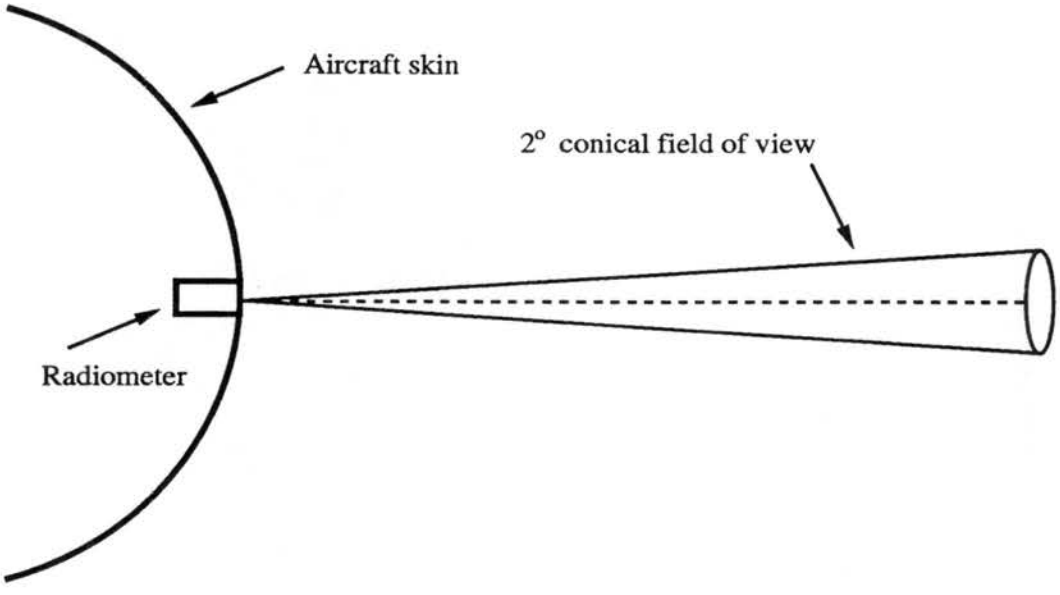

Figure 2.4: Diagram of the 2° conical field of view for the horizontally directed AOC modified Barnes PRT-5 radiometer aboard the P-3 aircraft. In this depiction the aircraft is traveling toward the page with a roll of 0°.

A CO_2 absorption band, centered at either 4.25 μm or 15 μm, is typically used since air becomes opaque at these wavelengths over a relatively short pathlength. CO_2 is a stronger absorber and emitter at 4.25 μm than 15 μm by an order of magnitude, thus the path length over which the observed radiance originates is longer at the 15 μm band. Hence, the roll of the aircraft in a vertical temperature gradient is important at the 15 μm band. Liquid water and ice also emit within the CO_2 bands. According to Irvine and Pollack (1968) liquid water is a stronger absorber, or emitter, at 15 μm than 4.25 μm by an order of magnitude (absorption coefficients of 3.6 m^{-1} versus 0.3 m^{-1} respectively), but ice is a weak absorber at both wavelengths (0.6 m^{-1}). When liquid water or ice particles are present in the sampled volume, the observed radiance, or temperature, is a weighted average of the emittance of the air and the particles. Thus, if the particles are a different temperature than the air, the observed temperature will be in error. Radiometric temperature measurements utilizing the 4.25 μm band would be

advantageous in a turbulent atmosphere with ample liquid water content (i.e. a hurricane), however, the radiometers onboard the NOAA WP-3D aircraft utilizes the 15 μm band. The roll of the aircraft and the temperature of the liquid-water or ice particles must be taken into account.

2.2.1 Aircraft Roll

During aircraft operation the radiometer is not typically oriented such that the field of view is centered directly along a path horizontal to the ground. Thus, the observed volume along the path length is not a uniform temperature, but rather an average over the vertical temperature gradient. Albrecht et al. (1979) showed that for a device sensing in the 15 μm band in clear air, at a height of 500 m, 90% of the signal that reached the instrument was from a path 200 m from the airplane. However in a stratus cloud with a liquid water content (q_l) of 0.2 g m^{-3}, 90% of the signal was from within 33 m of the aircraft. The calculation of path length is height dependent, and Astheimer (1967) showed at heights of 5 km (~550mb) in clear air that 90% of the signal would be from within 300 m from the plane. A radiometer on an airplane undergoing of a roll of only 10° from the horizontal in clear air is sensing air up to 35-50 m, depending upon altitude, vertically offset from flight level. Assuming a standard lapse rate of 7.0 °C km^{-1}, temperature errors can be 0.25-0.36°C. These errors could be removed by utilizing the lapse rate of the local environment, however local lapse rates are not well known or can quickly change in turbulent environments such as in hurricanes. A more effective technique would be to use clear air data only when the aircraft roll is minimized. For an aircraft undergoing a 10° roll in cloudy air, the shortened path length and near-moist adiabatic lapse rate result in maximum errors an order of magnitude smaller than those in clear air. Hence, it is reasonable to assume that in an optically thick cloud ($q_l > 0.2$ g m^{-3}) the temperature sensed by the radiometer is independent of roll and representative of flight level.

2.2.2 Liquid water and Ice

Liquid water and/or ice particles are encountered during hurricane penetrations. If the particles are at different temperatures (i.e. different emitted radiances) than the air, the air temperature derived from the observed volume average radiance will be in error. Thus, the determination of particle-air temperature differences for various environmental conditions must be examined. Through the laws of heat and vapor transfer, a liquid water or ice particle in steady state with its environment acquires the wet-bulb temperature of the environment. Only a motionless particle in saturated air has a wet-bulb temperature equivalent to the air temperature, however liquid or ice particles are not motionless and are not always in saturated environments.

Cloud liquid water drops typically have radii of 1-30 μm (Squires 1958) and terminal velocities on the order of 1 cm s^{-1} (Beard 1976). Thus, it can be assumed that cloud drops will acquire the vertical velocity of the air in which they are contained, resulting in the relative humidity of the air containing the drops as the primary factor in determining the temperature difference between cloud drops and the air. In updrafts, supersaturations are believed to be generally less than 1% with temperatures of growing cloud drops less than 0.1°C warmer than their environment (Pruppacher and Klett 1997). In downdrafts the air is typically subsaturated and the cloud drops acquire the wet-bulb temperature of the environment while evaporating. Shown in Figure (2.5) are wet-bulb depressions for various environmental relative humidities and temperatures observed within tropical cyclones at the 850 mb and 500 mb pressure levels. As shown, evaporating drops can be up to 3°C cooler than the air with larger differences at lower levels. However, cloud drops entering subsaturated regions with relative humidities less than 90% will evaporate in less than 20 s, and act to raise the humidity toward saturation. Thus observed cloud drop-air temperature differences in subsaturated regions with significant cloud liquid-water content will likely not exceed 1.0°C. Examples of such subsaturated regions include cloud edges and sustained updraft(cloudy)/downdraft(cloud-free) couplets where continuous mixing of cloud drops into the cloud-free downdraft by turbulent mixing can occur.

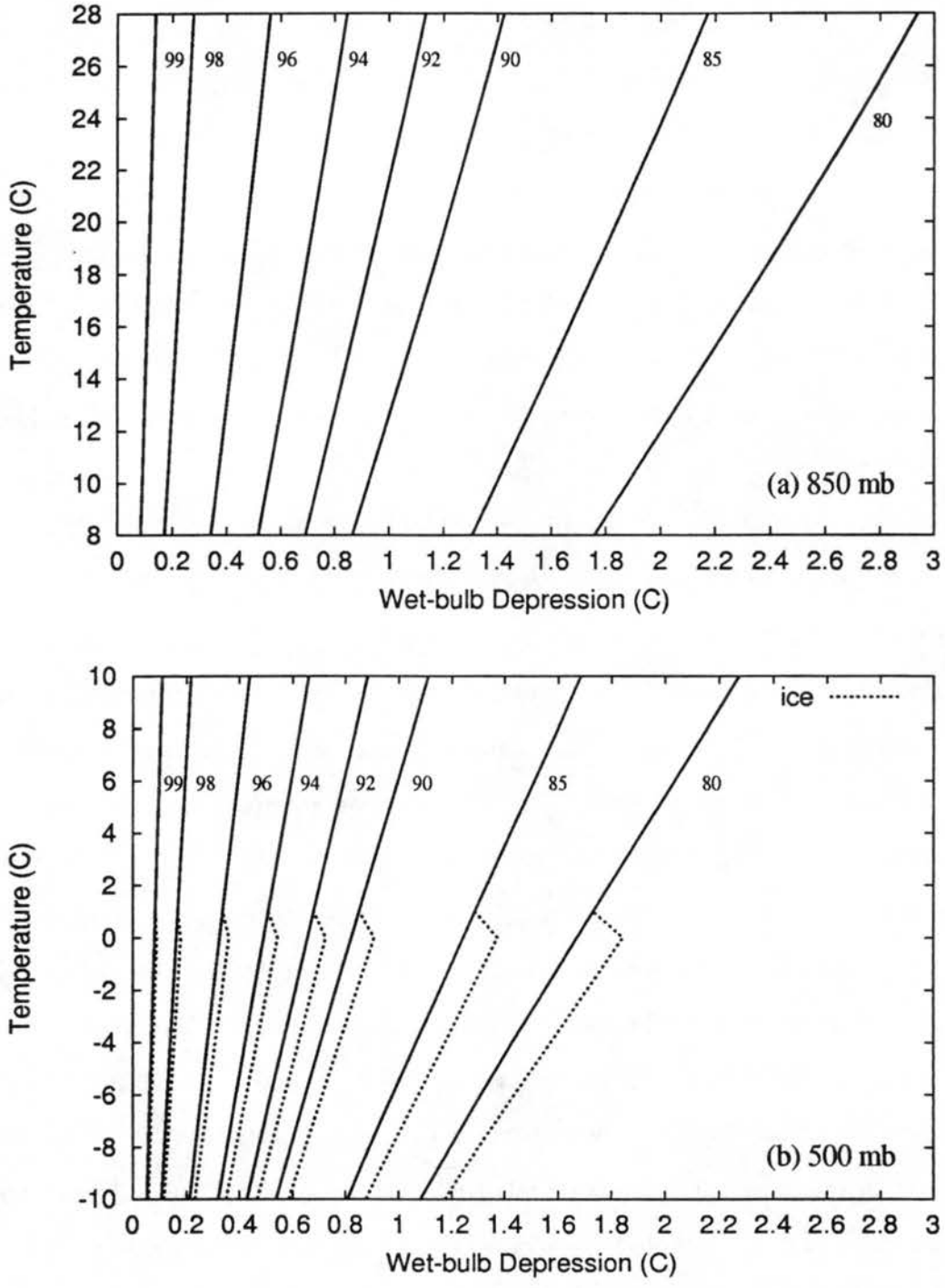

Figure 2.5: Wet-bulb depressions at (a) 850 mb and (b) 500 mb for given relative humidities over ranges of temperatures observed within hurricanes at the respective pressure levels. Assumed relative humidities are shown to the right of each line. Included at 500 mb is the wet-bulb depressions with respect to ice (dotted lines).

Telford and Warner (1962) investigated the subsaturation of a downdraft containing liquid water cloud droplets. For a parcel originally at saturation, the subsaturation becomes quasi-stationary within a few seconds (~10 s), and can be approximately described by the equation,

$$S_a \approx \frac{.0239w + 1.72 \times 10^{-6}n}{\sum r} \tag{2.13}$$

where S_a is the subsaturation of the air parcel expressed in percent, w is the vertical velocity in cm s^{-1}, n is the number of drops per gram of air, $\sum r$ is the sum in cm of the radii of all the drops in a gram of air. Assuming the typical cloud droplet concentrations and radii found in maritime trade wind cumuli of 6×10^4 drops per gram of air and 15 μm respectively (Squires 1958) are representative for clouds in hurricanes, a 5 m s^{-1} downdraft will result in a subsaturation of 0.9%. This corresponds to a wet-bulb depression of about 0.1°C for the evaporating cloud drops contained within the downdraft. A violent downdraft of 20 m s^{-1} results in a subsaturation of 3.6%, which is equivalent to a 0.2-0.4°C wet-bulb depression. However, it is likely sustained intense downdrafts will quickly evaporate the cloud drops. While violent downdrafts have been observed within tropical cyclones, 95% of all downdrafts are less than 3 m s^{-1} (Black et al. 1996). This agrees with other convective downdrafts observed in the tropics by Zipser and LeMone (1980) and Jorgensen and LeMone (1989). Thus, in this study it can be assumed cloud drops in updrafts and average downdrafts are in a saturated or quasi-saturated environment, and cloud drop temperatures are within 0.1°C of the air temperature.

Raindrops, having typical radii of 0.5-1.0 mm (Willis and Tattleman 1989) and terminal velocities of 5-8 m s^{-1} (Beard 1976), will not acquire the vertical velocity of the air in which they are contained, but rather their fall velocity will either be enhanced or slowed. In addition to the relative humidity of the air containing the raindrops, the actual fall velocity of the raindrops is a also a factor in determining the air-raindrop temperature difference. Falling liquid water drops attempt to come into thermal equilibrium with its local environment, either saturated or subsaturated, but their local environment is con-

stantly changing due to thermal and vapor gradients. Kinzer and Gunn (1951) derives an expression for the relaxation time, or the amount of time required for the difference between the steady state drop temperature and its actual temperature to decrease by a factor of e^{-1}, for a freely-falling water drop entering a new environment,

$$t_r = \frac{r^2 \rho_w c_w}{3 f_o (K + L_v D \frac{d\rho_{s,w}}{dT})} \tag{2.14}$$

where r is the drop radius, ρ_w is the density of water, c_w is the specific heat of water, f_o is the non-dimensional ventilation factor (approximately 10.0 for raindrops of 1 mm radii), K is the thermal conductivity of air, D is the coefficient of diffusion of water vapor in air, and $\frac{d\rho_{s,w}}{dT}$ is the mean slope of the saturated vapor-density-temperature curve between the drop surface and the environment (on the order of 10^{-4} kg K^{-1} m^3). Raindrops of radii 1 mm in a saturated environment have relaxation times of 7-8 s. Subsequently, large raindrops of radii 2.5 mm can have relaxation times up to 25 s[1]. Assuming a moist adiabatic lapse rate, saturation (thus, neglecting the second term in the denominator of (1.14)), and terminal velocities of 5-10 m s^{-1}, freely-falling raindrops of the aforementioned radii can be cooler than their steady-state thermal equilibrium (the local wet-bulb temperature) by 0.18°C and 1.25°C respectively. Equation (1.14) also predicts an evaporating drop will reach its equilibrium temperature in approximately one half the time of a non-evaporating drop. Thus, a drop in a subsaturated environment will be closer to the local wet-bulb temperature depending upon the extent of subsaturation. It seems evident large raindrops contain enough thermal mass that when freely-falling at a substantial velocity the rate of diffusion of heat by the environment to the drops can not maintain the drops at their local wet-bulb temperature, but rather at a slightly cooler temperature. Willis and Tattleman (1989), using a optical spectrometer, have shown that raindrop radii up to 2.5 mm have been observed in hurricane eyewalls and rainbands, but their concentration is two orders

---

[1]The relaxation time for typical cloud drops (radii $\approx$ 10 μm), assuming ambient saturation, is on the order of a few milliseconds. With terminal velocities around 1 cm s^{-1}, it can be assumed that cloud drops are at the local wet-bulb temperature.

of magnitude smaller than the concentration of the median raindrop radius of 1 mm. These results are consistent with numerous other raindrop concentration spectrums and fall speeds observed within the tropics and mid-latitudes. Therefore, for a given volume of air the average drop temperature departure from the local wet-bulb temperature is best represented by drops of radii 1 mm, with a departure for freely falling drops less than 0.2°C depending upon local relative humidities.

Raindrops within updrafts will either have their fall velocity reduced, or will be carried aloft in the updraft, depending upon the size of the raindrop and the strength of the updraft. The temperature gradient experienced by the drop during its relaxation time will be less, resulting in less of a drop temperature departure from the local wet-bulb temperature. Therefore, the assumption that raindrops within updrafts, assuming the updraft is saturated, are within 0.1°C of the local air temperature is reasonable. In downdrafts, raindrops will be falling faster than their terminal velocities and may be in a subsaturated environment. The temperature gradient which the drop experienced during its relaxation time increases, thus the drop may be additionally cooler than the local wet-bulb temperature. However, as shown earlier downdrafts begin to approach some degree of subsaturation even after a few seconds, and the raindrops will begin to evaporate. These two effects will tend to offset one another, and volume average drop temperatures in downdrafts would be within 0.2°C of the local wet-bulb temperatures. Raindrops in subsaturated regions not being influenced by significant vertical motions may be up to 3°C cooler than the air depending on local relative humidities, as shown in Figure (2.5).

So far, only the effects of liquid water drops on radiometric temperature measurements have been discussed, yet ice and graupel particles are typically observed during aircraft penetrations near and above the freezing level of hurricanes (Black and Hallett 1986). The absorption coefficient at 15 μm for ice (0.6 m^{-1}) is nearly an order of magnitude smaller than for water (3.6 m^{-1}) with little variation observed over the range of crystalline forms (Irvine and Pollack 1968). Thus, radiometric thermometers will only be significantly effected by ice particles in regions of high ice particle concentrations, or greater than 100

particles per liter, which is approximately 3.0 g m^{-3} of liquid water content assuming an ice bulk-density of 0.1 g cm^{-3}. Again, the possible particle-air temperature differences must be examined.

Small ice crystals growing by steady-state diffusion or riming processes in updrafts saturated with respect to water (supersaturated with respect to ice), are believed to be less than 0.1°C warmer than the ambient air (Pruppacher and Klett 1997). However, large ice particles and graupel undergoing heavy riming in regions of high supercooled water content may have an insufficient heat transfer to the air to balance the release of latent heat. Such particles may be warmer than the ambient air by more than 0.1°C. In subsaturated regions direct sublimation or a combination of melting and evaporation will occur. Shown in Figure (2.5b) are the wet-bulb depressions with respect to ice for various ambient relative humidities and temperatures observed within tropical cyclones at 500 mb. Direct sublimation of ice particles at heights above 0°C can lead to particle-air temperature differences of up to 2.0 °C. Melting can result in a more substantial particle-air temperature difference as the falling particle's temperature will remain near 0°C till all the ice is melted. The distance a particle travels below the 0°C level before complete melting depends on the crystal size, lapse rate, and ambient relative humidity. Theoretical distances for snowflakes of diameter 10 mm in an environment of 90% relative humidity and a lapse rate of 6.0°C km^{-1} are 500 m before complete melting (Pruppacher and Klett 1997), resulting in particle-air temperature differences of up to 3.0°C. This is consistent with typical brightband depths observed by radar in hurricanes. Graupel particles, with more mass to be melted and larger terminal velocities, would travel further distances before complete melting, and thus, particle-air temperature differences greater than 3.0°C are possible.

A few observational studies of ice particles in hurricanes have been made. Black and Hallet (1986) showed from observations in three hurricanes near and above the freezing level that high ice particle concentrations were typically found along updraft edges and in downdrafts associated with the eyewall and rainbands. Updrafts less than 5 m s^{-1} or

colder than -2.0°C were dominated by graupel and column ice particles with cloud liquid-water contents less than 0.5 g m^{-3}. Ice particle concentrations in such updrafts were 10-50 L^{-1}, of which 5-10 L^{-1} were graupel. Strong updrafts (> 5 m s^{-1}) near the freezing level were dominated by supercooled cloud liquid-water and raindrops. eyewall downdrafts contained the highest total ice concentrations with frequent values greater than 100 L^{-1}, of which 20-30 L^{-1} were graupel. Peak ice particle concentrations reached as high as 300 L^{-1}, of which the majority where columns. Less than 0.1 g m^{-3} of cloud liquid-water was found in the downdrafts. Ice particle concentrations in rainbands averaged 40-60 L^{-1} with some graupel, and 1-15 L^{-1} in stratiform regions with aggregates dominating. No cloud liquid-water was observed above the freezing level in stratiform regions. Black and Hallett (1986) argued that hurricane updrafts become quickly glaciated due to observed high concentrations of columns, which only grow near the -4.0°C level. Furthermore, downdrafts can seed adjacent updrafts with ice particles by turbulent mixing, maintaining graupel formation. Houze et al. (1992) confirmed many of these observations in Hurricane Norbert (1984).

These observations indicate ice particles will significantly effect the radiometer observed temperatures only along the edges of updrafts and in downdrafts, particularly in the eyewall. The edges either of strong updrafts or updrafts near the freezing level may contain heavily rimed graupel or ice particles that may be 0.2°C warmer than the ambient air. Ice found in updrafts colder than -2.0°C or weaker than 5 m s^{-1} will be less than 0.1°C warmer. Ice particles in downdrafts may be 2-3°C cooler than the ambient air due to sublimation or melting.

2.3 Cooled-mirror hygrometers

A cooled-mirror hygrometer measures dew point by minimizing the amount of liquid water condensed upon a chilled mirror with the assumption that the dew point of the ambient air is the temperature of the mirror when condensation first begins to form. While this procedure works well in clear air, the presence of clouds and precipitation introduce the possibility of water drops or ice contacting the chilled mirror. The hygrometer will

then react by heating the mirror in an attempt to evaporate the excess water or ice, resulting in an erroneously warm dew point. Such warm dew points have been observed by Jorgensen and LeMone (1989) in convective clouds. Within clouds, the error may be approximately corrected by assuming quasi-saturated conditions for an accurate air temperature measurement. Subsaturated regions encountered when the mirror is wetted will not be resolved, and can not be corrected for analytically since the degree of wetting is unknown. With the presence of condensation on the mirror being optically determined across the air flow through the sensor, particulates within the air may scatter the original signal producing a too-warm dew point even if the mirror was not wetted. Furthermore, cooled-mirror hygrometers, including the General Eastern Model 1011B used in this study, suffer from slow response times, as discussed by LeMone (1980). Such instruments either have response times on the order of 5-20 s, or can resolve vapor gradients of 2°C s^{-1}. Thus, at aircraft speeds of 130 m s^{-1}, vapor gradients associated with small clouds and cloud edges may not be accurately resolved or located.

2.4 Summary

Air temperatures observed from an aircraft are susceptible to errors in the presence of liquid water and ice. Immersion thermometers, such as the Rosemount 102 sensor, are directly sensitive to hydrometeor impingment upon their sensing surface. During hurricane penetrations theoretical temperature errors in warm clouds for a completely wetted sensor are 4-6°C. The errors may be 1-2°C larger if the ambient environment is subsaturated, or if the inner housing surface is also wetted. Temperature errors in cold clouds may be as large as 10°C. Likewise, dew point temperature errors from hydrometeor impingment upon the sensing surface produces erroneous supersaturations.

A horizontally directed infrared radiometer offers an alternative method of measuring flight-level air temperature without direct contact with the air or hydrometeors. The use of the 15 μm CO_2 spectral band introduces possible errors due to aircraft roll and hydrometeors in the sampled volume. Observed hydrometeors in tropical convection are typically either the same temperature as the air or less than 0.1°C different than the air, producing

minimal errors. However, in the melting layer and in subsaturated regions containing high liquid-water contents (e.g. strong precipitation-filled downdrafts, stratiform precipitation, and along cloud edges) air-hydrometeor temperature differences may be large, resulting in radiometer temperature errors greater than 0.1°C. More importantly, theoretical temperature errors produced by hydrometeors are an order of magnitude smaller for the 15 μm radiometer than the Rosemount immersion thermometer. Thus, accurate flight-level thermodynamic profiles in regions of clouds and precipitation can be obtained from the radiometer derived temperatures during periods of minimal aircraft roll if combined with a reasonable assumption of the dew point temperature when it erroneously exceeds the temperature.

2.5 Synopsis

- Immersion thermometers, such as the Rosemount 102 sensor, may theoretically experience temperatures errors of 4-10°C from instrument wetting during passage through clouds and precipitation.
- Immersion hygrometers, such as a cooled-mirror model, may erroneously measure high dew points due to instrument wetting during passage through clouds and precipitation.
- A radiometric thermometer can accurately measure air temperature through clouds and precipitation since errors induced hydrometers are typically less than 0.1°C.
- A radiometer can be used to obtain accurate flight-level thermodynamic profiles in regions of clouds and precipitation when combined with corrected dew points.

Chapter 3

DATA

3.1 Flight-level data

Flight-level data was obtained from the Hurricane Research Division (HRD) of NOAA for all hurricane penetration flights in which temperatures were acquired using the AOC modified Barnes PRT-5 CO_2 side-looking radiometer. The data was collected by the two NOAA WP-3D research aircraft (identified as H[1], or N42RF, and I, or N43RF) during 84 separate flights conducted from 1984 to 1996 through 25 Atlantic and 4 Eastern Pacific hurricanes. Flights were flown at pressure levels ranging from 900 mb to 400 mb with storm intensities ranging from Category 1 to 5 on the Saffir-Simpson scale. Various stages of intensity change were also encountered during different individual flights of a single storm and from one storm to another. Flight patterns are determined in advance and are generally maintained during penetration. However, flight patterns were occasionally deviated from to avoid strong convective cores within the eyewall (P. Black 1998, personal communication).

Flight-level radial legs were obtained from the HRD archived database for each flight with CO_2 side-looking radiometer temperatures. An inventory of these radial legs in given in Table (3.1), while an inventory of all WP-3D radial legs in the HRD archived database is given in Table (3.2). A radial leg is defined as either an inbound path toward the storm center or an outbound path from the storm center. The radial legs in the database were previously processed from the raw flight data using the methods described in Willoughby

---

[1]The CO_2 side-looking radiometer onboard the H aircraft had an optics failure in 1992. The radiometer has yet to be fixed since the primary temperature sensor is considered to be the Rosemount instrument (R. McNamara 1998, personal communication).

Table 3.1: Inventory of Atlantic and East Pacific hurricane radial legs with side-radiometer data. Included is the number of flights and the Saffir-Simpson category during flight.

Hurricane mb	Year Total	Number of Flights Category	Radial Legs 900	850	700	600	500	400	Total	Category
Diana	1984	7	10	80					90	1,2,3,4
Danny	1985	2		16					16	1
Elena	1985	7		88					88	1,2,3
Gloria	1985	7		10	32		6	4	52	1,2,3,4
Juan	1985	2		18					18	1
Emily	1987	3			16	2	38		56	3
Floyd	1987	1		12					12	1
Florence	1988	2	20						20	1
Gilbert	1988	6		22	28				50	2,3,4,5
Joan	1988	1		6					6	3
Dean	1989	1	4			8			12	1
Gabrielle	1989	1	4		8				12	3
Hugo	1989	6				28	8	4	40	2,3,4,5
Jerry	1989	1	9						9	1
Gustav	1990	4		10	30				40	1,2,3
Bob	1991	2		4			4		8	1
Claudette	1991	2			38				38	2,3
Emily	1993	3					16		16	1,3
Erin	1995	1			16				16	1
Iris	1995	1				8			8	1
Luis	1995	4				24	16		40	4
Opal	1995	1				4			4	2,3,4
Edouard	1996	2			22				22	4
Fran	1996	2		10		4		4	18	3
Hortense	1996	2		16					16	2,3
Norbert	1984	6		8	36		30		74	3,4
Jimena	1991	3		4	18	4			26	4
Tina	1992	2		20					20	1
Olivia	1994	2				30			30	2,3,4
ATL-Total		71	47	292	190	78	88	12	705	
EPAC-Total		13		32	54	34	30		150	
Total		84	47	324	244	112	118	12	855	

Table 3.2: Inventory of Atlantic and East Pacific hurricane P-3 radial legs in the HRD archive database by flight level and Saffir-Simpson category during flight times.

		Number of	Radial Legs							
Hurricane	Year	Flights	900	850	700	600	500	400	Total	Category
Anita	1977	1			20				20	5
David	1979	3		24					24	1
Frederic	1979	6	20	32			10		62	1,2,3,4
Allen	1980	11	4	28	49	32	12		125	3,4,5
Gert	1981	5		58					58	1,2
Alicia	1983	4		50					50	1,2,3
Diana	1984	7	10	80					90	1,2,3,4
Danny	1985	2		16					16	1
Elena	1985	9		122					122	1,2,3
Gloria	1985	7		10	32		6	4	52	1,2,3,4
Juan	1985	2		20					20	1
Emily	1987	3			16	2	38		56	3
Floyd	1987	3	10	12					22	1,2
Florence	1988	2	20						20	1
Gilbert	1988	6		22	28				50	2,3,4,5
Joan	1988	1		6					6	3
Dean	1989	2	4			8			12	1
Gabrielle	1989	2	4		8				12	3
Hugo	1989	6				28	8	4	40	2,3,4,5
Jerry	1989	1	9						9	1
Gustav	1990	9		48	36				84	1,2,3
Bob	1991	2		4			4		8	1
Claudette	1991	2			38				38	2,3
Andrew	1992	1						4	4	2,3
Emily	1993	7	10	14			20		44	1,3
Iris	1995	3		20		14			34	1
Luis	1995	4				24	16		40	4
Marilyn	1995	2		6					6	1
Opal	1995	1				4			4	2,3,4
Edouard	1996	5			22	30			52	4
Fran	1996	2		10		4		4	18	3
Hortense	1996	2		16					16	2,3
Lili	1996	3		28					36	1
Norbert	1984	6		8	36		30		74	3,4
Jimena	1991	3		4	18	4			26	4
Tina	1992	4		10	6	6		4	26	1,4
Olivia	1994	4			30	30			60	2,3,4
ALT Total		140	205	626	249	146	114	16	1,356	
EPAC Total		17		22	90	40	30	4	186	
Total		157	205	648	339	186	144	20	1,542	

et al. (1982), Willoughby and Chelmow (1982), and Samsury and Zipser (1995). A brief overview of the process is given here for completeness. Aircraft instrumentation records flight-level kinematic and thermodynamic data at a 1-Hz rate during each flight. The 1-Hz data is partitioned into a storm-relative coordinate system consisting of radial, tangential, and vertical winds, temperature, dew point, geopotential height, cloud water content (if available), and aircraft location given in latitude, longitude, and time. Flight-level winds were determined from dual inertial-navigation equipment (INE). In post-flight re-navigation the INE data was combined with Omega corrections through a Kalman filter, thus reducing errors due to a Schuler oscillation. The corrected INE derived winds were used to determine the dynamic storm center, the track, and then the storm relative fields with the storm motion vector removed from the winds. The storm-relative 1-Hz data was then partitioned into 0.5 km bins using a running Bartlett triangular-shaped filter of all the data within 1.0 km of the bin center. This is equivalent to filtering data within 7-8 s of the center of each bin, with 3-4 s between each bin, for typical aircraft speeds of 130 m/s. A Bartlett filter removes high frequency oscillations from the data without shifting the phase of the significant peaks. Each radial leg consists of 300 bins, or up to 150 km from the storm center of radial data. The temperatures and dew points were extrapolated along a moist-adiabat from flight level to the reference pressure level. This correction was typically small and applied uniformly along the leg. Furthermore, the temperature and dew point were obtained from the Rosemount immersion thermometer and General Eastern hygrometer respectively. In an attempt to remove instrument wetting errors (Willoughby 1997, personal communication), the temperature and dew point data were corrected according to the method described by Zipser et al. (1981). This method will be discussed in Chapter 4 and evaluated in Chapter 5. For future reference this dataset will be referred to as dataset "A".

To compliment the previously processed radial legs, the 1-Hz flight-level data of both air temperatures from the Rosemount immersion thermometer and the AOC modified Barnes PRT-5 radiometer, dew point, ambient air pressure, altitude, aircraft true airspeed,

roll, and the aircraft location given in latitude, longitude, and time were obtained for the entire length of each flight. A Bartlett triangular-shaped filter was applied using a running 11 s window width to all the 1-Hz data, and evaluated every 5 s. The original 1-Hz data was not retained due to computer hard disk storage capabilities given the large volume of data utilized in this study. For future reference this dataset will be referred to as dataset "B". Cloud-water content measured by the Johnson-Williams probe (discussed in more detail below) was also obtained in this data format, but for only a subset of the total radial legs with both cloud-water and radiometer data. The subset will be used to evaluate the definition of clear-air used in this study.

The effects of two different time filtering windows on the data was examined. A Bartlett filter with a 15 s (the equivalent for dataset A) and an 11 s window width was applied to a sample of 1-Hz temperature data from a single flight. The temperature difference between filtered data with the two windows widths was $0.00001 \pm 0.013°C$. The standard deviation is an order of magnitude less than the standard deviation between either filtered dataset with the original data ($\pm 0.19°C$). Thus, the the two windows widths over which the filter was applied does not introduce a significant difference between dataset A and B. This is important because datasets A and B will be combined during temperature profile reconstruction (described in Chapter 4). In the process, two adjacent 5 s temperature data points from dataset A may be linearly averaged to incorporate the data in the storm-relative grid system of dataset B. The temperature difference between linearly-averaged 11 s filtered data and 15 s filtered data is $0.0008 \pm 0.05°C$. Again, the variability is small over these scale, and a phase shift of significant peaks will not occur from the linearly weighted averaging.

The 1-s vertical air velocities in dataset "A" are determined by subtracting the vertical ground speed from the vertical airspeed. The vertical ground speeds are computed with an algorithm developed at AOC and described by Black et. al. (1994). The vertical airspeed is calculated from the standard "gust equation" (Axford 1968; Jorgenson et al. 1985; Jorgenson and LeMone 1989) and has an absolute accuracy of about ± 1.0

m s^{-1}. Jorgenson et al. (1985) noted offsets in the 1-s zero vertical velocity in non-convective regions that were typically 0.1-0.4 m s^{-1} and always positive. Samsury and Zipser (1995), using radial legs from database "A", computed the mean vertical velocity of each leg to determine the zero vertical velocity offset and removed the offset from the leg. Furthermore, they set a critical offset threshold of 1.5 m s^{-1}, and discarded radial legs with mean vertical velocities that exceeded the threshold. The mean vertical velocities were computed for each reconstructed radial leg (see Chapter 4 for reconstruction methodology and table of reconstructed radial legs), and the average offset was +0.2 m s^{-1} (0.45 m s^{-1} standard deviation) with a maximum offset of +2.3 m s^{-1}. All radial legs were visually inspected, particularily the 9 radial legs that exceeded the 1.5 m s^{-1} threshold, and the large positive offsets are believed to be an artifact of the dominance of convective updrafts in the hurricane inner core, as shown by Black et al. (1996). To check this the offset in non-convective regions ($|w| < 1.0$ m s^{-1}) was computed for each radial leg resulting in an average of 0.04 m s^{-1} (0.15 m s^{-1} standard deviation) with a peak offset of 0.52 m s^{-1}. Thus, the offsets are considered to be negligible (and not removed) since they are within the 1.0 m s^{-1} accuracy limits of the P-3 winds.

3.2 Cloud-Physics data

The cloud physics data collected by the WP-3D is comprised of cloud-droplet liquid water content measured by the Johnson-Williams (JW) instrument and precipitation particle measurements obtained from the Particle Measuring Systems (PMS) two-dimensional (2D) optical array probes. The JW sensor is a heated platinum wire sensitive to cloud drops primarily less than 0.03 mm in diameter (Knollenberg 1972). JW data was available for about 80% of the radial legs. The PMS cloud probe (2D-C) has a diameter sensitive range of 0.05-1.60 mm in 0.05 mm increments, and the precipitation probe (2D-P) has a range of 0.20-6.4 mm with increments of 0.2 mm. The PMS data was analyzed at HRD following the methods described by Black and Hallett (1986) and Houze et. al. (1992). PMS data collected at 500 mb and above contained primarily ice particles. In order to obtain liquid water contents, the effective ice particle bulk density was determined following

methods of Black (1990). The 2D data was averaged over 6 s (horizontal resolution of 0.9 km) for flights at 500 mb. In order to obtain a more stable estimate of the raindrop size distribution, the 2D data was averaged over 10 s (resolution of 1.3 km) for all flights at levels below 500 mb. Separate liquid water contents were calculated for each instrument and particle phase (if ice was present) from their respective observed particle distribution, resulting in up to four liquid water content values for any given data point. Processed PMS data was available for roughly 20% of the radial legs.

3.3 Best-track data

Individual storm tracks and intensities were determined from the "best track" database maintained by the Tropical Prediction Center (TPC), formerly the National Hurricane Center (NHC), for both the North Atlantic and Eastern North Pacific basins. The North Atlantic basin includes not only the subtropical and tropical North Atlantic Ocean, but also the Caribbean Sea and Gulf of Mexico. The term 'best' refers to a combination of all reliable existing track and intensity observations during post-season analysis to determine the most accurate track and intensities for each storm. The Atlantic basin database extends back to 1886, however previous studies (Neumann et al. 1993; Landsea 1993) have questioned the reliability of this database prior to routine aircraft reconnaissance flights, which started in 1944, and continuous coverage from geostationary and polar orbiting satellites, which began in 1966. The Eastern North Pacific database begins in 1949, however only data after 1965 is consider reliable due to the advent of continuous satellite coverage over the basin. Thus, for the storms in this study the "best track" data is reliable.

3.4 SST data

Sea surface temperatures (SST's) in the vicinity of each hurricane were determined from the high-resolution global COADS SST database described by Smith et al. (1996). The database consists of in situ ship and buoy SST data interpolated using empirical orthogonal functions (EOFs) onto a grid with 2° spacing, and are available as monthly

values for 1950-1990. For 1991-present, the in situ data is supplemented with satellite SST retrievals when available, and is available as monthly values on a global grid with 1° spacing. A monthly mean may not be representative of actual SST's under a hurricane at any given time due to the overturning of the oceanic mixed layer and a subsequent lowering of SST's during storm passage (Shay et al. 1989). The drop in SST has been observed to be 2-5°C in the rear of the storm, with an average drop over the storm circulation of 1-2°C. The drop in SST is a function the storm's intensity and translation speed, along with the depth of the oceanic mixed layer, or thermocline. Furthermore, SST values are derived from the top 10 m of the ocean, and in the case of satellite retrieval, the top 1 cm. Solar energy can easily warm the surface water 1°C above the mixed layer temperature. The passage of a hurricane will rapidly mix the warmer surface water with the mixed layer water below. The depth of the 26°C isotherm in the oceanic mixed layer may be up to 100 m, representing a significant deep source of energy despite the overturning. Thus, in recent years the heat content of the oceanic mixed layer has been argued to be a better measure of the energy to available to a storm than SST values (Shay 1998). However, considering the general lack of SST and mixed layer temperature available under hurricanes, the monthly values provide a reasonable, qualitative estimate of SST's for the large sample of storms used in this study.

3.5 Eyewall sounding data

Eyewall sounding data was collected using National Center for Atmospheric Research (NCAR) GPS dropwindsondes developed by Vaisala Inc. The sondes utilize the GPS satellite navigation to provide improved accuracy and resolution of altitude, winds, pressure, temperature and humidity over previous dropwindsondes. Measurements to the surface are possible with a vertical resolution of ~5 m. Performance specifications and instrument design are contained in Hock and Franklin (1999). In regards to this study, temperature is measured with a 3 mm silicon diaphragm designed for fast temperature response, however, a detectable response lag is present and removed in post-processing. The non-wettable silicon diaphragms shed water easily, thus instrument wetting errors are minimized. Hu-

midity is measured by a thin capacitive film dual-element sensor. Condensation and icing errors are minimized by the use of two sensors and a heating cycle: one sensor measures the relative humidity while the second sensor is heated and allowed to recover. Performance tests indicate temperatures are accurate in and out of cloud to 0.2°C, with humidity accurate to $< 5\%$, and pressure to 1.0 mb.

GPS sondes were first utilized in hurricanes during the 1997 season, and were deployed from the P-3 aircraft in intense Hurricanes Guillermo and Erika. Post-processing and quality control was performed at HRD. A total of 9 sondes were dropped in and near the eyewall of Guillermo on August 3, while 25 sondes were dropped in the eyewall of Erika on September 7 and 8. No concurrent flight-level data is available to date for either of these storms. Despite the dual element humidity sensor design, 9 of the 34 sondes observed saturation at the surface. Such soundings were suspected of relative humidity sensor wetting errors and not used in this study.

Chapter 4

TEMPERATURE PROFILE RECONSTRUCTION

4.1 Previous Reconstruction Methods

The accurate measurement of static air temperature can only be achieved with a completely dry temperature sensor. A completely wetted temperature sensor yields the wet-bulb temperature of the local ambient air. A partially wetted sensor yields a temperature between the static air temperature and the wet-bulb temperature depending upon the extent of wetting. Without knowledge of the extent of wetting on the sensor analytic corrections are impossible. Several methodologies have been proposed and widely used to remove instrument wetting errors. These previous methods along with the method used in this study are summarized below and in Table 4.1.

Zipser et al. (1981) examined GATE aircraft data and suggested that both immersion temperature and dew point instruments were most commonly wetted at the same time, with temperatures erroneously too cool, dew points erroneously too warm, and maximum errors of $\sim$ 1.5°C. Zipser et al. (1981) proposed a simple method to correct for these errors: If the temperature (T) exceeded the dew point (T_d), saturation was assumed, and both T and T_d were corrected to the average of the two measurements. Barnes et al. (1983), Jorgenson (1984a,1984b), Barnes and Stossmeister (1986), and Powell (1990) used this methodology to correct T and T_d during penetrations of hurricane clouds and precipitation. The T and T_d profiles for the storm-relative radial legs of dataset A also utilized this correction method. Barnes et al. (1983) had data available from a CO_2 radiometer, but questioned the absolute temperature values. Only the relative changes of the radiometer temperatures were used to provide confidence in the correction method.

Jorgenson and LeMone (1989) utilized the side-looking CO_2 radiometer (SR) onboard the P-3 aircraft for temperature profiles through tropical oceanic convection near Taiwan. A time-dependent calibration drift of the SR was removed by determining the bias between the temperature data of the SR and the Rosemount immersion sensor (ROSE) in air with no liquid water present, or so-called clear air. The bias was computed from about 100 s of data and then subtracted from the SR temperatures. If the dew point exceeded the SR temperature, saturation was assumed, and the dew point was set to the SR value. All data was utilized irrespective of aircraft roll. Jorgenson and LeMone (1989) noted liquid water also emits in the 15 μm band, and suggested significant errors up to 1.0 K could occur at the edges of clouds and in subsaturated precipitation where drops may be cooler than the air. Despite these concerns, liquid water drops were assumed to be the same temperature as the air. Barnes et al. (1991), Ryan et al. (1992), Lucas et al. (1994), and Barnes and Powell (1995) utilized this methodology to correct for instrument wetting.

In a more recent study, Wei et al. (1998) used a Ophir radiometer that senses at the 4.25 μm CO_2 band (effects from liquid water and aircraft roll are less than at the 15 μm band) to investigate buoyancy in TOGA COARE (Tropical Ocean Global Atmosphere Coupled Ocean-Atmosphere Response Experiment) convection from aircraft data. A ROSE sensor was used as reference in clear air, and the Ophir bias was removed. A lag of 10 s was commonly found between cloud exit, with a cloud defined as a region when the liquid water content exceeded 0.03 g m_{-3}, and the recovery of the ROSE upon drying. Therefore, data further than 20 s ($\sim$ 2.5 km) from a cloud was considered to be clear air. Temperature profiles through clouds were determined from a combination of low-pass filtered ROSE clear air data with high-pass filtered and despiked Ophir data.

The goal of the temperature reconstruction is to produce reliable thermodynamic radial profiles, free of significant instrument wetting errors. While liquid water must be present for instrument wetting to occur, the presence, or lack there of, does not indicate that wetting is, or is not, occurring. A cloud may be penetrated without any wetting of the sensors. Likewise, instruments may still be wetted for several seconds after exiting a

Table 4.1: Summary of reconstruction methods used to remove instrument wetting errors.

Proposed Method	Primary Temp. Sensor	Other Sensors Used	Clear Air Defined By	Temperature Correction	Dew point Correction
Zipser et al. (1981)	Rosemount	Cooled-mirror hygrometer	None	T set to average of T_{ROSE} and T_d when $T_d > T_{ROSE}$	Saturation assumed when $T_d > T_{ROSE}$
Jorgenson and LeMone (1989)	AOC modified Barnes PRT-5 (15 μm) radiometer	Rosemount Cooled-mirror hygrometer JW sensor PMS probes	Absence of LWC	T_{ROSE} assumed accurate in clear air. Average T_{SR} offset removed using clear air data. New T_{SR} assumed accurate in clouds.	Saturation assumed when $T_d > T_{SR}$
Wei et al. (1998)	Ophir (4.25 μm) radiometer	Rosemount Cooled-mirror hygrometer Lyman alpha hygrometer UV hygrometer FSSP probe	Absence of LWC	T_{ROSE} assumed accurate in clear air. T_{Ophir} offset removed using clear air data. Combine filtered T_{ROSE} and T_{Ophir} in clouds.	Saturation assumed when cloud LWC > 0.03 g m^{-3}
This study	AOC modified Barnes PRT-5 (15 μm) radiometer	Rosemount Cooled-mirror hygrometer JW sensor	T_{ROSE} - T_d < 0.2°C, |Roll| < 3.0°	T_{ROSE} assumed accurate in clear air. T_{SR} offset removed using clear air data. New T_{SR} assumed accurate in clouds. Linear interpolation through high-roll data.	RH of 99% assumed when $T_d > T_{SR}$

region with liquid water content depending upon the extent of wetting, as shown by Wei et al. (1998). The correction method proposed by Zipser et al. (1981) will accurately correct for wetting only when the dew point and temperature errors are coincidentally equal and opposite. However, the sensors have different exposures to the environment which could result in dissimilar wetting. Furthermore, the erroneous response of each instrument may be different for equivalent wetting. In either case, the temperature may be over-corrected or under-corrected. The correction method proposed by Jorgenson and LeMone (1989) did not consider aircraft roll, which can be considerable as discussed in Chapter 2. Furthermore, cloud and precipitation liquid water measurements were required to determine clear air from cloudy air in the latter two correction schemes. The goal of the present correction and reconstruction method is to minimize possible errors while maintaining quality in the maximum amount of data, even if cloud and precipitation liquid water measurements are not available.

4.2 Present Reconstruction Methodology

Shown in Figure (4.1) are the SR and ROSE temperatures, the dew point, the cloud water content measured by the JW instrument, and the difference between the SR and ROSE temperatures from dataset B for one penetration through hurricane Gilbert on September 14, 1988 at 700 mb. The center of the storm for this penetration is located at 36,750 s into the flight. In clear air both instruments are assumed to be properly measuring flight level air temperature during low aircraft roll situations without possible errors from liquid water. The SR temperature is offset from the ROSE temperature by a relatively constant bias (e.g. around 37000 s) due to the known time-dependent drift of the SR calibration. However, in saturated regions ($T_d \approx$ ROSE and JW > 0.0 g m^{-3}) the drift offset changes, indicating that instrument wetting is occurring during this penetration. Further evidence is provided when the dew point becomes greater than the ROSE temperature around 37,200 s and 36,800 s. Thus, the present reconstruction method will remove the drift bias from dataset B using clear air data, adjust the dew points when greater than the temperatures, and fit the data to a storm-relative grid system on

constant pressure surfaces. Shown in Figure 4.2 is a flow chart describing the temperature reconstruction method.

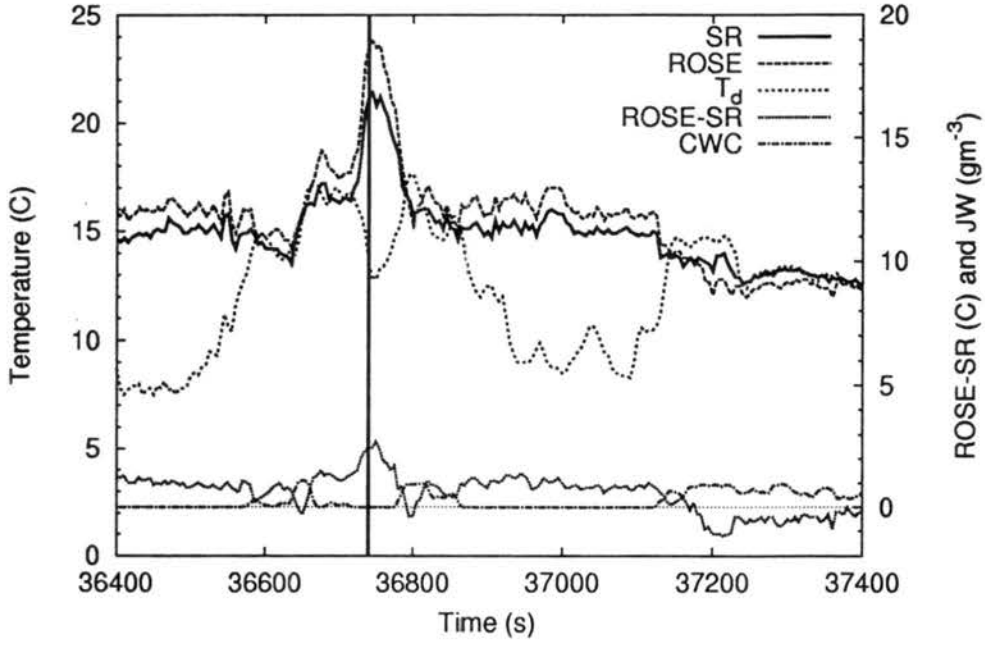

Figure 4.1: Thermodynamic data prior to temperature reconstruction for one penetration through hurricane Gilbert on September 14, 1988 at 700 mb. Shown are the SR, ROSE, and dew point (T_d) temperatures, cloud water content (CWC) measured by the JW instrument, and the difference between the SR and ROSE temperatures. The vertical solid line represents the center of the eye.

First, clear air is defined as a region with T_d < ROSE - 0.2°C. This definition was used for several reasons. First, the ROSE sensors and cooled-mirror hygrometers are rarely inoperative during research flights, however cloud and precipitation liquid water content instruments are frequently inoperative. Thus, restricting the clear air definition to the presence of liquid water would limit the amount of data that could be corrected and the ability to correct it. Up to 100 additional radial legs can be reconstructed with the present definition. Furthermore, hurricanes typically have large regions of cloud-free stratiform precipitation of low drop concentrations. The typical figure-four flight pattern may prevent the aircraft from exiting this stratiform region for severals hours during multiple penetrations of the eye. Thus, clear air defined by the lack of liquid water present would limit the available data used to remove the bias. With the bias being time

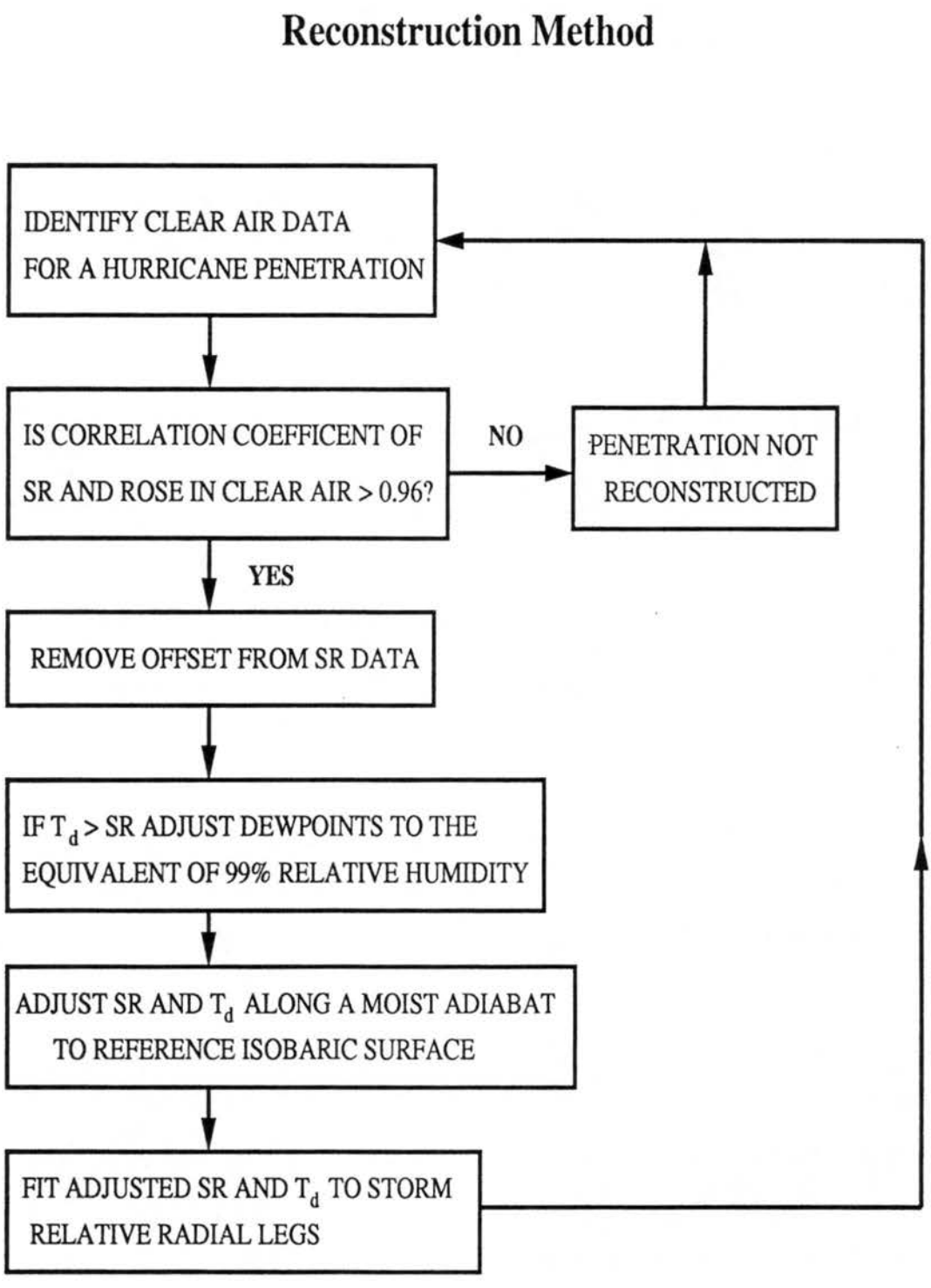

Figure 4.2: Flow chart describing the temperature reconstruction method.

dependent, temperature discrepancies between the SR and ROSE could be the result of the ineffective removal of the bias over such long periods, rather than instrument wetting. The critical value of 0.2°C was chosen because dew point data for storms prior to 1986 was prevented from exceeding the ROSE temperature during post-flight analysis. During visual inspection of data from Gloria 1985 the dew point was up to 0.2°C cooler than the ROSE temperature in regions of obvious instrument wetting. However, the advantage of this critical value is to place a buffer between the beginning or end of the instrument wetting (T_d > ROSE) and the clear air data. The buffer is similar to the time lag used by Wei et al. (1998) to permit sensors to completely dry after wetting. Finally, the use of the critical value will take into account slight instrument wetting in subsaturated regions due to stratiform precipitation where the dew point may not exceed the ROSE temperature despite the influence of liquid water drops. All data with $T_d \geq$ ROSE - 0.2°C is considered suspect of instrument wetting errors, or for future reference "wet air".

Next, the drift bias was removed from the SR values. A linear fit was applied to the clear air, low-roll SR and ROSE data of each hurricane penetration of each flight. A penetration consists of two radial legs, one inbound and one outbound, and is defined such that the first penetration begins once the aircraft has reached the desired flight level for observing the storm and continues to the temporal midpoint between the first and second eye passage, as shown in Figure (4.3). Subsequent penetrations are defined between these midpoints with the last penetration ending when the aircraft leaves the storm observation flight level for the return ferry. The application of the regression to individual storm penetrations minimizes the time dependence of the bias. Visual inspection of the data indicated that flight-level temperature deviations up to 2°C resulted during sampling of clear air while the aircraft was oriented with a large roll. Thus, in order to maximize the quality of flight level temperatures used for each linear fit, a critical roll value of 3.0° from the horizontal was used to distinguish between low and high roll data in clear air. Expected SR temperature deviations from flight level due to a 3.0° roll will only be 0.05-0.08°C for the altitude dependent pathlengths of 200-300 m respectively with a lapse rate of 6.5°C

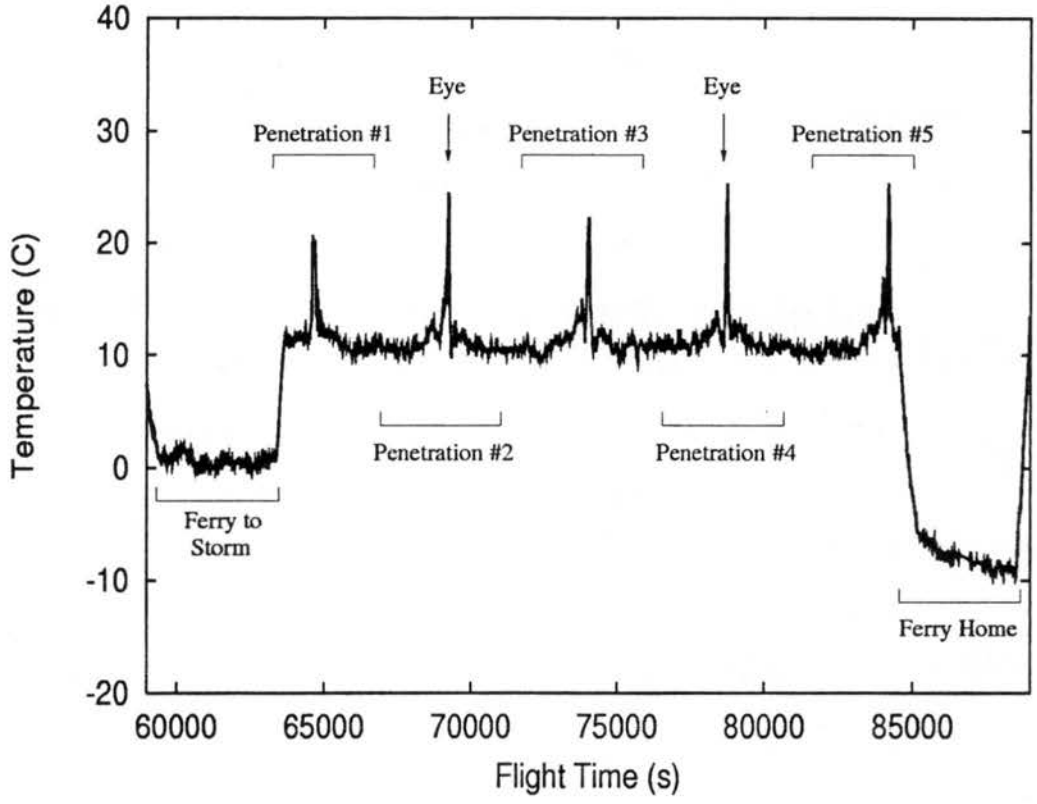

Figure 4.3: Depiction of penetrations through a hurricane defined using the SR temperature record for an entire flight. Large warm anomalies between 64000 s and 85000 s are the hurricane's eye.

km^{-1}, and nearly 89% of all flight level data is sampled with the aircraft roll less than 3.0° from the horizontal. An average of 100-200 clear-air, low-roll data points were used for the linear fit of each penetration. If the correlation coefficient from the linear-regression was ≥ 0.96, the best-fit equation was applied to all the SR data in the penetration to remove the bias, and the penetration was kept for reconstruction. Shown in Figure (4.4a) are the clear-air, low-roll data points for the same Gilbert penetration as shown in Figure (4.1). The drift bias of the SR can be easily seen. Performing a linear regression of the 393 data points yields a correlation coefficient of 0.987 and a standard deviation of 0.392°C. Shown in Figure (4.4b) are the same data points with the bias removed.

Observed dew points were maintained in clear-air regions, however, corrected dew points were calculated for both the ROSE and SR temperatures in wet air regions when necessary. Previous studies (e.g. Zipser et al. 1981; Jorgenson and LeMone 1989; and Wei et al. 1998) have assumed saturation during cloud penetration or if the dew point exceeded the air temperature. This assumption will overestimate relative humidities in subsaturated regions such as cloud edges, downdrafts, or cloud-free air containing raindrops as suggested by arguments in Chapter 2, but it is a good approximation in cloudy updrafts. From the definition of clear air, instrument wetting is suspected if the dew point depression (ROSE - T_d) is ≤ 0.2°C. A dew point depression of 0.2°C is equivalent to $\approx$ 98% relative humidity. In order to minimize errors, a relative humidity of 99% (dew point depression ≈ 0.1°C) was assumed uniformly for dew points associated with the ROSE data suspect of wetting errors. For SR dew point data in the same regions, if $T_d \geq SR$ a relative humidity of 99% was assumed, but if $T_d < SR$ the observed dew point was maintained. A relative humidity of 99% was assumed for all SR dew points in wet air for storms prior to 1986. The assumption of 99% relative humidity during the entire cloud penetration may underestimate dew points in updrafts, which are likely saturated. In this study the effects of instrument wetting errors on the virtual temperature (T_v), the virtual potential temperature (θ_v), the equivalent potential temperature (θ_e) calculated according to Bolton (1980), and the reversible equivalent potential temperature (θ_{er}) calculated according to

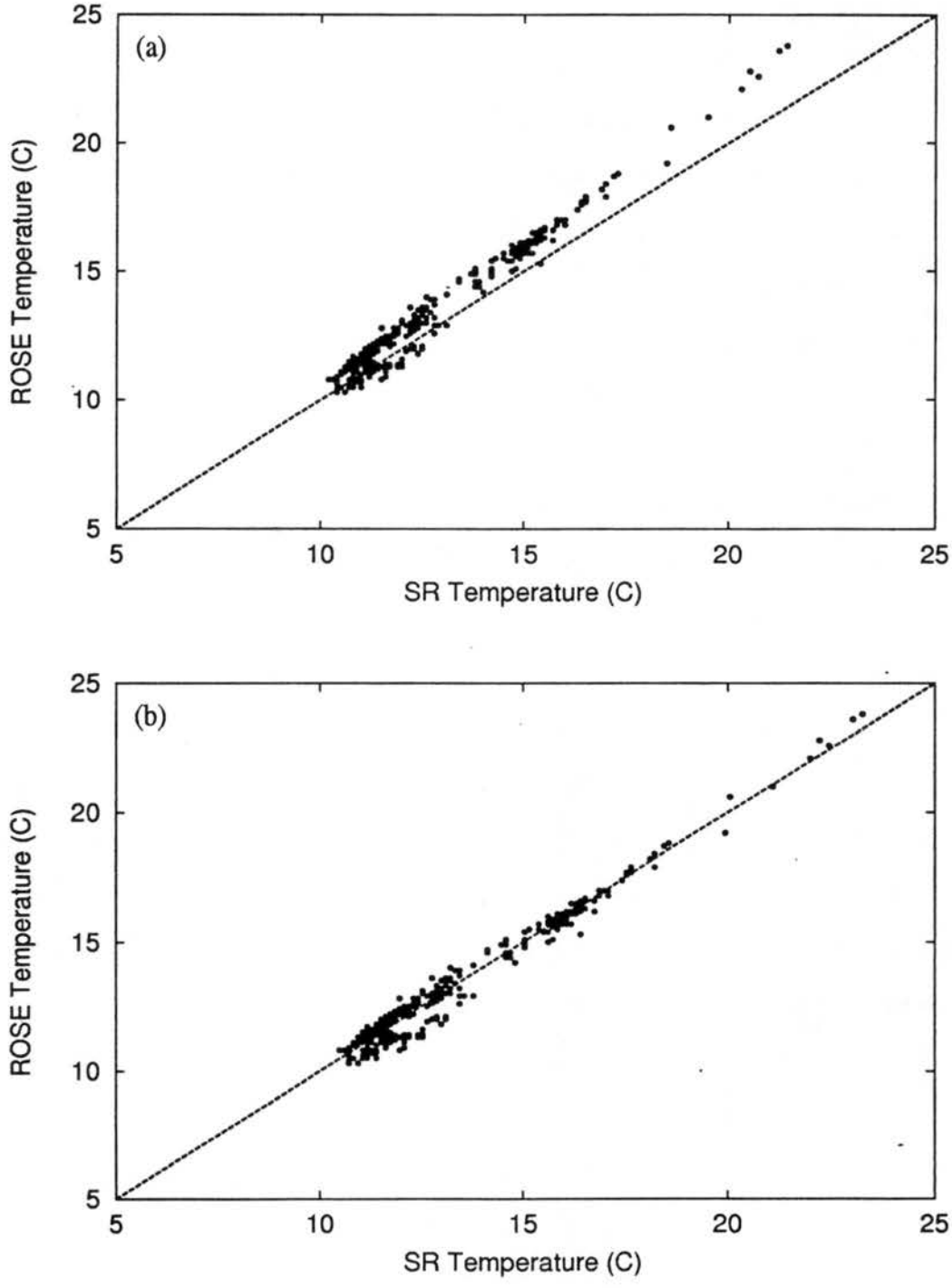

Figure 4.4: Corresponding measurements of clear air, low-roll temperatures from the SR and ROSE instruments (a) prior to the removal of the drift bias, and (b) after the drift bias was removed for the penetration of Gilbert on September 14, 1988 at 700 mb shown in Figure 4.1.

Emanuel (1994) are examined. Shown in Figure (4.5) are the differences of each of these quantites and specific humidity (q) for 99% rather than 100% relative humidity at the 850 mb and 500 mb pressure levels over temperature ranges observed in this study. The calculation of T_v and θ_v is relatively insensitive to a dew point error of this magnitude, however, average errors of 0.5 K result in the calculation of θ_e and θ_{er}.

The debiased temperatures and corrected dewpoint data were extrapolated along a moist-adiabat to the reference pressure level of the flight to be in agreement with dataset A. This correction is applied uniformally for standardization of the radial legs since some pentrations were flown at constant altitudes, and others at a constant pressure level. While this adjustment may not be accurate in all regions of the tropical cyclone, local lapse rates are unattainable along the entire flight path to properly adjust the data. The assumption of a moist-adiabatic lapse rate is reasonable. In active convection and outside the eyewall to within 175 km of the tropical cyclone center the lapse rate is nearly moist adiabatic (Sheets 1969). In an eye, the correction may act to slightly warm the air due to the stable lapse rate and the larger difference between flight-level and the referecne pressure level. However, the flight level is seldom more than 300 m from the reference pressure level so the errors from the temperature adjustment are small.

Finally, the corrected SR and ROSE temperatures and dewpoints of dataset B are fit to the storm-relative grid of dataset A to produce the reconstructed temperature profiles. Linear interpolation is used since A has a resolution of $\approx$ 3-4 s, and B has a resolution of 5 s. The roll of the aircraft is again considered for SR temperatures and dewpoints, and a critical roll value for accurate data is dependent upon the availability and amount of cloud water content (CWC) measured by the JW instrument[1]. If no CWC data was available, or if the CWC < 0.10 g m^{-3}, only data coincident with an aircraft roll within $\pm 3.0°$ of the horizontal was considered accurate. If the CWC was in the range 0.10-0.20 g m^{-3} only data coincident with a roll within $\pm 10.0°$ of the horizontal was considered accurate.

---

[1]The JW data used here was taken from dataset A, since JW data was originally obtained from HRD in the 5 s filtered format of dataset B for only a portion of the total radial legs with JW and SR data.

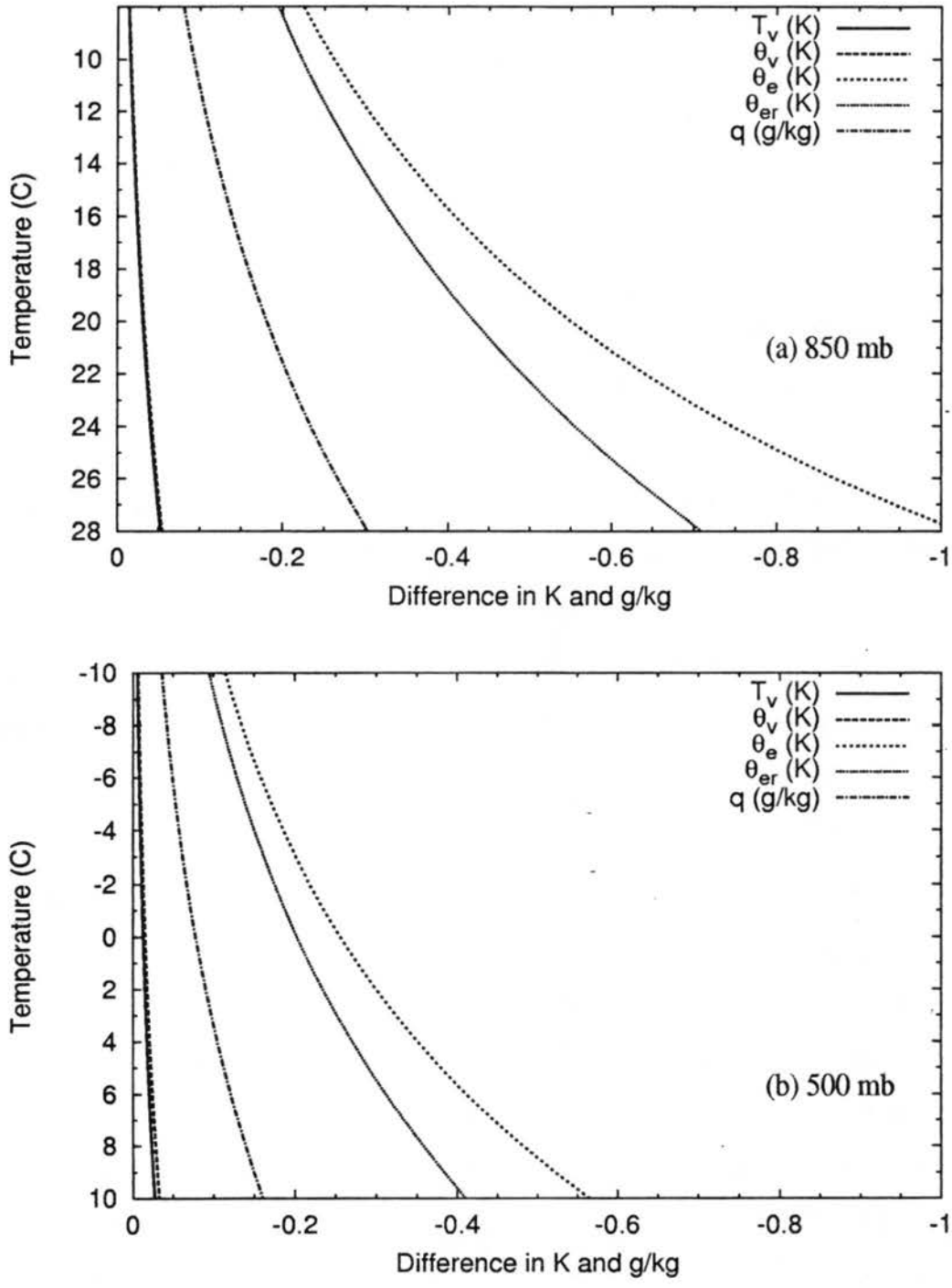

Figure 4.5: Resulting errors of virtual temperature (T_v), virtual potential temperature (θ_v), pseudo-adiabatic equivalent potential temperature (θ_e), reversible equivalent potential temperature (θ_{er}), and specific humidity (q) for assuming 99% relative humidity in a saturated environment.

A CWC of 0.10 g m^{-3} results in the majority of the observed radiance originating from within 100 m of the aircraft. For a 10.0° roll, temperature deviations from flight level will only be 0.07 K assuming a near moist-adiabatic lapse rate. If the CWC $\geq$ 0.20 g m^{-3}, the SR temperature was considered accurate irrespective of the aircraft roll due to the shortened path length (within $\approx$ 33 m of the aircraft) of the majority of the observed radiance, as shown by Albrecht et al. (1979). If the aircraft roll exceeds its critical value for the amount or availability of CWC, a linear average was taken between the nearest two data points that were within the accepted range of aircraft roll for the measured CWC.

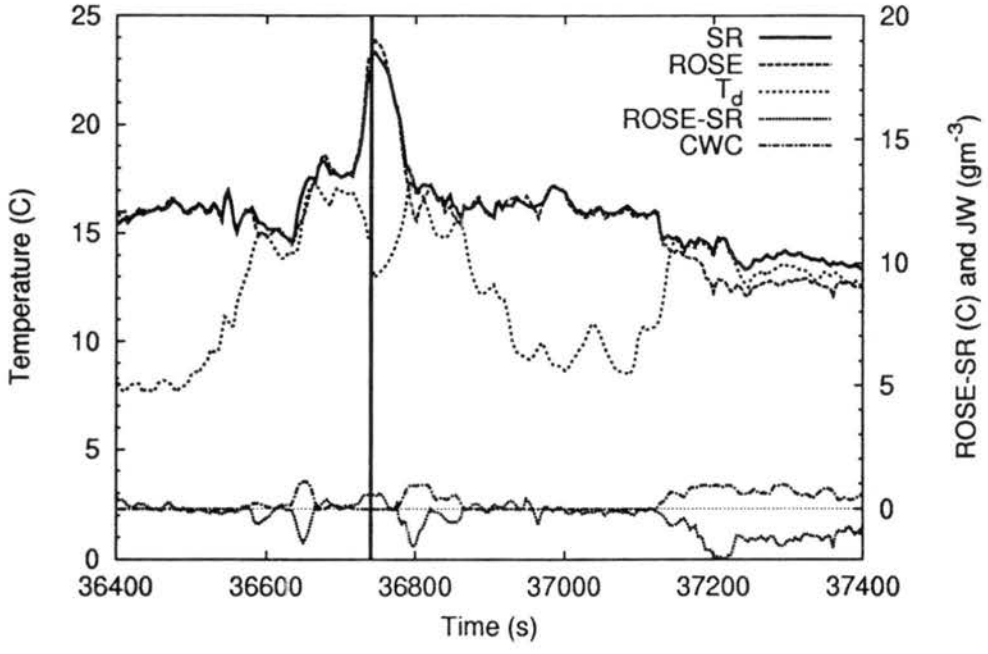

Figure 4.6: Thermodynamic data after temperature reconstruction for one penetration through hurricane Gilbert on September 14, 1988 at 700 mb. (Same penetration as in Figure (4.1)) Shown are the SR, ROSE, and dewpoint (T_d) temperatures, cloud water content (CWC) measured by the JW instrument, and the difference between the SR and ROSE temperatures. The vertical solid line represents the center of the eye.

Shown in Figure (4.6) are the reconstructed temperature profiles for the same penetration through Gilbert shown in Figure (4.1). The offset has been effectively removed and the SR and ROSE temperatures are in very good agreement in the unsaturated regions near 36500 s and 37000 s. Likewise, in regions where the dewpoint was greater than the ROSE temperature (e.g. near 36800 s and 37200 s), the dewpoints were adjusted and

the ROSE temperature is significantly cooler than the SR temperature. Coinciding with the significantly cooler ROSE temperatures was the presence of CWC, suggesting that instrument wetting was occuring in these regions as suspected. A total of 579 radial legs in hurricanes (shown in Table 4.2), with corrected thermodynamic profiles were reconstructed from the original 855 radial legs of flights with SR data collected. Reconstruction was not possible for 276 radial legs. The majority (65%) had a low SR/ROSE clear-air correlation coefficient for their penetration. Other radial legs were removed due to bad or incomplete SR data, bad dewpoint data, bad time stamps, or large temperature spikes[2]. Shown in Table (4.3) are the reconstructed radial legs accompanied by CWC measured by the JW instrument. An additional 99 radial legs could be reconstructed from the definition of clear air used in this study despite no CWC data. Table (4.4) stratifies the reconstructed radial legs from Table (4.2) by the intensity of the hurricane during the penetrations by category according to the Saffir-Simpson scale[3], the quadrant with respect to storm motion (see Figure 4.7), and the 12-hour intensity change centered on the time of the penetration. A hurricane was considered intensifying if the maximum wind increased by more than 10 knots over 12 hours, while a maximum wind decrease greater than 10 knots over the same time period was considered a filling hurricane. The maximum winds in steady storms changed less than or equal to 10 knots over 12 hours.

The available processed PMS data was also fit to the storm-relative grid, and linear interpolation was used due to the different temporal resolutions of the datasets. Prior to the fit, visual inspection of the PMS data revealed erroneous spikes in liquid water

---

[2]The large temperature spikes are due to lightning strikes on the aircraft temporarily disrupting the electronics of the instruments. Each temperature spike lasted only a few seconds during low aircraft roll, and the legs removed for this reason occured in Diana (1984) and Emily (1993).

[3]Intensity was determined for all hurricanes by maximum wind speed in the best track database except for the I1 flight on September 15 through Gilbert, the three flights through Gloria on September 26, and the flight through Gloria on September 27 at which times the typical wind-pressure relationship did not hold. Gilbert's maximum winds were 85-90 knots while the minimum central pressures were near 950 mb. Likewise, Gloria's maximum winds were 80-90 knots while the minimum central pressures were 940-950 mb. With the minimum central pressure directly related to the thermodynamics (the focus of this study) in the eye, pressure was used for these five flights to determine intensity.

Table 4.2: Inventory of reconstructed Atlantic and East Pacific hurricane radial legs by flight level. Included is the number of flights and Saffir-Simpson categories during the flights.

		Number of	Radial Legs							
Hurricane	Year	Flights	900	850	700	600	500	400	Total	Category
Diana	1984	4		41					41	1,2,3,4
Danny	1985	2		10					10	1
Elena	1985	5		54					54	1,2,3
Gloria	1985	7		7	30		6	3	46	1,2,3,4
Juan	1985	2		17					17	1
Emily	1987	2			14	1	35		50	3
Floyd	1987	1		11					11	1
Florence	1988	2	14						14	1
Gilbert	1988	5		16	28				44	2,3,4,5
Joan	1988	1		6					6	3
Dean	1989	1				8			8	1
Gabrielle	1989	1			4				4	3
Hugo	1989	4				22	4		26	3,4,5
Jerry	1989	1	5						5	1
Gustav	1990	4		6	30				36	1,2,3
Emily	1993	2					11		11	1,3
Erin	1995	1			16				16	1
Iris	1995	2				7			7	1
Luis	1995	2				4	12		16	4
Opal	1995	1				4			4	4,3
Edouard	1996	2			22				22	4
Fran	1996	1		4				4	8	3
Hortense	1996	1		8					8	2
Norbert	1984	6		5	34		19		58	3,4
Jimena	1991	3		2	17	4			23	4
Tina	1992	2		18					18	1
Olivia	1994	2				16			16	2,3,4
ATL-Total		54	19	180	144	46	68	7	464	
EPAC-Total		13		25	51	20	19		115	
Total		67	19	205	195	66	87	7	579	

Table 4.3: Inventory of reconstructed Atlantic and East Pacific hurricane radial legs by flight level with Johnson-Williams (JW) cloud-water content. Included is the number of flights and Saffir-Simpson categories during the flights.

		Number of	Radial Legs							
Hurricane	Year	Flights	900	850	700	600	500	400	Total	Category
Diana	1984	4		41					41	1,2,3,4
Danny	1985	1		6					6	1
Elena	1985	4		39					39	1,2,3
Gloria	1985	6		7	22		6	3	38	1,2,3,4
Juan	1985	2		13					13	1
Emily	1987	1					25		25	3
Floyd	1987	1		11					11	1
Florence	1988	1	10						10	1
Gilbert	1988	5		16	28				44	2,3,4,5
Joan	1988	1		6					6	3
Dean	1989	1				6			6	1
Gabrielle	1989	1			2				2	3
Hugo	1989	3				12	4		16	3,4,5
Jerry	1989	1	5						5	1
Gustav	1990	3		6	20				26	1,2,3
Emily	1993	2					11		11	1,3
Erin	1995	1			13				13	1
Iris	1995	2				6			6	1
Luis	1995	2				4	12		16	4
Opal	1995	1				4			4	4,3
Edouard	1996	2			22				22	4
Fran	1996	1		4				4	8	3
Hortense	1996	1		8					8	2
Norbert	1984	6		5	34		10		49	3,4
Jimena	1991	3		2	17	2			21	4
Tina	1992	2		18					18	1
Olivia	1994	2				16			16	2,3,4
ATL-Total		47	15	157	107	32	58	7	376	
EPAC-Total		13		25	51	18	10		104	
Total		60	15	182	158	50	68	7	480	

Table 4.4: Statistics of reconstructed radial legs in Atlantic and East Pacific hurricanes stratified by flight level.

	Radial Legs						
	900	850	700	600	500	400	Total
Total	19	205	195	66	87	7	579
Category 1,2	19	114	46	15	11		205
Category 3,4,5		91	149	51	76	7	374
Front Quadrant	4	58	54	17	23	4	160
Left Quadrant	7	43	46	15	21	2	134
Back Quadrant	3	55	52	17	21		148
Right Quadrant	5	49	43	17	22	1	137
Intensifying	9	121	78	5	35	3	251
Steady	8	28	83	32	16		167
Filling	2	56	34	29	36	4	161

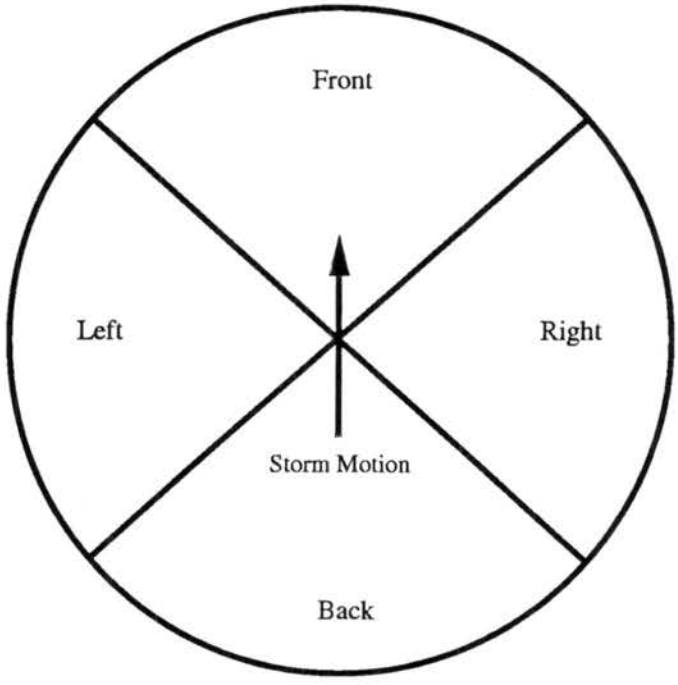

Figure 4.7: Quadrants defined with respect to the storm motion. The front quadrant is centered along the motion vector.

content occassionally occurred along the edges of updraft cores. The spikes were the result of broken rimed ice crystals and/or large splashes that were not removed during the original processing. In each case, the erroneous value was replaced with the average of the two adjacent values. The average values are very close to the liquid water content calculated from a re-integration of the drop-size spectra without the bad particles (Black 1998, personnal communication). If more than two consecutive values of liquid water content were in error, no average was taken, and a data gap was left. Shown in Table (4.5) are the reconstructed radial legs accompanied by PMS data, and in Table (4.6) are the radial legs with a full compliment of both JW and PMS cloud-physics data.

4.3 Evaluation of the Present Reconstruction Methodology

No comparisons between the AOC modified Barnes PRT-5 CO_2 radiometer with an immersion thermometer have appeared in formal literature to date. PRT Inc. gives an accuracy of $\pm 0.5°C$ for their CO_2 radiometer prior to the AOC modifications. This value has never been verified during aircraft operation, and with the radiometer having a known

Table 4.5: Inventory of reconstructed Atlantic and East Pacific hurricane radial legs by flight level with PMS data. Included is the number of flights and Saffir-Simpson categories during the flights.

		Number of	Radial Legs							
Hurricane	Year	Flights	900	850	700	600	500	400	Total	Category
Emily	1987	3			13	1	35		49	3
Dean	1989	1				5			5	1
Gustav	1990	4		6	22				28	1,2,3
Norbert	1984	2			30				30	3,4
Total		10		6	65	6	35		112	

Table 4.6: Inventory of reconstructed Atlantic and East Pacific hurricane radial legs by flight level with JW and PMS data. Included is the number of flights and Saffir-Simpson categories during the flights.

		Number of	Radial Legs							
Hurricane	Year	Flights	900	850	700	600	500	400	Total	Category
Emily	1987	1					25		25	3
Dean	1989	1				5			5	1
Gustav	1990	3		6	14				20	1,2,3
Norbert	1984	2			30				30	3,4
Total		8		6	44	5	25		80	

drift bias, cannot be achieved from the raw output of the instrument. However, once the drift bias is removed, is the given accuracy SR achievable? Furthermore, is the clear-air definition used in this reconstuction reasonable at seperating clear air from regions with possible instrument wetting errors? An evaluation of the present reconstruction methodology and the accuracy of the resulting SR temperatures is presented to provide confidence in the reconstructed temperature profiles.

Shown in Figure (4.7) is the distribution of the difference between the SR and ROSE temperatures in clear air for all reconstructed hurricane radial legs, assuming the ROSE temperature is the true temperature. Data points in which the SR temperature is an average of the nearest two acceptable low roll points are omitted. The average difference is 0.007°C and the standard deviation of the difference is 0.26°C for more than 62000 data points. Futhermore, 95% of the reconstructed SR measurements are within 0.5°C of the ROSE values. The excellent agreement between the two temperatures is expected due to the SR/ROSE correlation constraints placed on the data. However, the fact that 80% of the radial legs with SR data available could be reconstructed lends support for the validity and accuracy of the majority of all SR temperature measurements after the drift bias removal process. Thus, the accuracy of the SR instrument is achieved for the reconstructed radial legs used in this study once the drift bias is removed.

Figure (4.8) is the distribution of the difference between the clear-air SR and ROSE temperatures in which the SR temperature is an average of the nearest two acceptable low roll points. The average difference is -0.06°C and the standard deviation of the difference is 0.46°C for about 8000 data points. Despite the large standard deviation, 90% of the data points are within ±0.5°C of each other, suggesting even the linearly averaged clear-air data points are relatively accurate. Furthermore, only 10% of all reconstructed data points needed to be linearly averaged, resulting in less than 1% of the data outside the accuracy of the SR instrument. The excellent agreement between all the reconstructed SR and ROSE temperatures in clear air provides strong support for accurate temperatures

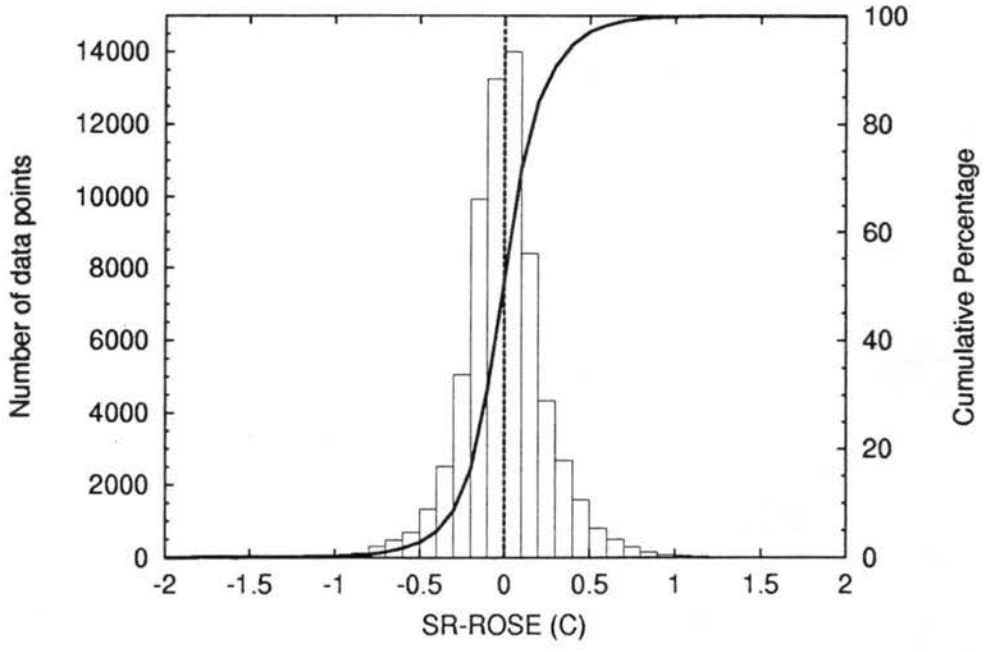

Figure 4.8: The distribution of SR-ROSE temperature difference in clear air regions. Data points in which the SR temperature is an average of the nearest two acceptable low roll points are omitted. The solid line is the cumulative percentage.

through regions where instrument wetting was supsected, assuming the effects of liquid water on SR values are minimal.

The definition of clear air used for this study was evaluated and compared to the previous methods based on the absence of cloud liquid water. JW cloud water content was obtained for 196 radial legs in the 5 s filtered format of dataset B. These radial legs were reconstructed using the same methodology defined above except with two different clear-air definitions. The first defintion was the one used in this study based on dewpoint depression (hereafter referred to as the TDD definition). The second defines clear-air as a region with CWC < 0.05 g m^{-1}. Furthermore, data within 20 s after passing through a region of CWC ≥ 0.05 g m^{-1}, or a cloud, was not considered clear air. This second definition (hereafter referred to as the LW definition) is in accordance with the clear-air definition used by Wei et al. (1998). The aircraft roll considerations used in the TDD definition was also used in the LW definition. The presence of precipitation in cloud-free regions was not considered due to lack of data. For this subset of radial legs, the average

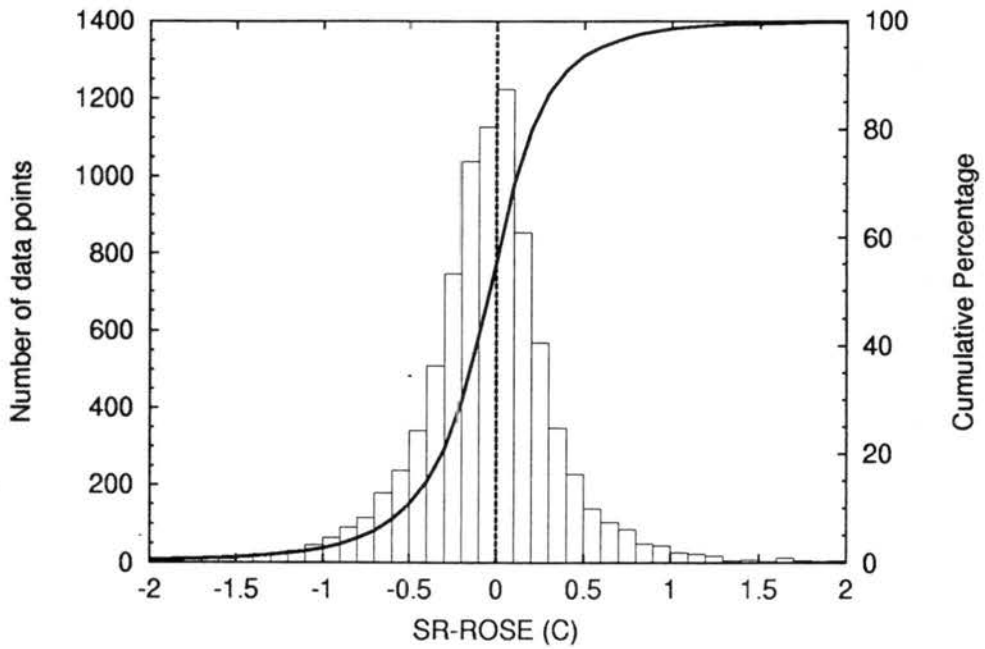

Figure 4.9: The distribution of SR-ROSE temperature difference in clear air regions in which the SR temperature is an average of the nearest two acceptable low roll points. The solid line is the cumulative percentage.

difference between the SR and ROSE temperatures in clear air, using the TDD definition, is 0.005°C with a standard deviation of 0.26°C for about 22000 data points. Thus, the subset of radial legs is represetative of the complete radial leg dataset. Shown in Figure (4.9) is the distribution of the difference between reconstructed SR temperature data considered in clear-air by both the TDD and the LW definitions. The average difference is -0.011°C with a standard deviation of 0.08°C for about 16000 data points. No temperature difference ever exceeded ±0.5°C. Shown in Figure (4.10) is the distribution of the difference between SR temperature data considered in clear air by either the TDD or the LW definition, but not both (i.e. the data was suspect of instrument wetting by only one of the clear air definitions). The average difference is -0.019°C with a standard deviation of 0.13°C for about 9000 data points. Only 1% of the these temperature differences exceed ±0.5°C. With essentially all the clear-air SR temperature differences between the two clear-air definitions normally distributed about zero and within the accuracy of the instrument,

the TDD clear-air definition used in this study can be considered valid with a high degree of confidence.

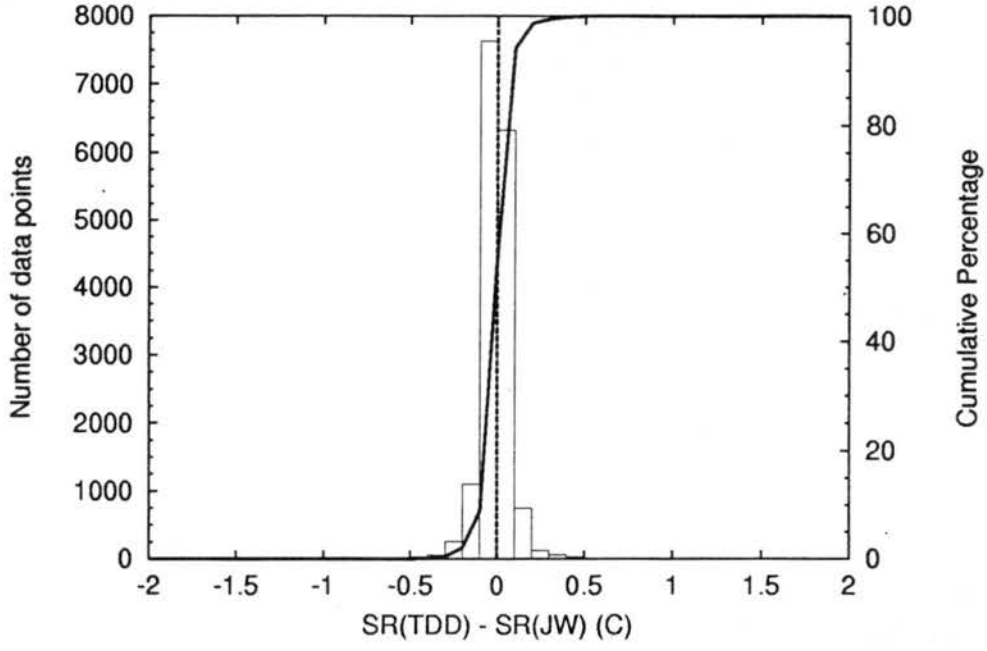

Figure 4.10: Distribution of the difference in clear air between the SR temperature derived from the TDD reconstruction method and the LW reconstrcution method.

4.4 Summary

SR temperatures were used to remove instrument wetting errors from (reconstruct) nearly 600 thermodynamic radial profiles from 27 hurricanes. The reconstruction method is similar to previous methods, as a time-dependent bias in the radiometer is first removed from the SR temperature data assuming the ROSE temperatures are accurate in clear air. In contrast to previous reconstruction methods, clear air was defined entirely from the ROSE and T_d temperatures with considerations of aircraft roll due to the lack of cloud and precipitation microphysical data. If the resulting linear correlation of the SR and ROSE temperatures in clear air exceeded 0.96 the erroneously large dewpoints (T_d > SR) were adjusted to the equivalent of 99 percent relative humidity, and then all temperatures and dewpoints were further adjusted along moist adiabats to an isobaric level. Finally,

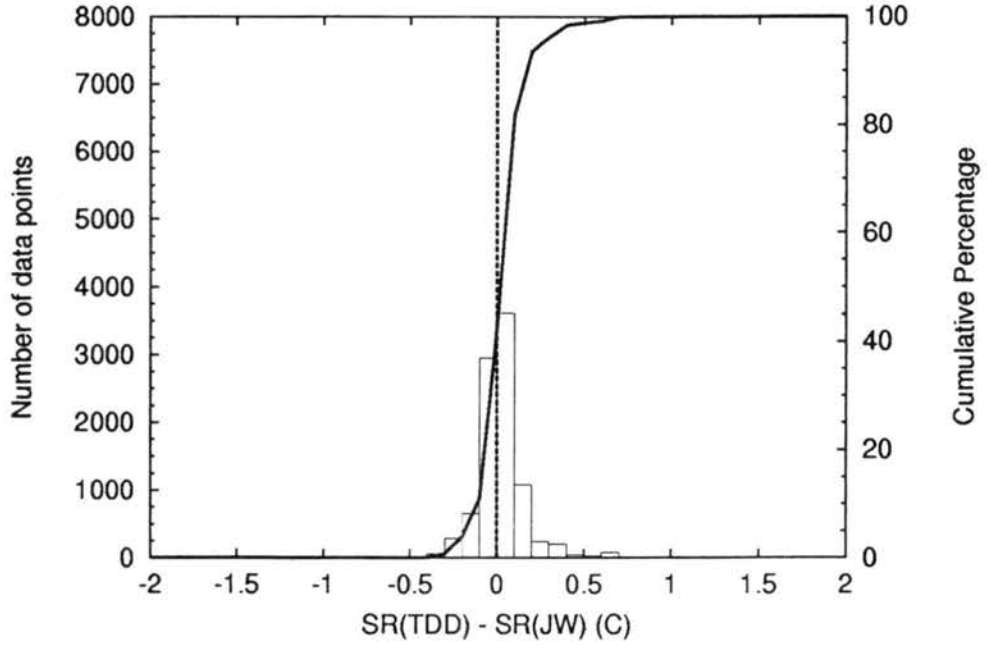

Figure 4.11: Distribution of the difference between the SR temperature derived from the TDD reconstruction method and the LW reconstrcution method when the data was considered in clear air by only one method.

the thermodynamic data is fit to a storm-relative grid using linear interpolation of the nearest acceptable low-roll data points.

An examination of the reconstructed temperature profiles indicate that the given SR accuracy of $\pm 0.5°C$ was achieved in clear air, accounting for over 95 percent of the data points. The accuracy is achieved even when a linear average is taken through regions of large aircraft roll, accounting for over 90 percent of the data points. The clear air definition was tested by reconstructing a subset of the same profiles using clear air defined by the lack of cloud liquid water. No significant temperature differences were found in the resulting profiles from the two clear air definitions. Thus, the validity of the clear air definition used in this study is supported, and further suggests that reliable reconstruction of radial legs without coincident microphysical data can be achieved using this definition. Neither the accuracy of the moist-adiabat adjustment from flight level to a reference pressure level, nor the assumption of 99 percent relative humidity in regions of erroneously large dewpoints can be evaluated. However, observations and theory suggest

these assumptions are reasonable and will result in errors significantly smaller than errors induced by instrument wetting. Therefore, the SR temperature and dewpoint profiles produced from the presented reconstruction methodology can be considered, with a high degree of confidence, accurate and free of instrument wetting errors.

4.5 Synopsis

- Instrument wetting errors were accurately removed from nearly 600 thermodynamic radial profiles from 27 hurricanes with the use of a flight-level radiometer.
- The reconstruction method removed a time-dependent bias from the radiometer temperatures using data in clear air, corrected supersaturated dewpoints to 99 percent relative humidity, adjusted the resulting temperatures and dew points to an isobaric level, and fit the data to a storm-relative grid.
- The use of clear air defined by dewpoint depression from the Rosemount temperatures resulted in statistically similar temperature profiles compared to when clear air is defined by the lack of hydrometeors, and thus, thermodynamic profiles can be accurately reconstructed *without microphysical data.*

Chapter 5

INSTRUMENT WETTING OBSERVATIONS

5.1 Performance of Temperature Sensors in Clouds and Precipitation

Rosemount thermometer wetting errors are the result of hydrometeors contacting the sensing element, and thus such errors must occur during or shortly after passage through air containing hydrometeors. However, the presence of hydrometeors in the sampled air does not imply wetting errors exist. Instrument design limits hydrometeor contact with the sensing element such that the sensor may never become wet. Furthermore, instrument design may lead to only partial wetting of the sensor and an error smaller than the calculated theoretical error. Shown in Figure (5.1) is the distribution of the difference between the SR and ROSE temperatures (SR-ROSE), or temperature error, in wet air (defined from the definition of clear air from Chapter 4) assuming the SR temperature is the true temperature. Data points in which the SR temperature is an average of the nearest two acceptable low-roll points are omitted. The average temperature difference for more than 52000 data points is 0.41 ± 0.85°C. The distribution is skewed toward positive SR-ROSE values, with 25% of the temperature differences exceeding 0.5°C and only 20% less than 0.0°C. These results seem to suggest that while the SR and ROSE instruments are occasionally in good agreement through wet air, significant ROSE instrument wetting errors exist within the reconstructed hurricane radial leg database.

As discussed in Chapter 2, the SR may provide erroneously low temperatures when hydrometeor temperatures are significantly lower than the air temperature. A favorable location for such errors is a subsaturated region with a high liquid water content. In Figure (5.1) less than 1% of the temperature differences are less than -0.5°C, and less than 100 of the 52000 temperature differences, or 0.2%, are less than -1.0°C. The majority of the

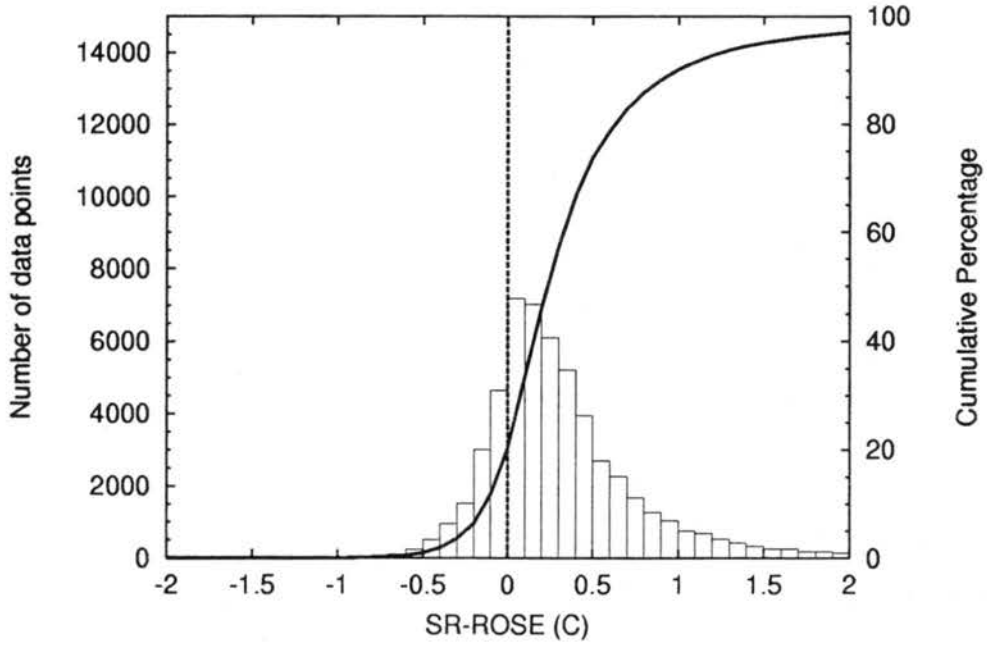

Figure 5.1: The distribution of SR-ROSE temperature difference in wet air regions. Data points in which the SR temperature is an average of the nearest two acceptable low roll points are omitted. The solid line is the cumulative percentage.

temperature differences less than -0.5°C occurred in regions with a RH $< 90\%$ and were collocated with cloud liquid water. However, utilizing the temperature difference between the two sensors to find locations where the SR is erroneously too low requires the ROSE to be performing properly, where in fact it may be experiencing wetting errors itself. For this reason, all the radial legs were individually inspected, but no such locations could be visually detected. Despite the lack of precipitation data to further indicate regions of high liquid water content, the SR appears to perform very well in wet air.

5.2 Comparisons of temperature error to drop size and liquid water content

The Rosemount immersion total temperature sensor utilizes inertial separation of hydrometeors from the air prior to reaching the sensing element. Previous studies have indicated that despite the instrument designs, sensor wetting still occurs, and the resulting temperature errors may be a function of drop size and total water content. Lenschow and Pennell (1974) argued that small droplets may not be effectively removed from the

air by inertial separation, allowing them to impinge on the sensing element. During an investigation of stratocumulus clouds Albrecht et al. (1979) noted the highest correlations between temperature error and drop concentration was for drops with radii in the 0.0045-0.011 mm range. However, 88% of the total liquid water observed was from drops with radii in this range. Lawson and Cooper (1990) found during penetrations of small, thin cumulus clouds containing light precipitation that the temperature error of a partially wetted sensor was dependent upon liquid water content (Figure 5.2). Temperature errors increased with liquid water content such that nearly all temperature errors were positive for liquid water contents greater than 1.0 g m^{-3}. They argued that the dependence is related to the collection efficiency of drops on the sensing element, and this collection efficiency is a function of drop size. The reconstructed hurricane database is examined for a similar dependence of temperature error on the liquid water content of small cloud drops.

Shown in Figure (5.3) is the CWC from the JW sensor plotted against the SR-ROSE temperature error for all data points with CWC $>$ 0.0 g m^{-3} in warm clouds. CWC measurements from the JW sensor are indicative of only small cloud drops with diameters less than 0.03 mm. The majority (73%) of temperature errors are positive in the presence of CWC, and errors of 1-3°C typically occur. Only a few data points achieve the theoretical error values of 4-6°C for a completely wet sensing element at typical true airspeeds, indicating that the sensor is rarely wetted completely. The distribution of temperature errors for CWC $<$ 1.0 g m^{-3} is slightly skewed toward positive errors (Figure 5.4a). The skewed distribution is more pronounced for CWC $>$ 1.0 g m^{-3} (Figure 5.4b) and only 6% of the temperature errors are negative. The relationship between temperature error and liquid water content found by Lawson and Cooper (1990) in thin cumulus clouds is evident within this data as well, however, it is not as strong. Unlike Lawson and Cooper, the majority of maximum temperature errors ($>$ 2.0°C) occur in conjunction with CWCs of 0.5-1.0 g m^{-3}, while errors of only 0.5-1.0°C occur in regions of maximum CWC $>$ 4.0 g m^{-3}.

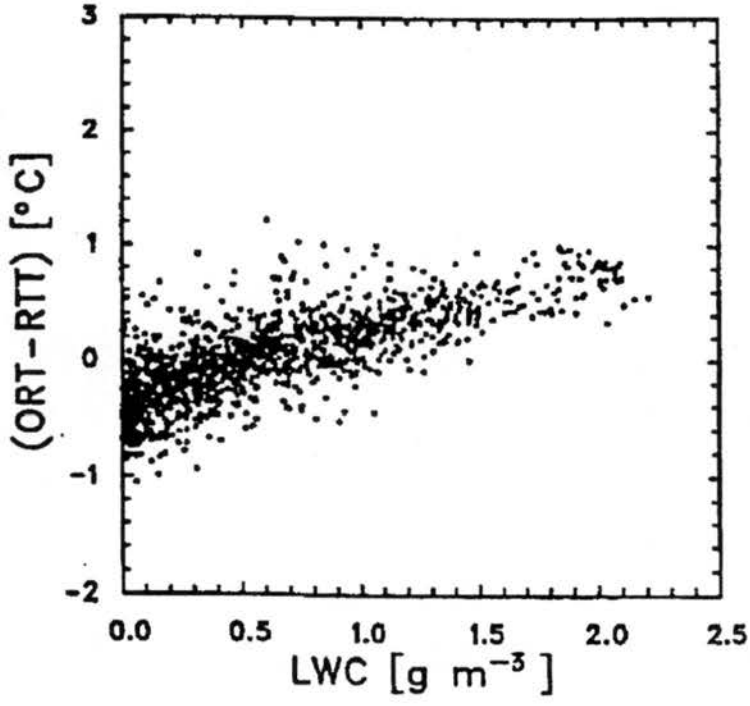

Figure 5.2: Temperature error (ORT-RTT) as a function of cloud drop liquid water content (LWC). The temperature error is the difference between an Ophir radiometric thermometer (ORT) and a Rosemount total temperature sensor (RTT). From Lawson and Cooper (1990).

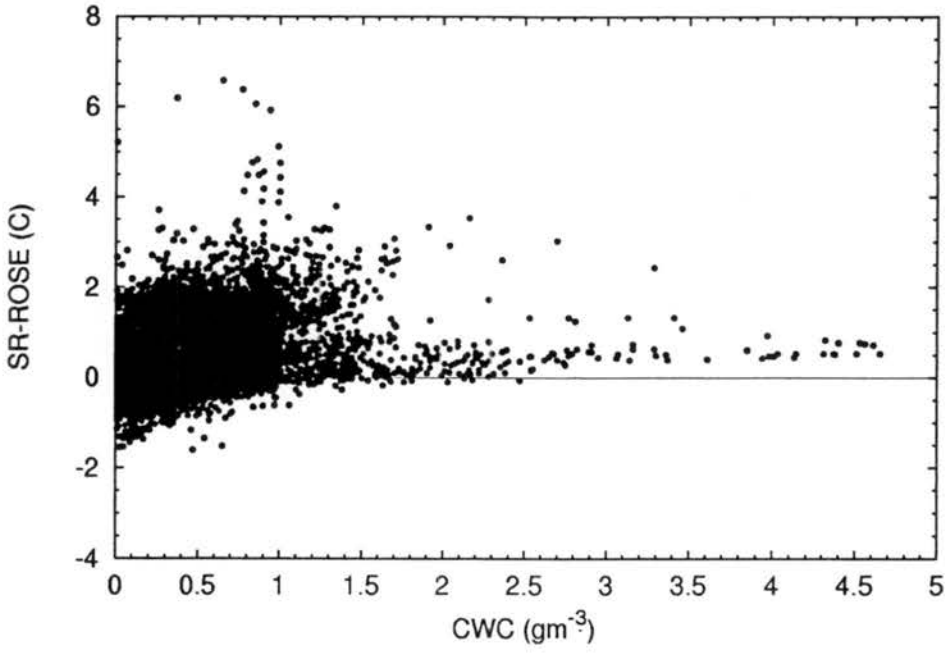

Figure 5.3: SR-ROSE temperature errors as a function of CWC for all data with measurable CWC in warm clouds.

Measurements in supercooled clouds with the Rosemount immersion temperature probe have shown evidence of instrument wetting (Blyth et al. 1988; Lawson and Cooper 1990). Figure (5.5) is similar to Figure (5.3) but rather for radial leg data in cold clouds, and CWC measurements represent only small supercooled cloud drops (i.e. not ice crystals) with diameters less than 0.03 mm. The maximum errors (~12.0°C) are larger in cold-clouds and more data points achieve, and in some cases exceed, the theoretical error values of 5-7°C for a completely ice-covered sensing element. Similar features are evident in the cold cloud data as in the warm-cloud data. The distributions of temperature errors for CWC < 1.0 g m^{-3} and CWC > 1.0 g m^{-3} (not shown) are similarly skewed toward positive values. Again, the majority (78%) of temperature errors are positive, but significant scatter exists. Over 97% of all temperature errors in locations with CWC > 1.0 g m^{-3} are positive, but errors rarely exceeded 4.0°C. In contrast, the maximum temperature errors and errors > 4.0°C frequently occur in conjunction with CWC < 1.0 g m^{-3}.

The increase in maximum error magnitude from warm cloud to cold cloud data was expected due to the additional cooling produced by melting after supercooled drops freeze

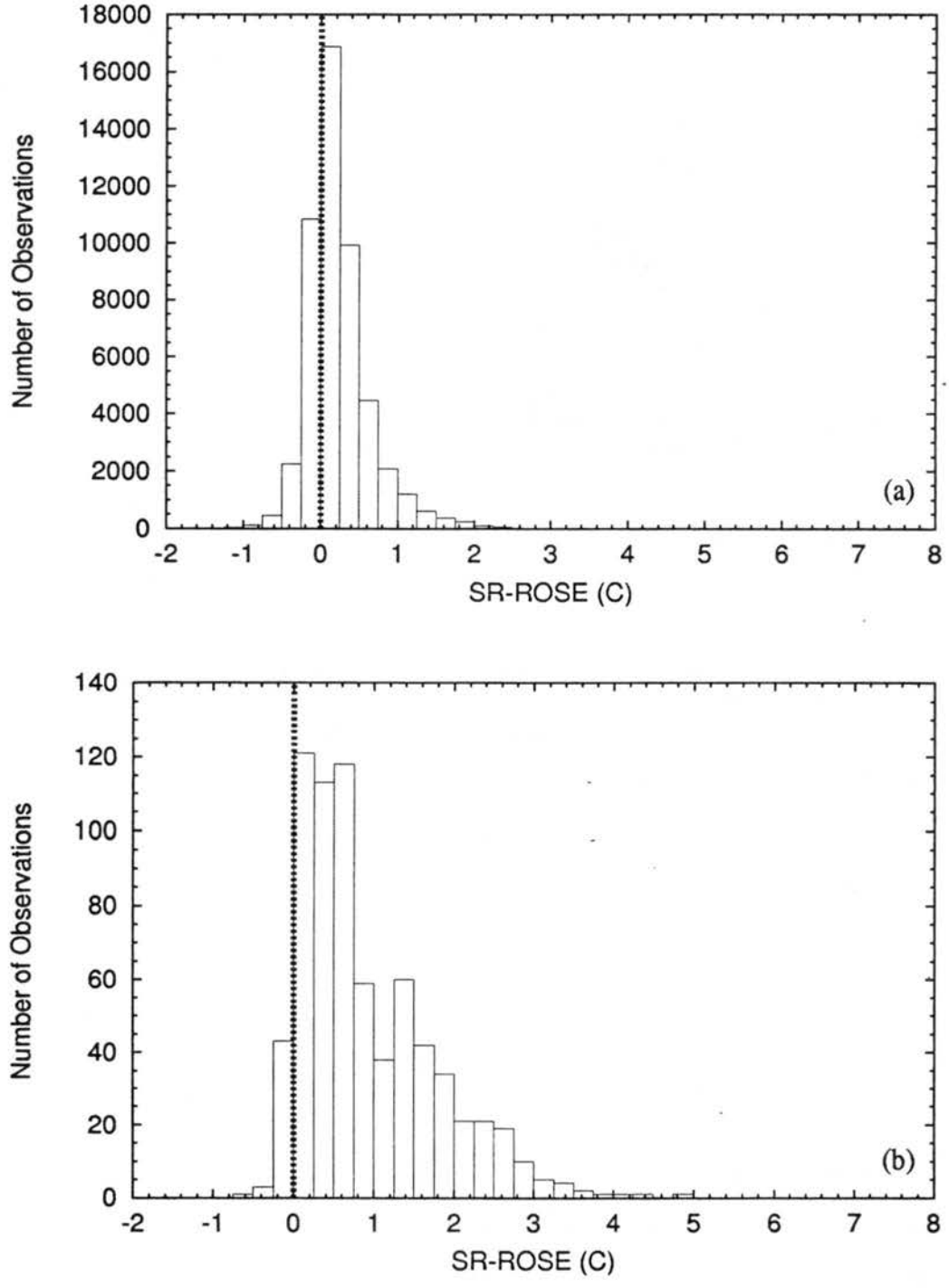

Figure 5.4: Distribution of SR-ROSE temperature errors for all data in warm clouds with measurable (a) CWC < 1.0 g m^{-3} and (b) CWC > 1.0 g m^{-3}.

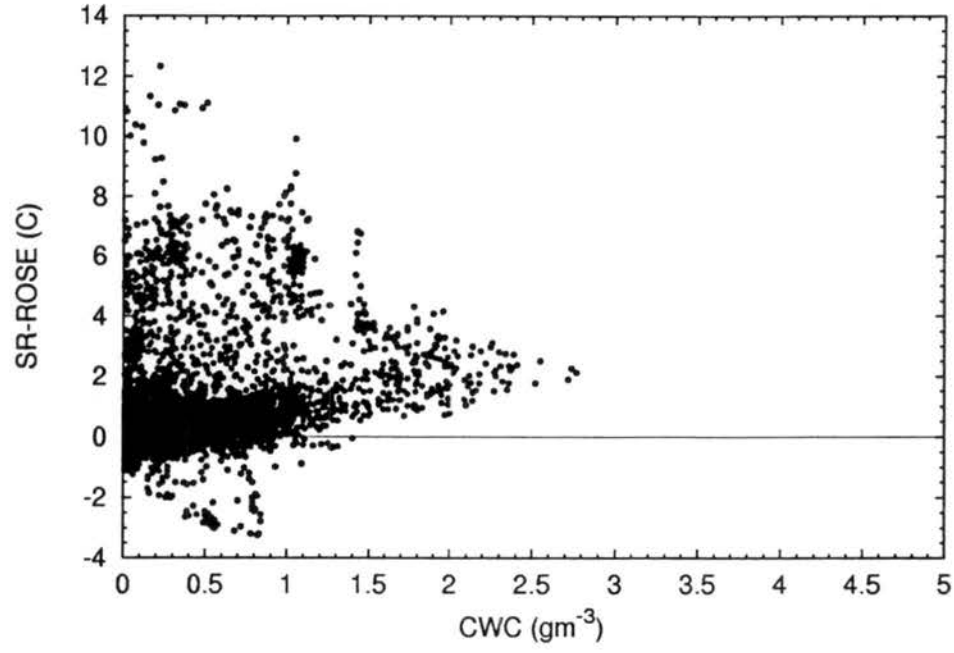

Figure 5.5: SR-ROSE temperature errors for all data in cold clouds with measurable CWC.

on the sensing element, however, the increase in the number of data points achieving theoretical error values was not. One plausible explanation is that additional time is required to melt the ice on the sensor. Thus, the sensing element cannot "shed" the impinging cloud drops as fast, and a buildup of water and/or ice on the sensor ensues. A larger percentage of the sensor surface becomes wet resulting in a larger net temperature error during cold cloud penetrations.

One might naturally ask why are the maximum temperature errors in both warm and cold clouds associated with lower CWC? The buildup of ice and water on the sensor during cloud penetrations (described above for cold clouds) can result in a time lag between maximum temperature errors and regions of high CWC, thus partially explaining why such large temperature errors occur in regions with low CWC. Previous studies (Blyth et al. 1988 and Lawson and Cooper 1990) have presented evidence of evaporative cooling spikes of 1-2°C upon cloud exit, particularily with the Rosemount 102 deiced model. The increase, or spike, in temperature error upon entering a subsaturated environment is predicted by (2.9). Thus, the observed large temperature errors may be partially the result

of a subsaturated environment in which a measurable CWC still exists[1]. Visual inspection of the data provides occasional evidence of maximum temperature errors during or near cloud exit, however, the majority of maximum errors occurred near the center of clouds, or the maximum of CWC (evidence of this will be presented later).

A plausible hypothesis is that during penetrations of precipitating clouds, drops greater than 0.03 mm in diameter are not inertially separated from the air due to turbulent motions within the housing, and are also contacting the sensing element. Furthermore, the associated low CWC contents are the result of larger drops (raindrops) reducing the number concentration of small cloud drops via collision-coalescence processes. The hypothesis is examined using the subset of radial legs with cloud and precipitation water content measured by both the JW and PMS probes (Table 4.4). Since the size ranges of the 2D-C and 2D-P overlap, and the 2D-C has better resolution than the 2D-P, the larger of the two PMS probe data values were considered most representative of the water content at time of observation. The use of PMS data introduces larger drops with possible diameters of 0.05-6.4 mm into the liquid water contents.

Figure (5.6) contains the normalized distributions of temperature error in warm clouds for all points with measurable CWC from the entire reconstructed database (from Figure 5.3), all points with measurable CWC from the subset of radial legs containing CWC and PMS data, and all points with measurable total liquid water content (CWC+PMS) from the subset of data stratified by regions with liquid water content < 1.0 g m^{-3} (Figure 5.6a) and liquid water content > 1.0 g m^{-3} (Figure 5.6b). The distributions are normalized with respect to the temperature error bin with the maximum number of occurrences. The skewed distributions of temperature error, determined solely as a function of CWC, from the entire dataset and the subset are qualitatively very similar. The inclusion of the PMS

---

[1]The Bartlett filter applied to the data prior to analysis may smooth over subsaturated cloud free regions bound by air containing observable CWC and will have the effect of widening the cloud. Furthermore, no statistically significant or consistent time lag between maximum CWC and maximum temperature error was found. The filtering may prevent any quantitative determination if the lag is only a few seconds. The use of higher temporal resolution (1-Hz) reconstruction data is likely needed to resolve any time lag.

drop data to the liquid water content shifted the skewed distributions of the subset such that a greater number of temperature errors $> 1.0°C$ were associated with liquid water contents > 1.0 g m^{-3}. This result suggests that larger cloud and precipitation drops may also be impinging on the sensor, however, significant scatter still exist even after the inclusion of the PMS data (Figure 5.7). The linear correlation coefficient is only 0.46. The scatter may be partially due to an incomplete representation of the entire drop size spectrum, and thus the calculated liquid water contents.

The cold-cloud PMS data contained liquid water contents from both ice and liquid particles. Similar results were found in the normalized cold cloud temperature distributions (not shown) after the inclusion of *only supercooled liquid water* PMS data. There is no apparent relationship between temperature error and ice particle liquid water content (Figure 5.8), suggesting ice particles do not cause temperature errors. Previous studies (e.g. Riehl and Malkus 1961; Hawkins and Imbembo 1976) have suspected temperature errors in only warm and mixed-phase clouds since eyewall temperatures in cold clouds composed entirely if ice were very near values expected from moist adiabatic ascent. Inspection of radial legs in cold clouds indicate that temperature errors greater than 1.0°C occur only when supercooled drops are present. The large errors shown in Figure 5.8 occurred when either ice and supercooled particles were both present, or when only ice particles were present soon after exiting a region of high supercooled liquid water content. Thus, the reconstructed database suggests large temperature errors do not occur when only ice crystals are present.

A weak linear relationship was found in hurricane data between the observed SR-ROSE temperature errors and the total liquid water content, however, only 20% of the total variance was explained. The lack of drop size spectra, concentrations, and a significant amount of PMS data prevents a more detailed study of wetting errors in relation to these microphysical quantities. Qualitatively, a relationship between the total liquid water content of small drops and temperature error, as found by Albrecht et al. (1979) and Lawson and Cooper (1990), was found in hurricanes. However, several other wetting

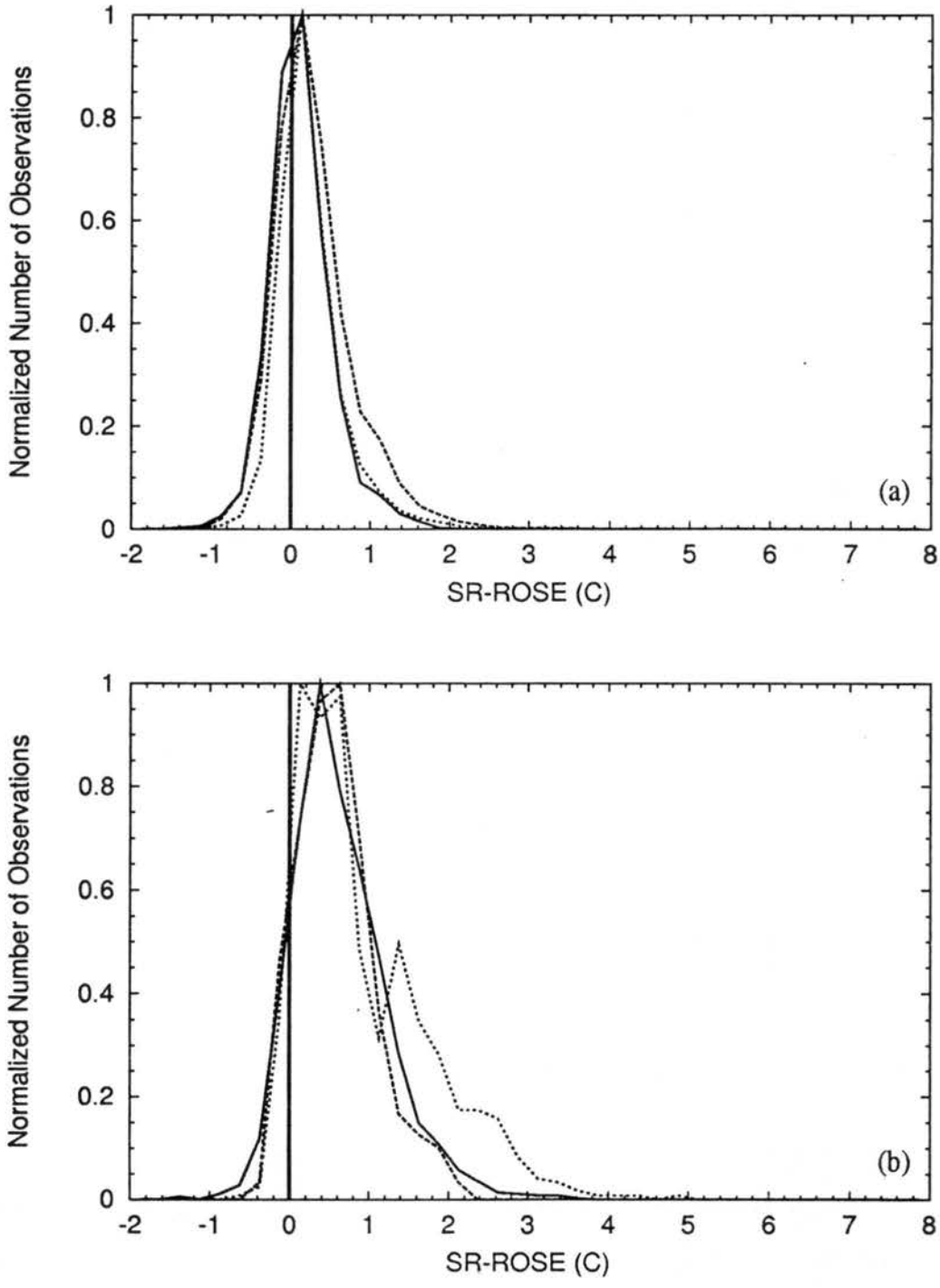

Figure 5.6: Normalized distributions of SR-ROSE temperature errors in warm clouds for all data points with measurable CWC from the entire reconstructed database (short dashes), all points with measurable CWC from the subset of radial legs containing CWC and PMS data (long dashes), and all points with measurable total liquid water content (CWC + PMS) from the subset of data (solid) for (a) liquid water contents < 1.0 g m^{-3} and (b) liquid water contents > 1.0 g m^{-3}.

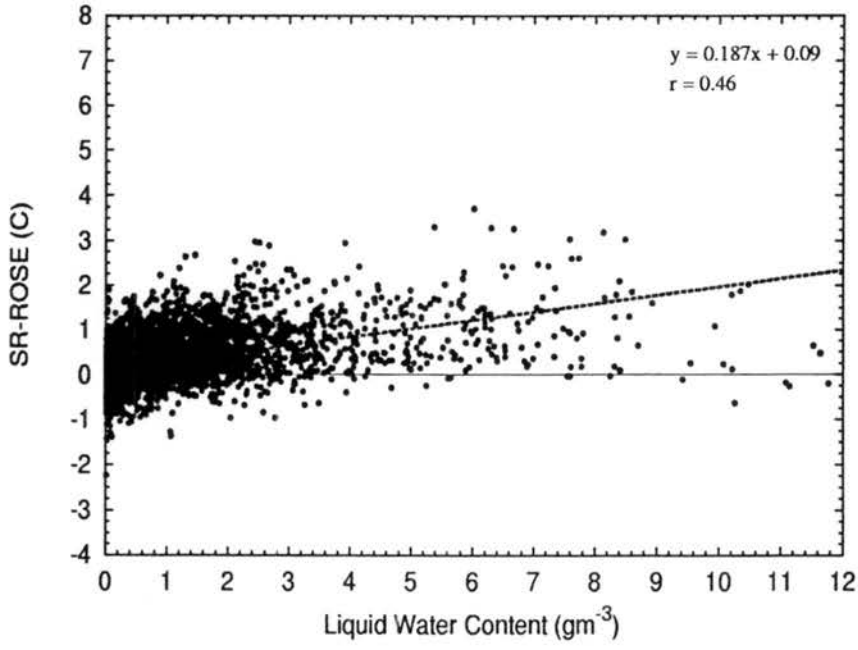

Figure 5.7: SR-ROSE temperature errors in warm clouds for all points in the subset of radial legs containing CWC and PMS data with measurable liquid water content (CWC + PMS). The dashed line is the linear fit.

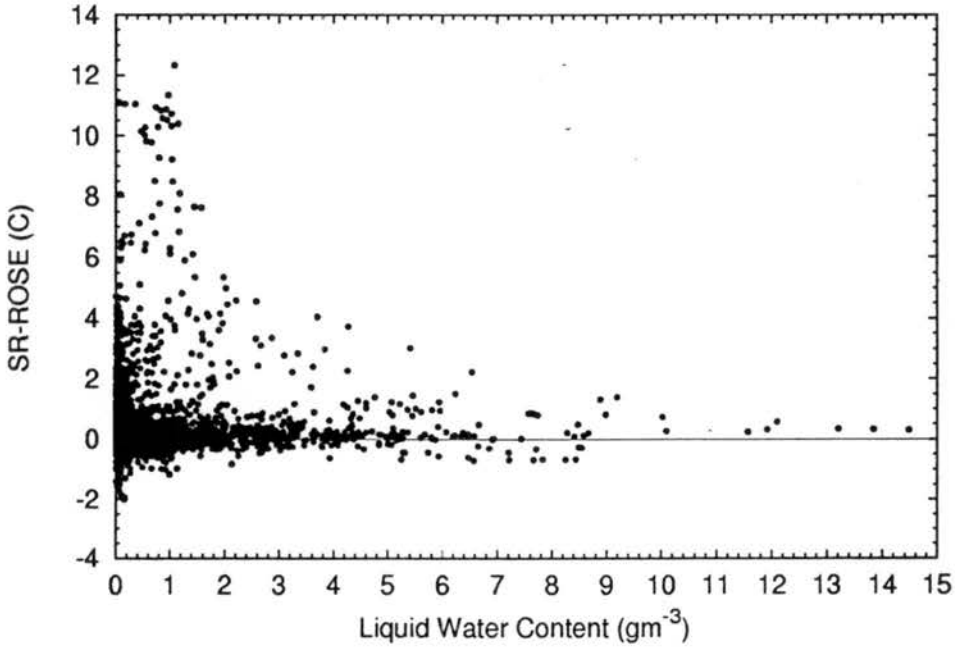

Figure 5.8: SR-ROSE temperature errors in cold clouds for all points in the subset of radial legs containing CWC and PMS data with measurable liquid water content from ice particles. Liquid water contents are derived solely from the ice particles.

effects (as discussed in Chapter 2) can contribute to temperatures errors, and thus explain part of the large scatter with respect to liquid water content. Cloud and precipitation drops can come in contact with the inner housing surface, and the evaporation of this liquid cools the air before it reaches the sensing element. Similarly, ice buildup in the housing can produce errors. Wetting and/or icing of the housing is never directly known, but very likely occurs. In thick clouds and heavy rain, the housing may become completely inundated with water that must evaporate. Furthermore, small-scale fluctuations in cloud-drop size spectra and concentrations that are undetectable in total CWC measurements combined with turbulence within the housing may result in differential wetting of the sensing element, and thus temperature errors. The weak correlation found between total liquid water contents and temperature error suggests that each case of instrument wetting is apt to be unique from the next, either caused by drops of any size impinging on the sensor element, or the inner housing surface, or some combination of the two. The fact remains that instrument wetting is producing temperature errors during penetrations of clouds and precipitation in hurricanes.

5.3 Instrument Wetting Locations

5.3.1 Definition of an Instrument Wetting Location

Each reconstructed radial leg was examined to identify locations of significant SR-ROSE temperature errors caused by wetting. In order to eliminate subjectivity in the determination of Instrument Wetting Locations (IWLs), specific criteria were adopted. IWLs were defined as regions where the ROSE temperature was cooler than the SR temperature by three standard deviations of the SR-ROSE difference in clear air continuously for 2.5 km. This strict criteria were chosen to ensure that the temperature difference was instrument wetting, rather than superimposed instrument noise. Furthermore, each IWL is required to be separated by 10 km from another IWL. This criteria is used in order to prevent the identification of two adjacent IWL that are essentially the same IWL separated by a few data points with the SR-ROSE difference slightly less than three standard deviations of the temperature difference in clear air. Shown in Figure (5.9) is the distri-

bution of the standard deviations of the SR-ROSE temperature difference in clear air for all radial legs. A new standard deviation is calculated for each penetration during the reconstruction process. The average standard deviation is 0.25°C, resulting in temperature errors in IWLs exceeding 0.75°C on average.

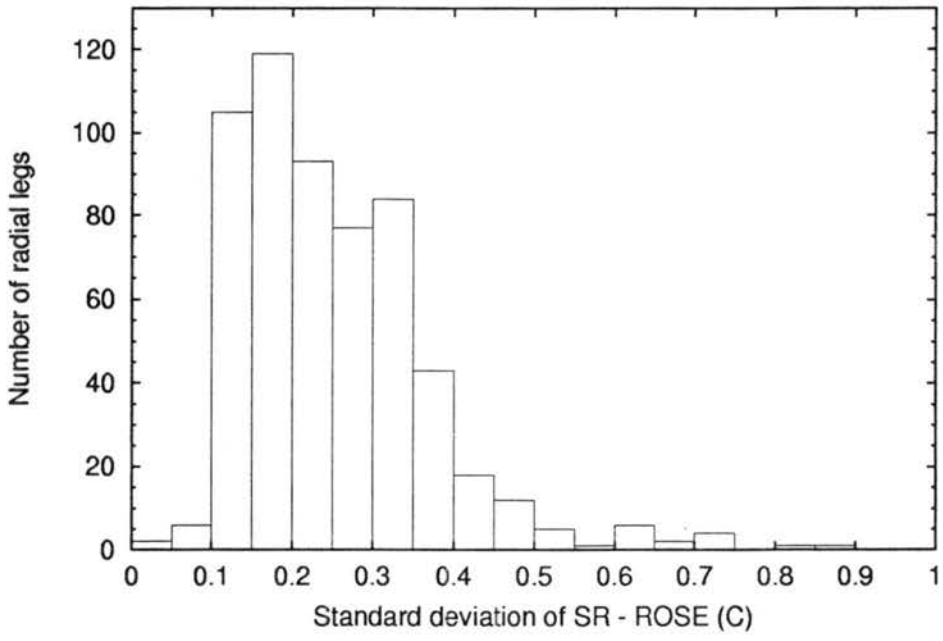

Figure 5.9: Distribution of the standard deviations of clear air SR-ROSE calculated for each radial leg.

A total of 364 IWL were identified in the 579 reconstructed radial legs. The number of IWL per radial leg ranged from 0 to 3. A total of 287 radial legs, or 50% of all radial legs, contained at least one IWL. The number of radial legs per hurricane with at least one identified IWL is presented in Table 5.1. The percentage of radial legs with IWL was highly variable from hurricane to hurricane. More than 50% of the radial legs in 12 hurricanes (Diana 1984, Emily 1987, Gilbert 1988, Hugo 1989, Emily 1993, Iris 1995, Luis 1995, Edouard 1996, Hortense 1996, Norbert 1984, Tina 1992, and Olivia 1994) contained an IWL. Only 2 hurricanes (Gabrielle 1989 and Jerry 1989) contained no IWLs in their radial legs.

Shown in Figures (5.10) and (5.11) are four representative examples of radial legs from the reconstructed database with identified IWLs. In Figure (5.10a) are the SR and

Table 5.1: Inventory of reconstructed Atlantic and East Pacific hurricanes radial legs with at least one identified IWL by flight level. Included is the number of flights and Saffir-Simpson categories during the flights.

		Number of	Radial Legs							
Hurricane	Year	Flights	900	850	700	600	500	400	Total	Category
Diana	1984	4		26					26	1,2,3,4
Danny	1985	2		5					5	1
Elena	1985	4		16					16	1,2,3
Gloria	1985	6		1	15		4		20	1,2,3,4
Juan	1985	2		6					6	1
Emily	1987	2			11	1	22		34	3
Floyd	1987	1		2					2	1
Florence	1988	1	1						1	1
Gilbert	1988	5		8	21				29	2,3,4,5
Joan	1988	1		2					2	3
Dean	1989	1				4			4	1
Gabrielle	1989	0							0	3
Hugo	1989	4				12	3		15	3,4,5
Jerry	1989	0							0	1
Gustav	1990	3		2	6				8	1,2,3
Emily	1993	2					6		6	1,3
Erin	1995	1			4				4	1
Iris	1995	1				5			5	1
Luis	1995	2				4	5		9	4
Opal	1995	1				2			2	4,3
Edouard	1996	2			21				21	4
Fran	1996	1		3				1	4	3
Hortense	1996	1		5					5	2
Norbert	1984	6		4	16		10		30	3,4
Jimena	1991	3		1	7	4			12	4
Tina	1992	2		12					12	1
Olivia	1994	2				9			9	2,3,4
ATL-Total		47	1	76	78	28	40	1	224	
EPAC-Total		13		17	23	13	10		63	
Total		60	1	93	101	41	50	1	287	

ROSE temperatures, CWC, and vertical motion for a radial leg at 500 mb from Gloria (1985). An ROSE temperature decrease of 6.0°C occurs as the plane passes through the eyewall cloud centered at 35 km. The SR temperature experiences no decrease, but rather an increase of 1.0°C. The radial width of the identified IWL is 9.0 km, and is comparable to the width of the eyewall cloud (As shown by the CWC). Figure (5.10b) depicts similar data for a radial leg at 600 mb from Hugo (1989). A IWL is identified in the eyewall cloud with a maximum temperature error of 1.7°C and a width of 7.5 km. In a radial leg at 700 mb from Gilbert (1988) (Figure 5.11a) an IWL was identified beginning near 60 km and extending 48.5 km radial outward. The IWL was not located in the primary eyewall, but rather associated a concentric eyewall (see Black and Willoughby 1992), and the average temperature error across the IWL was 1.75°C. The primary eyewall cloud, centered near 10 km, contained similar CWC and showed some signs of instrument wetting, however the magnitude of the errors over the width prevented an IWL from being identified. Two IWLs are identified in a radial leg (Figure 5.11b) at 700 mb from Gustav (1990). The first is located in the eyewall cloud near 35 km with a maximum temperature error of 2.3°C and a width of 7.0 km. The second IWL is located in a rainband near 140 km with maximum temperature error of 1.9°C and a width of 3.0 km.

The four radial legs first suggest that while a few IWL can be easily identified by visual inspection of the ROSE data, such as the radial leg of Gloria (Fig.5.10a), most IWL are not easily identified through visual inspection, such as in Hugo (Fig. 5.10b). Visual detection can be difficult because the observed ROSE radial temperature gradient across eyewalls or rainbands agrees with temperature gradients commonly observed and expected from thermal wind calculations or theory. Furthermore, radial widths of the identified IWLs in the four radial legs were typically smaller than the clouds in which the IWL were located. Large temperature errors (compared to where no CWC was observed) were commonly present across the entire width of the clouds, but the errors were not consistently large over the cloud width. Thus, the definition of an IWL identifies only the continuous, large temperature errors due to wetting. Smaller and/or less continuous

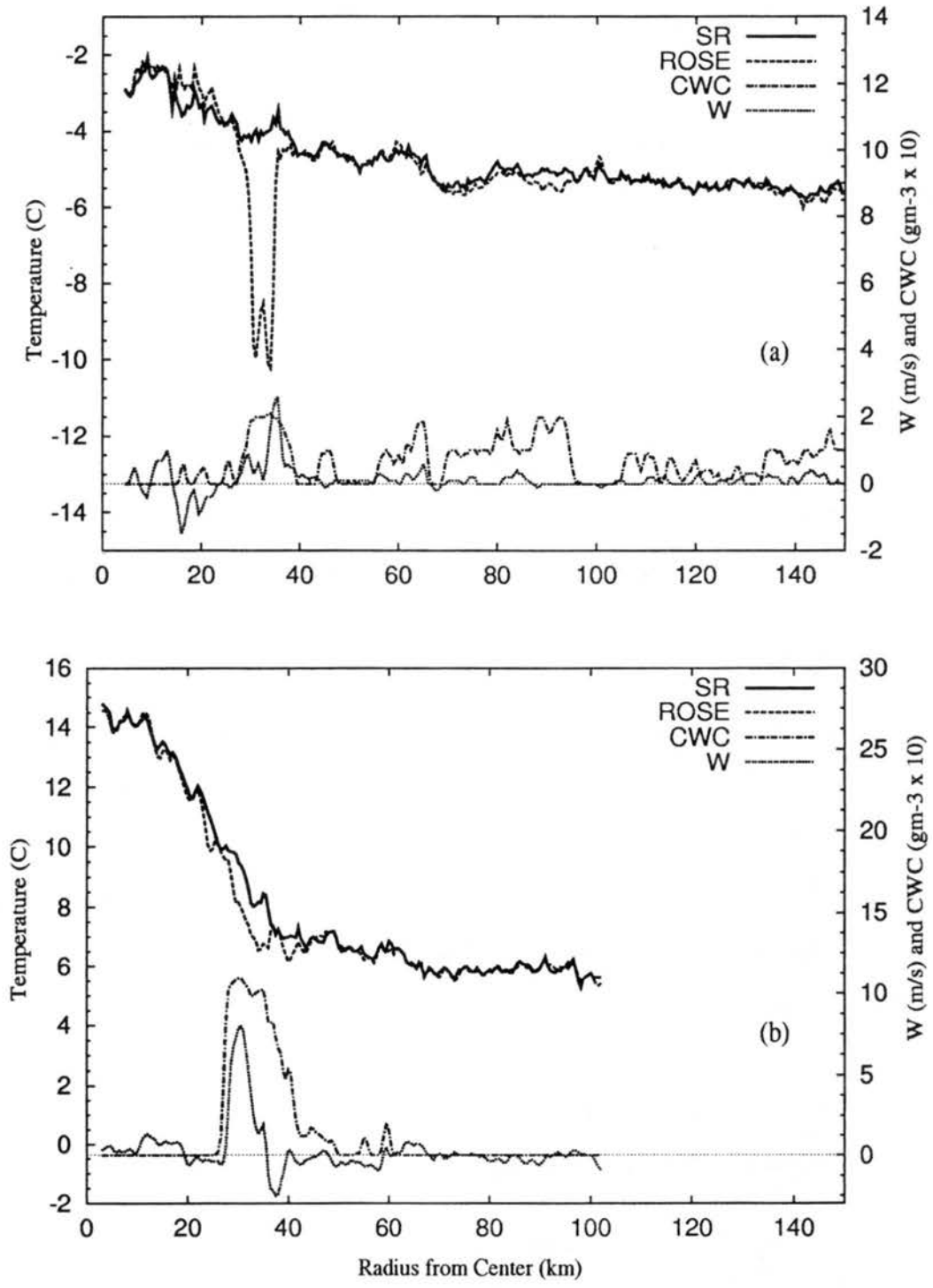

Figure 5.10: Examples of radial legs with identified Instrument Wetting Locations (IWL). Shown are the side radiometer (SR) and Rosemount (ROSE) temperatures, cloud water content (CWC) measured by the JW probe, and vertical motion (w) for (a) Hurricane Gloria (1985) on August 22 at 500 mb, and (b) Hurricane Hugo (1989) on September 21 at 600 mb.

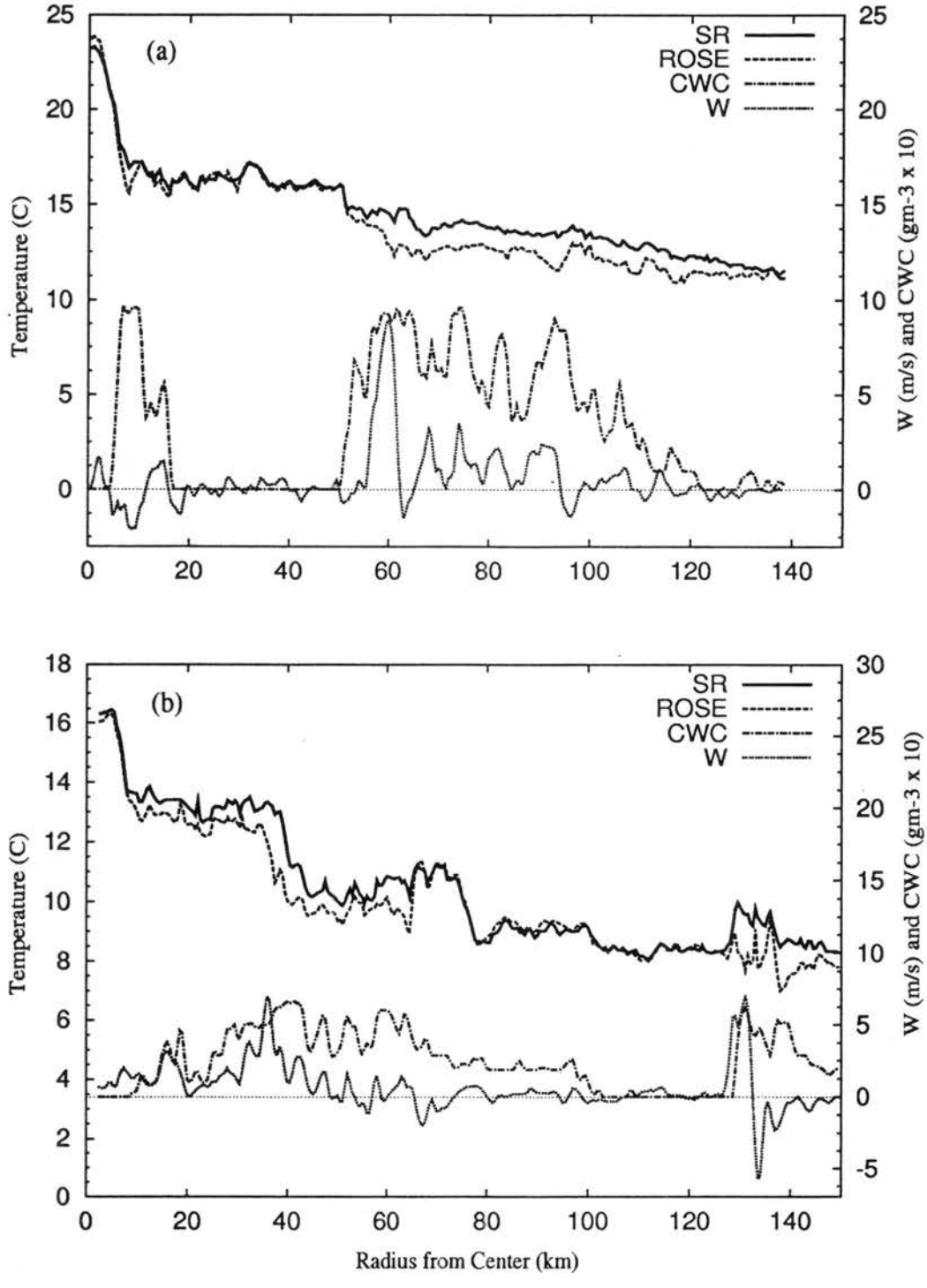

Figure 5.11: Same as figure 5.10 except for (a) Hurricane Gilbert (1988) on September 14 at 700 mb, and (b) Hurricane Gustav (1990) on August 29 at 700 mb.

instrument wetting errors may be frequent during hurricane penetrations, and will be addressed later.

5.3.2 Variability

Large variability exists between the IWL identified in the four radial legs of Gilbert, Hugo, Gloria, and Gustav shown in Figures (5.10) and (5.11). The IWL ranged from being radially wide with small temperatures errors and low CWC, to radially narrow with large temperature errors and relatively high CWC. It was found that IWL were located in eyewalls, concentric eyewalls, and rainbands. Does similar variability exist amongst all identified IWL? What are average features and error values in IWL? Shown in Figure (5.12) is the maximum SR-ROSE temperature error of each IWL as a function of SR temperature at the maximum error. The maximum errors at temperatures warmer than 5°C typically ranged from 0.5-4.0°C, with only two exceeding 4.0°C. The maximum errors at temperatures colder than 5°C frequently exceeded 4.0°C with two exceeding 10.0°C. As shown earlier, temperature errors in clouds containing supercooled drops, or cold clouds, are observed to be be 2-3 times larger than errors in warm clouds. However, at all ambient temperatures theoretical error values are rarely attained, suggesting the sensing element is rarely wetted completely.

The width of each IWL is shown in Figure (5.13) as a function of the maximum SR-ROSE temperature error. The average width for all IWL is 8 km, however, widths > 15 km frequently occur with 3 IWL wider than 40 km. Separation of the IWL into warm and cold cloud cases reveals substantial differences in variability and average widths. The average warm cloud IWL width was 6.5±5.0 km, while cold cloud IWL average 13.5±14.5 km in width. Figure (5.14) depicts the radial distance of the maximum SR-ROSE temperature error from the Radius of Maximum Updraft (RMU) in the eyewall (see Section 5.4 Composites at Eyewall RMU for a complete description of how the eyewall RMU was identified). A positive (negative) distance indicates the the IWL is located outside (inside) the eyewall. Nearly 70% of all IWL maxima are located within 20 km of the eyewall RMU. The majority of the remaining IWL are located radially outside the

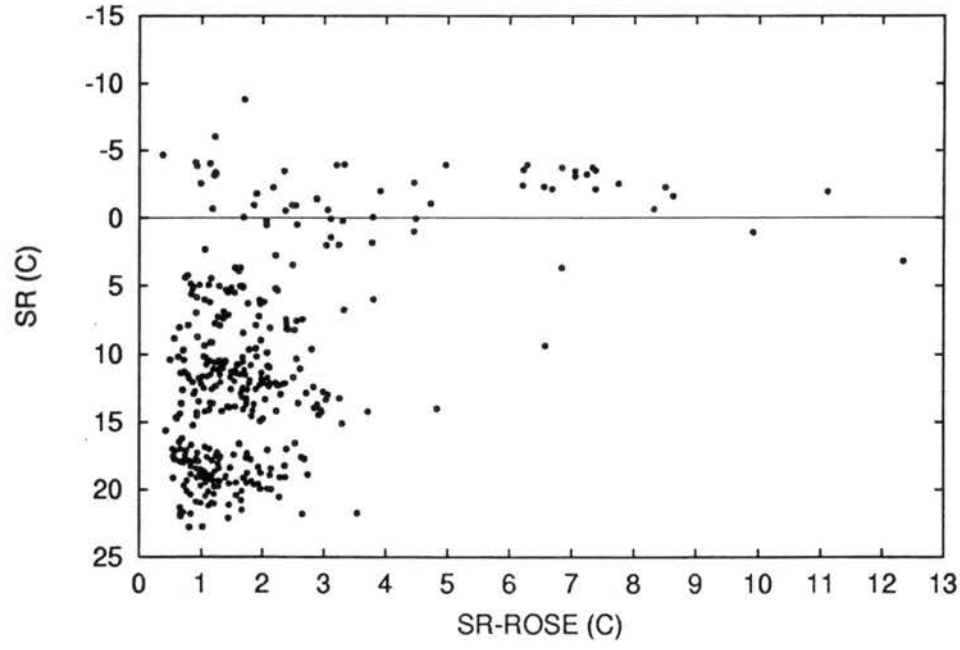

Figure 5.12: Maximum SR-ROSE temperature error of each identified IWL.

eyewall RMU and are associated with concentric eyewalls or rainband convection. Only 5 IWL are located more than 20 km radially inside the eyewall RMU, and in each case the aircraft was in a cloud. Three of the five IWL occurred in wide eyewalls dominated by downdrafts such that the RMU was located along the outer edge of the eyewall and the IWL was along the inner edge.

Shown in Figure (5.15) is the average vertical motion across the IWL as a function of the maximum SR-ROSE temperature error. Over 88% of IWL were located within regions dominated by updrafts. A weak relationship is evident between average updraft vertical velocity and the maximum temperature error. Since temperature errors were shown to have a weak positive correlation with liquid water content and strong updrafts generate more CWC and precipitation than weak updrafts, the presence of larger temperature errors collocated with strong updrafts is to be expected. However, nearly 10% of IWL were located in regions dominated by downdrafts, and visual inspection of these IWL were made. Over 90% were located in eyewall clouds that contained a weak and narrow updraft flanked on each side by wider downdrafts, and roughly 50% maximum temperature errors

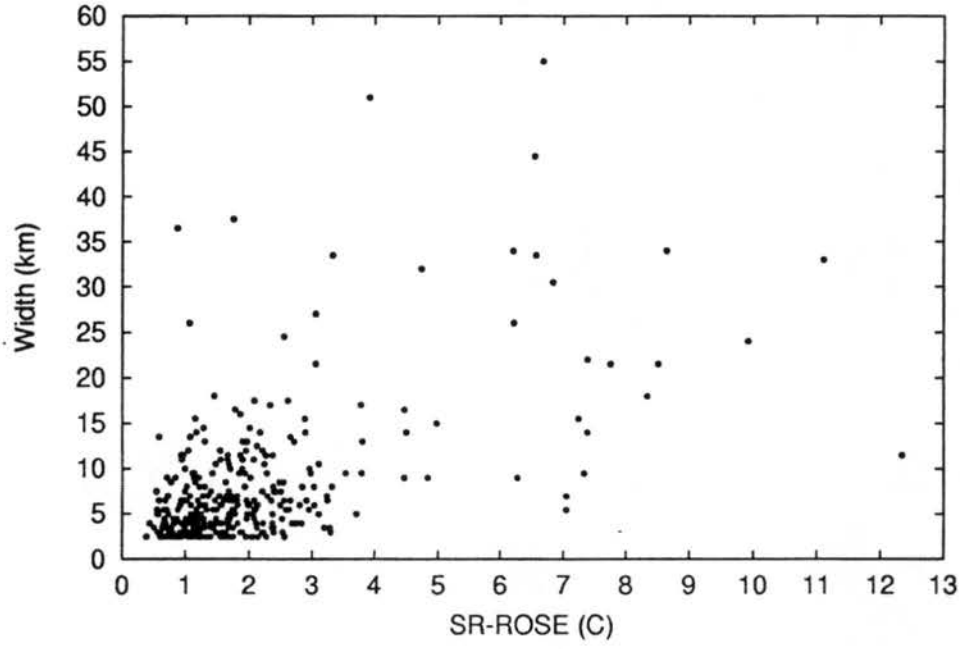

Figure 5.13: The radial width of each identified IWL.

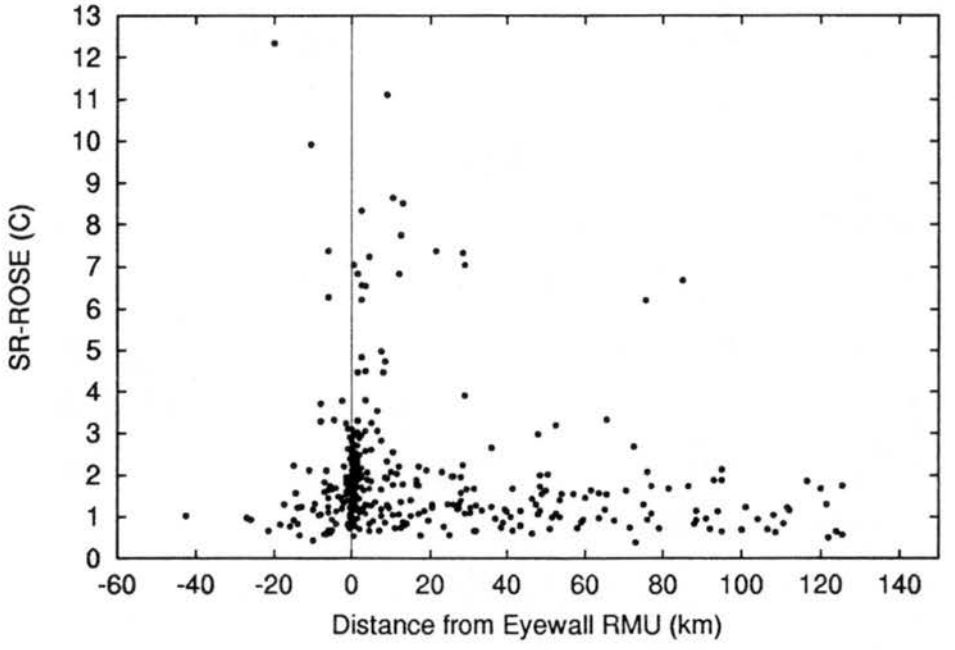

Figure 5.14: The radial distance of each identified IWL from the eyewall RMU. Positive (negative) values are outside (inside) the eyewall.

were located in the weak updraft. Other IWL were in eyewall clouds composed entirely of downdrafts. All but one IWL dominated by downdrafts was in a region of CWC, but the CWC values were typically less than 0.2 g kg^{-1}. Black and Hallett (1986) and Houze et al. (1992) showed the CWC maxima was collocated with the eyewall updraft such that the convective downdrafts contained minimal CWC. Peak precipitation-sized particle concentrations tended to occur on the outside edges of eyewall updrafts and in convective downdrafts associated with the eyewall updraft. Thus, liquid water is typically present in updrafts and downdrafts, permitting instrument wetting errors in both.

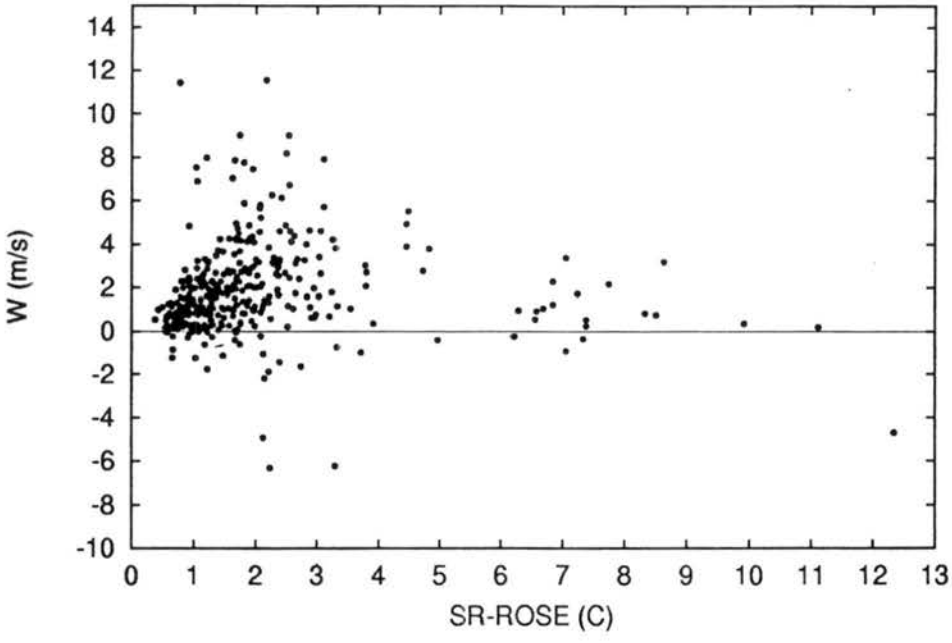

Figure 5.15: Average vertical motion across each identified IWL.

Composites were constructed at the 850, 700, 600, and 500 mb pressure levels to determine average features of IWLs. The composites were centered on the Radius Maximum SR-ROSE Temperature Error (RMTE) of each IWL. Shown in Figure (5.16) are the composite vertical motion and CWC for all IWL at the given pressure levels. The RMTE is located at 0 km on the abscissa, with positive (negative) values representing the distance radially outward(inward) from the maximum error. (The abscissa will be labeled using this method for all future composite plots centered on either the RMTE

or the eyewall RMU.) On average the RMTE is 0.5-1.5 km radially outward from the local maxima of vertical motion (Figure 5.14a), which increases in magnitude from 1.5 m s^{-1} at 850 mb to 3.4 m s^{-1} at 500 mb[2]. Radially outward from the RMTE the average vertical motion decreases to near zero within 5 km at all levels. However, radially inward the vertical motion does not drop to near zero for 10-15 km, further suggesting that the RMTE is outside local maxima of vertical motion, but still in an updraft. Furthermore, the RMTE is either collocated with or just outside a maxima of CWC (Figure 5.16b), as average CWC at the RMTE increases from 0.4 g m^{-3} at 850 mb to 0.8 g m^{-3} at 500 mb. The composite radial structure of vertical velocity and CWC about the RMTE agree with previous observational and composite studies across eyewalls. Jorgensen (1984b), Black and Hallett (1986), and Houze et al. (1992) showed that CWC maxima coincide with updraft maxima, while peak precipitation particle concentrations tended to occur in convective downdrafts outside the eyewall updraft, resulting in total liquid water content maxima along the outside edges of eyewall updrafts.

Figure (5.17a) depicts the average SR-ROSE temperature error for all IWL composited about the RMTE. Average errors at the RMTE increase from 1.2°C at 850 mb to 4.3°C at 500 mb. The corresponding standard deviation of SR-ROSE for each radial distance from RMTE is shown for in Figure (5.17b). Standard deviations increase from 850 to 500 mb at the RMTE, however, at 850, 700, and 600 mb standard deviations never exceed 1.0°C and are nearly constant across the composite IWL. At 500 mb standard deviations average 2.0°C across the composite IWL with a maxima of 2.8°C at the RMTE. Despite the large standard deviations, the average temperature errors are significant at the 99.9% confidence level at all pressure levels and distances within 10 km of the RMTE.

The specific humidity errors calculated from the reconstructed dew points corresponding to the respective SR and ROSE temperatures are shown in Figure (5.18a). During

---

[2]A second vertical motion maxima of 2.2 m s^{-1} at 500 mb is found 7.5 km radially inward from the RMTE. The secondary maximum is the result of several IWL identified outside the eyewall of Hurricane Emily (1987), which consistently contained some of the strongest directly measured updrafts ever observed in tropical cyclones (see Black et al. 1994).

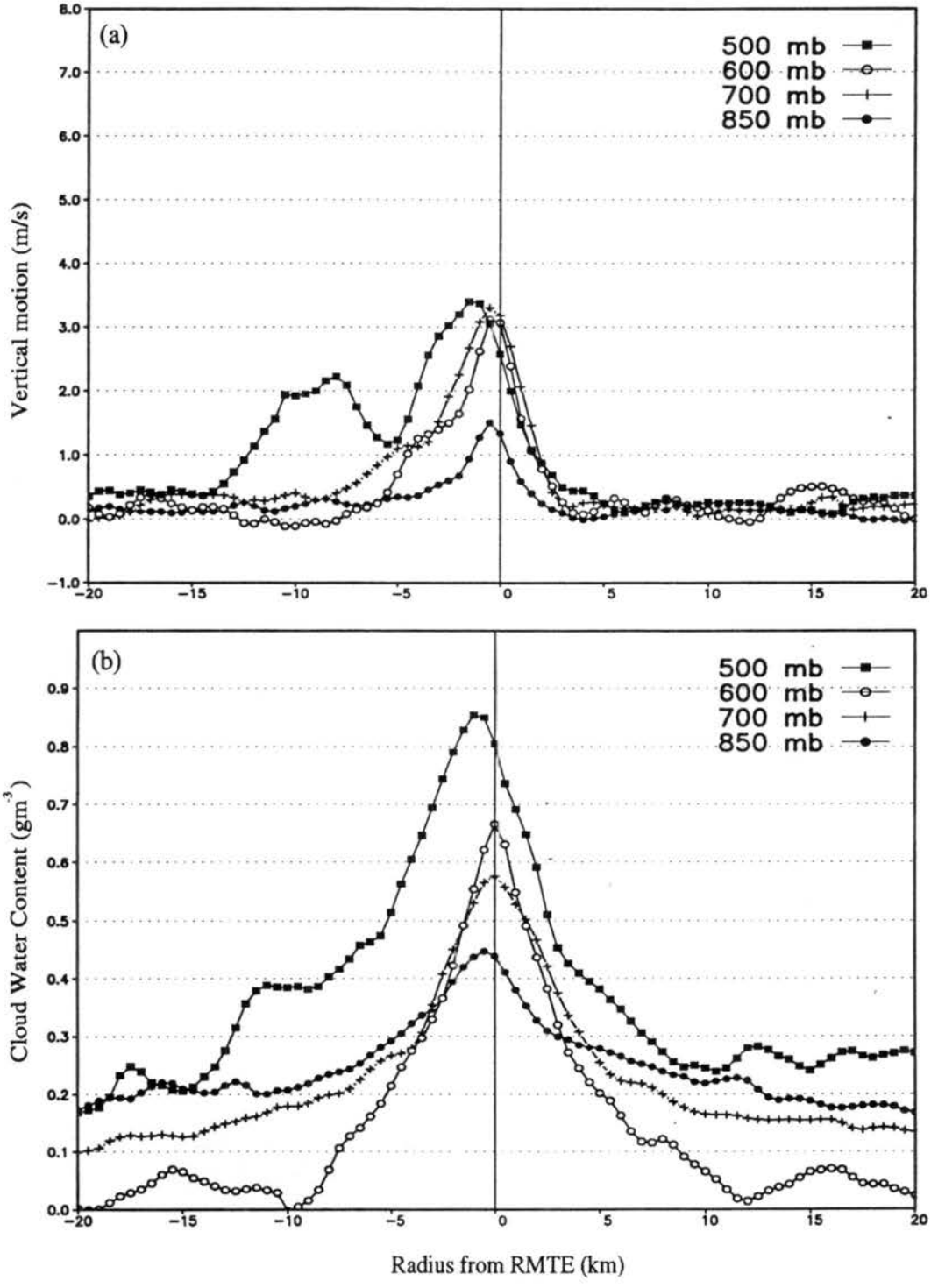

Figure 5.16: Composite IWL (a) vertical motion and (b) CWC at 850, 700, 600, and 500 mb about the Radius of Maximum Temperature Error (RMTE). The RMTE is at 0.0 km on the abscissa and positive (negative) distances are radially outward (inward) from the RMTE.

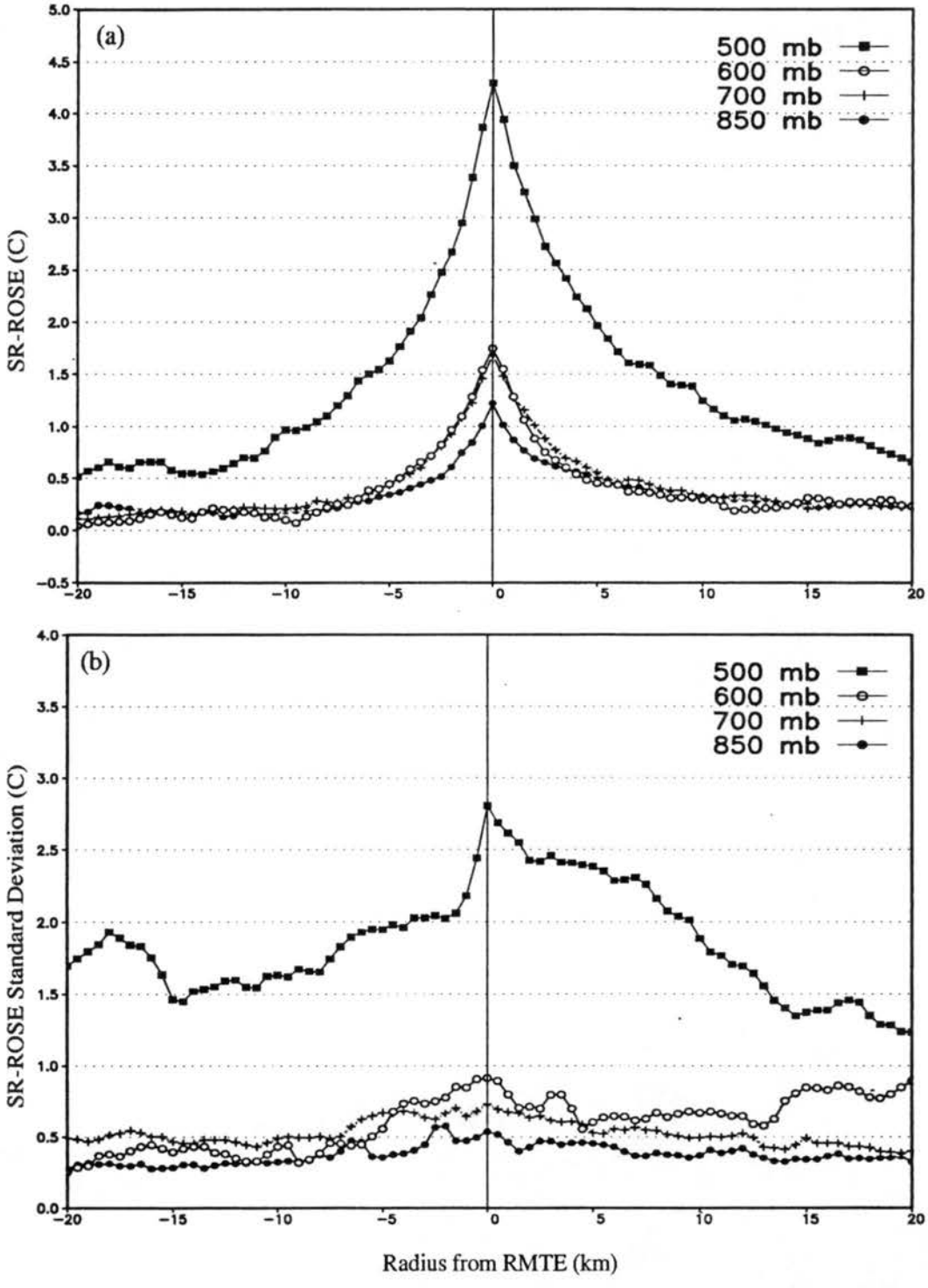

Figure 5.17: Composite IWL (a) SR-ROSE and (b) standard deviation of SR-ROSE at 850, 700, 600, and 500 mb about the RMTE.

reconstruction, if the dew point exceeded either, or both, the SR or ROSE temperature, the dew point was adjusted to a value corresponding to 99% relative humidity for the observed SR or ROSE temperature that was exceeded. Thus, the specific humidity errors are not a result of the reconstruction process increasing the relative humidity of the air, but rather maintaining the dew point near saturation for a warmer SR temperature. Average specific humidity errors due to instrument wetting are nearly equivalent across the composite IWL between 850 and 600 mb with an average maxima of 1.2 g kg^{-1} at the RMTE. At 500 mb specific humidity errors are up to a factor of 2 larger than the errors at the other pressure levels, with a maxima of 1.8 g kg^{-1} at the RMTE. The standard deviations of specific humidity are shown in Figure (5.18b) and maxima near the RMTE range from 0.5 g kg^{-1} at 850 mb to 1.0 g kg^{-1} at 500 mb. The average specific humidity errors are also significant at the 99.9% level at all pressure levels and distances within 10 km of the RMTE.

Average temperature errors greater than 1.0°C combined with specific humidity errors greater than 1.0 g kg^{-1} can have significant effects on other thermodynamic parameters, calculated from the observed quantities, that are typically used to describe hurricane structure. Shown in Figure (5.19) are the resulting average errors of virtual temperature (T_v), virtual equivalent potential temperature (θ_v), the pseudo-adiabatic equivalent potential temperature (θ_e) calculated according to Bolton (1980), and the reversible equivalent potential temperature (θ_{er}) calculated according to Emanuel (1994). At the RMTE average T_v errors range from 1.5°C to 4.5°C; θ_v errors range from 1.5 K to 5.5 K, θ_e errors range from 5.0 K to 11.5 K, and θ_{er} errors range from 4.5 K to 10.0 K. The standard deviations (shown in Appendix B) are roughly half the average error values near the RMTE, and as a result the average errors of T_v, θ_v, θ_e, and θ_{er} are significant at the 99.9% confidence level at all pressure levels and distances within 10 km of the RMTE.

5.3.3 Stratifications

Up to this point, IWL have been stratified by either flight level or whether the IWL was found in a cold or warm cloud regime. However, the organization, symmetry, and

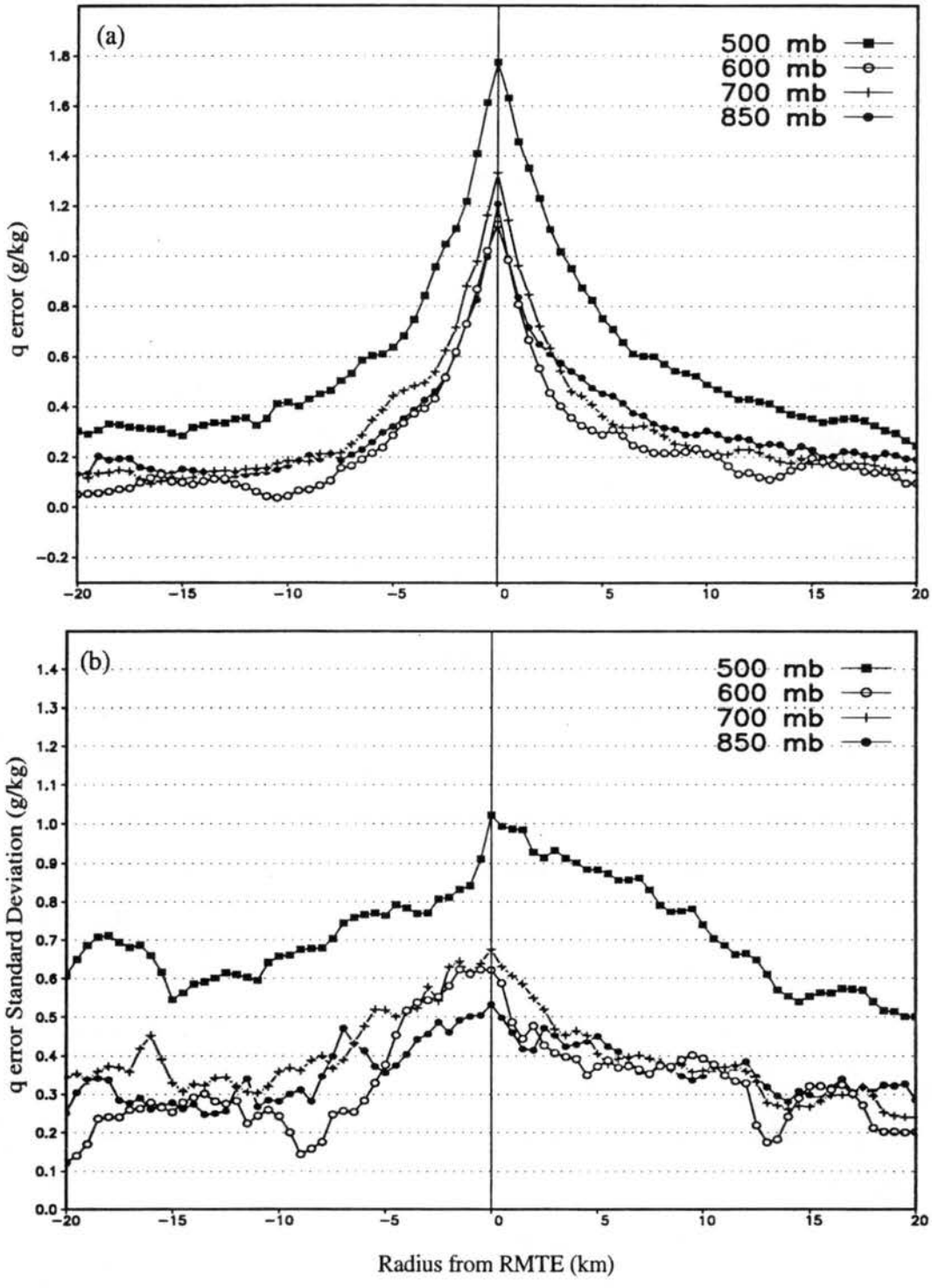

Figure 5.18: Composite IWL (a) specific humidity error and (b) standard deviation of the specific humidity error calculated from the SR and ROSE temperatures and adjusted dew points at 850, 700, 600, and 500 mb about the RMTE.

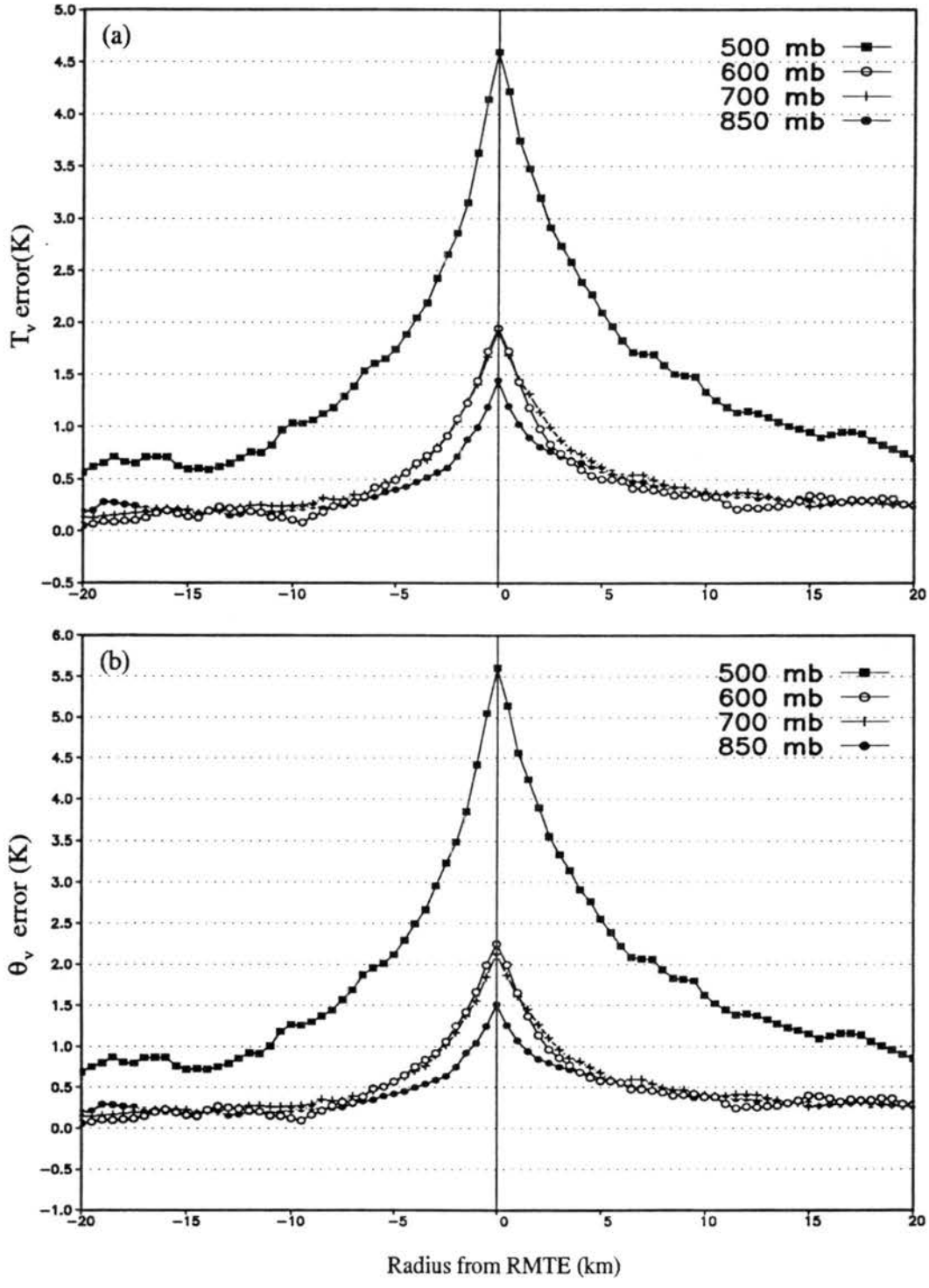

Figure 5.19: Composite IWL errors of (a) T_v, (b) θ_v, (c) θ_e, and (d) θ_{er} calculated from the SR and ROSE temperatures and adjusted dew points at 850, 700, 600, and 500 mb about the RMTE.

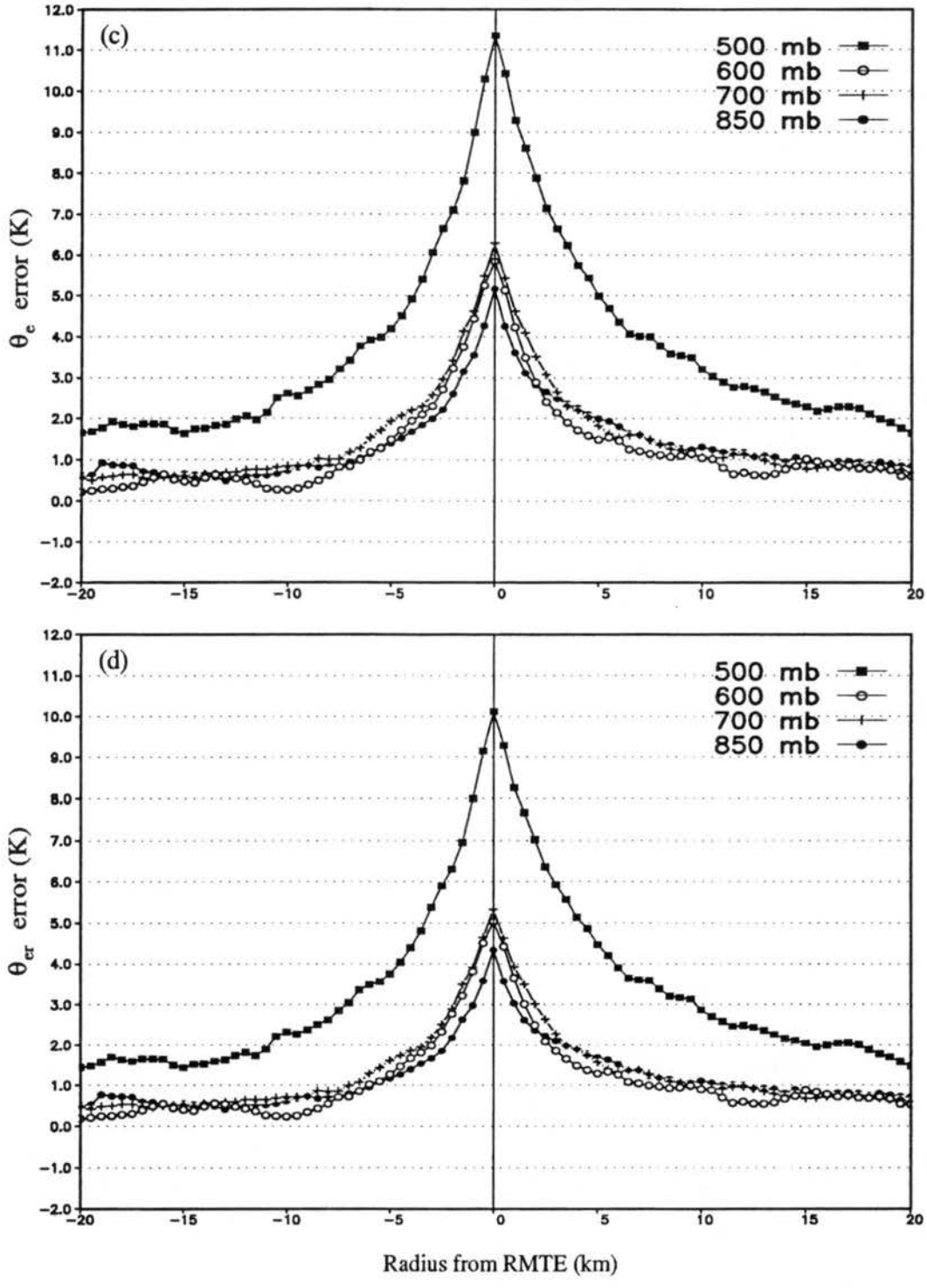

Figure 5.19: Continued.

intensity of the hurricane convection is observed to vary during a cyclone's lifetime. Variations in convection directly vary liquid water content, and thus, the magnitude and frequency of instrument wetting errors may vary accordingly. Table (5.3) further stratifies the radial legs with at least one identified IWL by the intensity of the storm during the penetration, the quadrant with respect to storm motion, and the 12-hour intensity change centered on the time of the penetration[3]. Included in Table (5.2) is the percentage of total radial legs that contain at least one IWL. Table (5.3) utilizes the same stratifications but for the total number of IWL, and includes the average number of IWL in each radial leg with at least one IWL identified.

Table 5.2: Statistics of radial legs in Atlantic and East Pacific Hurricanes with at least one identified IWL stratified by flight level. The percentage (%) of the total radial legs examined for each stratification is included.

	Pressure Level						Total Legs with IWL	Total All Legs	%
	900	850	700	600	500	400			
Total	1	93	101	41	50	1	287	579	50
Category 1,2	1	49	10	9	5		74	205	36
Category 3,4,5		44	90	32	45	1	213	374	57
Front Quadrant		24	35	16	14	1	90	160	56
Left Quadrant	1	26	26	7	11		71	134	53
Back Quadrant		23	24	6	10		63	148	43
Right Quadrant		20	16	12	15		63	137	46
Intensifying		52	41	3	23		119	251	47
Steady	1	11	42	22	8		84	167	50
Filling		30	18	16	19	1	84	161	52

Intensity

Intense hurricanes (Category 3, 4, and 5 on the Saffir-Simpson scale) are required in balanced theory to have a stronger and more organized secondary circulation (i.e eyewall

[3]Stratifications unrelated to hurricane structure, such as the direction a radial leg was flown and the P-3 aircraft used to make the penetration, were also made. No significant differences in frequency, magnitude, or radial shift of the RMTE from the local updraft or CWC maxima was found between inbound and outbound radial legs. The I aircraft was found to contain a greater percentage of radial legs with at least one IWL than the H aircraft. However, this variability between aircraft is likely a function of the hurricanes each aircraft penetrated and the pressure level of penetrations since the same thermodynamic instrumentation is mounted at identical locations along the forward fuselage of each aircraft, thus providing similar exposures.

Table 5.3: Statistics of IWL found in Atlantic and East Pacific Hurricanes. The last column represents the average number of IWL per leg, given that at least one IWL was identified in the leg.

	Pressure Level						Total	Legs with	
	900	850	700	600	500	400	IWL	IWL	IWL/Leg
All	1	111	133	58	60	1	364	287	1.27
Category 1,2	1	58	13	13	6		91	74	1.23
Category 3,4,5		53	120	45	54	1	273	213	1.28
Front Quadrant		32	50	23	21	1	127	90	1.41
Left Quadrant	1	31	31	10	12		85	71	1.20
Back Quadrant		26	31	8	10		75	63	1.19
Right Quadrant		22	21	17	17		77	63	1.22
Intensifying		61	52	6	29		148	119	1.24
Steady	1	13	59	32	10		115	84	1.37
Filling		37	22	20	21	1	101	84	1.20

convection) compared to minimal hurricanes (Category 1 and 2) in order to satisfy momentum and mass budgets and maintain the intensity of the primary circulation (Ooyama 1969; Gray 1997). Black (1993) showed eyewall vertical motions > 10 m s^{-1} were more frequently observed in intense hurricanes than in minimal hurricanes. Larger vertical motions produce larger liquid water contents and increase the possibility of instrument wetting errors. However, neither the vertical motion nor the CWC (both not shown) composited about the RMTE for IWL in minimal and intense hurricanes indicate any significant systematic increase with intensity. Likewise, the composite SR-ROSE temperature errors (also not shown) are effectively invariant with intensity. The lack of increase in composite temperature errors with intensity is a result of the averages being dominated by maximum errors < 2.5°C (see Figure 5.20). However, maximum errors > 2.5°C are much more common in intense hurricanes, comprising 24% of all IWL compared to only 5% in minimal hurricanes. Furthermore, from Table (5.2) intense hurricanes contain more radial legs with IWL (57%) than minimal hurricanes (36%).

Quadrant

Asymmetric convection is commonly observed in hurricanes. Shapiro (1983) showed that storm motion produces enhanced boundary layer convergence leading to asymmetric convection in front of and to the right of a moving storm. Marks (1985) observed max-

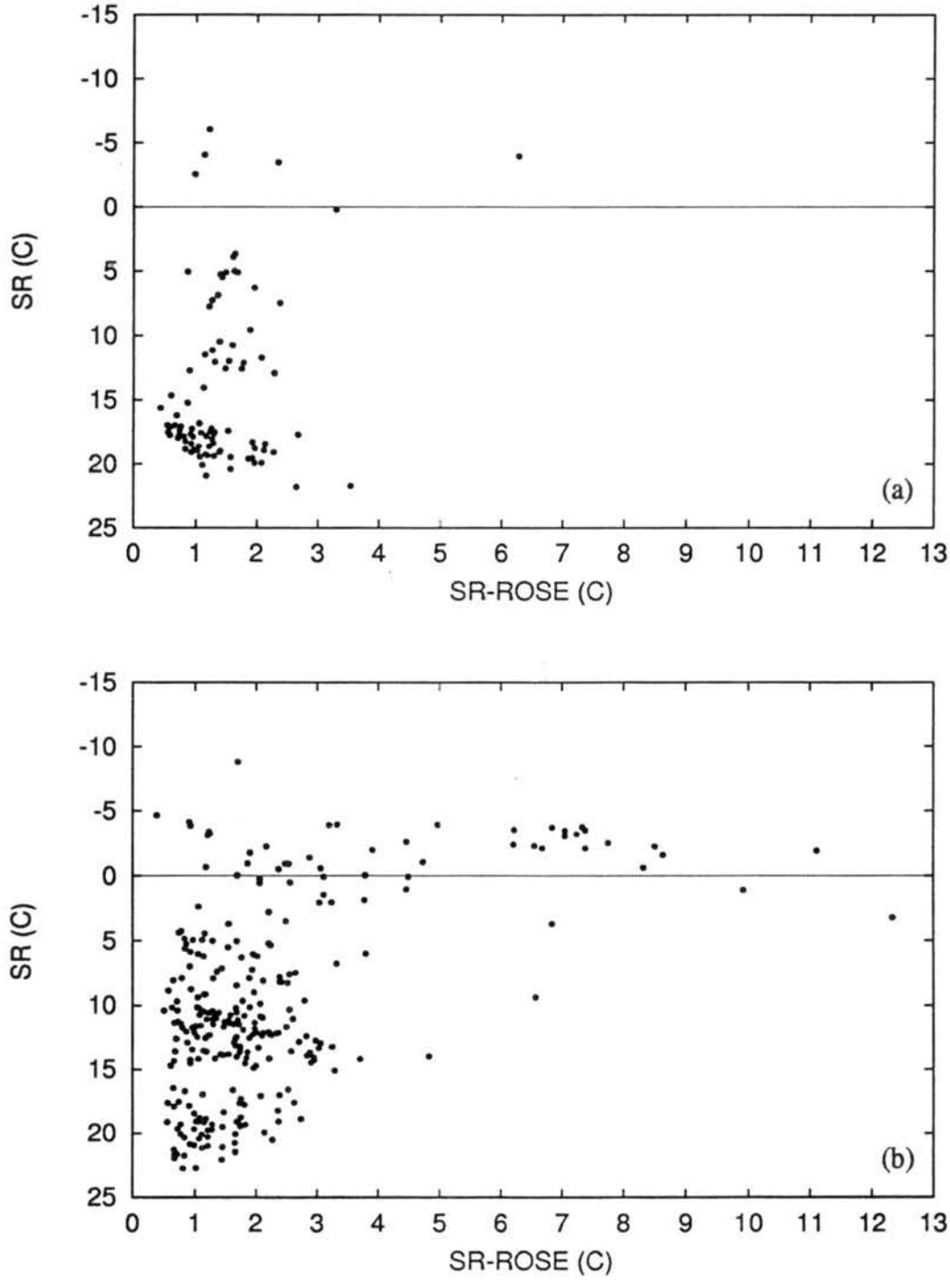

Figure 5.20: Maximum SR-ROSE temperature error of each identified IWL for (a) minimal hurricanes, and (b) intense hurricanes.

imum rainfall amounts from the eyewall and rainbands in the front and right quadrants, respectively, of Hurricane Allen (1980), confirming the theoretical arguments of Shapiro (1983). In recent years, modeling studies of the effects of environmental vertical shear on a vortex (e.g. Jones 1995; DeMaria 1996; and Bender 1997) have also shown enhanced convection results on the downshear side of the vortex due to isentropic lifting (via dry dynamics), vorticity advection (via moist dynamics), and an decrease in the vertical stability. Thus, convective asymmetries forced by storm motion and environmental vertical wind shear may result in asymmetries of instrument wetting errors. Due to the lack of adequate environmental shear data for all the hurricanes included in this study, only quadrant variations with respect to storm motion were investigated.

IWL are most frequently observed in the front quadrant (Table 5.2) with 56% of the radial legs containing an IWL. In contrast, only 43% the radial legs in the back quadrant contain an IWL. Furthermore the front quadrant averaged 1.4 IWL per radial leg with an IWL compared to 1.2 on average in the other quadrants (Table 5.3). The IWL composite vertical velocities and CWC (both not shown) were significantly larger (at the 90% confidence level) in the front quadrant than the back quadrant at all levels[4] supporting the theoretical arguments of Shapiro (1983). However, composite temperature errors (also not shown) vary little with quadrant and differences are not systematically significant. The lack of significant observed variability of IWL average temperature errors between quadrants may be partially due to convective asymmetries induced by vertical shear. Such asymmetries can act to offset asymmetries due to translation if the storm motion and shear vectors are opposite. Furthermore, Marks and Houze (1987) found the total liquid water content patterns in Hurricane Alicia (1983) were less asymmetric and radially confined than the active convection due to the cyclonic and upward advection of the precipitation.

---

[4]All other differences of composite vertical velocity and CWC between quadrants are comparable and not significant.

Intensity Change

Black (1993), using a vertically pointing Doppler radar, showed that intensifying hurricanes contained more eyewall vertical motions > 10 m s^{-1} than filling hurricanes. Rodgers and Adler (1981), using analyzes of a passive microwave radiometer in typhoons, found that intensification was indicated by an increase in radiometer-derived latent heat release, or total volumetric liquid water content. Marks (1985) found that the total volumetric rainfall and latent heat release in the eyewall region of Hurricane Allen remained constant through several changes in intensity. However, Marks (1985) further showed that the mean rainfall rate in the eyewall was six times larger than that in the rainbands, and the eyewall rainfall rate increased as the eyewall radius decreased during intensification periods. Thus, larger and more frequent instrument wetting errors, particularily in the eyewall, were expected in radial legs flown during intensification.

Table (5.3) indicates that roughly 50% of radial legs contain IWL regardless of the storm's current intensity change with a slightly greater percentage of radial legs contained an IWL during filling (52%) than during intensification (47%). Furthermore, 73% of IWL found in filling hurricanes were associated with eyewall convection compared to 70% in intensifying hurricanes and 64% in steady-state hurricanes. Therefore, intensifying hurricanes contained neither the greatest percentage of radial legs with an IWL, nor the greatest percentage of IWL associated with eyewall convection. No statistically significant differences of average vertical velocity, CWC, or SR-ROSE temperature errors between any rate of intensity change were found at any level near the RMTE. An intensity change stratification was made using a ± 5 knot and ± 15 knot and, rather than ± 10 knots, change in maximum wind speed over 12 hours to distinguish between intensifying, filling, and steady-state storms, and no significant differences in SR-ROSE temperature errors were found either.

5.4 Composites at eyewall RMU

The eyewall embodies the upward branch of the secondary circulation of a hurricane, and can be generalized as a ring of cumulonimbus convection surrounding the eye. The eyewall coincides with the sharpest radial pressure and temperature gradients and contains the maximum winds. Eyewall convection either thermodynamically or dynamically forces a radial mass convergence to replace the mass carried aloft. Convergence outside the eyewall occurs both in the friction layer and above the friction layer. The mid-level convergence imports angular momentum to spin up the primary circulation, while the convergence in the friction layer extracts energy from the ocean to feed the eyewall convection. On the other hand, convergence of air from the eye into eyewall at middle and lower levels results in adiabatic sinking, and warming, in the eye and hence a pressure fall. The pressure fall further sharpens the radial pressure gradient causing the maximum winds to increase. Thus, eyewall convection plays a primary role in maintaining the hurricane circulation and producing intensity changes, and the accurate representation of thermodynamic quantities and their variability in and near the eyewall are essential to understanding hurricane life cycles. Average IWL temperature errors range from 1.2°C at 850 mb to almost 5.0°C at 500 mb. Maximum observed errors exceeded 3.0°C in warm clouds and 10°C in cold clouds. With errors of these magnitudes and nearly 70% of all IWL located within 20 km of the eyewall RMU, significant errors in eyewall thermodynamic quantities can exist.

In order to determine hurricane average features all reconstructed radial legs at the 850, 700, 600, and 500 mb pressure levels were composited about the eyewall RMU. The large data set and lack of radar data made the identification of the eyewall RMU difficult. The radial legs were first visually inspected to ensure that the Radius of Maximum tangential Wind (RMW) was associated with the primary eyewall rather than a stronger secondary wind maximum (Samsury and Zipser 1995) associated with a rainband or outer concentric eyewall. If a weaker tangential wind maximum with nearby convection ($w > 1.0$ m s^{-1} and CWC > 0.0 g m^{-3}) was identifiable inside the RMW, the RMW was shifted

to the inner maximum. The RMW was adjusted for a total of 75 radial legs, and many were identified by Samsury and Zipser (1995) as containing secondary wind maximum. The eyewall RMU was then indentified by locating the maximum upward vertical velocity within 20 km of the RMW. Since many hurricane eyewalls consist of asymmetric active convection, some eyewall passes are dominated by downdrafts flanked by unsaturated updrafts, or are composed entirely of weak unsaturated updrafts. Thus, the indentified RMU for a given leg is not necessarily in saturated active convection. To minimize incorrect RMU indentifications, each leg was visually inspected. If the identified RMU was associated with an unsaturated updraft while a saturated, but weaker, updraft was nearby and still within 20 km of the RMW, the RMU was adjusted to the weaker updraft. If no saturated updraft could be found, the indentified RMU was maintained. Dew point depression and CWC were used to make such distinctions, and the RMU was adjusted for a total of 35 radial legs.

The resulting composite vertical motion and CWC are shown in Figure (5.24). The eyewall RMU is located at 0 km on the abscissa, with positive (negative) values representing distances radially out(in) from the maximum vertical motion. Average vertical motion in the eyewall (Figure 5.24a) ranges from 2.0 m s^{-1} at 850 mb to 7.0 m s^{-1} at 500 mb and is the primary signal in the vertical motion composite [5]. Average CWC in the eyewall peaks at the RMU (Figure 5.21b) and ranges from 0.3 g m^{-3} at 850 mb to 0.7 g m^{-3} at 500 mb. Only radial legs with CWC in the eyewall were used to create the composite.

The SR-ROSE temperature errors and the standard deviations of the error composited about the eyewall RMU are shown in Figure (5.22). Error maxima (Figure 5.22a) are

---

[5]One must be careful to assume from this composite that vertical motion increases with height in the hurricane eyewall. Observations will be presented in Chapter 6 to support such an increase with height. However, only after the radial legs are stratified by intensity since intense hurricanes have observed stronger eyewall vertical motions than minimal hurricanes. The vertical motion composite in Figure (5.21a) is not stratified by intensity and a portion of the apparent increase with height is a result of more radial legs from intense hurricanes found at upper levels while more radial legs in minimal hurricanes were found at lower levels.

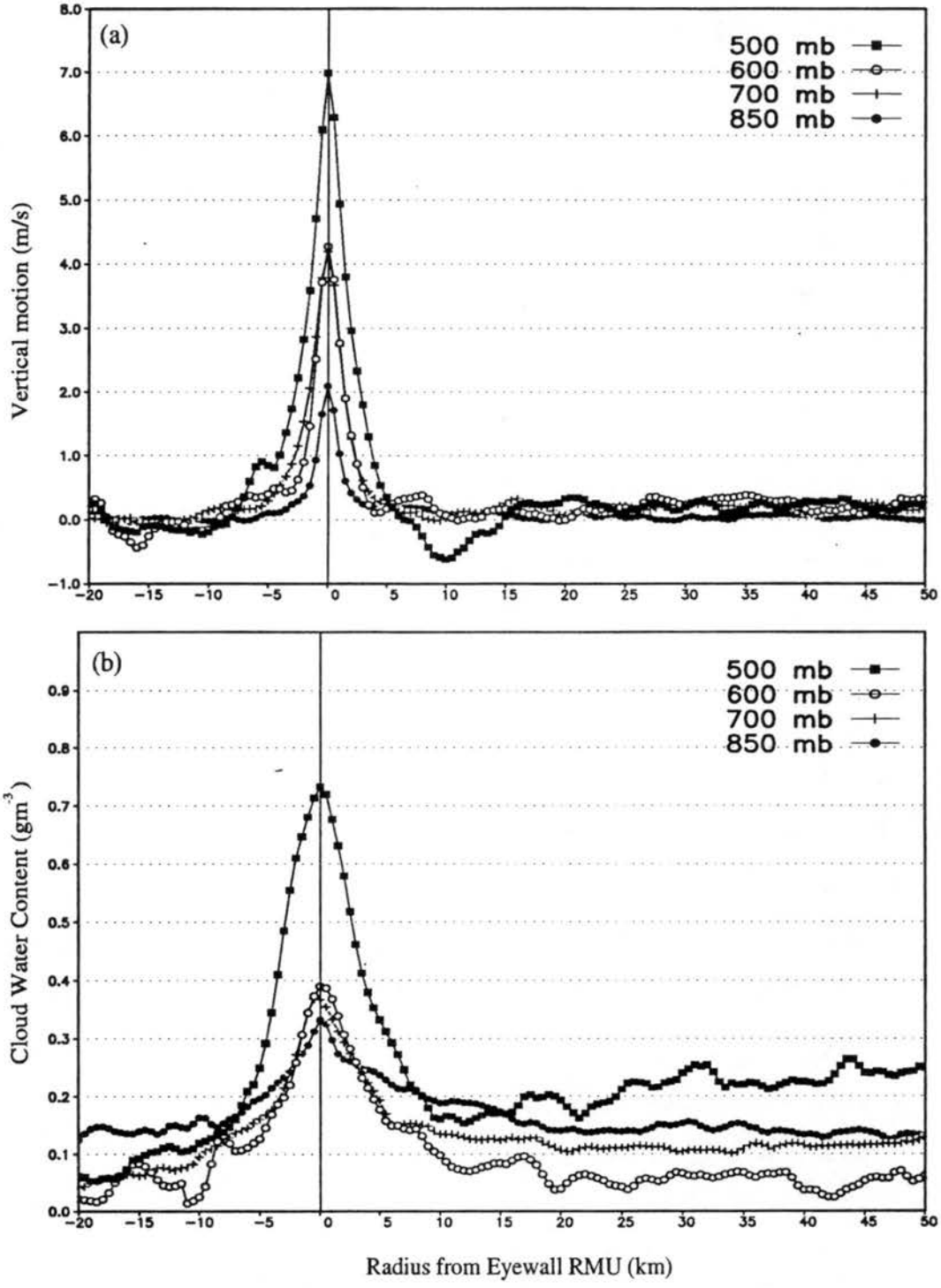

Figure 5.21: Composite (a) vertical motion and (b) CWC at 850, 700, 600, and 500 mb about the eyewall Radius of Maximum Updraft (RMU). The RMU is at 0.0 km on the abscissa and positive (negative) distances are radially outward (inward) from the RMU. Only radial legs with CWC in the eyewall were used to create the CWC composite.

located 0.5-1.0 km outside the RMU and range from 0.5 °C at 850 mb to 1.8°C at 500 mb. The composited eyewall maximum errors are 2-3 times smaller than the error maxima at the RMTE for the composite IWL (Figure 5.17a). Standard deviations of the errors (Figure 5.22b) range from 0.3°C to 2.0°C over the composited radii, and are maximum near the RMU but not collocated with the maximum errors. Although the standard deviations are the same magnitude or larger than the errors[6], the error averages at all pressure levels are significant at the 95% confidence level from within 5 km inside the RMU to 50 km outside the RMU. Errors rapidly decrease with radius to zero within 15 km inside the RMU, while outside the RMU errors decrease up to a factor of 4 less with radius and are still non-zero 50 km outside the eyewall. The radial distribution of temperature errors agrees qualitatively with the observed radial distribution of total liquid water (cloud and precipitation) within a mature hurricane. Maximum total liquid water is located in and just outside the convective eyewall updraft, with a minimum of liquid water in the eye, and a nearly continuous radial presence of liquid water outside the eyewall due to stratiform precipitation and convective bands at variable radii. (e.g. Jorgensen 1984b; Black and Hallett 1986).

The composite specific humidity errors and the standard deviations calculated from the reconstructed dew points corresponding to the respective SR and ROSE temperatures are shown in Figure (5.23). Remember the specific humidity errors are not a result of the reconstruction process significantly increasing the relative humidity of the air, but rather maintenance of the dew point near saturation for a warmer SR temperature. Thus, maximum specific humidity errors are collocated with temperature errors at or just outside the RMU, and range from 0.45 g kg^{-1} at 850 mb to 0.82 g kg^{-1} at 500 mb. The radial distribution of specific humidity errors is similar to the distribution of temperature errors. Standard deviations are maximum near the RMU, and are the same magnitude as the

---

[6]The large standard deviations 5-10 km radially outside the eyewall at 500 mb are due to wide IWL with the eyewall updraft offset toward the inner edge of the IWL. Such IWL occurred when large regions of supercooled water extended beyond the eyewall updraft.

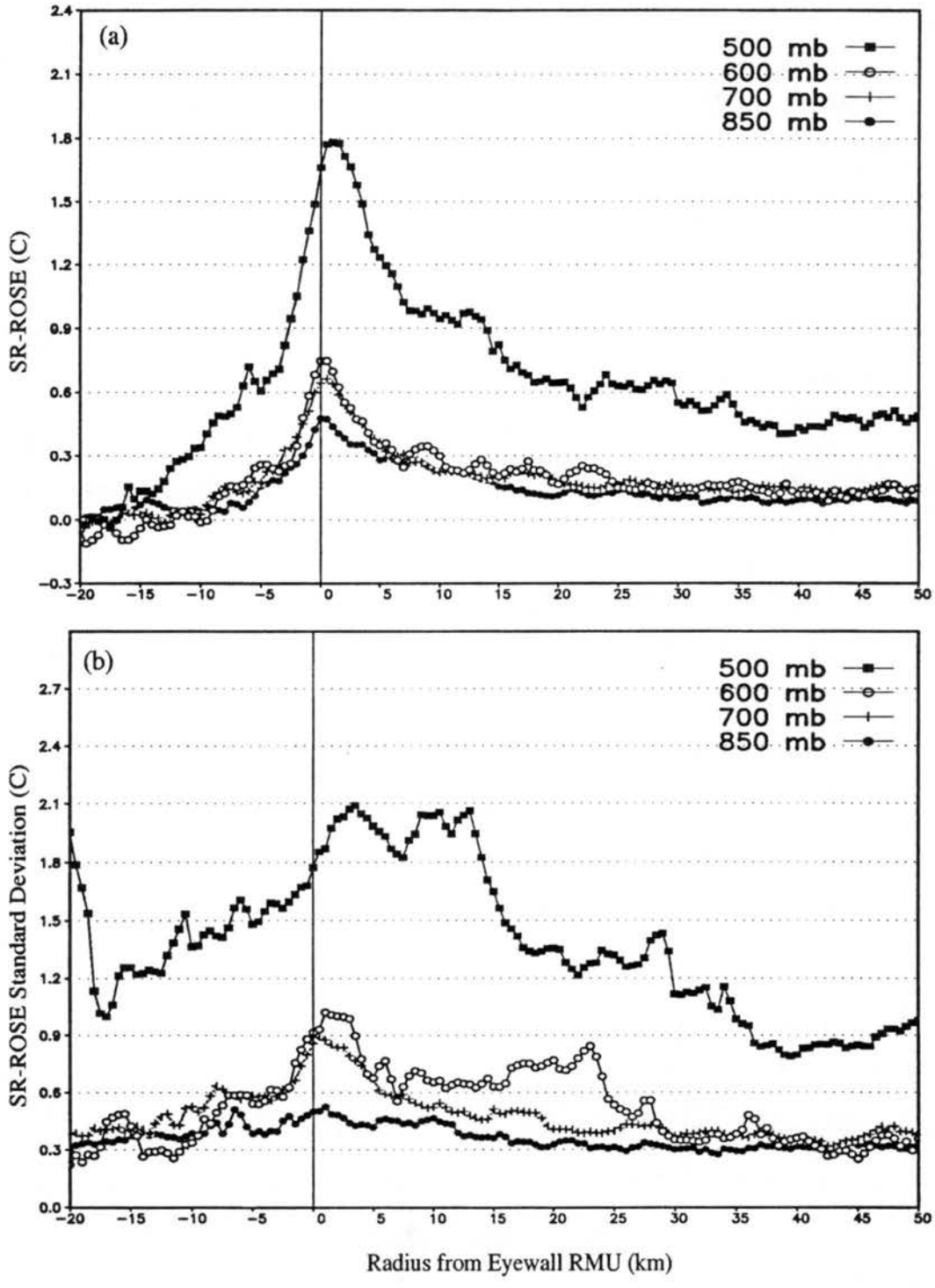

Figure 5.22: Composite (a) SR-ROSE and (b) standard deviation of SR-ROSE at 850, 700, 600, and 500 mb about the eyewall RMU.

average errors. However, the specific humidity errors at all pressure levels are significant at the 95% confidence level from within 5 km inside the RMU to 50 km outside the RMU.

Average temperature errors greater than 0.4 °C near the eyewall RMU combined with specific humidity errors greater than 0.4 g kg^{-1} have significant effects on other calculated thermodynamic quantities used to understand hurricane structure, intensity, and intensity change. Shown in Figure (5.24) are the composite errors of T_v, θ_v, θ_e, and θ_{er}. Average T_v errors near the RMU range from 0.6°C at 850 mb to 2.0°C at 500 mb, while θ_v errors range from 0.6 K to 2.4 K, θ_e errors range from 2.0 K to 5.0 K, and θ_{er} errors range from 1.5 K to 4.5 K near the RMU. Despite standard deviations of the same magnitude or larger than their respective average errors (not shown), the T_v, θ_v, θ_e, and θ_{er} errors at all pressure levels are significant at the 95% confidence level from within 5 km inside the RMU to 50 km outside the RMU.

5.5 Significance of Observed Errors

One may argue these composite errors are small and will have little effect upon the large-scale thermodynamic structure of an average hurricane. However, the composite errors are in fact composite values of all reconstructed radial legs, irrespective of whether a IWL was identified in the radial leg or if an identified IWL was associated with the eyewall. If a case study of a hurricane was performed in which more than 90% of the radial legs contained IWL, such as Edouard (1996), erroneous conclusions may be arrived at due to the presence of instrument wetting errors. The temperature errors in such a case study may reach values representative of a composite about the eyewall RMU of all radial legs with at least one identified IWL, as shown in Figure (5.25a). The eyewall temperature errors range from 0.75-3.0°C. Assuming specific humidity errors of only 0.4-0.8 g kg^{-1} results in θ_v errors of 1.0-4.0 K and θ_e errors of 2.0-8.0 K in a convective region. Furthermore, maximum observed temperature errors reached 5.0-10.0°C in some radial legs, which would produce θ_v errors of 6.5-13.0 K and θ_e of 12.0-24.0 K in a convective region! The scale at which a study is focusing is also important. A convective or mesoscale thermodynamic study would be severely affected by even small wetting errors, while a

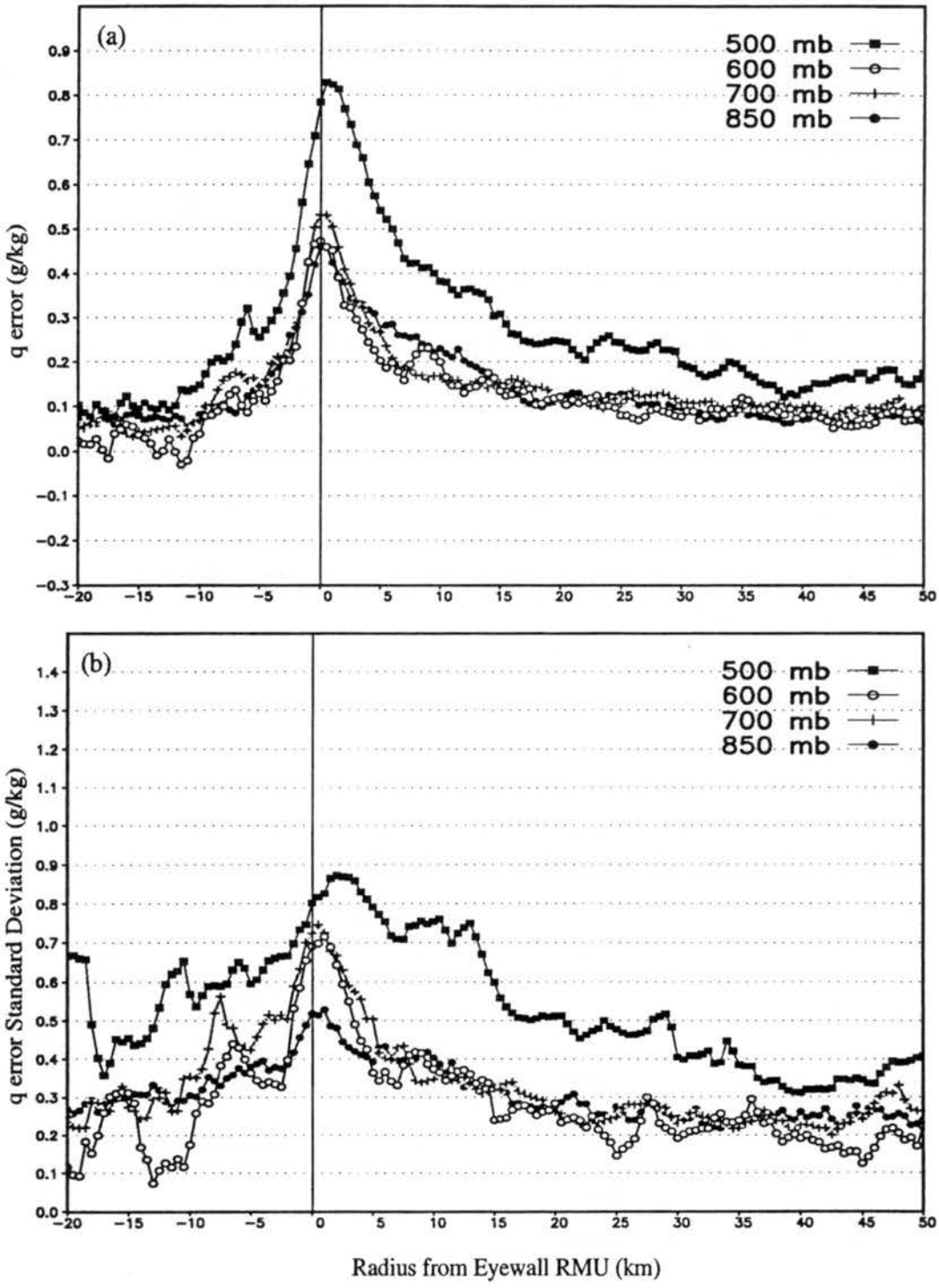

Figure 5.23: Composite (a) specific humidity error and (b) standard deviation of the specific humidity error calculated from the SR and ROSE temperatures and adjusted dew points at 850, 700, 600, and 500 mb about the eyewall RMU.

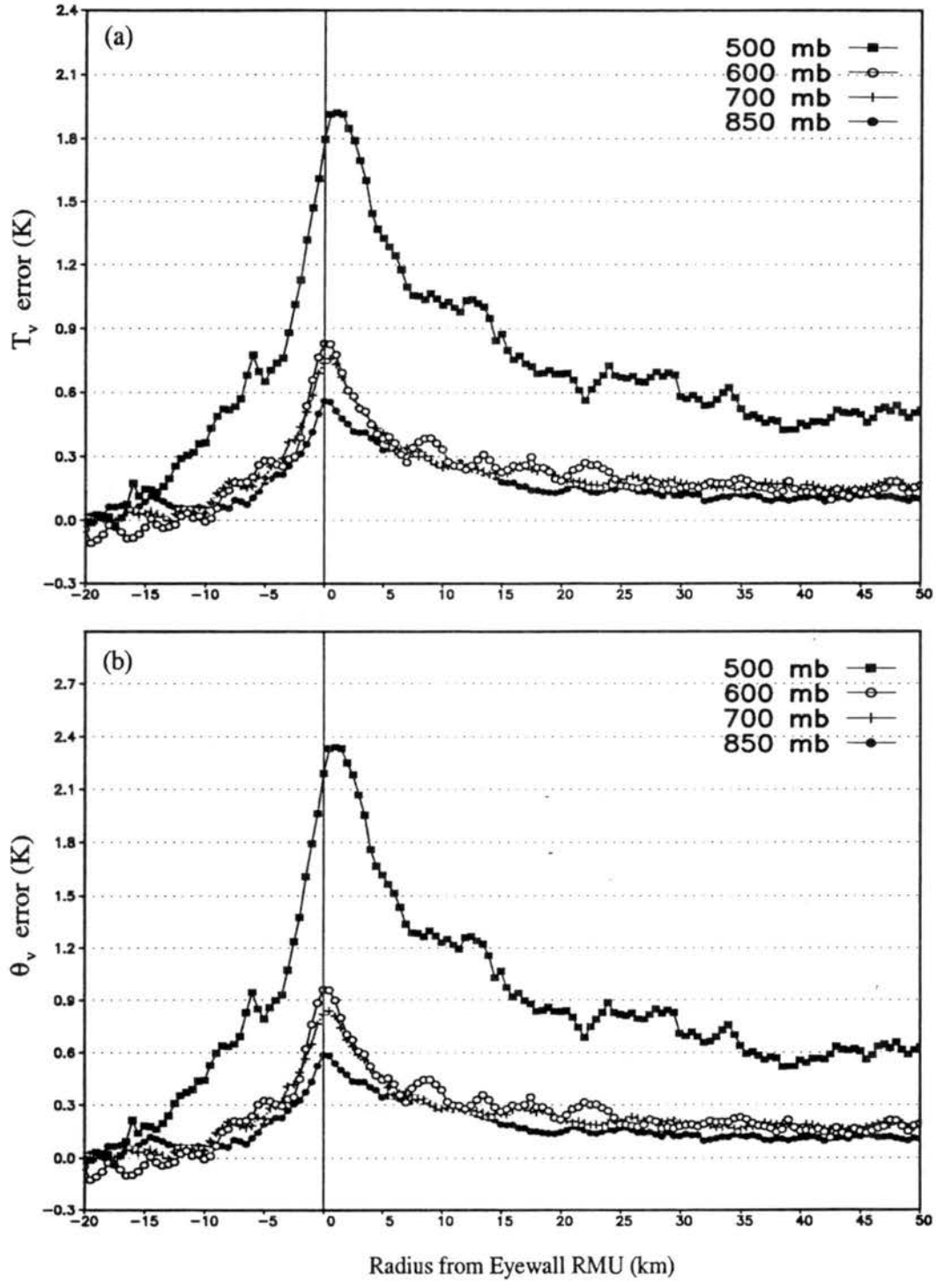

Figure 5.24: Composite errors of (a) T_v, (b) θ_v, (c) θ_e, and (d) θ_{er} calculated from the SR and ROSE temperatures and adjusted dew points at 850, 700, 600, and 500 mb about the eyewall RMU.

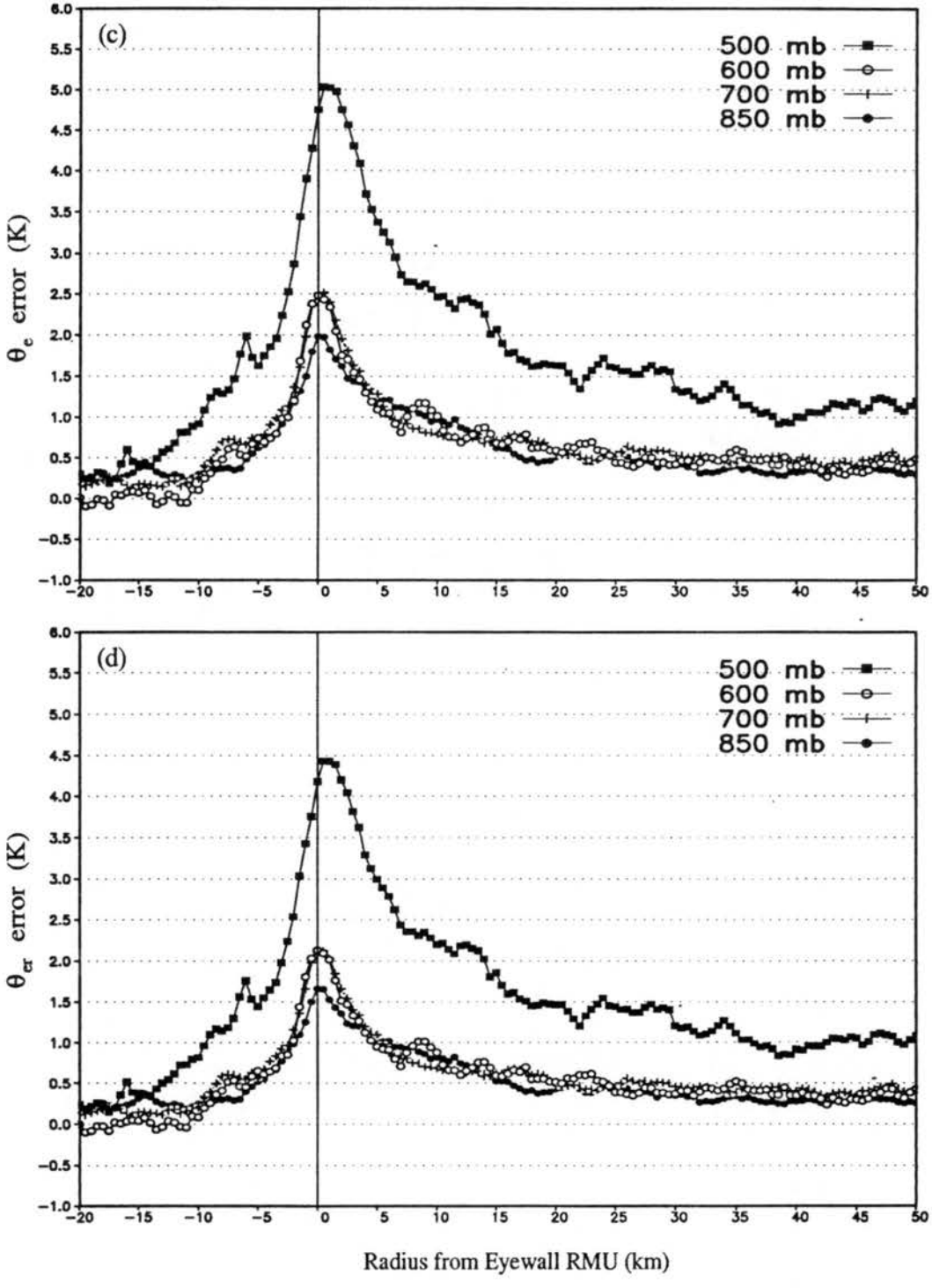

Figure 5.24: Continued.

large-scale study may be affected depending upon the magnitude and frequency of the wetting errors in the data.

To emphasize not only the strict definition of an IWL used in this study, but also the frequency of instrument wetting during eyewall penetration a composite of all radial legs in which *no* IWL was identified was constructed about the RMU (Figure 5.25b). Average temperature errors near the RMU were positive, ranging from 0.15-0.4°C, and the errors were statistically significant at the 95% confidence level within 2 km of the RMU! Therefore, significant instrument wetting errors occur during the majority of eyewall passages!

5.6 Evaluation of a previous temperature correction method

The temperature correction method proposed by Zipser et al. (1981) has been widely used in recent years (e.g. Willoughby et al. 1982; Barnes et al. 1983; Jorgenson 1984a and 1984b; Barnes and Stossmeister 1986; Powell 1990). The correction method is based upon the premise that both the immersion thermometer and chilled-mirror hygrometer are wetted at the same time in a saturated environment, and the resulting errors are equal in magnitude but opposite in sign with the dew point exceeding the temperature. Thus, the algebraic average of the two erroneous observations result in the correct temperature and dew point assuming saturation. However, the sensors are not collocated on the aircraft fuselage and have different exposures to the environment, which could result in dissimilar wetting. Furthermore, the erroneous response of each instrument may be different for equivalent wetting. The CO_2 side-looking radiometer provides an independent, accurate temperature measurement, making the evaluation of the temperature correction method possible. Due to the method's wide use, an evaluation is warranted.

The archived radial legs obtained from HRD were processed using the temperature correction method proposed by Zipser et al. (1981). Thus, using the previously identified IWL, the difference between the SR temperature and the corrected immersion temperatures (ROSECORR) was evaluate within each IWL to determine the performance of the correction method at removing the wetting errors. The RMTE within each IWL was

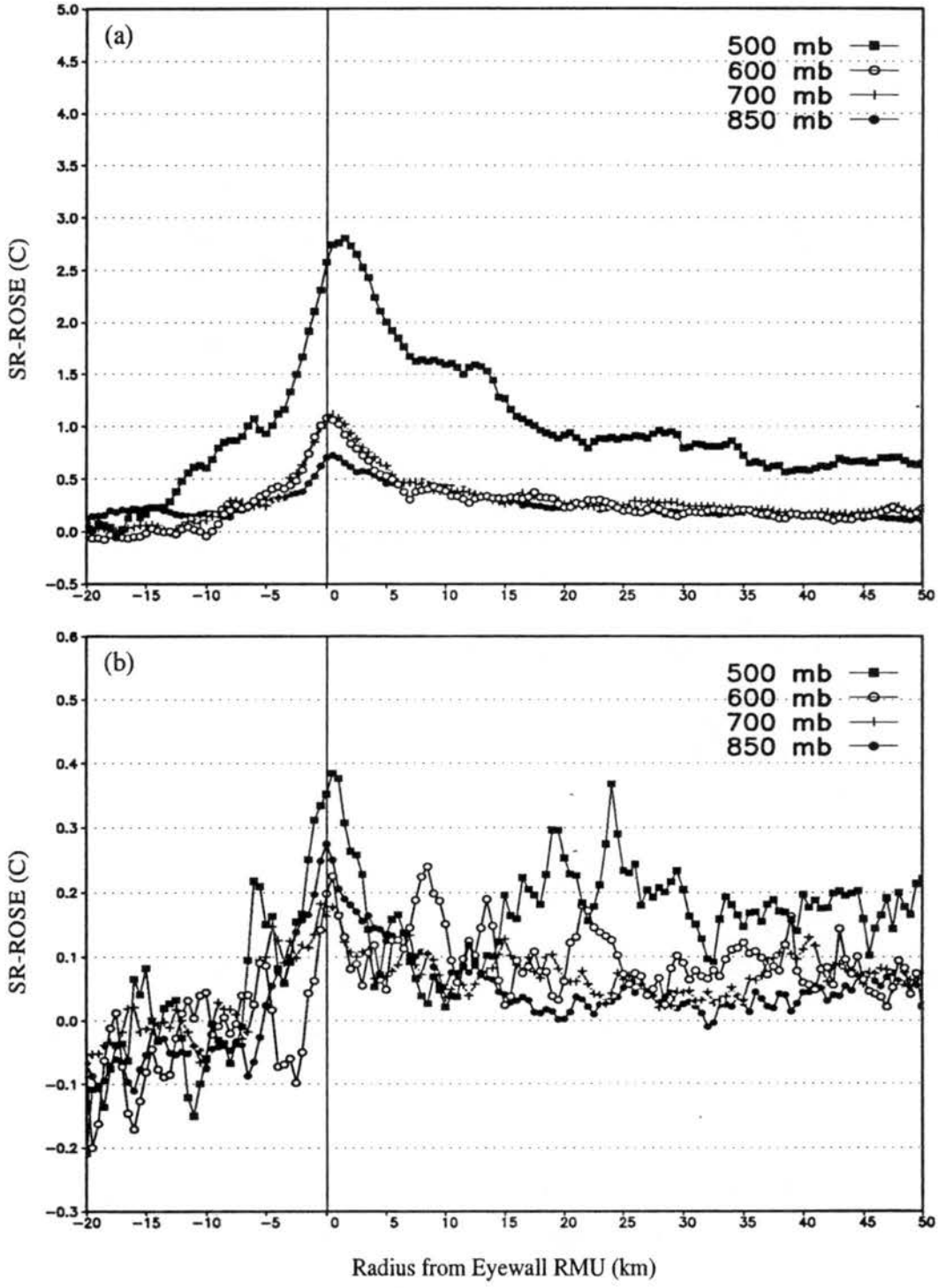

Figure 5.25: Composite SR-ROSE at 850, 700, 600, and 500 mb about the eyewall RMU of (a) all radial legs *with at least one* identified IWL, and (b) all radial legs with *no* identified IWL.

maintained as the largest SR-ROSE temperature difference and not changed to the largest SR-ROSECORR temperature error. Shown in Figure (5.26) is the SR-ROSECORR temperature error at the RMTE as a function of SR temperature at the RMTE. Over 70% of the errors were greater than 0.5°C after the correction was applied with maximum errors still greater than 2.0°C in warm clouds and greater than 5.0°C in cold clouds. The correction method adjusted only 26% of the cases to within ±0.5°C of the SR temperature, while the method over-adjusted the temperature in 2% of the cases, or 7 IWL. On average the correction method reduced the temperature errors by ~50%.

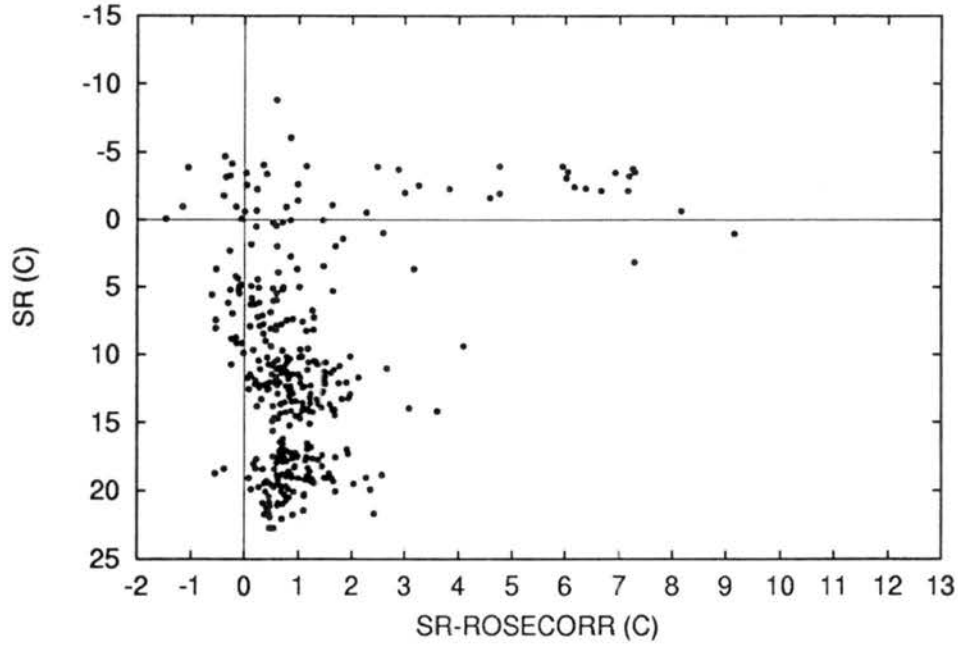

Figure 5.26: Maximum SR-ROSECORR temperature error of each identified IWL.

Figure (5.27) contains two radial legs, one from Gilbert (1988) (Figure 5.27a) and one from Luis (1995) (Figure 5.27b) with examples of ineffective temperature corrections in IWL. The ROSECORR, SR, and ROSE temperatures, along with the observed dew point are shown for each radial leg. In the radial leg from Gilbert an IWL spans the 50-130 km distance from the center of the storm, and the average SR-ROSE error is near 1.0°C. The observed dew point exceeds the ROSE temperature between 50-100 km, however, the dew point only exceeds the SR temperature near 60 km. Thus, the excess dew point

error is smaller in magnitude than the ROSE error such that the resulting ROSECORR temperature is still less than the SR temperature and remains in error by 0.5-1.0°C across the IWL. In contrast, an IWL in a radial leg from Luis (Figure 5.27b) is located in the near 35 km with an average SR-ROSE error of 1.5°C. The observed dew point exceeds both the ROSE and SR temperatures such that the resulting ROSECORR exceeds the SR temperature by as much as 1.5°C near 40 km.

The correction method appears to be ineffective in the majority of cases at removing the wetting errors. The ROSE sensor and cooled-mirror hygrometer are apparently either not being equally wetted, or their erroneous response to equal wetting is different. In either case, the temperature errors are predominately larger than the dew point errors as a majority of significant positive SR-ROSECORR errors exist. The average SR-ROSECORR errors are thus documented at the RMTE for all legs with at least one IWL and at the eyewall RMU for all reconstructed radial legs. The resulting errors of q, T_v, θ_v, θ_{ep}, and θ_{er} are also presented for each composite.

5.6.1 Composites at RMTE

The composite SR-ROSECORR temperature errors and standard deviations about the RMTE are shown in Figure (5.28). Errors at the RMTE range from 0.5°C to 2.5°C. Despite the fact that the composite SR-ROSECORR errors are a factor of two smaller than the SR-ROSE errors and are the same magnitude as their standard deviations, the SR-ROSECORR errors at 850, 700, and 500 mb are statistically significant at the 95% confidence level within 10 km of the RMTE. At 600 mb the errors are significant at the 95% level within only 2 km of the RMTE. The composite specific humidity errors and standard deviations calculated from the reconstructed dew points corresponding to the respective SR and ROSECORR temperatures are shown in Figure (5.29). Maximum specific humidity errors are located at the RMTE with values ranging from 0.2 g kg^{-1} to 1.0 g kg^{-1}. The errors may be up to 0.2 g kg^{-1} larger since a relative humidity of 99% in regions of instrument wetting was assumed for the SR dew point during reconstruction, while saturation was assumed for the ROSECORR dew point in accordance with Zipser

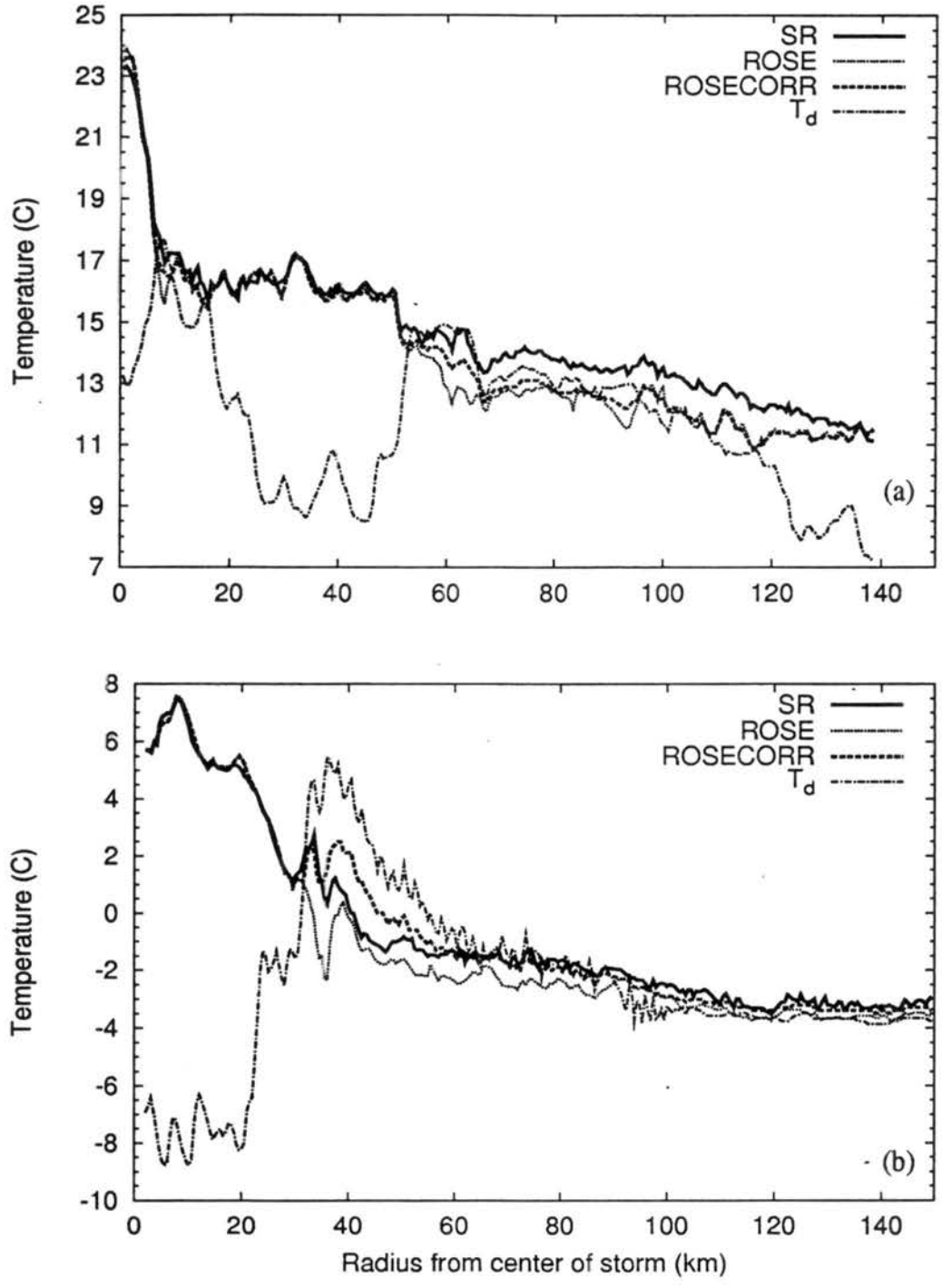

Figure 5.27: Examples of radial legs with ineffective temperature corrections within an identified IWL. Shown are the side radiometer (SR), Rosemount (ROSE), corrected Rosemount (ROSECORR) and uncorrected dew point (T_d) temperatures for (a) Hurricane Gilbert on September 14, 1988 at 700 mb and (b) Hurricane Luis on September 4, 1995 at 500 mb.

et al. (1981). Despite standard deviations of the same magnitude as, or larger than, the averages, the specific humidity errors at 850, 700, and 500 mb are significant at the 95% confidence level within 5 km of the RMTE. At 600 mb the specific humidity error is significant at the 95% level only at the RMTE.

The resulting calculated errors of T_v, θ_v, θ_{ep}, and θ_{er} are shown in Figure (5.30). Average T_v errors near the RMTE range from 0.5°C to 2.5°C at 500 mb, while θ_v errors range from 0.5 K to 3.0 K, θ_e errors range from 1.0 K to 6.0 K, and θ_{er} errors range from 1.0 K to 5.5 K near the RMTE. The θ_e and θ_{er} errors may be up to 0.8 K larger since a relative humidity of 99% in regions of instrument wetting was assumed for the reconstructed SR dew point, while saturation was assumed for the ROSECORR dew point. The assumed humidity difference will have an insignificant effect (< 0.05 K) upon the T_v and θ_v errors. The T_v, θ_v, θ_e, and θ_{er} errors at the 850, 700, and 500 mb levels are significant at the 95% level within 10 km of the RMTE, while the errors at 600 mb are significant within 1 km of the RMTE.

5.6.2 Composites at Eyewall RMU

The SR-ROSECORR temperature errors and the standard deviations of the error composited about the eyewall RMU are shown in Figure (5.31). Error maxima (Figure 5.31a) are located at the RMU and range from 0.2 °C to 0.8°C while standard deviations of the errors (Figure 5.31b) range from 0.3°C to 1.8°C. The maximum SR-ROSECORR errors are a factor of 2 or 3 smaller than the maxima at the RMTE (Figure 5.17a) and a factor of 2 smaller than the SR-ROSE errors at the RMU (Figure 5.22a). The standard deviations are nearly a factor of two larger than the average errors, however, the SR-ROSECORR errors at 850, 700, and 500 mb are significant at the 95% confidence level from within 5 km inside the RMU to 25 km outside the RMU. Temperature errors at 600 mb are negligible at all radii except at the RMU where the maximum positive error is found.

Shown in Figure (5.32) are the composite specific humidity errors and standard deviations calculated from the reconstructed dew points corresponding to the respective SR

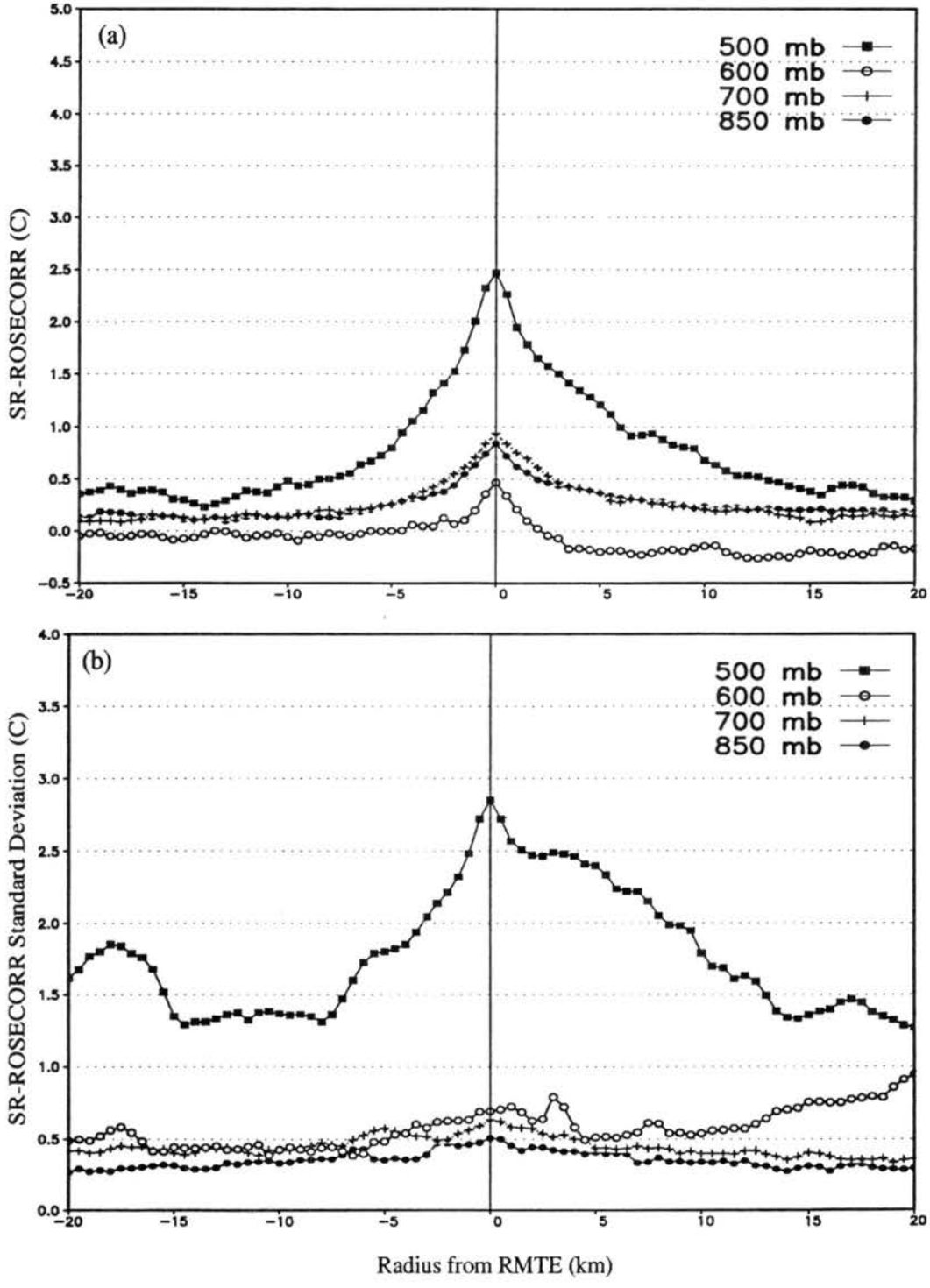

Figure 5.28: Composite IWL (a) SR-ROSECORR and (b) standard deviation of SR-ROSECORR at 850, 700, 600, and 500 mb about the RMTE.

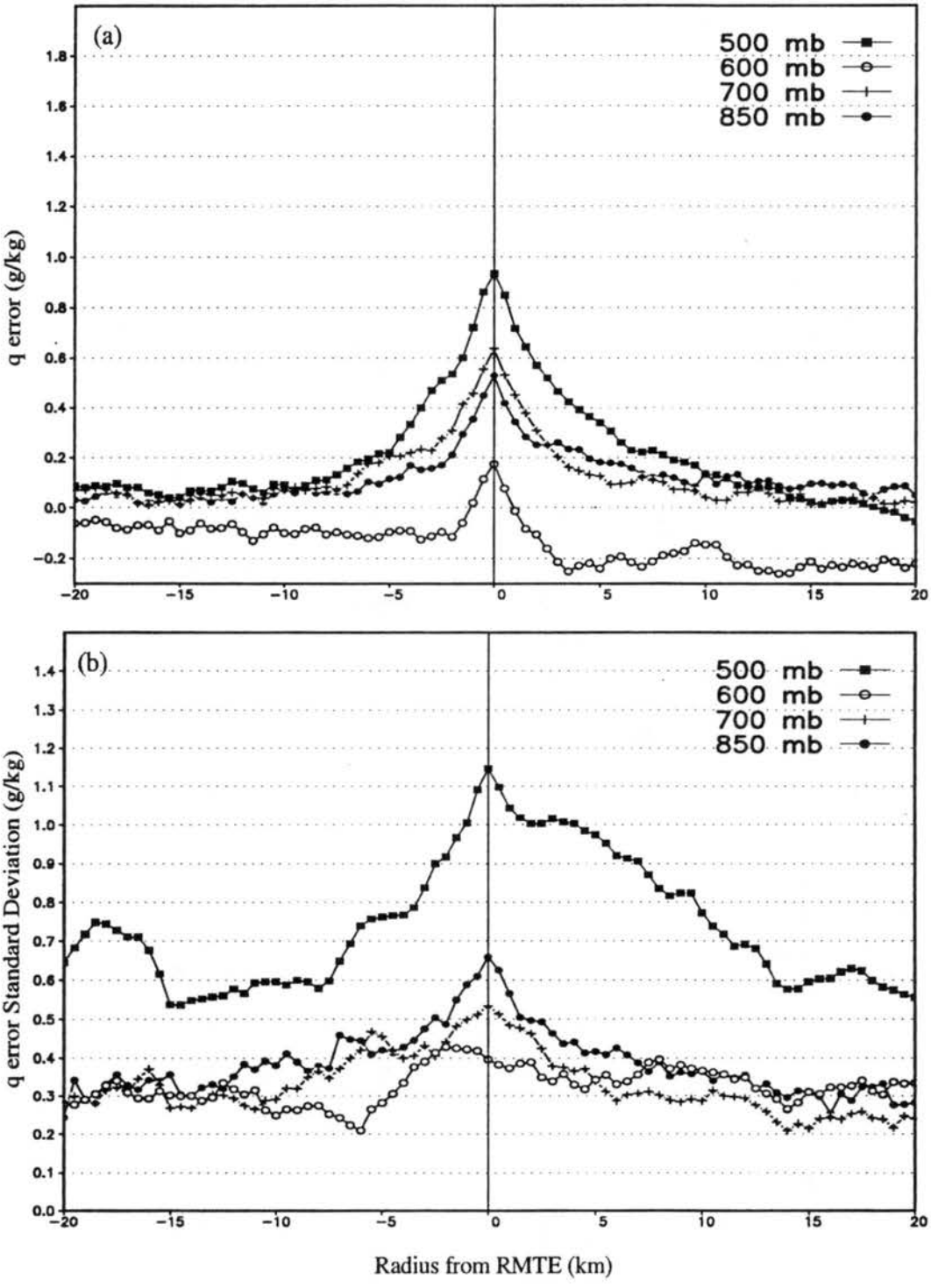

Figure 5.29: Composite IWL (a) specific humidity error and (b) standard deviation of the specific humidity error calculated from the SR and ROSECORR temperatures and adjusted dew points at 850, 700, 600, and 500 mb about the RMTE.

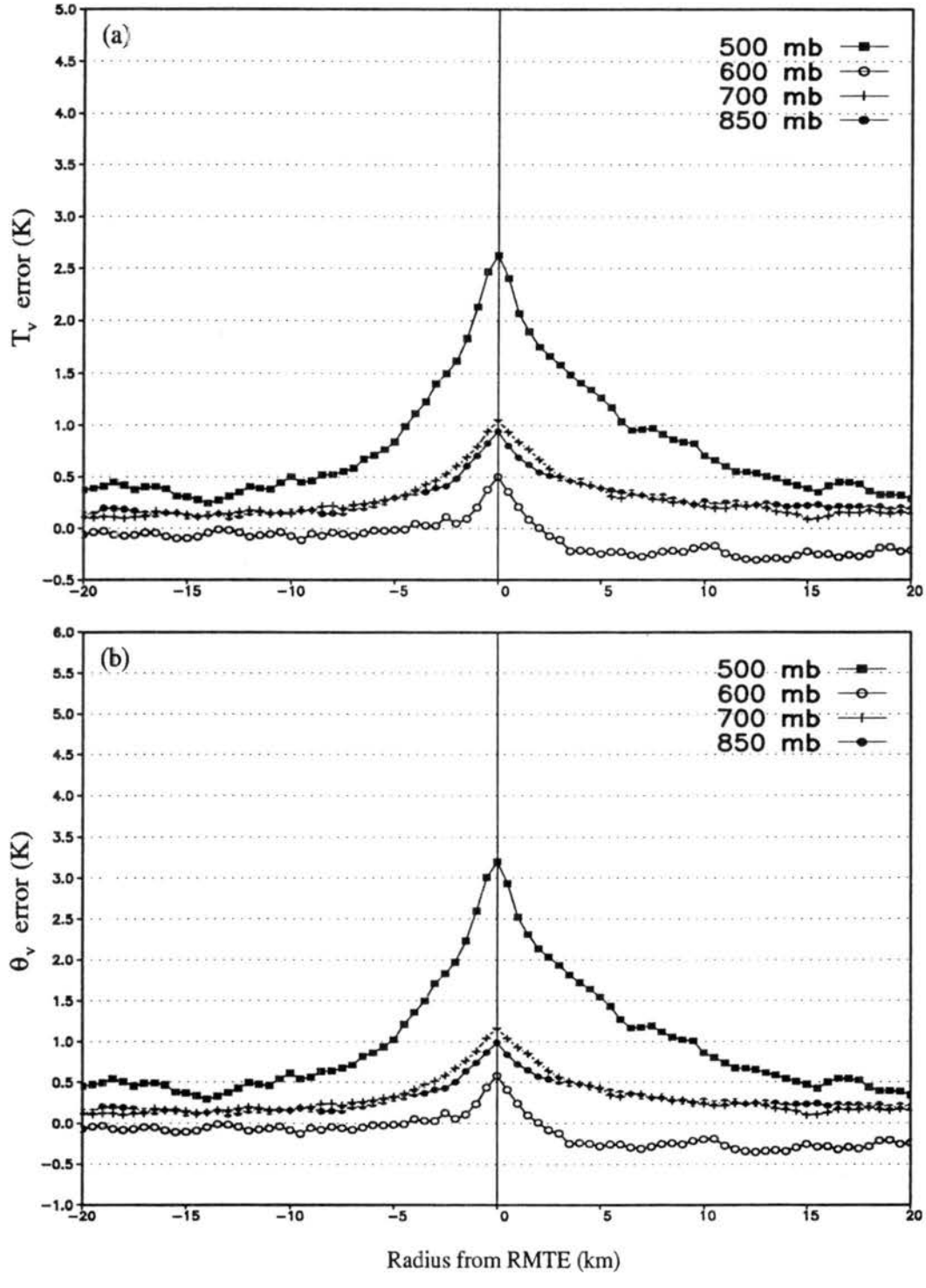

Figure 5.30: Composite IWL errors of (a) T_v, (b) θ_v, (c) θ_e, and (d) θ_{er} calculated from the SR and ROSECORR temperatures and adjusted dew points at 850, 700, 600, and 500 mb about the RMTE.

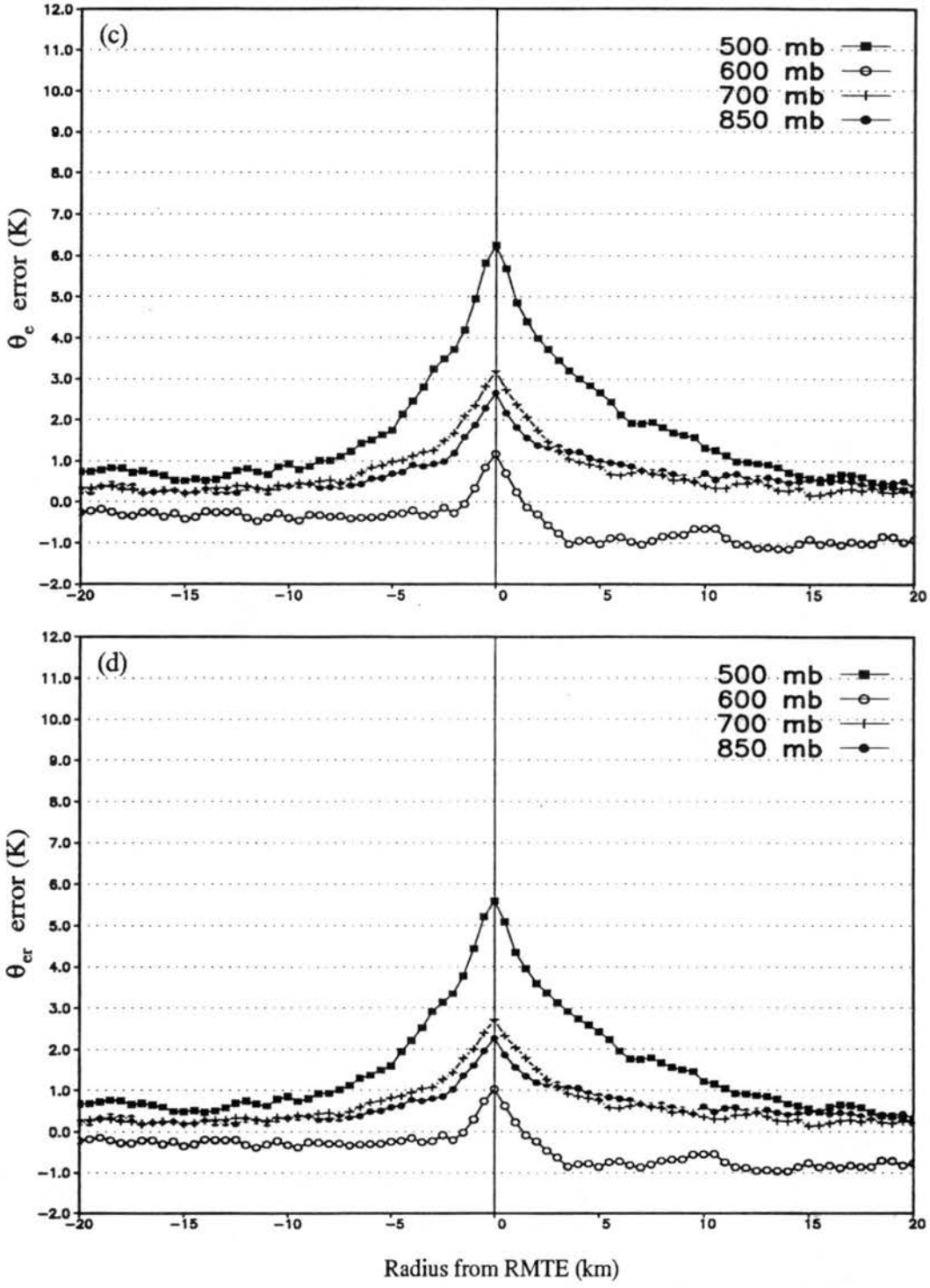

Figure 5.30: Continued.

and ROSECORR temperatures. Maximum specific humidity errors at 850, 700, and 500 mb are located at the eyewall RMU with a value near 0.25 g kg^{-1} at all three levels. At 600 mb the specific humidity errors range from 0.0 g kg^{-1} to -0.1 g kg^{-1} across the composite. The negative errors are a combination of the slight overcorrection of the ROSECORR temperature (Figure 5.32a) at this level and the different humidity assumptions for the SR and ROSECORR adjusted dew points. Standard deviations of specific humidity errors range from 0.2-0.8 g kg^{-1} with maxima near the RMU. The specific humidity errors at 850 and 700 mb are significant at the 95% level within 10 km of the eyewall RMU. The errors at 600 and 500 mb show no statistical significance across the composite.

The resulting calculated errors of T_v, θ_v, θ_e, and θ_{er} about the eyewall RMU are shown in Figure (5.33). Average T_v errors near the RMU range from 0.2°C to 0.9°C, while θ_v errors range from 0.2 K to 1.0 K, θ_e errors range from 0.25 K to 2.0 K, and θ_{er} errors range from 0.25 K to 1.7 K near the RMU. The T_v and θ_v errors are significant at the 95% level within 10 km of the RMU at 850, 700, and 500 mb, while the θ_e, and θ_{er} errors are significant within 10 km of the RMU at only 850 and 700 mb. The θ_e, and θ_{er} errors at 500 mb are significant within 2 km of the RMU. Neither the T_v, θ_v, θ_e, nor the θ_{er} errors are significant at 600 mb across the composite.

The composite SR-ROSECORR thermodynamic errors are small, particularly when all the reconstructed radial legs are composited by the eyewall RMU. For such large composites the temperature correction method proposed by Zipser et al. (1981) reduces the average temperature errors to within the accuracy of the instruments. However, the majority of instrument wetting errors at the RMTE were not completely removed by the temperature correction method, as over 70% of the SR-ROSECORR temperature errors were still greater than 0.5°C. Several errors remained greater than 2.0°C, which results in θ_v errors greater than 2.5 K and θ_e errors greater than 5.0 K after the correction was applied! Thus, case studies of mesoscale or convective scale thermodynamic features in a single hurricane may still contain significant instrument wetting errors even after the temperature correction method proposed by Zipser et al. (1981) is applied to the data.

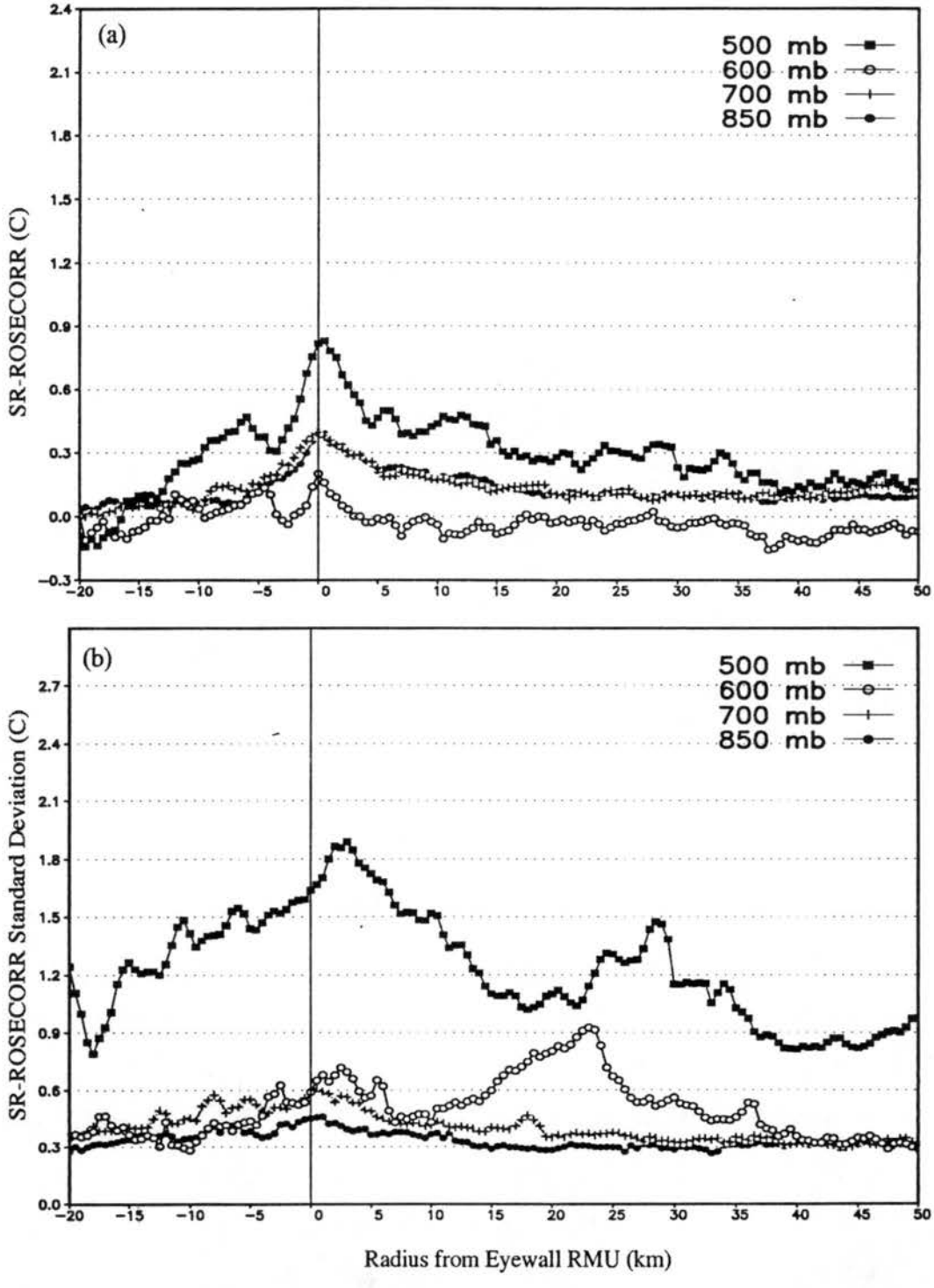

Figure 5.31: Composite (a) SR-ROSECORR and (b) standard deviation of SR-ROSECORR at 850, 700, 600, and 500 mb about the eyewall RMU.

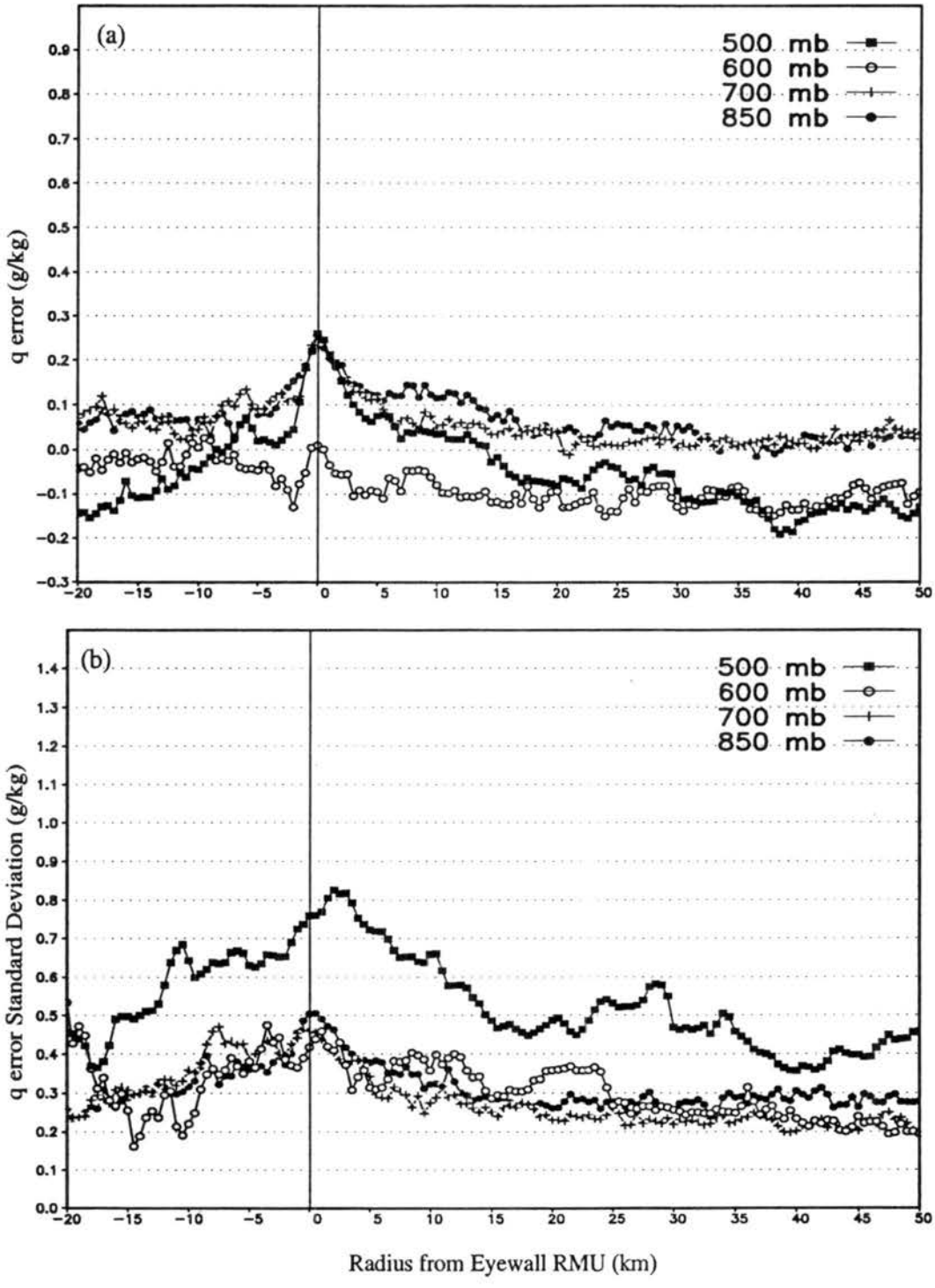

Figure 5.32: Composite (a) specific humidity error and (b) standard deviation of the specific humidity error calculated from the SR and ROSECORR temperatures and adjusted dew points at 850, 700, 600, and 500 mb about the eyewall RMU.

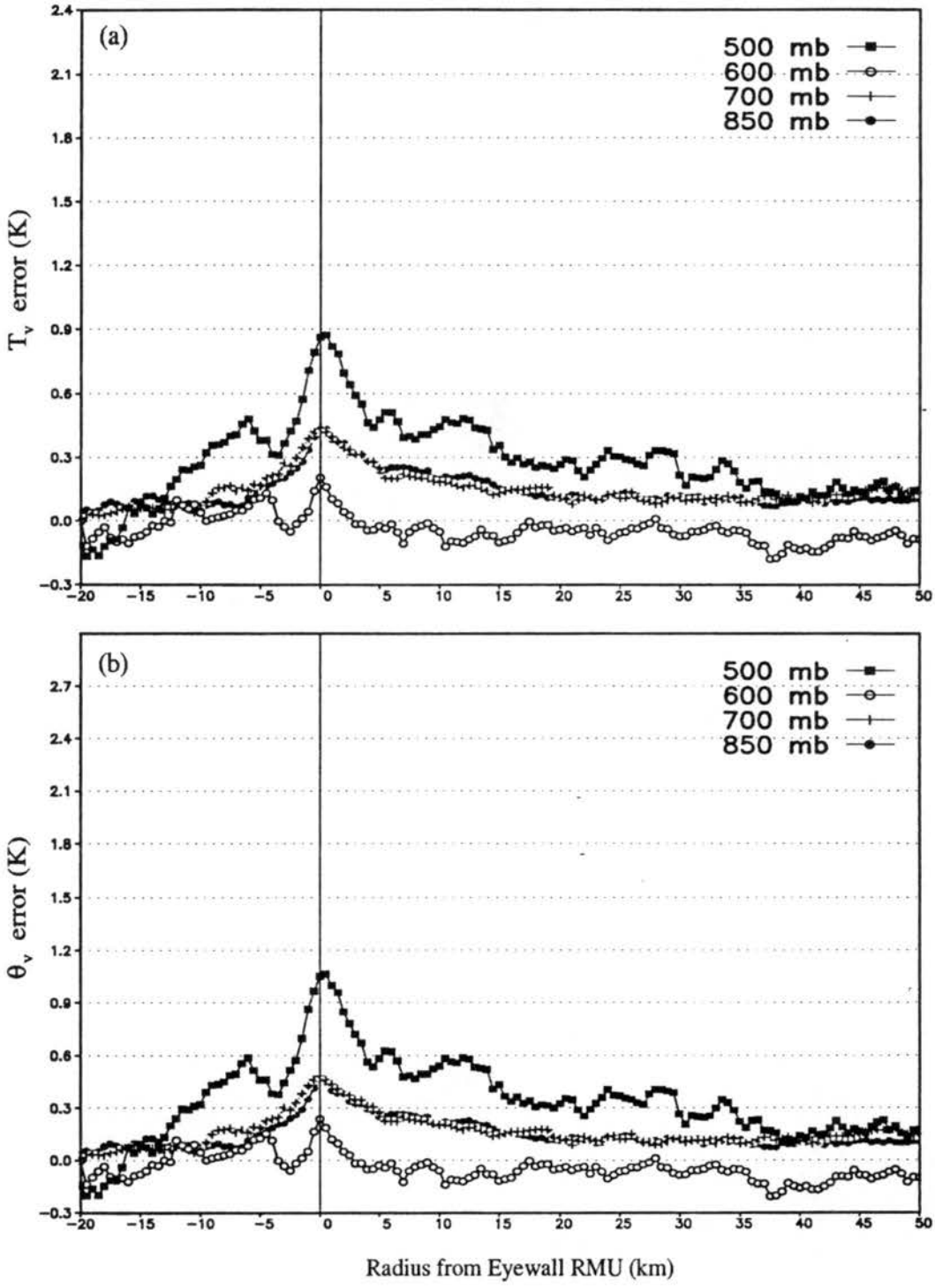

Figure 5.33: Composite errors of (a) T_v, (b) θ_v, (c) θ_e, and (d) θ_{er} calculated from the SR and ROSECORR temperatures and adjusted dewpoints at 850, 700, 600, and 500 mb about the eyewall RMU.

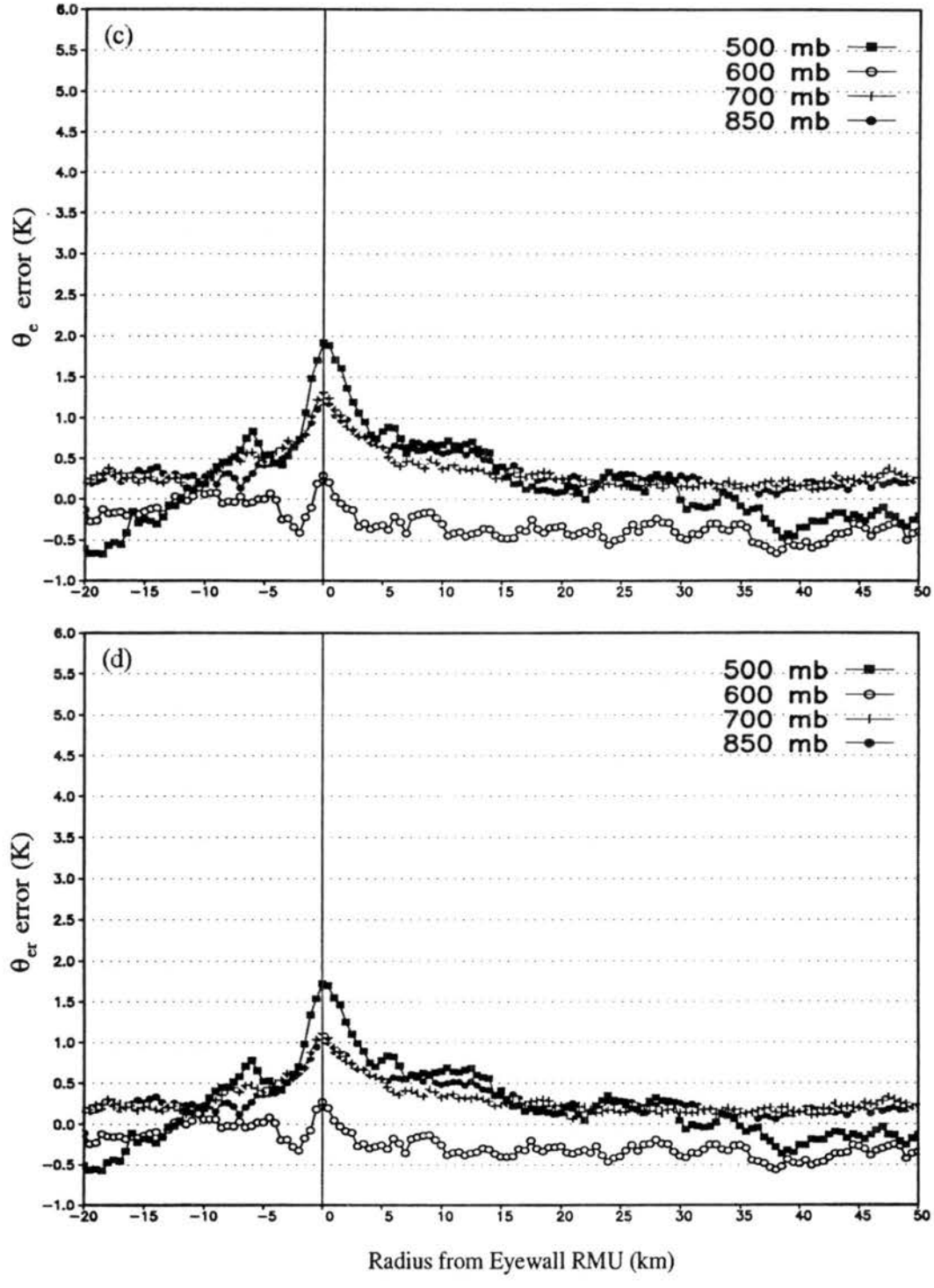

Figure 5.32: Continued.

5.7 Summary

Instrument wetting errors were shown to frequently occur in hurricane clouds and precipitation. The examination of the errors in conjunction with cloud microphysics reveals only a weak correlation between the total liquid water content and the magnitude of the temperature error. A strict definition of an instrument wetting location (IWL) was used to further examine the errors, resulting in roughly one half of the radial legs containing at least one IWL. Large variability in the number of IWL was found from hurricane to hurricane, however, IWL were more frequent and contained larger temperature errors in intense hurricanes than in minimal hurricanes. Furthermore, large variability in location, radial extent, and magnitude of the maximum temperature error was found between the IWL. The majority of IWL were centered in cloudy updrafts of either the eyewall or rainbands and extended < 15 km with maximum temperature errors $< 5.0°$C. Theoretical temperature error magnitudes were rarely achieved.

Thermodynamic errors from instrument wetting were composited with respect to the RMTE and the eyewall RMU. Composites with respect to the RTME were composed of all identified IWL, while composites with respect to the eyewall RMU consisted of all radial legs, irrespective of whether an IWL was near the eyewall or even found in the radial leg. Shown in Table 5.4 is a summary of the thermodynamic errors at the RMTE and eyewall RMU before and after applying the Zipser et al. (1981) correction method to the data. Quantities such as T_v and θ_e are commonly used to describe convective processes and balance thermodynamic budgets, however, composited errors about the RMTE are 1.5 - 4.5°C and 5.0 - 11.0 K respectively, and only decrease to roughly one third of these values when composited by eyewall RMU. If only radial legs containing an IWL at the eyewall were similarly composited average thermodynamic errors would be roughly two thirds the IWL averages. Furthermore, composited radial legs *without* an identified IWL still contained a significant temperature error of 0.2 - 0.4°C in the eyewall. The application of the Zipser et al. (1981) correction method to the data prior to compositing reduced the

errors by roughly 50 percent, however, the method was ineffective at removing the errors in over 70 percent of the IWL.

Table 5.4: Summary of thermodynamic errors at the RMTE and the eyewall RMU calculated from the observed Rosemount temperatures (SR-ROSE) and corrected Rosemount temperatures using the method proposed by Zipser et al. (1981) (SR-ROSECORR). The thermodynamic values derived from the SR temperature and adjusted dew points are assumed to be correct. Bold values indicate statistical significance at the 99.9% confidence level, while italicized values are statistically significant at the 95% level, and underlined values are not significant. Temperature, T_v, θ_v, θ_e, and θ_{er} errors are given in K, while specific humidity errors are in g kg^{-1}.

Thermodynamic Quantity	Average Errors at RMTE 850	700	600	500	Average Errors at eyewall RMU 850	700	600	500
				SR-ROSE				
SR-ROSE	**1.2**	**1.7**	**1.8**	**4.3**	*0.46*	*0.66*	*0.74*	*1.68*
q	**1.2**	**1.3**	**1.1**	**1.8**	*0.45*	*0.53*	*0.47*	*0.79*
T_v	**1.4**	**1.9**	**1.9**	**4.6**	*0.6*	*0.8*	*0.8*	*1.8*
θ_v	**1.5**	**2.2**	**2.3**	**5.6**	*0.6*	*0.8*	*1.0*	*2.2*
θ_e	**5.1**	**6.2**	**5.9**	**11.4**	*2.0*	*2.4*	*2.5*	*4.8*
θ_{er}	**4.4**	**5.0**	**5.2**	**10.1**	*1.7*	*2.2*	*2.3*	*4.2*
				SR-ROSECORR				
SR-ROSECORR	*0.5*	*0.9*	*0.8*	*2.5*	*0.40*	*0.40*	*0.21*	*0.81*
q	*0.5*	*0.6*	*0.2*	*0.9*	*0.25*	*0.25*	0.01	0.25
T_v	*0.9*	*1.0*	*0.5*	*2.6*	*0.4*	*0.4*	0.2	*0.9*
θ_v	*1.0*	*1.2*	*0.6*	*3.2*	*0.5*	*0.5*	0.2	*1.0*
θ_e	*2.6*	*3.1*	*1.1*	*6.2*	*1.2*	*1.3*	0.3	*1.9*
θ_{er}	*2.3*	*2.7*	*1.0*	*5.6*	*1.0*	*1.1*	0.3	*1.7*

The results presented in this chapter indicate that statistically significant instrument wetting errors are common, particularily in the eyewall, during hurricane penetrations. Since the convective nature of the eyewall plays a primary role in the maintainence and changes in the hurricane circulation, the accurate determination of thermodyanmic quantities in and near the eyewall is crucial to understanding hurricane structure and intensity changes. Thus, a *broad* re-examination of hurricane thermodynamic structure is warranted.

5.8 Synopsis

- Instrument wetting errors are frequently found in hurricane flight-level thermodynamic data and are more common in intense hurricanes, but are highly variable from hurricane to hurricane.

- The error magnitudes are not well correlated with total liquid water content, rarely achieve their theoretical values, and are highly variable.

- The majority of instrument wetting locations (IWL) were found in cloudy updrafts of either the eyewall or rainbands and extended < 15 km radially, with maximum temperature errors $< 5.0°$C.

- Composites of all instrument wetting locations with respect to their Radius of Maximum Temperature Error (RMTE) resulted in statistically significant T_v and θ_e errors of 1.5 to 4.5°C and 5.0 to 11.0 K respectively.

- Composites of *all* radial legs with respect to the eyewall Radius of Maximum Updraft (RMU) resulted in statistically significant T_v and θ_e errors of 0.6 to 1.8°C and 2.0 to 5.0 K respectively.

- Composites of radial legs *without* an identified IWL still contained a significant temperature errors of 0.2 to 0.4°C in the eyewall.

- The application of the Zipser et al. (1981) correction method to the data reduced the composite errors by roughly 50 percent, but was ineffective at removing the errors in over 70 percent of the IWL.

Chapter 6

HURRICANE THERMODYNAMIC STRUCTURE

6.1 Composite radial structure

Absolute values of observed thermodynamic quantities from regions of clouds and precipitation in hurricanes have historically been questioned due to possible instrument wetting errors. Results from Chapter 5 indicate that individual IWLs can contain large temperature errors resulting in large q, T_v, θ_v, and θ_e errors. Furthermore, radial composites may contain large thermodynamic errors depending upon the magnitude and frequency of instrument wetting errors found in the radial legs composited. Presented in this section are radial composites of standard thermodynamic and dynamic quantities at 850, 700, 600, and 500 mb upon removal of instrument wetting errors. Radial legs were stratified by intensity, intensity change, quadrant with respect to storm motion, basin, and latitude, and composited with respect to both the RMW and the eyewall RMU. Significant differences (according to a t-test) were noted within the various stratifications, but stratification by intensity resulted in the largest, systematic, significant differences. Composites with respect to the RMW and the eyewall RMU were very similar since the eyewall RMU is typically 1-3 km inside the RMW (Jorgenson 1984a; Samsury and Zipser 1995; this study (see Table 6.1)), however, composites with respect to the RMU will specifically emphasize expected radial thermodynamic gradients across the eyewall. Thus, only radial composites with respect to the eyewall RMU for minimal and intense hurricanes are presented (see Figures 6.3-6.9).

The geographic locations of each hurricane during which time aircraft were penetrating the storm are shown in Figure (6.1). Hurricanes were sampled in the Atlantic Basin from 10-40°N and from 50-95°W during the months of August through October, however,

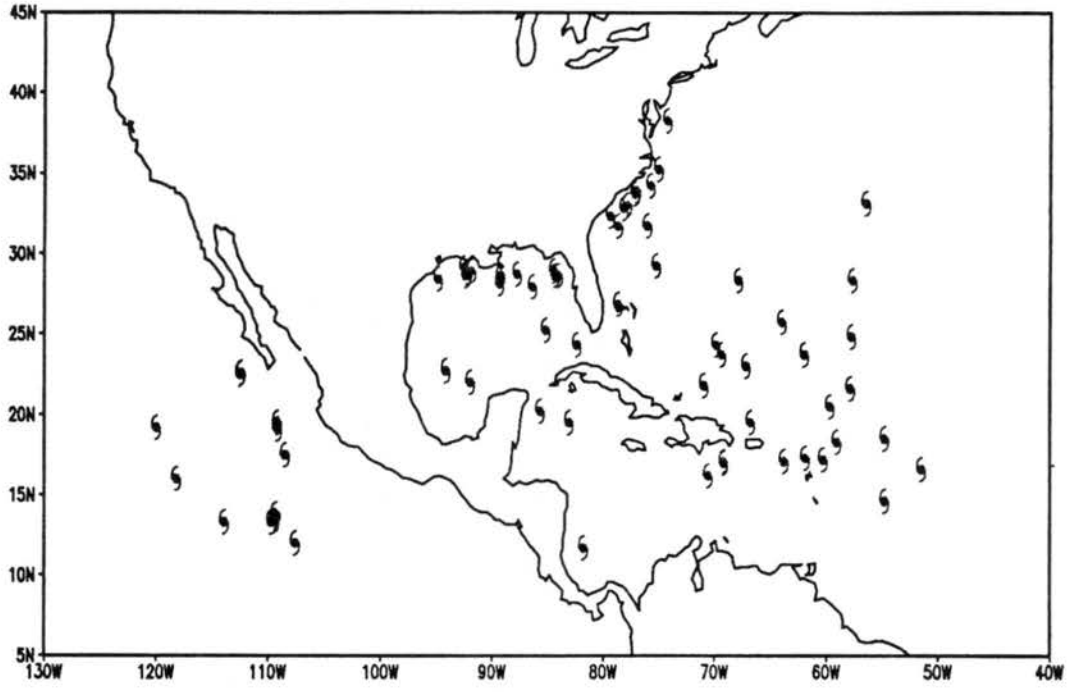

Figure 6.1: Locations of hurricanes when radial legs used in this study were collected.

over 60% of the Atlantic basin radial legs were obtained during the month of September. Hurricanes sampled in the Eastern North Pacific were confined to a smaller, predominately tropical, region and were sampled only in the month of September[1]. Table 6.1 contains the composite average values of RMW, eyewall RMU, eyewall slope determined as the departure from the vertical of the secondary circulation vector at the eyewall RMU (see Figure 6.2), minimum surface pressure, eyewall surface pressure (calculated using method outlined in Section 6.4), SST, 12-hour intensity change, and translation speed, stratified by intensity and pressure level. In general the radial composites presented represent a steady-state hurricane translating to the west-northwest at 5-6 m s^{-1} over 28°C oceans.

One must be cautious about inferring vertical structure from the radial composites. Only Hurricanes Norbert (1984) and Emily (1987) were simultaneously sampled at multiple levels (see section 6.2), and thus each pressure level composite is composed of data

[1]The wider climatological variability inherent within an Atlantic basin inner-core composite compared to an Eastern North Pacific basin composite likely explains their insignificant differences despite known climatological differences in the large-scale atmosphere.

from different storms and/or the same storm at different times. Statistics in Table 6.1 are presented to help clarify discrepancies between pressure levels that may be related to storm intensity, intensity change, motion, local environment, or structural variability from storm to storm. Composite vertical structure will be inferred in Section 6.3 in regards to the eyewall, but only qualitatively.

Table 6.1: Statistics of composite radial legs from Atlantic and East Pacific Hurricanes stratified for the 850-500 mb flight levels. Average statistics are the RMW and RMU given in km from the center of the storm, eyewall slope (λ) determined as the departure from the vertical of the secondary circulation wind vector at the RMU, minimum central pressure (P_{cen}), surface pressure under the eyewall (P_{sfc}) (eyewall surface pressure was calculated assuming undilute moist adiabatic ascent, an eyewall slope of 30°, and a boundary layer depth of 300 m.), monthly mean SST, the 12-hour intensity change as a function of maximum wind (12-hour ΔV_{max}) in knots and minimum pressure (12-hour ΔP_{cen}) in mb, and the translation speed (SPD) in knots.

	850 mb	700 mb	600 mb	500 mb
Category 1,2				
RMW	48.3	48.3	39.7	39.0
RMU	46.4	43.8	37.6	34.6
λ(°)	27.6	45.9	47.0	9.3
P_{cen}(mb)	980	976	978	980
P_{sfc}(mb) Eyewall	993	992	997	997
SST(°C)	27.8	28.2	28.1	28.0
12-hour ΔV_{max}	1.1	0.0	1.1	-4.6
12-hour ΔP_{cen}	-3.3	0.3	-1.2	-2.5
SPD(knots)	4.3	5.7	5.9	4.7
Category 3,4,5				
RMW	33.8	27.8	25.1	29.8
RMU	31.6	26.6	24.6	28.3
λ(°)	18.3	22.2	26.8	27.8
P_{cen}(mb)	955	943	941	953
P_{sfc}(mb) Eyewall	974	963	963	980
SST(°C)	27.8	27.9	27.8	28.4
12-hour ΔV_{max}	7.9	3.7	-13.1	1.1
12-hour ΔP_{cen}	-5.6	-2.5	5.2	-2.2
SPD(knots)	4.7	6.5	5.9	6.1

Shown in Figure 6.3-6.9 are the composite SR temperature anomaly, specific humidity, relative humidity, θ_e, θ_{er}, cloud water content, and vertical velocity with respect to the eyewall RMU for minimal and intense hurricanes. The temperature anomaly was

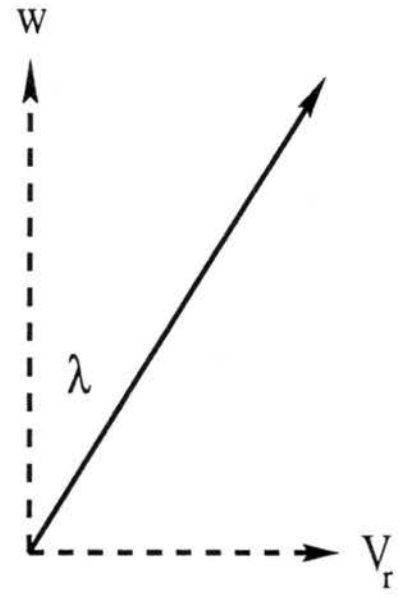

Figure 6.2: Diagram depicting the determination of eyewall slope from the secondary circulation. The slope (λ) is the angular departure from the vertical of the secondary circulation vector (solid line) composed of the vertical (w) and radial (V_r) velocities.

calculated by subtracting the average temperature at all radii 10 km beyond the RMU (i.e. outside the eyewall) from each leg from the measured temperature. Thus, the environment is defined as the average temperature starting 10 km outside the eyewall to the end of the radial leg. Included in Appendix B are the associated radial composites of SR temperature, SR temperature deviation from the hurricane season mean tropical atmosphere (Jordan 1958b), potential temperature, vertical mass flux, tangential velocity, angular velocity, relative vorticity, radial velocity, radial divergence, and pressure surface height. All thermodynamic quantities are calculated from the corrected SR temperatures and the adjusted dew points. Shown in Table (6.2) are composite values of dynamic and thermodynamic quantities at the eyewall RMU for minimal and intense hurricanes.

The lower and middle level warm core is very pronounced in the composite temperature anomalies (Fig. 6.3). In the eye, average temperature deviations from the environment range from 2-4°C in minimal hurricanes and from 3-8°C in intense hurricanes at and below 500 mb. These values are consistent with the temperature anomalies found by LaSeur and Hawkins (1963), Hawkins and Rubsam (1968), and Hawkins and Imbembo (1976) considering the composite temperature anomalies represent a deviation

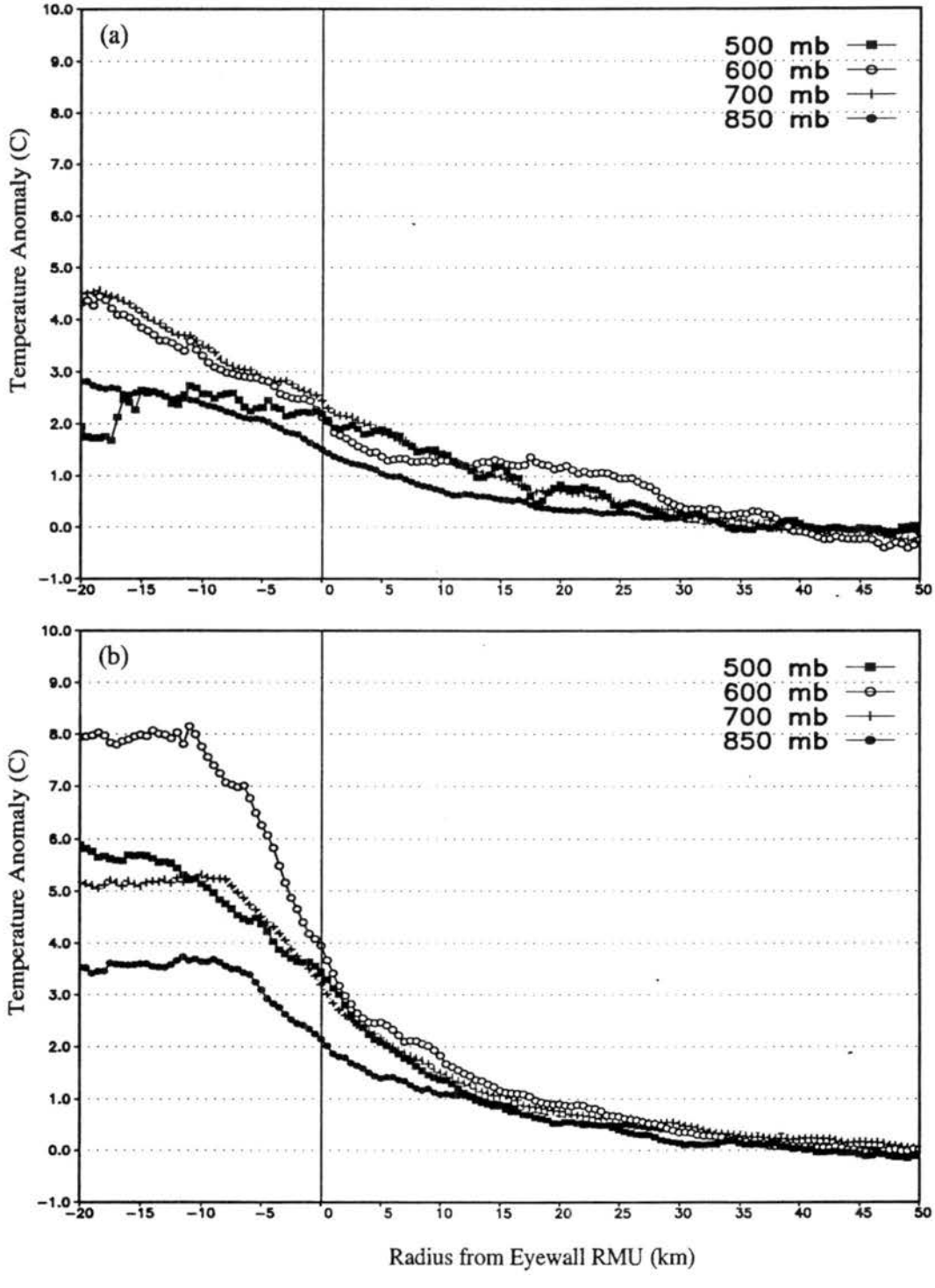

Figure 6.3: Composite SR temperature anomaly from the average environment 10 km outside the eyewall RMU for (a) minimal and (b) intense hurricanes at 850, 700, 600, and 500 mb about the eyewall RMU.

Table 6.2: Composite values of dynamic and thermodynamic quantities at the eyewall RMU for minimal and intense hurricanes. Thermodynamic quantities are calculated from the corrected SR temperatures and adjusted dew points. The temperature (SR) is given in Celsius, while the temperature anomaly from the local environment (ΔT_{env}) (defined as the deviation from the average temperature from 10 km outside the eyewall to the end of the radial leg), the temperature anomaly from the Jordan (1958b) mean hurricane season sounding (ΔT_{JM}), θ, θ_e, and θ_{er} are in K. Specific humidity (q) is given in g kg^{-1}, relative humidity (RH) is in percent, cloud water content (CWC) is given in g m^{-3}, vertical motion (w) is in m s^{-1}, and pressure surface heights (z) are in meters.

	Minimal Hurricanes				Intense Hurricanes			
Quantity	850	700	600	500	850	700	600	500
SR	18.6	12.4	6.4	-2.0	20.3	14.3	8.8	0.0
ΔT_{env}	1.5	2.4	2.1	2.2	2.1	3.2	4.0	3.4
ΔT_{JM}	1.3	3.8	5.0	4.9	2.9	5.7	7.3	6.9
q	15.3	11.4	9.1	5.8	17.5	13.6	10.7	7.3
RH	95.2	90.2	91.0	98.3	97.8	92.0	90.6	95.2
θ	305.7	316.2	323.5	330.5	307.4	318.3	326.3	333.0
θ_e	351.9	351.6	353.1	348.2	360.3	361.4	361.3	357.5
θ_{er}	345.2	345.7	348.0	344.5	351.7	354.5	356.4	353.0
CWC	0.37	0.37	0.47	0.41	0.33	0.44	0.44	0.90
w	1.9	1.8	2.4	2.6	2.3	4.9	4.8	7.6
z	1724	2982	4301	5767	1158	2753	4045	5640

from the local environment rather then the tropical mean sounding (Jordan 1958b). The temperature anomaly at the eyewall is 2-4°C and represents roughly 50-70% of the total anomaly from the environment. The radial temperature gradient maximizes just outside the eyewall RMU with an average value of 0.35°C km^{-1}. These results are consistent with Shea and Gray (1973), however, Shea and Gray found a slightly weaker gradient of 0.2°C km^{-1}. The difference can be easily attributed to the magnitude of instrument wetting errors (see Figure 5.25). Previous studies (e.g. LaSeur and Hawkins 1963; Shea and Gray 1973) have noted the warmest temperatures along the inner edge of the eyewall in many hurricanes. No noticeable local temperature anomaly is evident inside the eyewall from the composites, however, some individual legs do contain such an anomaly.

Shown in Figures (6.4) and (6.5) are the composite specific and relative humidity, respectively. The specific humidity is consistently 1-2 g kg^{-1} higher in intense hurricanes, with radial maxima located in the eyewall. The specific humidity in the eye is equivalent to or larger than values outside the eyewall for all pressure levels. Hawkins and Imbembo (1976) also observed high specific humidities in the eye below 500 mb and attributed the high values to turbulent mixing between the eyewall and eye. In contrast, the relative humidity is substantially lower in the eye than in or outside the eyewall. Soundings taken in hurricane eyes have shown warm, dry air aloft separated by an inversion near 850-700 mb from moist, usually cloudy, air near the surface (e.g. Jordan 1952; Willoughby 1998). Evidence of this vertical eye structure is found in the intense hurricane composite radial data with relative humidities at 850 mb (~90%) consistently more moist than at 500 or 600 mb (~65%). Composite relative humidities are near maximum in the eyewall, ranging from 90-97% in intense hurricanes. The lack of saturated conditions in the eyewall is indicative of asymmetric active convection, and mixing with unsaturated convective downdrafts in and near the eyewall. Outside the eyewall the composite relative humidity ranges from 80-95% and is nearly constant with radius at a given pressure level.

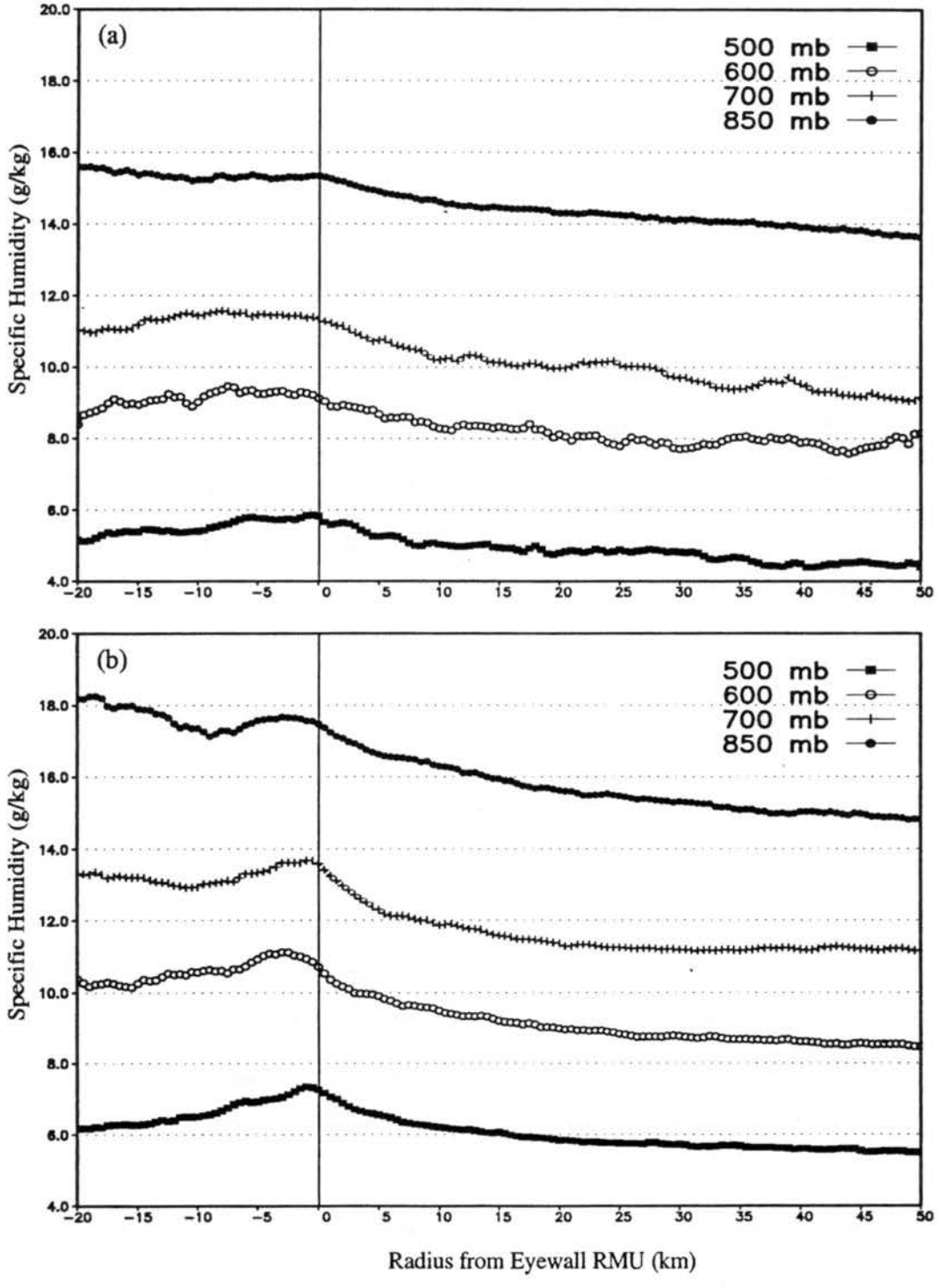

Figure 6.4: Composite specific humidity for (a) minimal and (b) intense hurricanes at 850, 700, 600, and 500 mb about the eyewall RMU.

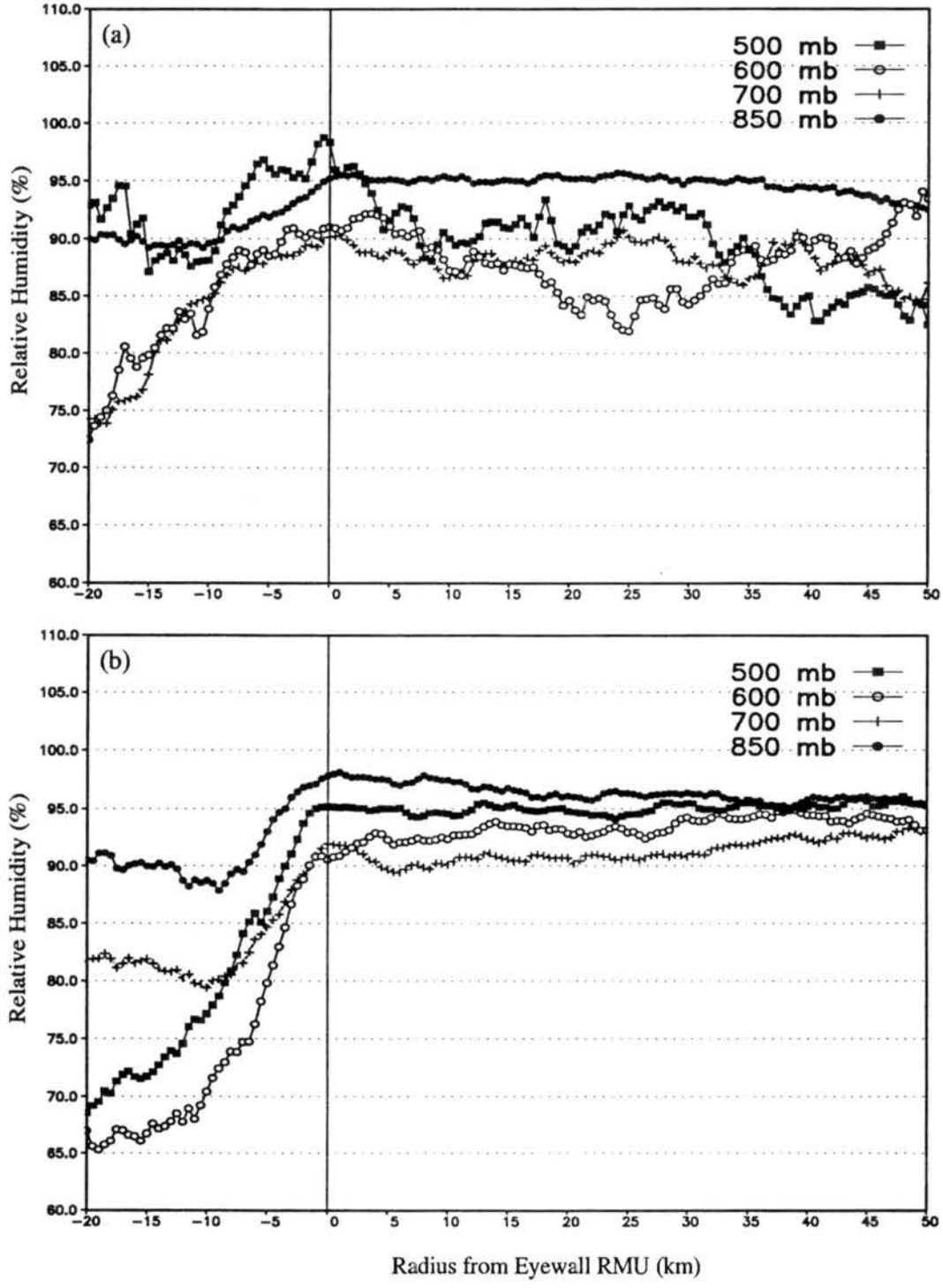

Figure 6.5: Composite relative humidity for (a) minimal and (b) intense hurricanes at 850, 700, 600, and 500 mb about the eyewall RMU.

Figures (6.6) and (6.7) are the θ_e and θ_{er}[2] radial composites. In general, θ_e values in intense hurricanes are 5-10 K larger at all radii than in minimal hurricanes. Maximum values are found in the eye due to the warm air (despite the dryness) where θ_e is nearly constant with radius. In intense hurricanes, composite θ_e ranges from 357-366 K in the eye. These values are consistent with values found by Hawkins and Imbembo (1976). In the eyewall θ_e is 0-5 K lower than the eye, averaging 351 K and 360 K in minimal and intense hurricanes respectively. The maximum radial gradient of θ_e is found just outside the eyewall as θ_e decreases to values 5-10 K lower than the eyewall within 20 km. Jorgenson (1984b) noted a channel of high θ_e that sloped radially outward and coincided with strong downward motion just inside the eyewall of Hurricane Allen (1980). In a modeling effort of Hurricane Andrew (1992), Liu et al. (1997) also noted higher θ_e values along the inner edge of the eyewall that were associated with strong descending motion. Neither elevated θ_e nor a persistent mesoscale downdraft (Figure 6.9) is found in the radial composites just inside the eyewall RMU. However, inspection of individual radial legs reveals such local θ_e maxima are occasionally present, and typically associated with a downdraft.

Shown for completeness in Figures (6.8) and (6.9) are the composite cloud water content and vertical velocity. In general, intense hurricanes contain stronger eyewall updrafts and more cloud water content than minimal hurricanes, with the cloud water content and vertical velocity maxima collocated and highly correlated (Jorgenson 1984a). Average cloud water content ranges from 0.3-0.9 gm^{-3} and are in agreement with eyewalls values found by Jorgenson et al. (1985). Average eyewall vertical velocities in intense hurricanes range from 2-8 m s^{-1} and are consistent with previous studies by Gray (1965), Jorgenson et al. (1985), and Black et al. (1996)[3]. There is evidence of convective downdrafts commonly located just outside the eyewall RMU on the order of 0.5-1.0 m s^{-1} at 500 and

---

[2]The cloud water content (Figure 6.8) was included in the computation of θ_{er}, however, no precipiation water content was. In the lower to middle troposhere θ_{er} is 5-8 K less than θ_e by definition.

[3]Flight level data from the seven storms analyzed in Black et al. (1996) are included in this study, however, the storms analyzed in Gray (1965) and Jorgenson et al. (1985) are not.

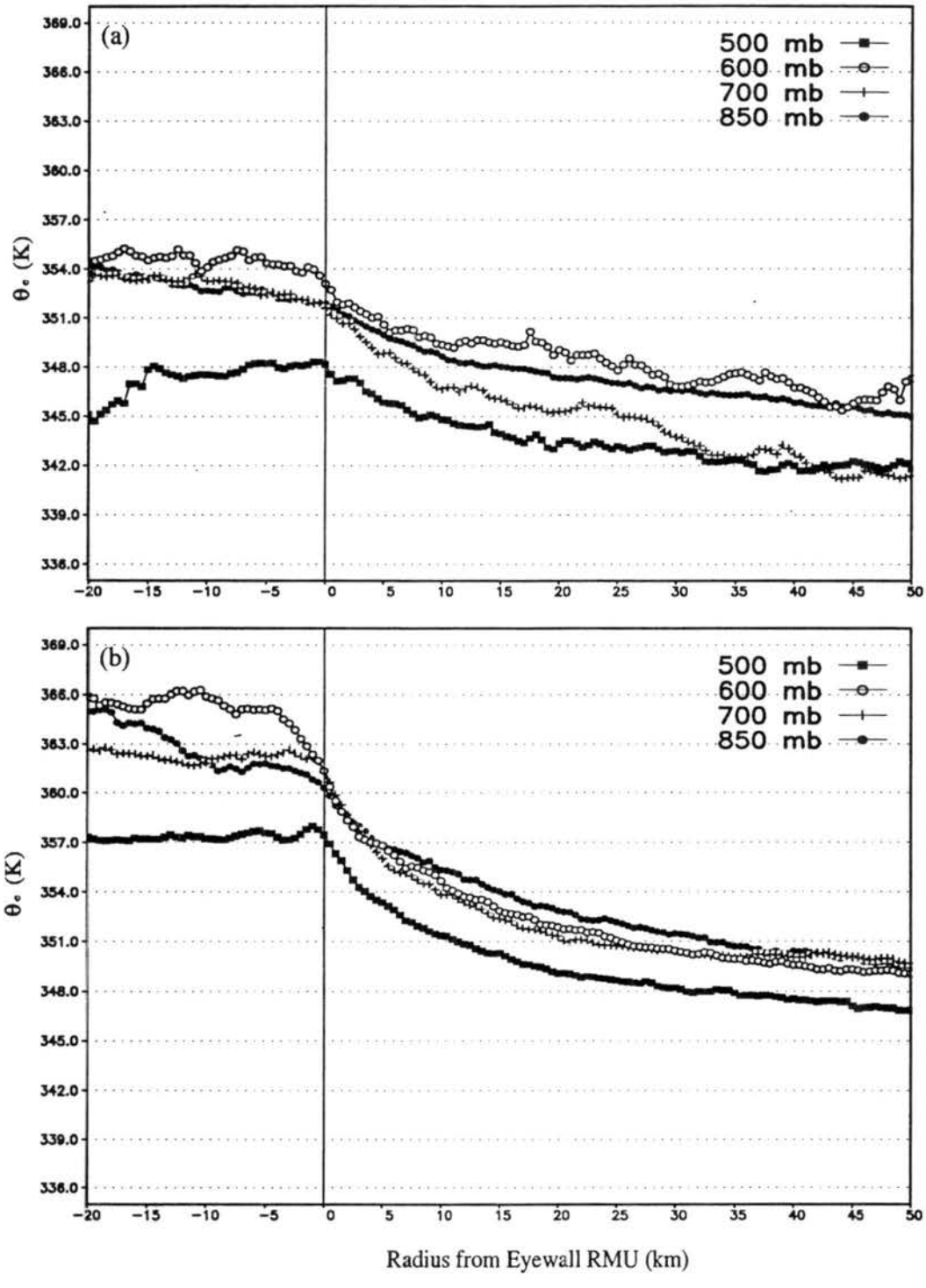

Figure 6.6: Composite θ_e for (a) minimal and (b) intense hurricanes at 850, 700, 600, and 500 mb about the eyewall RMU.

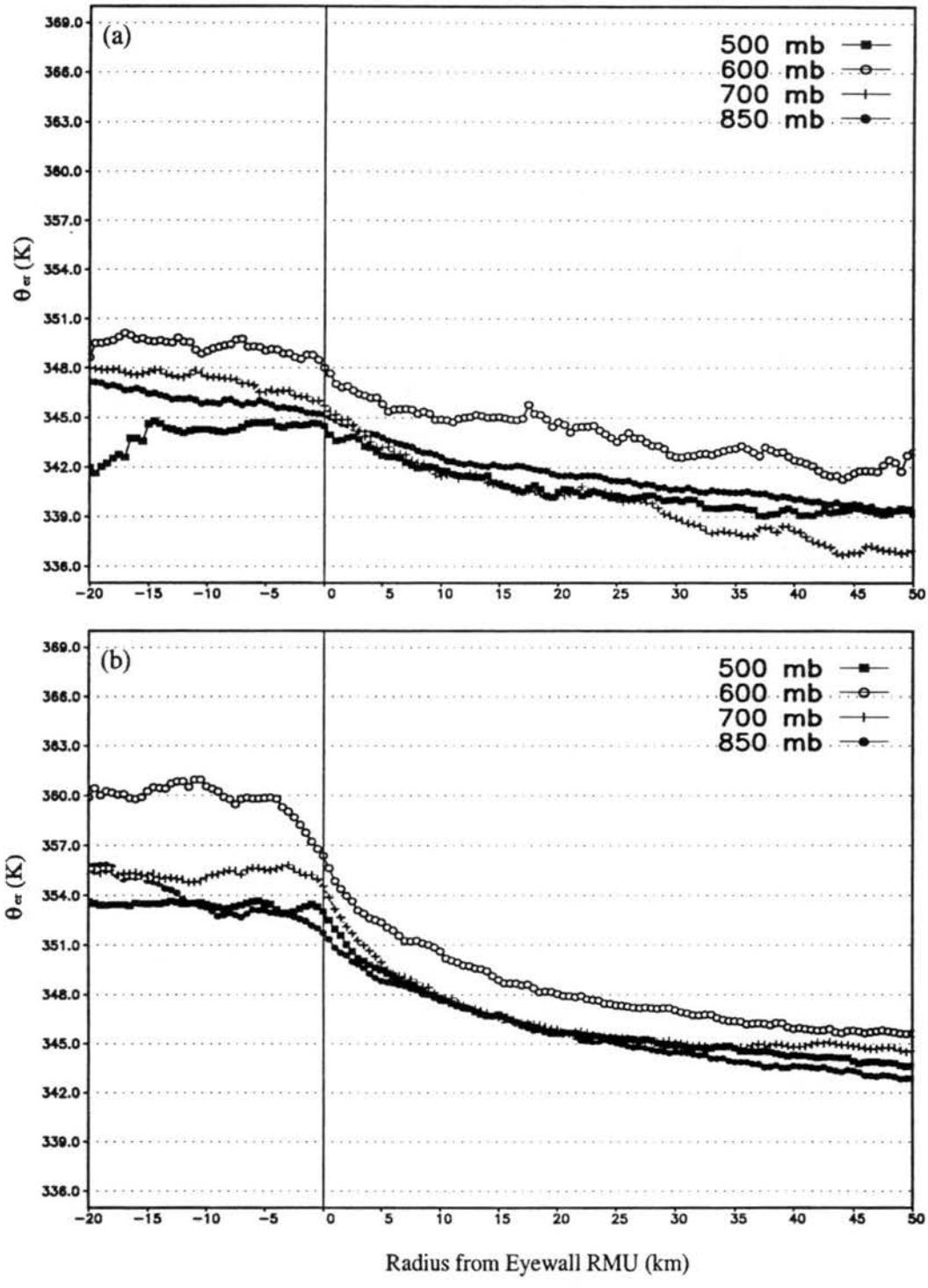

Figure 6.7: Composite θ_{er} for (a) minimal and (b) intense hurricanes at 850, 700, 600, and 500 mb about the eyewall RMU.

600 mb. Similarly located convective downdrafts were found by Jorgenson (1984b), Black and Hallett (1986), Marks and Houze (1987), and Black et al. (1994) and were collocated with radar reflectivity maxima and thus believed to be a result of water loading. Visual inspection of the data reveals frequent downdrafts in and outside the eyewall at all levels, however, compositing about the eyewall RMU can smooth over downdrafts adjacent to updrafts if the updrafts are of variable radial extent. The data also suggests that eyewall updrafts increase in magnitude, diameter, and mass flux (see Figure B.4) with height, particularily in intense hurricanes.

6.2 Thermal wind balance

A balanced, steady-state, frictionless vortex is in thermal wind balance. Thus, the vertical shear of a warm-core vortex, such as a hurricane, is directly related to the radial temperature gradient through the approximate symmetric thermal wind relationship given in cylindrical coordinates:

$$\left(f + \frac{2V_\theta}{r}\right)\frac{\partial V_\theta}{\partial p} = -\frac{R}{p}\left(\frac{\partial T_v}{\partial r}\right)_p \tag{6.1}$$

where f is the Coriolis parameter, R is the gas constant for dry air, V_θ is the tangential velocity, T_v is the virtual temperature, p is pressure, and $()_p$ denotes differentiation along a constant pressure surface. Equation (6.1) can be written as:

$$WS = B \tag{6.2}$$

where

$$W = \left(f + \frac{2V_\theta}{r}\right) = \textit{inertial parameter} \tag{6.3}$$

$$S = \frac{\partial V_\theta}{\partial p} = \textit{vertical wind shear} \tag{6.4}$$

$$B = -\frac{R}{p}\left(\frac{\partial T_v}{\partial r}\right)_p = \textit{baroclinicity} \tag{6.5}$$

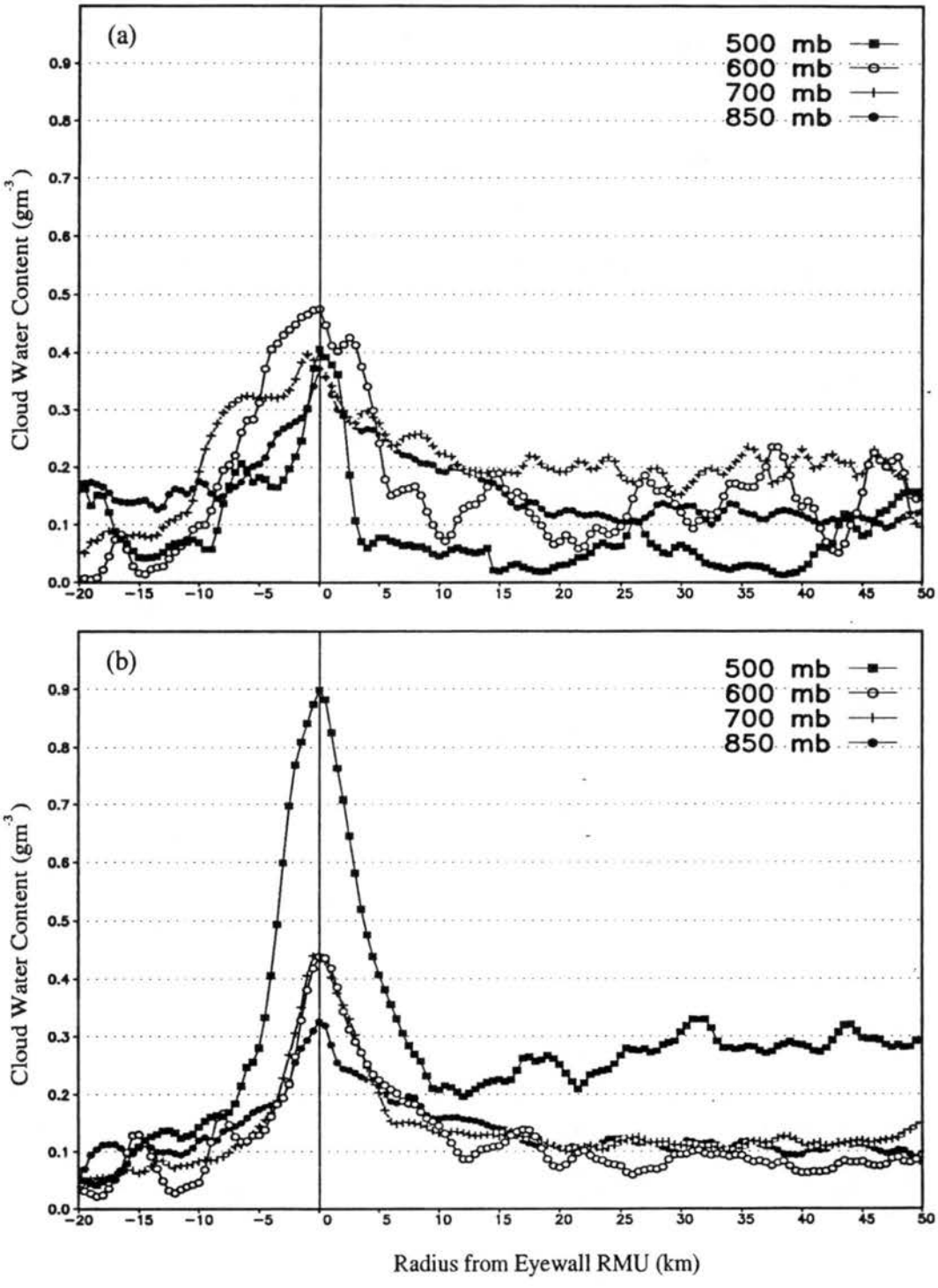

Figure 6.8: Composite cloud water content for (a) minimal and (b) intense hurricanes at 850, 700, 600, and 500 mb about the eyewall RMU.

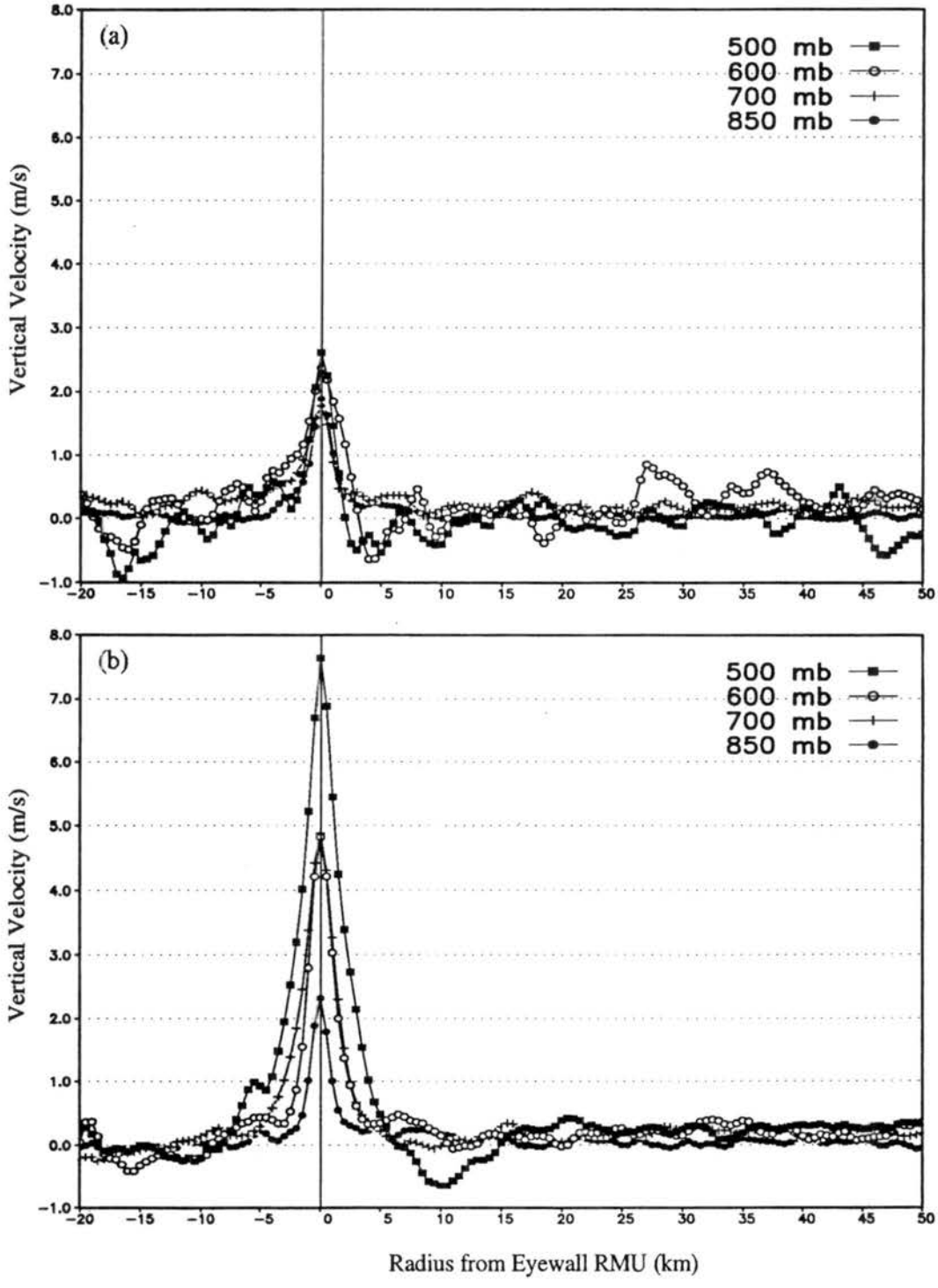

Figure 6.9: Composite vertical velocity for (a) minimal and (b) intense hurricanes at 850, 700, 600, and 500 mb about the eyewall RMU.

A measure of the thermal wind imbalance can also be defined as the baroclinicity excess (B_{ex}) where,

$$B_{ex} = B - WS \tag{6.6}$$

Previous studies have investigated the thermal wind balance (or imbalance) of hurricanes. Gray (1967) and Gray and Shea (1973) calculated large differences near the RMW between the observed vertical wind shear and the wind shear computed from the thermal wind relationship for individual hurricanes. They argued that large thermal wind imbalances are expected in non-steady hurricanes, and are the result of vertical advection of momentum near the eyewall reducing the vertical shear. In contrast, Hawkins and Rubsam (1968) in a case study of Hurricane Hilda (1964) showed the storm was in thermal wind balance. Jorgenson (1984b) in a case study of Hurricane Allen (1980) also showed the storm was in thermal wind balance on two separate days over a period of 6 hours. For each study the effects of instrument wetting may have had an significant effect upon the radial temperature gradient near the RMW. Thus, the thermal wind balance or imbalance of hurricanes is re-investigated with the reconstructed temperature profiles.

Simultaneous, multi-level flights with radiometer temperatures have been rare. Only four cases are available for the evaluation of thermal wind balance. The results presented here are for a multi-level penetrations of Hurricane Emily (1987), but three separate multi-level penetrations of Hurricane Norbert (1984) were also analyzed and similar results were found. Two research aircraft investigated Hurricane Emily between 1500-2200 UTC September 22, 1987. Emily was located about 220 km south east of the island of Hispaniola moving to the northwest at 8 m/s. A more complete description of the history, track, and large-scale environment of the storm is found in Case and Garrish (1988). Emily was near the end of a period of rapid deepening according to the 24-hour pressure tendency criteria established by Holliday and Thompson (1979) for typhoons, and contained very intense vertical velocities in the eyewall (Black et al. 1994). A total of 14 radial legs at 700 mb

and 35 radial legs at 500 mb were available for the 7 hour period. Axisymmetric averages of V_θ and T_v were computed and the thermal wind relationship was evaluated.

Shown in Figure (6.10) are the WS, B, and B_{ex} computed from the axisymmetric radial profiles of Emily. The eyewall slopes outward approximately 20° from the vertical between 700 and 500 mb resulting in an average RMW of 28 km with the average eyewall RMU located near 25 km. Near the RMU the imbalance (B_{ex}) maximizes with the baroclinicity being 20% larger than the inertial wind shear term (WS). The inertial wind shear term dominates 20 km outside the RMU and is roughly 30% larger than the baroclinicity. However, to a good approximation Emily is in axisymmetric thermal wind balance, and the outward sloping eyewall is indicative of thermal wind balance. Shown in Figure (6.11) are the same terms computed using profiles of T_v calculated from the ROSE sensor rather than the radiometer. Therefore, instrument wetting errors are present in the thermal wind calculation. The erroneous temperatures roughly double the imbalances. Thus, without the removal of instrument wetting errors the extent of thermal wind balance or imbalance may be erroneously concluded.

6.3 Composite vertical structure

Early observation and conceptual studies of hurricane eyewalls suggested that parcels rise nearly undilute in "hot towers" along moist-adiabats (Malkus 1958; Riehl and Malkus 1961; Hawkins and Imbembo 1976), resulting in minimal local potential buoyancy. More recently, Emanuel (1986) hypothesized that the eyewall is undilute following a reversible moist-adiabat (i.e. retaining all condensed moisture during ascent). On the other hand, observational studies (Gray and Shea 1973; Hawkins and Rubsam 1968; Jorgenson 1984b) have presented evidence that θ_e in the eyewall is variable with height, and ample potential moist buoyancy exists. Gray and Shea (1973) assumed a linear decrease of relative humidity with height from 90% to 70% between 900 and 500 mb to account for asymmetric eyewall convection and found the resulting composite vertical profile at the RMW and various radii outside the RMW supported substantial potential buoyancy (i.e. a large decrease in θ_e) up to approximately 700 mb. Above 700 mb, stability was noted by a

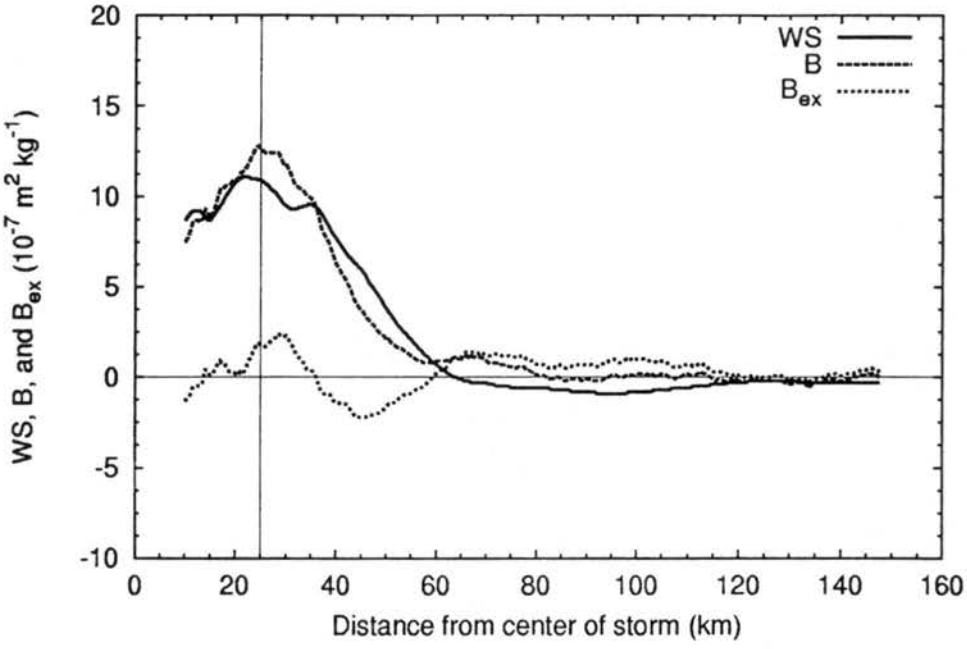

Figure 6.10: Profiles of WS, B, and B_{ex} computed from axisymmetric radial profiles of V_θ and T_v derived from the radiometer for Emily (1987) on September 22, 1987 between 1500-2200 UTC. The solid vertical line is the average eyewall RMU at 25 km. The average RMW is at 28 km.

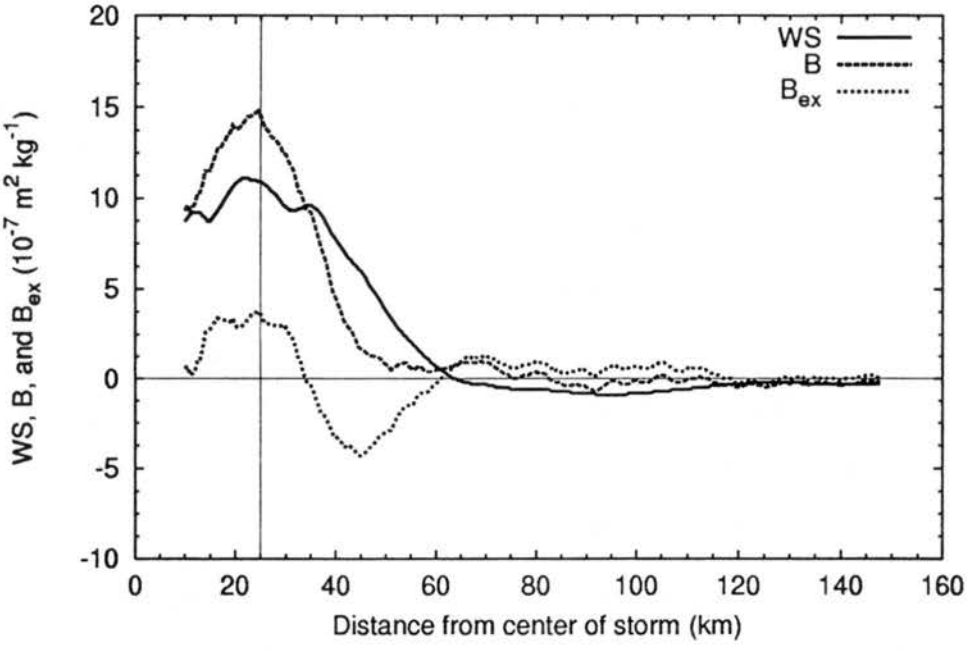

Figure 6.11: As in Figure 6.9 except computed from axisymmetric radial profiles of T_v derived from the Rosemount sensor.

the large increase in θ_e with height. Even when saturation was assumed at the RMW, θ_e decreased 4-5 K from 900 to 700 mb, supporting the potential for low level buoyancy near the eyewall. Decreases in θ_e of this magnitude is equivalent to a temperature decrease of $\sim$1°C, or the magnitude of commonly observed instrument wetting errors in the eyewall (see Figure 5.22). Thus, instrument wetting errors may have played a substantial role in the conclusions made by Gray and Shea (1973).

Shown in Figure (6.12) are the composite vertical profiles of θ_e without instrument wetting errors at various radii with respect to the eyewall RMU for minimal and intense hurricanes. Shown for comparison is the mean tropical sounding for the Atlantic hurricane season (Jordan 1958b). At the eyewall RMU no significant decrease of θ_e with height is apparent between 850 and 700 mb, and neither is a significant increase between 700 and 500 mb. Considering the variability present in the composites at each level (Table 6.1), the eyewall is nearly moist-adaibatic. Shown in Figure (6.13) at the composite vertical profiles of θ_{es} and θ_{er} at the eyewall RMU for minimal and intense hurricanes, and again values are nearly constant in the vertical. Therefore, to a *first approximation* the composite eyewall is neutral to moist-adiabatic and reversible moist-adiabatic ascent with minimal potential for buoyancy.

Hawkins and Imbembo (1976) observed minimum of θ_e at 700 mb outside the eyewall. Jorgenson (1984b) noted a similar minimum of θ_e near 700 mb in Allen (1980) on one day, but no such minimum on a subsequent day. The composite vertical profiles (Figure 6.12) indicate that in minimal hurricanes a θ_e minimum is located at 700 mb on average and becomes more pronouced at larger distances from the eyewall. However, considering the inherent variability present in the composites at each level the minimum may not be significant. Furthermore, no such significant minimum exist is intense hurricanes. On the other hand, the vertical profiles indicate a slight decrease in θ_e through the lower to middle troposphere to a *first approximation.* While this may again be the result of variability present in the composites, studies have shown that θ_e is substantially higher in the hurricane boundary layer than above (Ryan et al. 1992; Barnes and Powell 1995)

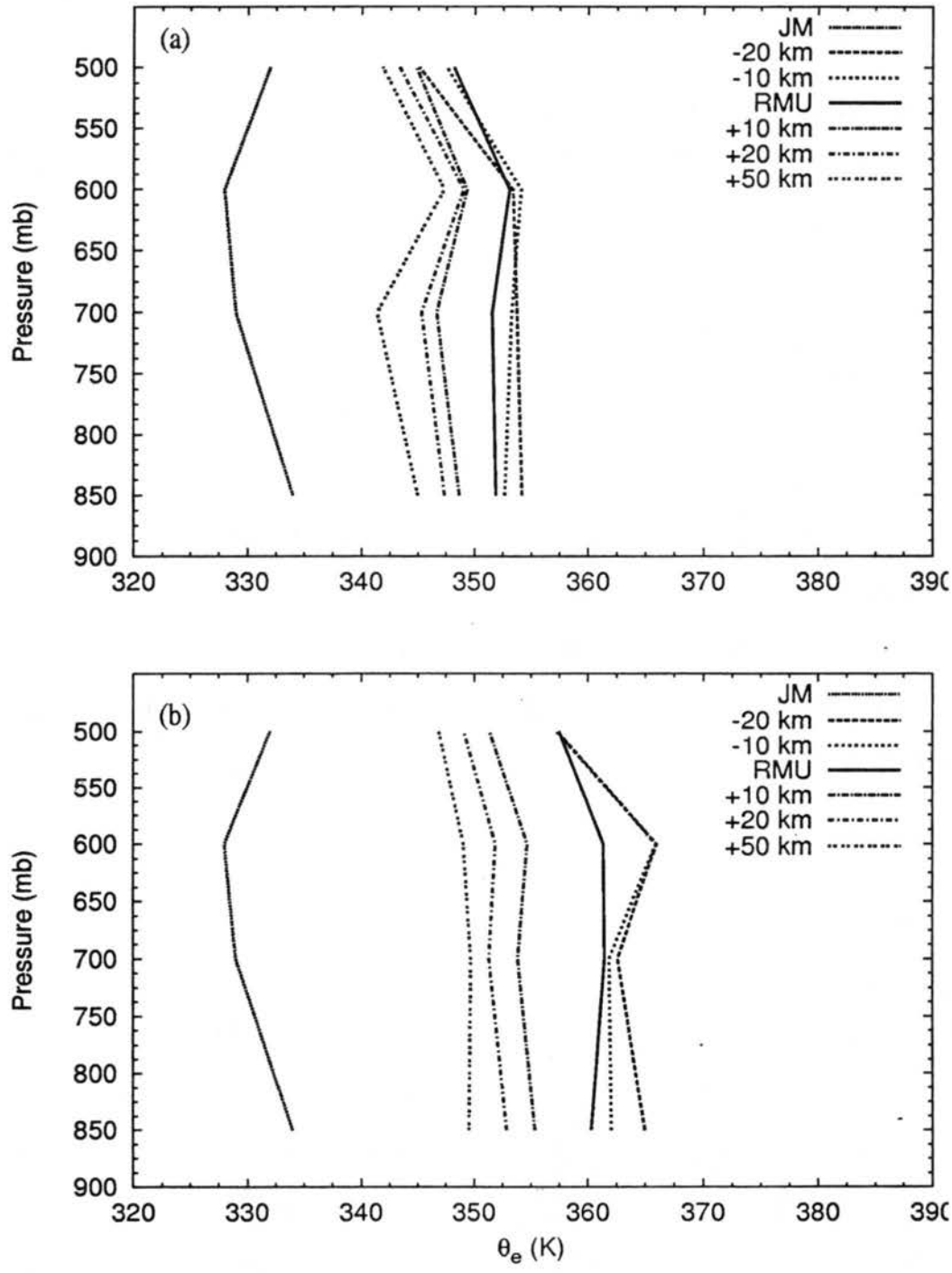

Figure 6.12: Composited vertical profiles of θ_e at the eyewall RMU and several radial distances from the RMU for (a) minimal and (b) intense hurricanes. Also shown for comparison is the mean hurricane season profile taken from Jordan (1958b).

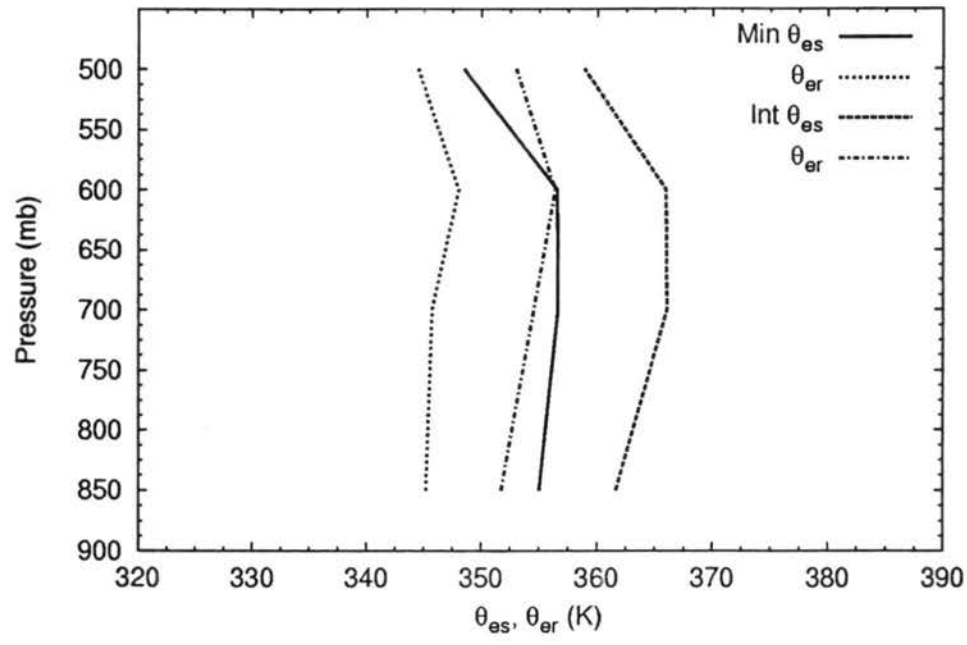

Figure 6.13: Composited vertical profiles of θ_{es} and θ_{er} at the eyewall RMU for minimal and intense hurricanes.

, and Gamache et al. (1993) noted that melting and evaporation of stratiform precipitation outside the eyewall can lead to a net cooling below the melting level (~500 mb). Furthermore, composite soundings of the hurricane inner core have shown the presence of conditional instability at low to middle levels (e.g. Sheets 1969; Frank 1977). Therefore, it is compelling to argue that outside the eyewall below the 0°C isotherm the hurricane environment is conducive on average to buoyant convection.

6.3.1 Comments on eyewall buoyancy

One is now naturally tempted to ask whether buoyant parcels exists in the eyewall of a hurricane, and if so, how important is buoyancy to hurricane maintenance and intensity change? At the present time there are significantly different opinions and answers to these questions. Emanuel (1986, 1988, 1991) and Rotunno and Emanuel (1987) argue that hurricanes are maintained against dissipation and intensify entirely by air-sea fluxes with no contribution from buoyancy except to counter the effects of turbulent mixing. The continual vertical redistribution of heat acquire from the sea surface maintains a re-

versibly moist-adiabatic eyewall neutral to slantwise convection. Ooyama (1982) argues that a steady-state hurricane can be maintained in the absence of eyewall buoyancy given adequate air-sea fluxes are available to maintain moist neutral ascent. However, the direct cause of intensification cannot be the frictionally induced inflow because the air-sea fluxes and radial pressure gradient that drives the inflow can only increase when the primary circulation increases. Thus, during intensification the eyewall must be convectively unstable such that buoyant parcels can radially entrain middle level air into the updraft and be lifted to the outflow layer. The entrainment induces a radial inflow above the friction layer that conserves angular momentum and spins up the hurricane vortex while increasing the eyewall mass flux with height. Gray (1999) argues that buoyancy plays a crucial role in the maintenance and intensification of hurricanes. In order to maintain a steady-state hurricane against frictional dissipation, buoyancy must drive an additional tangential momentum flux across the 2×RMW radius that is 2.5 times larger than what is required by friction alone. These three arguments are not the only ones, but demonstrate the present range of opinions as to the presence and role of eyewall buoyancy in a hurricane.

Indirect observations tend to suggest that positively buoyant air exists in and near the eyewall. Vertical velocities on the order of 15-20 m s^{-1} have been observed in hurricane eyewalls (Black et al. 1986; Ebert and Holland 1992; Black et al. 1994; Black et al. 1996). The maximum and average vertical velocity tend to increase with height, and the correlation between average vertical velocity and updraft diameter also increases with height, reflecting the tendency of the eyewall to organize into larger and stronger updrafts during ascent (Jorgenson et al. 1985). Likewise, the vertical mass flux increases with height (see Figure B.4). Marks and Houze (1987) noted convective bubbles of enhanced vertical motion were embedded in the general slantwise updraft of the eyewall, and maximum vertical velocities were located above the freezing level. Model results of Lord et al. (1984) suggest peak updrafts should be found above the freezing level due to enhanced buoyancy by the latent heat of fusion during freezing of supercooled drops. Convective cloud forms are seen along the inner edge of the eyewall in photographs (Fig. 20 in Jorgenson 1984b). Visible

satellite imagery shows convective clouds penetrating the quasi-laminar eyewall outflow near the tropopause. Finally, the episodic occurrence of negative lightning flashes in numerous hurricane eyewalls (Cecil and Zipser 1999; Molinari et al. 1999) tends to suggest the presence of strong, localized, buoyant updrafts that can simultaneously support the needed large quantities of liquid water, large graupel, and ice above the freezing level to produce significant charge separation according to current non-inductive charge theories.

The composite vertical profiles of θ_e shown in Figure (6.12) indicate that the eyewall is moist-adiabatic and neutral to a *first approximation.* One would expect this in active convection, but it *does not indicate that buoyancy does not exist in the eyewall.* According to parcel theory, active updrafts that are accelerating upwards will have a positive buoyancy. Neglecting water loading, entrainment, and vertical pressure gradient forces, an active parcel is warmer (less dense) than its local environment. A positive temperature deviation of only 0.1°C can accelerate a parcel to 6 m s^{-1} over 5km assuming the parcel was initially at rest. Such a temperature deviation is within the accuracy of thermodynamic instruments and corresponds to a θ_e deviation of roughly 0.5 K. The standard deviations of the composite eyewall θ_e are 4-5 K. Therefore, the temperature deviation of positively buoyant eyewall parcels are well within the composite variability and the determination of whether the eyewall is conducive to buoyant convection from composited θ_e, considering the variability present at each level, is impossible. Previous statistical studies (e.g. Jorgenson et al. 1985) were not able to determine updraft buoyancy or vertical heat flux due to instrument wetting errors. A statistical study of individual eyewall cores is needed.

6.3.2 Comments on pseudo-adiabatic and reversible ascent

Results presented in Figure (6.12) and (6.13) indicate that, given the variability in the composites, the eyewall is neutral to *both* pseudo-adiabatic and reversible ascent to a *first approximation.* Is θ_e or θ_{er} a better representation of active eyewall convection? Each is an extreme representation of active convection since θ_e assumes all condensed water (and ice) is immediately removed, where as θ_{er} maintains all condensed water with

the parcel during ascent. Observations show that the eyewall produces copious amounts of precipitation as typical radar reflectivities are greater than 35 dBZ (Marks 1985; Marks and Houze 1987). The outward slope of the eyewall permits precipitation to fall out of the updraft, and thus unload the rising air. Furthermore, cloud base mixing ratios are typically 17-19 g kg^{-1} for tropical convection and likely higher for hurricane eyewalls. The adiabatic liquid water content for a parcel rising from cloud base to 5 km is nearly 10 g kg^{-1}. However, the composited cloud water contents (Figure 6.8) are roughly 5-10% of their expected adiabatic values for reversible ascent. Thus, it seems evident that the weak updrafts (compared to continental convection) in the eyewall permit the development of a full precipitation drop-size spectrum that cannot be supported by the updrafts even before the air rises to the freezing level, and thus a significant amount of liquid water falls out as rain at low levels. This is supported by the observed rapid conversion of supercooled liquid water to ice just above the freezing level and low reflectivities above the freezing level (Black and Hallett 1986; Marks and Houze 1987; Black et al. 1996). Therefore, observations indicate that the hurricane eyewall is markedly more represented by constant θ_e rather than θ_{er}, and questions reversible representations of the eyewall (Emanuel 1986, 1988; Rotunno and Emanuel 1987). Lucas et al. (1994) also noted that tropical convection off Australia was not reversible. While, the application of θ_{er} to non-precipitating clouds is accurate, active tropical convection, particularly the hurricane eyewall, is far from reversible.

6.4 Estimation of eyewall surface pressure and temperature

Accurate thermodynamic measurements in the boundary layer of a hurricane inner core have been rare. The lack of observations in this region have resulted in assumptions regarding the thermodynamic structure of the boundary layer and ocean-atmosphere exchanges of momentum, heat, and moisture. Historically the inflow has been assumed to be isothermal at approximately 1°C cooler than the SST with relative humidities of 80-90% (e.g. Miller 1958; Hawkins and Imbembo 1976; Holland 1987; Willoughby 1995). The isothermal inflow was assumed to be maintained by heat fluxes from the ocean and ver-

tically mixing from aloft acting to balance evaporational and adiabatic cooling (Malkus and Riehl 1960; Frank 1977,1984). Thus, through diabatic expansion a constant supply of high θ_e air with respect to the environment would be available to maintain the transport of energy aloft by eyewall convection and sustain the hurricane warm core structure. Such thermodynamic assumptions have been utilized in conceptual models of the maximum potential intensity (MPI) of hurricanes (Malkus and Riehl 1960; Emanuel 1988, 1991; Holland 1997), however, hurricanes rarely achieve their MPI. One plausible reason is that the boundary layer air is modified along its trajectory from the environment such that upon arrival at the eyewall its θ_e cannot support the required deep convection.

Modeling efforts have suggested that evaporational cooling of sea spray and rainfall (Fairell et al. 1995) along with convective downdrafts of cool and/or dry air (Betts and Simpson 1987) can substantially lower θ_e in the boundary layer. Cool, dry, convective downdrafts associated with rainbands have been observed to lower boundary layer θ_e (e.g. Barnes et al. 1983; Powell 1990). A recent study by Cione et al. (1999) composited buoy observations of the hurricane boundary layer with respect to the center of 34 hurricanes. Large radial temperature gradients were found and average air-sea temperature differences inside 100 km was 2.5°C with maximum values near 5°C. Furthermore, the average near surface relative humidity inside 80 km was 96% with maximum values at saturation. Large radial gradients or relative humidity were also found. The average temperature difference was based upon 100 individual observations with the SST > 27°C, while only 16 observations comprised the average relative humidity. In an attempt to ensure data quality, Cione et al. (1999) considered temperature decreases greater than 1.5°C over 1-3 hours as suspect of instrument wetting errors and the data were not used, however, the presence of saturated air within a few meters of the surface seems unlikely, and suggests a few instrument wetting errors may still be present in the data. Regardless, the results tend to indicate that the boundary layer inflow is neither isothermal nor isodrosothermal, and the increase in θ_e from its environmental value may be small. Despite the compositing efforts of Cione et al. (1999), observations of the hurricane inner-core boundary layer,

particularily near the eyewall, are still rare. An alternative method of determining features of the inner core boundary layer is extrapolation from flight-level data, however, the known presence of instrument wetting errors have prevented confident estimates in the past. Thus, with a few assumptions that are shown to be reasonable, the reconstructed flight level data is used to independently estimate surface pressure and temperature beneath the eyewall.

6.4.1 Methodology

Surface pressure and temperature beneath the eyewall are estimated from each radial leg by extrapolation from flight-level at the eyewall RMU along a moist-adiabat, assuming a constant eyewall slope with height of 30° from the vertical, to a cloud base height of 300 m (i.e. depth of the boundary layer), and then to the surface assuming a well-mixed boundary layer. For simplicity the eyewall was considered saturated at flight level. Eyewall surface pressures are more accurately obtained by adjusting the depth of the moist-adiabatic layer for the outward slope of the eyewall. Since surface pressure is a vertical integral of the mass aloft and flight level data is isobaric, the radial distance of the eyewall at the surface from the flight-level eyewall RMU is calculated from the height of the isobar at the RMU assuming a 30° slope from the vertical. The height of the flight-level isobar directly above the eyewall at the surface is then determined by moving the calculated radial distance along the radial leg. The moist-adiabat extrapolation is then performed from the new isobaric height, using θ_{es} at the eyewall RMU, down to cloud base (see Figure 6.14). The only deviation from this method is when the radial adjustment for a 30° slope is larger than the eyewall RMU, or if the calculated eyewall surface pressure is lower than the minimum central pressure. For such cases, the slope is relaxed, making the eyewall more vertical, until both criteria are satisfied.

Estimates of surface pressure and temperature beneath the eyewall require accurate extrapolation from flight level and reasonable assumptions of boundary layer depth and eyewall slope. Are the assumptions stated above reasonable? The primary simplifying assumption is that the eyewall can be represented by undilute moist-adiabatic ascent above a well-mixed boundary layer. As shown in section 6.3 the composite eyewall is

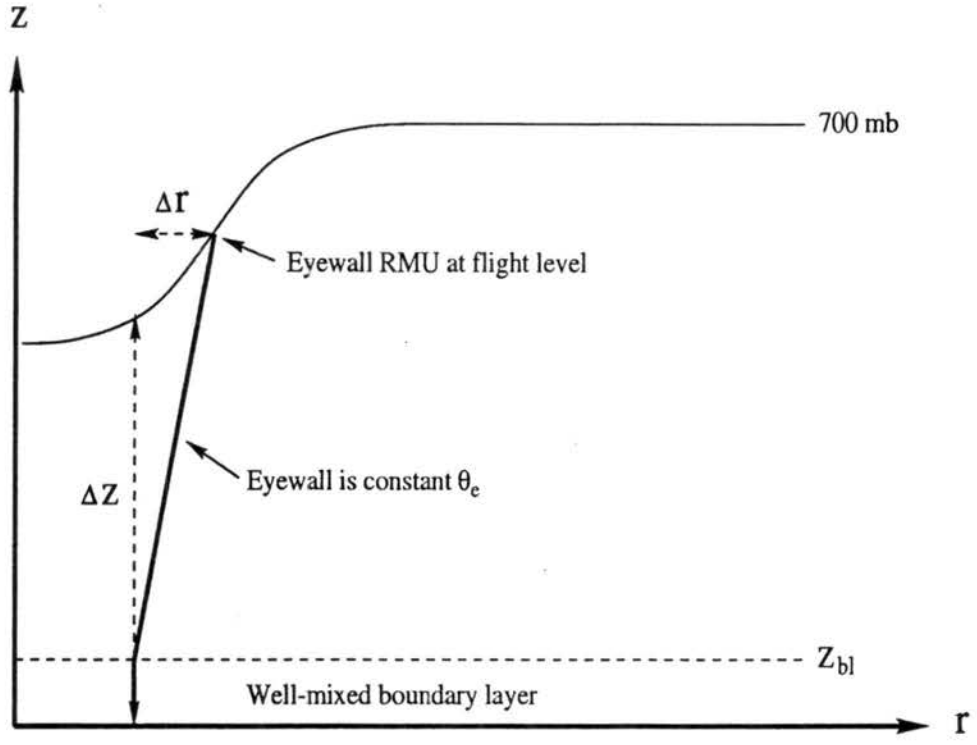

Figure 6.14: Diagram depicting the more accurate determination of eyewall surface pressure and temperature by accounting for an outward slope. The eyewall (thick solid line) is assumed to be constant θ_e above a well-mixed boundary layer. The height ($\triangle$z) of the flight-level isobar (in this case 700 mb) directly above the eyewall at the surface is determined by the radial distance ($\triangle$r) from the eyewall RMU for an assumed slope of 30°.

an undilute moist-adiabat to a first approximation. Recent observations taken by GPS sondes (Powell et al. 1999) confirm a well-mixed boundary layer near the eyewall, with mixed-layer depths of ~300 m. Shown in Table (6.3) are the observed boundary layer depths or surface relative humidities noted near and under the eyewall in past studies. Observations indicate the depth of the boundary layer near the eyewall ranges from 100 to 500 m, which corresponds to 96%-80% relative humidity. Aircraft reconnaissance observers indicate cloud base is typically between 300 and 500 m.

Table 6.3: Observed depths of hurricane boundary layer or surface relative humidity near the eyewall from previous studies. Observed depths are visual approximations from flight-level, while observed surface relative humidities are from composited rawinsondes and buoy observations inside 0.75° from the center. The quantity not in parenthesis was given. The quantity in parenthesis corresponds to the given value for a well mixed boundary layer.

	Δz(m)	RH(%)
Riehl and Malkus (1961)	500	(80)
Frank (1977)	(120)	95
Riehl and Meitin (1979)	360	(85)
Cione (1999)	(100)	96

Shown in Table (6.1) are the average eyewall slopes in the lower to middle troposphere for minimal and intense hurricanes. Eyewalls in intense hurricanes tend to have smaller slopes (i.e. the eyewall is more vertical) than minimal hurricanes, and the slope increases with height. Jorgenson (1984a) noted that the eyewall slope is related to the size of the eye and the intensity of the storm, such that eyewalls are more vertical for intense storms with small eyes due to angular momentum conservation. Previous observations (Shea and Gray 1973; Hawkins and Imbembo 1976) support near vertical eyewalls in intense storms. However, eyewall slopes up to 60° from the vertical have been observed (e.g. Black 1993). Furthermore, negatively sloped eyewalls (i.e. the eyewall convection tilts toward the center) are possible on the upshear side of storms experiencing vertical shear. Thus, in reasonable agreement with observations, a constant slope with height of 30° from the vertical is assumed.

6.4.2 Sensitivity to control parameters and assumptions

The observed sensitivities of calculated surface pressure and temperature to the assumed boundary layer depth, eyewall slope, flight-level relative humidity, and entrainment cooling (or warming) are determined directly from the reconstructed radial legs. First, the surface pressure and temperature are calculated assuming the eyewall has a slope of 30° from the vertical and is a saturated, undilute, moist-adiabat from flight-level down to a cloud base of 300 m and a well-mixed boundary layer below. This is considered the "control" eyewall. The sensitivity of each parameter is then calculated as the difference in temperature and pressure between the control and a variation from the control. The sensitivities are determined for one parameter at a time, while the other parameters are held fixed to their control value. This is repeated for each reconstructed radial leg, resulting in a pressure and temperature sensitivity, or average error, for variations each parameter directly from the data. Sensitivities are calculated for boundary layer depths ranging from 25-825 m, eyewall slopes ranging from -20° to 60° from the vertical (positive values indicate an outward sloping eyewall), flight-level relative humidities ranging from 70%-100%, and previously experienced entrainment cooling of -1°C to 4°C (negative values would be indicative of entraining warmer air from the eye into the eyewall). Lower surface pressures, or positive errors, are expected for large boundary layer depths, large eyewall slopes, and previously large cooling due entrainment. Subsaturated conditions always result in higher surface pressures, or negative errors[4]. Higher surface temperatures, are expected for large boundary layer depths, nearly vertical eyewalls, and previously large cooling due entrainment, resulting in negative errors. Subsaturated conditions always result in lower surface temperatures, or positive errors.

---

[4]The sensitivity of surface pressure and temperature to relative humidity is primarily from assuming saturated conditions at flight level. Decreasing relative humidity will result in lower θ_e and a cooler vertical profile of temperature. The sensitivity of surface pressure to water vapor content in the air is less than 1 mb for the most extreme conditions, and acts to offset the cooling effect by increasing surface pressure for decreasing relative humidity.

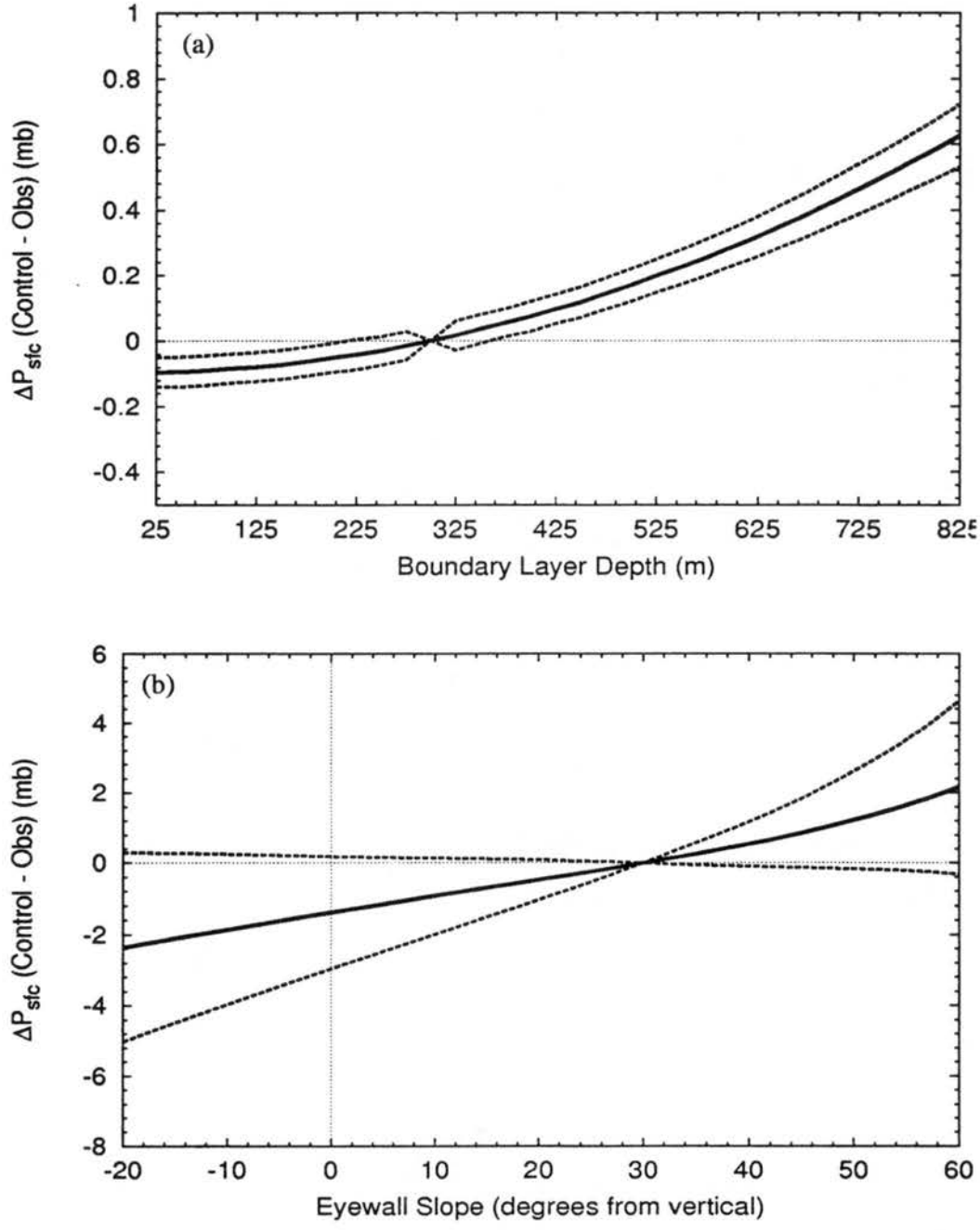

Figure 6.15: Calculated average eyewall surface pressure errors (mb) due to variations in (a) boundary layer depth, (b) eyewall slope, (c) flight-level relative humidity, (d) and entrainment. Also shown is the spread for one standard deviation of the pressure error. The control parameters are: boundary layer depth = 300 m, slope = 30°, flight-level relative humidity = 100%, and entrainment = 0°C. Positive (negative) ΔP_{sfc} errors represent pressures lower (higher) than calculated from the control parameters. A positive (negative) slopes represent an outward (inward) sloping eyewall. Positive (negative) entrainment indicates the eyewall at flight-level was warmer (cooler) than at cloud base.

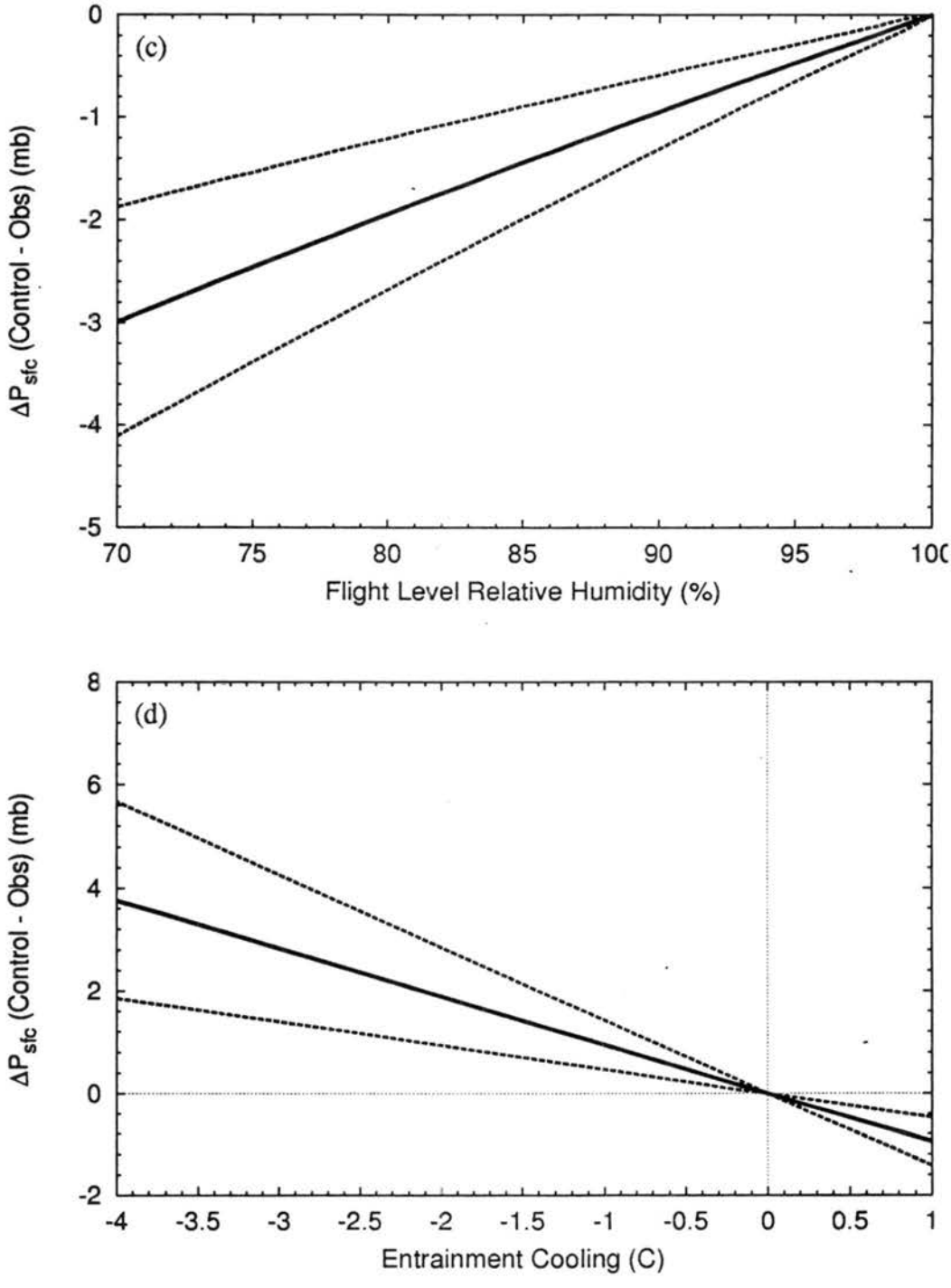

Figure 6.15: Continued.

Shown in Figure (6.15) are the calculated average surface pressure errors due to variations in the assumed control parameters, and the spread for one standard deviation of the pressure error. Estimated eyewall surface pressure is relatively insensitive to boundary layer depth. Errors due to flight-level relative humidity and entrainment will likely be less than 2 mb since over 80% of eyewall RMU updrafts were at least 90% saturated and the eyewall is an undilute moist-adiabat to a first approximation. Variations in eyewall slope may present the largest surface pressure errors (~4-6 mb), as large variations are commonly observed during the lifetime of a given hurricane and from one hurricane to another. Finally, the calculated average errors are approximately additive, such that if a saturated eyewall sloped outward 60° and had experienced 2°C of cooling up to flight level from a cloud base of 800 m, the surface pressure would be ~5 mb lower than calculated using the control parameters.

Shown in Figure (6.16) are the calculated average surface temperature errors due to variations in the assumed control parameters. Estimated surface temperatures are relatively insensitive to eyewall slope, but errors due to entrainment and boundary layer depth may be as high as 1-2°C. The largest surface temperature errors may result from variations in flight-level relative humidity, as 85% subsaturated air can produce errors of 1.5°C. Again, the errors are additive such that if a saturated eyewall sloped outward 60° and had experienced 2°C of cooling up to flight level from a cloud base of 800 m, the surface temperature would be ~4-5°C warmer than calculated using the control parameters.

6.4.3 Estimated eyewall surface pressures

Shown in Figure (6.17) are the eyewall surface pressures estimated from the control parameters for each radial leg as a function of the observed (not saturated) flight-level θ_e. In general, higher eyewall θ_e corresponds to lower surface pressures as expected. In fact, the 17 data points with eyewall $P_{sfc} < 930$ mb and flight level $\theta_e > 370$ K are from Hurricane Gilbert when its central pressure was less than 890 mb on September 13-14, 1988. The linear fit has a correlation of -0.77. A few noticeable outliers with eyewall surface pressures near 985 mb and $\theta_e < 340$ are from Hurricane Juan on October 28, 1995

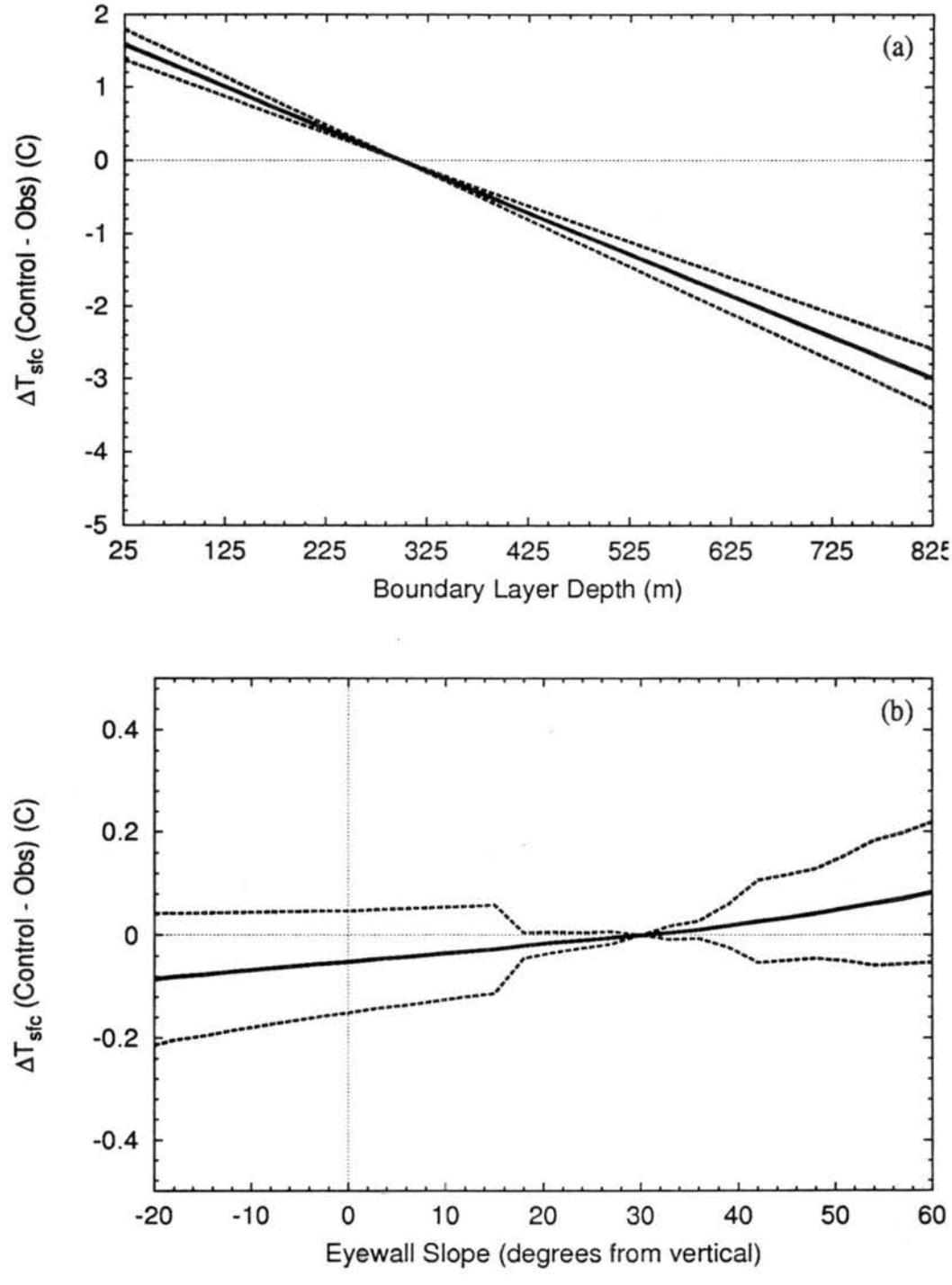

Figure 6.16: As in Figure 6.15 except for average surface temperature errors (°C). Positive (negative) ΔT_{sfc} errors represent temperatures cooler (warmer) than calculated from the control parameters.

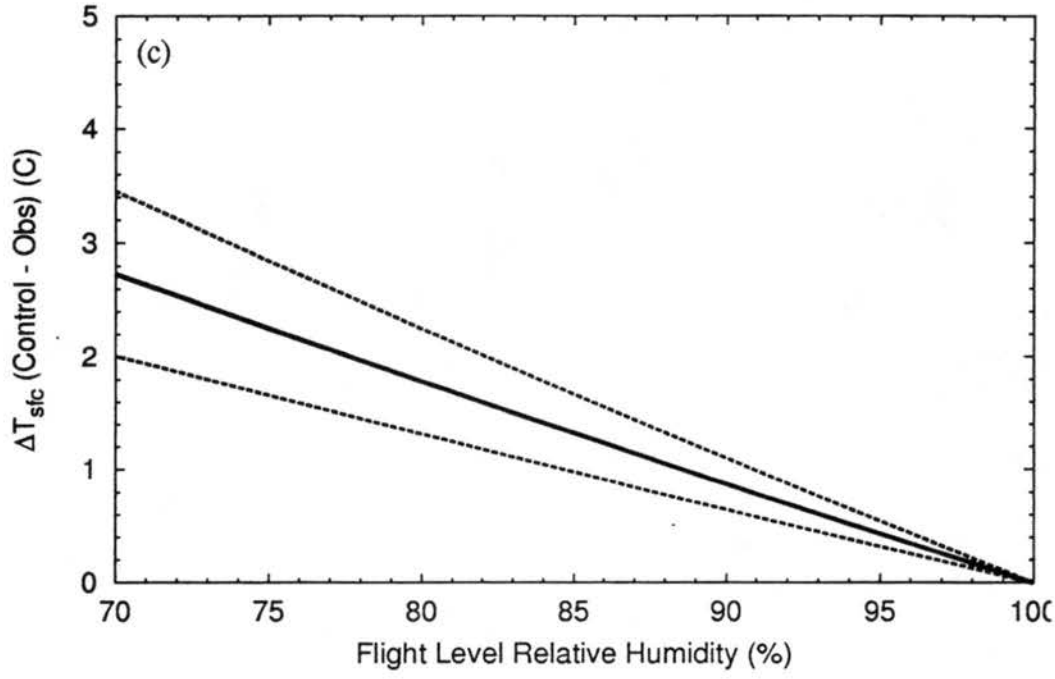

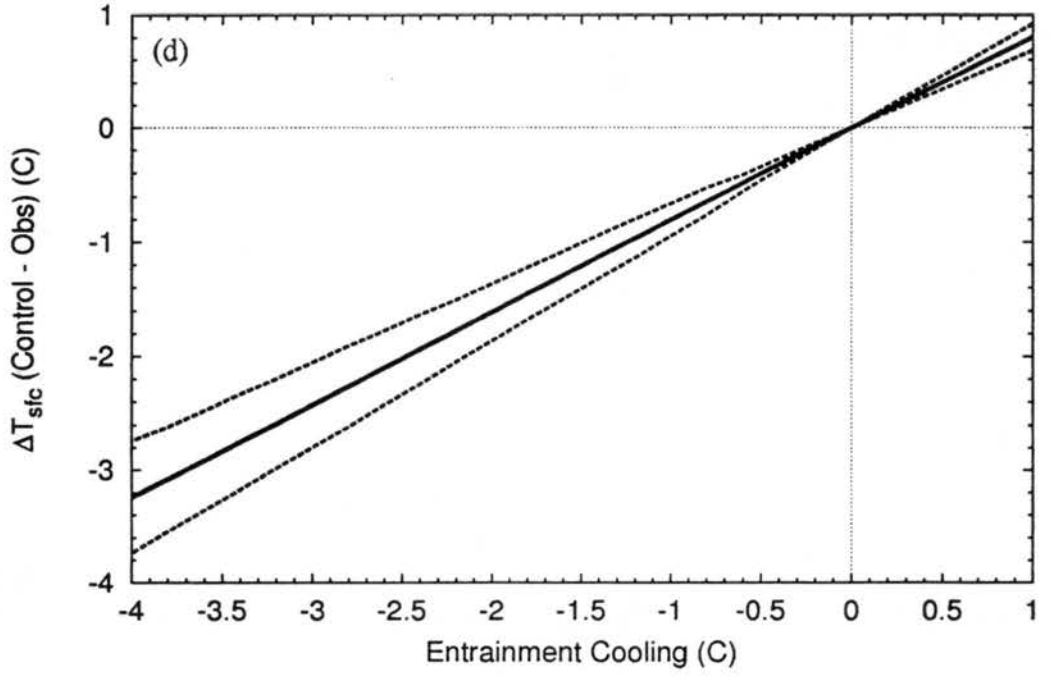

Figure 6.16: Continued.

when it was located in the northern Gulf of Mexico with climatological SST's of 24-25°C. Removal of the 11 radial legs from Juan (1985) increases the correlation coefficent to -0.82. Stratification by flight-level results in nearly identical fits and correlation coefficents.

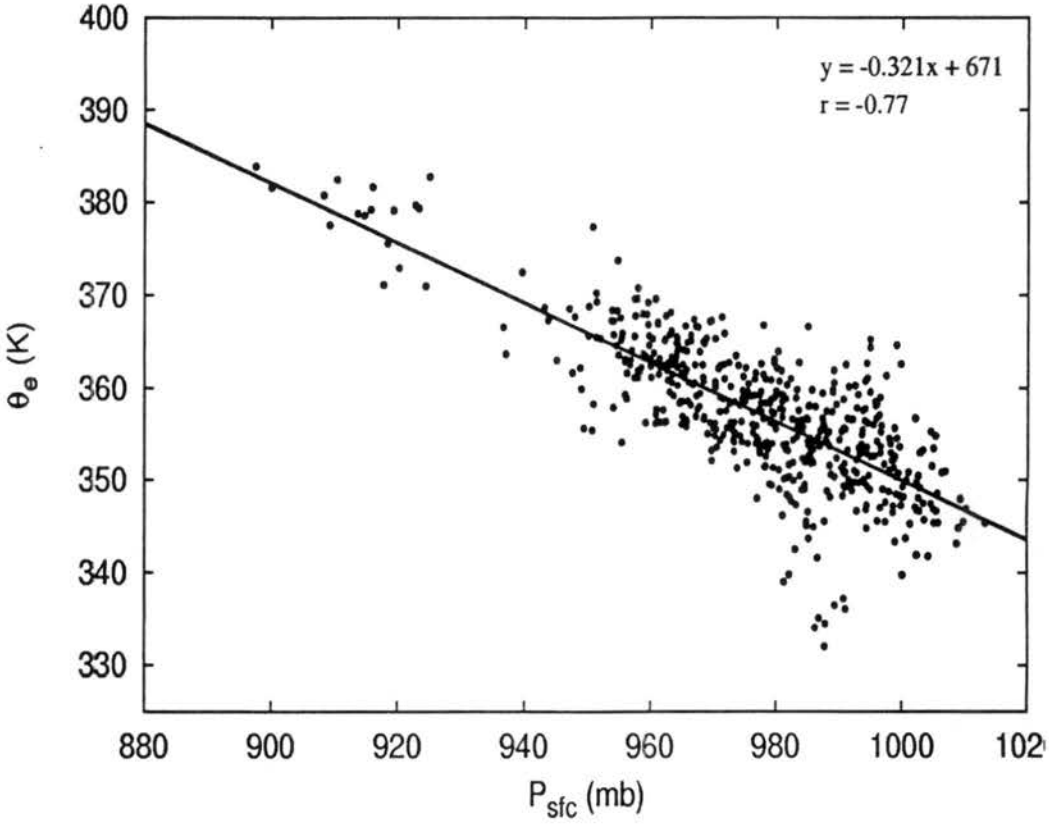

Figure 6.17: Scatter plot of the estimated eyewall surface pressure using the control parameters as a function of the observed flight-level θ_e. The linear fit to the data is shown.

In order to independently determine if the proposed methodology of determining eyewall surface pressure is reasonable, GPS sondes dropped in and near the eyewalls of Guillermo (1997) and Erika (1997) were compared. The sondes provide accurate measurements of both flight level θ_e and surface pressure, however, a given sonde does not represent a vertical profile through the eyewall updraft due to cyclonic advection as it falls. Regardless, the sondes provide the best available ground truth. Figure (6.18) is the same as Figure (6.17) with the GPS sonde data added. Only sondes found in eyewall reflectivities $>$ 30 dBz are shown. The sondes appear to fall 1-5 K lower than the linear fit, but well within the scatter. Considering the large gradient of θ_e found near the eyewall

(see Figure 6.6), the use of radar imagery may have introduced a slight low θ_e bias since the maximum of reflectivity is typically 2-4 km outside the eyewall updraft (Jorgenson 1984a). The removal of such bias would improve the fit of the sonde data to the estimated data.

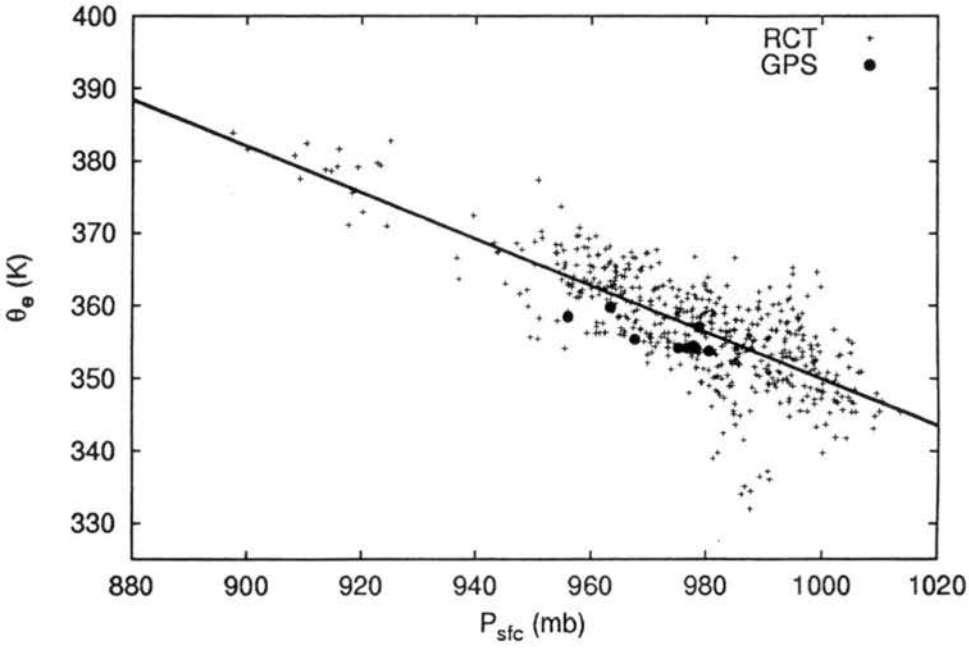

Figure 6.18: Same as Figure 6.16 except including data from GPS sondes dropped in the eyewalls of Hurricanes Erika (1997) and Guillermo (1997).

On average the ratio of eyewall surface pressure to minimum central pressure is 1.02±0.01. Utilizing this ratio, further independent validation of the linear fit and proposed methodology to estimate eyewall surface pressure can be made. Flight-level measurements were made at 190-200 mb in Typhoon Flo (1990), and observed values of θ_e in the eyewall were between 374 and 381 K[5] (Holland 1997). The minimum central pressure was determined to be 891 mb from a dropsonde in the eye. Using the ratio results in an eyewall surface pressure of 909 mb, and again the observed θ_e values are in agreement

[5]Thermodynamic observations at 200 mb are made in cold clouds with no super-cooled liquid water. Thus, as shown earlier in Chapter 5 instrument wetting effects are expected to be minimal and not degrade the measurements. The eyewall θ_e values given by Holland (1997) are considered accurate.

with the linear fit. This also provides further evidence of moist adiabatic ascent in the eyewall to the upper levels.

The assumed parameters appear to reasonably estimate eyewall surface pressure. Some of the scatter is due to the variability in the actual parameters, but such variability was shown to account for 10-15 mb at most. Given an eyewall θ_e of 360 K, surface pressures range from 950-1000 mb. Thus, another 35-40 mb of variability must be explained. The only parameter than can explain this much varaibility in θ_e is the boundary layer surface temperature.

6.4.4 Estimated eyewall air-sea temperature difference

Surface temperatures alone do not provide much information, but rather the temperature difference between the air and sea surface, or air-sea contrast (ASC) (SST -T_a), provides information about the fluxes of heat from ocean, and the thermodynamic modification experienced by inflowing air prior to arriving at the eyewall. Shown in Figure (6.19) is the ASC beneath the eyewall estimated from the control parameters for each radial leg as a function of the estimated surface pressure. The SST is the monthly climatological value, thus, placing an upper bound on inner-core SST that may be cooler due to storm-induced upwelling (Shay et al. 1989). Only radial legs with flight-level relative humidity $> 95\%$ are shown. Significant scatter exists among the ASC values as estimated air temperatures are up to 5°C cooler than the SST. The majority are > 1.0°C with an average ASC of 2.05 ± 1.10°C. It should be noted that if significant entrainment cooling occurred up to flight-level or the depth of the boundary layer was > 300 m, the ASC would decrease. Likewise, storm-induced upwelling of cooler waters would also decrease the ASC. Despite these possible errors in estimation of the air temperature and SST cooling, the average and maximum values compare well with the buoy observations from Cione et al. (1999), and further suggest the inflow is not isothermally maintained at an ASC of 1°C.

Finally, a general trend is apparent in Figure (6.19) that suggests the ASC beneath the eyewall is large in minimal hurricanes, while intense hurricanes have smaller ASC. Betts and Simpson (1987) argued that to achieve θ_e values of $\sim$375 K in the eyewall, the

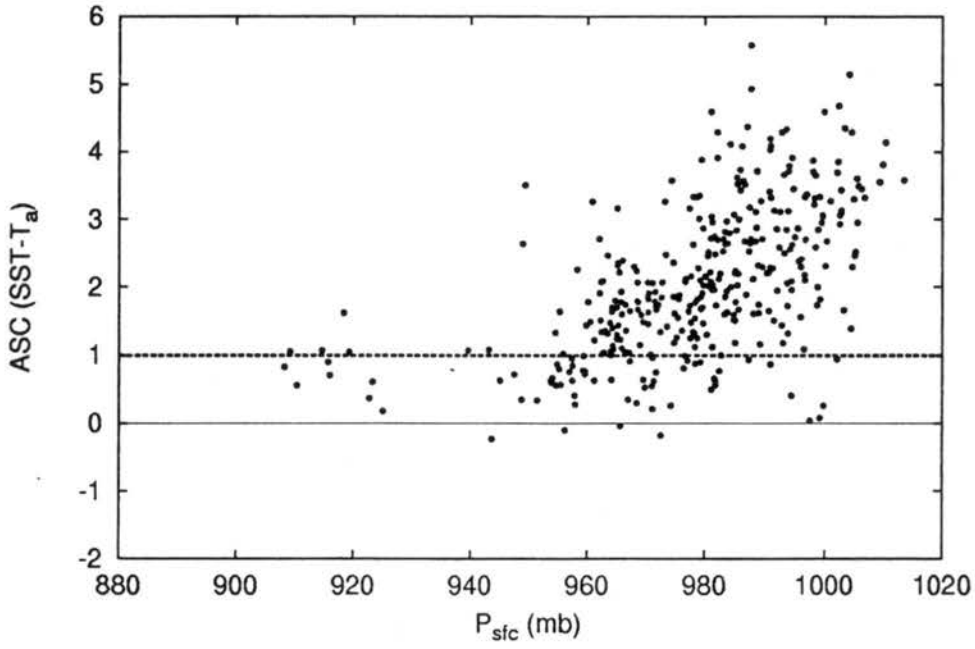

Figure 6.19: Scatter plot of the air-sea contrast (ASC), calculated from the estimated surface temperature using the control parameters and the climatological monthly SST, as a function of the estimated eyewall surface pressure. Only data with flight-level relative humidity > 95% at the eyewall RMU are shown.

boundary layer temperature must be nearly equivalent to the SST (i.e. an ASC < 1°C). The estimated ASCs for Hurricane Gilbert on September 13-14, 1988 when its eyewall surface pressures were less than 920 mb are roughly 1°C or less. Gilbert was near its climatological MPI at this time, and observed eyewall θ_e was 370-380 K. While data is sparse between 920-960 mb to solidify the presence of the apparent trend, the trend does suggest that the assumption of ASC $\leq$ 1°C in conceptual models used to estimate MPI (Emanuel 1991; Holland 1997) is not unrealistic. Large positive ASC at the eyewall in minimal hurricanes may be the result of cool, dry convective downdrafts outside the eyewall lowering the boundary layer θ_e beyond recovery (Powell 1990; Cione et al. 1999), and thus preventing some hurricanes from attaining their MPI. Previous studies of hurricane rainbands and tropical squall lines have shown that cool, dry convective downdrafts are the result of evaporation induced by entraining dry air into the convection. The composite relative humidity (Figure 6.5) indicates that the air outside the eyewall is more moist in intense hurricanes than in minimal hurricanes. Therefore, downdrafts penetrating into

the boundary layer in intense hurricanes will likely be warmer and more moist on average than in minimal hurricanes, and thus, maintaining a lower boundary layer ASC.

6.5 Summary

A preliminary re-examination of hurricane thermodynamic structure after instrument wetting errors were removed from the data revealed that the composite radial structure differed little from previous compositing and case studies. The most significant observational differences were elevated thermodynamic quantities in the eyewall. Such differences resulted in: weaker temperature and θ_e gradients across the eyewall RMU, but larger gradients just outside; eyewall temperature anomalies equivalent to 50-70% of the total anomaly from the environment observed in the eye; radial maxima of specific humidity are in the eyewall but values in the eye are greater than or equal to values outside the eyewall; and eyewall θ_e 0-5 K lower than values in the eye. Average eyewall θ_e is 351 K and 360 K in minimal and intense hurricanes, respectively with maximum observed values near 385 K. Considering the limitations and variability in the flight-level radial composites the eyewall was found to moist-adiabatic with height to a *first approximation.* However, slight differences from this approximation could lead to significant eyewall vertical accelerations. Instrument wetting errors are also shown to produce significant thermal wind imbalances, but when removed approximate balance was found for two hurricanes.

Finally, using the observation that the eyewall is moist-adiabatic to a first approximation, surface pressures and temperatures were estimated beneath the eyewall from flight-level. Values of boundary layer depth and eyewall slope were also assumed, but supported by observations, and the eyewall slope was hyrdostatically accounted for. The ratio of eyewall surface pressure to minimum central pressure was 1.02 ± 0.01 on average. A linear relationship between flight-level θ_e and estimated eyewall surface pressure is determined from the reconstructed data and independently supported by direct observations from GPS sondes. The estimated average ASC beneath nearly-saturated eyewalls was 2°C with maximum values near 5°C and tended to decrease with eyewall surface pressure.

6.6 Synopsis

- Removal of instrument wetting errors significantly raised composited thermodynamic quantities in and near the eyewall.
- Maximum radial temperature and θ_e gradients are located just outside the eyewall.
- Temperature anomalies from the environment are equivalent to 50-70% of the total anomaly observed in the eye.
- Radial specific humidity maxima are located in the eyewall. However, the specific humidity in the eye is greater than or equal to values outside the eyewall, and less than 1 g kg^{-1} lower than the maxima in the eyewall.
- Average eyewall θ_e is 351 K and 360 K in minimal and intense hurricanes respectively, but is 0-5 K lower than values in the eye. Maximum observed eyewall θ_e are near 385 K.
- Instrument wetting errors can produce significant thermal wind *imbalances.*
- The composite eyewall is moist-adiabatic with height to a *first approximation*, allowing surface pressures and temperatures to be estimated beneath the eyewall.
- The average ratio of estimated eyewall surface pressure to minimum central pressure was 1.02±0.01.
- The estimated average air-sea temperature contrast (ASC) (SST-T_a) beneath nearly-saturated eyewalls was 2°C with maximum values near 5°C, and the ASC tended to decrease with eyewall surface pressure.

Chapter 7

CONCLUSIONS

7.1 Summary and Discussion

Observations in hurricanes of thermodynamic quantities in regions of clouds and precipitation have historically been questioned due to possible errors caused by the wetting of immersion thermometers. Thermodynamic budget and mesoscale structure analysis in hurricanes rely heavily on accurate thermodynamic measurements, however, the net effect of such wetting errors is to underestimate thermodynamic quantities in clouds and precipitation. This study removed instrument wetting errors from a flight-level database, examined the frequency, magnitude, and location of instrument wetting errors in hurricanes, and then re-examined various aspects of hurricane inner-core thermodynamics.

In order to complete this study data from a radiometric thermometer was used to provide an independent and accurate temperature measurement from the standard Rosemount immersion thermometer. Theory and observations suggest that radiometric temperature errors due to the presence of hydrometeors will be less than 0.1°C, except in subsaturated regions with high liquid water contents. In contrast, theoretical errors due to wetting of the Rosemount immersion thermometer are typically an order of magnitude larger and can be as large as 7°C in warm clouds and 10°C in cold clouds. A temperature correction method was developed to remove a time-dependent bias from the radiometric temperatures. Following previous methods, the bias is removed assuming the Rosemount temperatures are accurate in clear air. However, in contrast to previous methods and in order to retain as much data as possible, clear air was defined not by the absence of liquid water but rather by dew point depression and aircraft roll. The new definition of clear air was tested and resulted in statistically similar temperature profiles compared to

when clear air is defined by the absence of liquid water. The reconstruction method also corrected supersaturated dew points to 99 percent relative humidity, adjusted the resulting temperatures and dew points to an isobaric level, and fit the data to a storm-relative grid. The application of the method to a hurricane database resulted in the accurate removal of instrument wetting errors from nearly 600 thermodynamic radial profiles from 27 hurricanes.

The subsequent examination of the thermodynamic radial profiles showed that instrument wetting temperature errors frequently occurred during penetrations of hurricane clouds and precipitation. A weak linear relationship was found between the magnitude of the temperature error and the liquid water content of cloud drops, and the correlation only increased slightly when raindrops were included. The lack of drop size spectra, concentrations, and a significant amount of raindrop data prevented definitive conclusions of relationships between wetting errors and the microphysical properties of the clouds and precipitation encountered. However, since instrument wetting temperature errors can arise from drops of any size impinging on either the sensing element, the inner housing surface, or some combination of the two, each case of instrument wetting is apt to be unique from the next, and may not be well correlated with microphysical properties. In any case, the fact remains that instrument wetting is producing temperature errors during penetrations of clouds and precipitation in hurricanes.

In order to identify regions of significant instrument wetting an Instrument Wetting Location (IWL) was defined. Despite a strict definition, roughly one half of the total radial legs contained at least one IWL. The number of identified IWL was variable from hurricane to hurricane. However, IWL were more frequent in intense hurricanes than in minimal hurricanes, and were comprised of larger temperature errors. The majority of IWL were located in either eyewall or rainband updrafts and extended < 15 km radially with maximum temperature errors $< 5.0°$C. Theoretical error magnitudes were rarely achieved. Pressure level composites of all IWL with respect to their Radius of Maximum Temperature Error (RMTE) resulted in statistically significant temperature errors ranging

from 1.2 to 4.5°C between 850 and 500 mb and specific humidity errors ranging from 1.2 to 1.8 g kg^{-1}. Such average errors can result in T_v and θ_e errors of 1.5 to 4.5°C and 5.0 to 11.0 K, respectively, that can lead to a gross over-estimation of entrainment cooling and an under-estimation of parcel buoyancy in convective and mesoscale studies.

Over 70 percent of IWL are found in and near the eyewall. Composites with respect to the eyewall RMU of *all* radial legs, irrespective of whether an IWL was found in the eyewall, indicate that statistically significant average temperature errors in the eyewall range from 0.5 to 1.8°C, resulting in T_v and θ_e errors of 0.5 to 2.0°C and 2.0 to 5.0 K respectively. While errors of these magnitude may not have a significant effect on the general large-scale thermodynamic structure of hurricanes, such errors can impact the structure and our conceptual understanding of the convective and mesoscale forcing in the eyewall along with the associated interactions with its local environment by severely affecting calculations of entrainment, buoyancy, and thermodynamic budgets. Errors in T_v of 0.5 - 2.0°C are comparable to the magnitude of cloud buoyancy. Likewise, instrument wetting erroneously lowers eyewall temperatures toward values found radially outside the eyewall. Thus, earlier eyewall studies using data containing wetting errors may have underestimated values of eyewall buoyancy and lateral entrainment from the eye while overestimating entrainment from radially outside the eyewall. These quantities are crucial to conceptual understanding of the hurricane's secondary circulation and the resulting feedbacks to the primary circulation.

The frequency of instrument wetting errors during eyewall passage is very important in composite studies. If only radial legs containing an IWL at the eyewall were similarly composited, average thermodynamic errors would double, resulting in T_v and θ_e errors of 1.0 to 4.0°C and 4.0 to 10.0 K respectively. Futhermore, some temperature errors may approach their theoretical values of 5.0 to 10.0°C, which would produce T_v errors of 6.0-11.0°C and θ_e of 12.0-24.0 K in a convective region! In contrast, if radial legs *without* an IWL were composited a statistically significant temperature error of 0.2 to 0.4°C still exists, and emphasizes not only the strict definition of an IWL used in this study, but

also the frequency of instrument wetting errors during eyewall penetrations. Therefore, instrument wetting errors occur (and likely occurred in the past) during the majority of eyewall passages and may have had lead to erroneous conclusions in regards to eyewall thermodynamics.

An evaluation of the temperature correction method proposed by Zipser et al. (1981) indicates that when applied to the data over 70 percent of instrument wetting errors are ineffectively removed. In some cases the method over-adjusts the temperature by more than 0.5°C, while in contrast, errors as large as 4.0°C were found to still exist. Composites with a large data sample indicate that average thermodynamic errors are reduced by half after the method is applied, however, the resulting errors are still positive and statistically significant. Thus, case studies of mesoscale or convective scale thermodynamic features in a single hurricane may still contain instrument wetting errors even after the temperature correction method proposed by Zipser et al. (1981) is applied to the immersion thermometer data, leading to incorrect conclusions.

Various aspects of hurricane inner-core thermodynamic structure were re-examined without concern for instrument wetting errors. As expected, the removal of the errors significantly raised composited thermodynamic quantities in and near the eyewall. Composites with respect to the eyewall RMU of radial legs from hurricanes with similar intensities indicated that the eyewall temperature anomalies from the environment are equivalent to 50-70% of the total anomaly observed in the eye and the maximum radial temperature and θ_e gradients are located just outside the eyewall. Eyewall composite θ_e is 0-5 K lower than values in the eye, but up to 10 K higher than values similar distances outside the eye. Finally, radial specific humidity maxima are located in the eyewall, however, the specific humidity in the eye is typically less than 1 g kg^{-1} lower than the eyewall maxima and greater than or equal to values outside the eyewall.

These observations, particularily the latter, are important toward understanding typical interactions between the eye and the eyewall. A number of studies have argued that turbulent mixing on the inner edge on the eyewall is required to force the necessary eye

subsidence while maintaining the heat, moisture, and momentum budgets of the subsiding air (Malkus 1958; Kuo 1959; Gray 1999), and to amplify the entropy in the eye such that realistic intensification rates are achieved (Emanuel 1997). Schubert et al. (1999) argues that asymmetric mixing between the eye and the eyewall can theoretically occur due to barotropic instabilities that form along annular rings of elevated vorticity associated with the eyewall. Recently, Kossin and Eastin (1999) presented observational evidence, using flight-level data between 850-500 mb, that elevated vorticity is commonly found in the eyewall during intensification periods and that turbulent vorticity exchange between the eye and eyewall typically occurs. Since specific humidity is essentially a tracer during advective processes in the absence of phase changes, the observed small differences in average specific humidity between the eye and the eyewall supports such substantial mixing between the two[1].

The composite eyewall was found to be moist-adiabatic with height to a *first approximation*, averaging 351 K and 360 K in minimal and intense hurricanes respectively with maximum values near 385 K. The eyewall is best represented by pseudo-adiabatic ascent rather than reversible ascent. This is not to say that the eyewall is always moist-adiabatic with no CAPE. In fact, substantial observational evidence suggests that buoyant convection occurs in the eyewall. The presence of eyewall vertical velocities on the order of 10-20 $m\,s^{-1}$, the convergence of air into the eyewall above the friction layer (Figure B.9), and the increase of the vertical velocity and mass flux with height (Figure B.4) suggest that buoyant parcels exist in the eyewall and act to radially entrain mid-level air into the updraft to maintain the hurricane circulation. Furthermore, considering the strong evidence for

---

[1]Willoughby (1998) argues that the hurricane eye consists of two distinct volumes of air separated by an inversion typically near 850-700 mb. The air above the inversion is described as a closed volume in dynamic and thermodynamic isolation while the air below freely interacts with the eyewall during a hurricanes lifetime. The air above the inversion experiences only weak subsidence (less than 100 mb) in its lowest layers due to eyewall contractions during the hurricane's lifetime. The observed small differences in average specific humidity between the eye and the eyewall at lower levels also supports this theory. However, results by Kossin and Eastin (1999) indicate that turbulent mixing between the eyewall and the eye is observed to occur throughout the 850-500 mb layer, suggesting the air above the inversion is neither in dynamic nor thermodynamic isolation from the eyewall.

mixing between the eyewall and the eye (Kossin and Eastin 1999) and average θ_e higher in the eye than the eyewall, the mixing may provide a source of buoyancy by advecting higher θ_e air into the eyewall destabilizing the local lapse rate. Thus, it seems plausible that significantly buoyant parcels exist asymmetrically in the eyewall and are embedded in the general slantwise vertical velocities forced by frictional inflow and thermal wind balance, however, their importance to the hurricane's life-cycle remains unclear.

Instrument wetting errors were shown to produce significant thermal wind imbalances in two hurricanes, however, removal of the errors reduced the imbalances by half, and thus suggesting the storms was closer to a state of balance. Hawkins and Rubsam (1968) showed Hurricane Hilda (1964) was near thermal wind balance. Jorgenson (1984b) noted that Hurricane Allen (1980) was also near a state of thermal wind balance over a similar time period despite possible instrument-wetting errors. Gray (1967) and Gray and Shea (1973) noted large thermal wind imbalances existed in the inner-core over a period of a few hours. It is important to note that the present evaluation does not resolve the debate over thermal wind balance in hurricanes, but rather indicates that large imbalances may be a result of instrument errors. However, it seems plausible that a steady-state storm will be near thermal wind balance over the course of several hours, and this is consistent with the scaling arguments of Shapiro and Willoughby (1982). On the other hand, sporadic pulses of asymmetric convection that are commonly observed in hurricanes (Zehr 1992) and precede intensification (Black et al. 1986) can temporarily produce large thermal wind imbalances. Therefore, a given hurricane is will typically cycle through periods of balance and imbalance during its lifetime, and thus, the previously observed states of thermal wind balance may be a function of the extent and strength of the asymmetric convection that produced the imbalance, and when the storm is observed.

Surface pressures and temperatures were estimated beneath the eyewall, assuming the eyewall was saturated and moist-adiabatic from flight-level to cloud base with a well-mixed boundary layer below, and an assumed eyewall slope was hydrostatically accounted for. As expected, estimated eyewall surface pressures decrease as observed flight-level θ_e increase,

and direct observations by GPS sondes deployed in eyewalls independently suggest the relationship is valid. The ratio of estimated eyewall surface pressure to minimum central pressure was 1.02±0.01 on average. The estimated average Air-Sea temperature Contrast (ASC) beneath nearly-saturated eyewalls was 2°C with maximum values near 5°C. This supports the results found by Cione et al. (1999) in the hurricane boundary layer.

Furthermore, the average estimated ASC tended to *decrease* with *decreasing* eyewall surface pressure (i.e. *increasing* wind speed). In contrast, Korolev et al. (1990) and Pudov (1992) suggest that ASC *increases* with with *increasing* wind speed. Cione et al. (1999) found only a weak positive correlation between ASC and wind speed, and thus argues that the large observed ASC's are a result of unsaturated convective downdrafts transporting cool, dry air into the boundary layer. Previous studies of hurricane rainbands and tropical squall lines have shown that unsaturated convective downdrafts are the result of evaporation induced by entraining dry air into the convection. The composite relative humidity (Figure 6.5) indicates that the air outside the eyewall is more moist in intense hurricanes than in minimal hurricanes. Therefore, less evaporative cooling can occur on average during entrainment in intense hurricanes than in minimal hurricanes, and thus, the downdrafts penetrating into the boundary layer in intense hurricanes will likely be warmer and more moist on average, allowing for the maintainence of a lower boundary layer ASC. Thus, the decrease of eyewall ASC with decreasing eyewall surface pressure supports the argument by Cione et al. (1999) and further questions a positive correlation between ASC and wind speed. Finally, the trend may suggest that the assumption of ASC ≤ 1°C in conceptual models used to estimate the Maximum Potential Intensity (MPI) of hurricanes is not unrealistic. Numerous direct observations of pressure and temperature beneath hurricane eyewalls are needed to confirm these ASC conclusions.

7.2 Future work

The results from this study suggest that instrument wetting errors can produce the largest errors over convective and mesoscale spatial scales. Previously, the determination of thermodynamic structure over such scales was severely hindered due to instrument

wetting errors. An in-depth statistical and conceptual investigation of convective and mesoscale thermodynamic structure is needed. Therefore, numerous opportunities for future work arise and research topics that are being, or should be, undertaken include:

- Investigate the magnitude and scale of buoyancy in eyewall and rainband convection. Buoyancy derived from classic parcel theory and moist symmetric instability of slantwise convection should be examined for both updrafts and downdrafts. The determination of buoyancy in hurricanes has historically been difficult due to the determination of water-loading and the difficulty in defining an environment for parcels embedded in a large radial temperature gradient. These topics should also be addressed.

- Determination of lateral mass entrainment and moisture flux between the eye, the eyewall, and the environment.

- Determination of vorticity and potential vorticity generation in the eyewall and rainbands. Buoyant eyewall parcels may act to enhance the vertical gradient of vertical velocity and thus increase the potential vorticity generation via stretching. Recent work by Montgomery and Enagonio (1998) has shown that vortex intensification can occur from the axisymmetrization of potential vorticity anomalies.

- Determine the magnitude and sign of the vertical eddy fluxes at or near the top of the boundary layer. Previous studies (e.g. Frank 1984) have estimated from observations that may have contained wetting errors that a net downward flux of temperature occurs. However, typical instrument wetting errors in an updraft results can erroneously result in large downward flux.

- Examine each of the proposed research topics above prior to and during various periods of intensity change.

- Determination of thermodynamic structures associated with concentric eyewall cycles that are commonly observed to occur in intense hurricanes (e.g. Black and Willoughby 1992).

- Continuously expand the database as more SR temperature data is collected and becomes available. The temperature correction method can also be applied to the original 1-s flight-level data to permit more accurate determination of convective and mesoscale thermodynamic structure.

It is essential that the research proposed above be conducted. The basic physical and conceptual understanding of hurricane structure and intensity change depend upon the magnitude, sign, and frequency of buoyancy, lateral entrainment, and vertical heat fluxes. Each results in feedbacks to the primary circulation, and in some cases may help induce rapid changes in the primary circulation. With the present lack of skill in intensity change forecasting (Elsberry et al. 1992), knowledge of such quantities may help to improve not only our conceptual understanding of hurricanes, but also aid in the prediction of intensity changes.

Acknowledgements

I wish to thank the P-3 flight crews from NOAA's Aircraft Operations Center (AOC) and HRD for their dedicated and tireless efforts over the past two decades to collect the copious amounts of flight-level data used in this study. I am indebted to Dr. Hugh Willoughby and the staff at HRD for making the flight-level database to me and for partially supporting travel and lodging during visits to the lab each of the past two summers. My time was well spent as I had many fruitful discussions about this research and hurricanes in general during my visits. I am especially grateful to Dr. Peter Black (HRD) for suggesting this research as a "good 2-week project" during my first visit to HRD and his continual support throughout its completion. I am indebted to Dr. Robert Black (HRD) for providing me the processed PMS data, to Mr. Richard McNamara (AOC) for many helpful discussions regarding the P-3 instrumentation, Mr. Ed Rahn (HRD) and Mr. Chris Samsury for answering numerous questions about the processed flight-level data, to Dr. Joe Cione (HRD) for many insightful discussions about the hurricane boundary layer, and to the combined efforts of Dr. Frank Marks Jr., Mr. Michael Black, Mr. Steven Feuer, and Mr. James Franklin (all of HRD) for providing me the GPS sonde data.

I will always be grateful to my advisor William M. Gray for his leadership, guidance, and support throughout the completion of this work. I wish to thank my committee members Professors Wayne Schubert and Bob Meroney for providing helpful comments toward the completion of this work. Additional insightful discussions were held with Dr. Michael Montgomery, James Kossin (who also provided me with the original code to produce the radial composites), John Knaff, Ray Zehr, and Todd Kimberlain. Valuable computer assistance was provided by Bill Thorson, Rick Taft, Barbara Brumit, and Amie Hedstrom.

This research was supported by the National Science Foundation Grant No. ATM-9616818 with additional support from the NOAA/CIRA GOES I-M Product Assurance Plan Grant No. NA67RJ0152.

REFERENCES

Albrecht, B. A., S. K. Cox, and W. H. Schubert, 1979: Radiometric measurements of in-cloud temperature fluctuations. *J. Appl. Meteor.*, 18, 1066-1071.

Astheimer, R. W., 1967: Air absorption length for specific CO_2 band filter. Barnes Engineering Memorandum, May 1967.

Axford, D. N., 1968: On the accuracy of wind measurements using an inertial platform in an aircraft, and an example of a measurement of the vertical mesostructure of the atmosphere. *J. Appl. Meteor.*, 7, 645-666.

Barnes, G. M., E. J. Zipser, D. Jorgenson, and F. Marks Jr., 1983: Mesoscale and convective structure of a hurricane rainband. *J. Atmos. Sci.*, 40, 2127-2137.

Barnes, G. M., and G. J. Stossmeister, 1986: The structure and decay of a rainband in Hurricane Irene (1981). *Mon. Wea. Rev.*, 114, 2590-2601.

Barnes, G. M., J. F. Gamache, M. A. LeMone, and G. J. Stossmeister, 1991: A convective cell in a hurricane rainband. *Mon. Wea. Rev.*, 119, 776-794.

Barnes, G. M., and M. D. Powell, 1995: Evolution of the inflow boundary layer of Hurricane Gilbert (1988). *Mon. Wea. Rev.*, 123, 2348-2368.

Beard, K. V., 1976: Terminal velocity and shape of cloud and precipitation drops aloft. *J. Atmos. Sci.*, 33, 851-864.

Bedingfield, C. H., and T. B. Drew, 1950: Analogy between heat transfer and mass transfer - A psychometric study. *Ind. Eng. Chem.*, 42, 1164-1173.

Bender, M. A., 1997: The effect of relative flow on the asymmetric structure in the interior of hurricanes. *J. Atmos. Sci.*, 54, 2076-2087.

Betts, A. K., and J. S. Simpson, 1987: Thermodynamic budget diagrams for the hurricane subcloud layer. *J. Atmos. Sci.*, 44, 842-849.

Black, M. L., 1993: Comparisons of tropical cyclone intensity with eyewall vertical velocities. Preprints, *20nd Conf. on Hurricanes and Tropical Meteorology*, San Antonio, TX, Amer. Meteor. Soc., 520-523.

Black, M. L., and H. E. Willoughby, 1992: The concentric eyewall cycle of Hurricane Gilbert. *Mon. Wea. Rev.*, 120, 947-957.

Black M. L., R. W. Burpee, and F. D. Marks Jr., 1996: Vertical motion characteristics of tropical cyclones determined with airborne Doppler radial velocities. *J. Atmos. Sci.*, 53, 1887-1909.

Black P. G., F. D. Marks Jr., and R. A. Black, 1986: Supercell structure in tropical cyclones. Preprints, *23nd Conf. on Radar Meteorology*, Snowmass, CO, Amer. Meteor. Soc., JP255-259.

Black, R. A., 1990: Radar reflectivity-ice water content relationships for use above the melting level in hurricanes. *J. Appl. Meteor.*, 29, 955-961.

Black, R. A., and J. Hallett, 1986: Observations of the distribution of ice in hurricanes. *J. Atmos. Sci.*, 43, 802-822.

Black, R. A., H. B. Bluestein, and M. L. Black, 1994: Unusually strong vertical motions in a Caribbean hurricane. *Mon. Wea. Rev.*, 122, 2722-2739.

Blyth, A. M., W. A. Cooper, and J. B. Jensen, 1988: A study of the source of entrained air in Montana cumuli. *J. Atmos. Sci.*, 45, 3944-3964.

Bolton, D., 1980: The computation of equivalent potential temperature. *Mon. Wea. Rev.*, 108, 1046-1053.

Byers, H. R., and R. R. Braham, 1949: The Thunderstorm. U.S. Govt. Printing Office, 287 pp.

Case, R. A., and H. P. Garrish, 1988: Annual summary Atlantic hurricane season of 1987. *Mon. Wea. Rev.*, 116, 939-949.

Cecil, D. J., and E. J. Zipser, 1999: Relationships between tropical cyclone intensity and satellite-based indicators of inner core convection: 85-GHz ice-scattering signature and lightning. *Mon. Wea. Rev.*, 127, 103-123.

Cione, J. J., P. G. Black, and S. H. Houston 1999: Surface Observations with in the hurricane environment. *Mon. Wea. Rev.*, (Submitted).

Colon, J. A., 1964: On the structure of Hurricane Helene (1958). National Hurricane Research Project Report No. 72, U.S. Weather Bureau, 56 pp.

DeMaria, M., 1996: The effect of vertical shear on tropical cyclone intensity change. *J. Atmos. Sci.*, 53, 2076-2087.

Ebert, E. E., and G. J. Holland, 1992: Observations of record deep convection in Tropical Cyclone Hilda. *Mon. Wea. Rev.*, 120, 2240-2251.

Elsberry, R. L., G. J. Holland, H. Garrish, M. DeMaria, and C. P. Gaurd, 1992: Is there any hope for tropical cyclone intensity change prediction?–A panel discussion. *Bull. Amer. Meteor. Soc.*, 73, 264-275.

Emanuel, K. A., 1986: An air-sea interaction theory for tropical cyclones. Part I: Steady-state maintenance. *J. Atmos. Sci.*, 43, 585-604.

Emanuel, K. A., 1988: The maximum intensity of hurricanes. *J. Atmos. Sci.*, 45, 1143-1155.

Emanuel, K. A., 1991: The theory of hurricanes. *Annu. Rev. Fluid Mech.*, 23, 179-196.

Emanuel, K. A., 1994: *Atmospheric Convection*, Oxford.

Emanuel, K. A., 1997: Some aspects of hurricane inner-core dynamics and energetics. *J. Atmos. Sci.*, 54, 1014–1026.

Fairell C. W., J. D. Kepert, and G. J. Holland, 1995: The effect of sea spray on surface energy transports over the ocean. *Atmosphere Ocean System*, 2, 121-142.

Frank, W. M., 1977: The storm structure and energetics of the tropical cyclone: I. Storm Structure. *Mon. Wea. Rev.*, 105, 1119-1135.

Frank, W. M., 1984: A composite analysis of the core of a mature hurricane. *Mon. Wea. Rev.*, 112, 2401-2420.

Gamache, J. F., R. A. Houze, and F. D. Marks Jr., 1993: Dual-aircraft investigation of Hurricane Norbert Part III: Water Budget. *J. Atmos. Sci.*, 50, 3221-3243.

General Eastern Instruments, 1987: Model 1011B dew point hygrometer for aircraft preliminary operating manual. Doc. 40076135A. Available from Buck Research, Boulder, CO.

Gray, W. M., 1965: Calculations of cumulus draft velocities in hurricanes from aircraft data. *J. Appl. Meteor.*, 4, 463-474.

Gray, W. M., 1967: The mutual variation of wind shear, and baroclinicity in the cumulus convective atmosphere of the hurricane. *Mon. Wea. Rev.*, 95, 55-73.

Gray, W. M., and D. J. Shea, 1973: The hurricane's inner core region: II. Thermal stability and dynamic characteristics. *J. Atmos. Sci.*, 30, 1565-1576.

Gray, W. M., 1997: The tropical cyclones Maximum Potential Intensity (MPI). Preprints, *22nd Conf. on Hurricanes and Tropical Meteorology*, Fort Collins, CO, Amer. Meteor. Soc., 288-289.

Gray, W. M., 1999: *Tropical Cyclones*, World Meteorological Organization, in preparation.

Hawkins, H. F., and D. T. Rubsam, 1968: Hurricane Hilda, 1964 II. Structure and budgets of the hurricane on October 1, 1964. *Mon. Wea. Rev.*, 96, 617-636.

Hawkins, H. F., and S. M. Imbembo, 1976: The structure of a small, intense hurricane - Inez, 1966. *Mon. Wea. Rev.*, 104, 418-442.

Heymsfeild, A. J., J. E. Dye, and C. J. Biter, 1979: Overestimates of entrainment from wetting of aircraft temperature sensors in cloud. *J. Appl. Meteor.*, 18, 92-94.

Hilleary, D. T., and F. E. Christensen, 1957: Instrumentation of National Hurricane Research Project aircraft. National Hurricane Research Project Report No. 11, U.S. Weather Bureau, 71 pp.

Hock, T. F., and J. L. Franklin, 1999: The NCAR GPS dropwindsonde. *Bull. Amer. Meteor. Soc.*, 80, 407-420.

Holland, G. J., 1987: Mature structure and structure change. *A Global View of tropical Cyclones*, R.L. Elsberry, ed., Office of Naval Research., Monterey, pp. 13-52.

Holland, G. J., 1997: The maximum potential intensity of tropical cyclones. *J. Atmos. Sci.*, 54, 2519-2541.

Holliday, C. R., and A. H. Thompson, 1979: Climatological characteristics of rapidly intensifying typhoons. *Mon. Wea. Rev.*, 107, 1022-1034.

Houze, R. A., F. D. Marks Jr., and R. A. Black, 1992: Dual-aircraft investigation of the inner core of Hurricane Norbert. Part II: Mesoscale distribution of ice particles. *J. Atmos. Sci.*, 49, 943-962.

Irvine, W. M., and J. B. Pollack, 1968: Infrared optical properties of water and ice spheres. *Icarus*, 8, 324-360.

Jones, S. C., 1995: The evolution of vortices in vertical shear. Part II: Initially barotropic vortices. *Quart. J. Roy. Meteor. Soc.*, 121, 821-851.

Jordan, C. L., 1952: On the low-level structure of the typhoon eye. *J. Meteor.*, 9, 285-290.

Jordan, C. L., 1958a: The thermal structure of the core of tropical cyclones. *Geophysica*, 6, 281-297.

Jordan, C. L., 1958b: Mean soundings for the West Indies area. *J. Meteor.*, 15, 91-97.

Jorgensen, D. P., 1984a: Mesoscale and convective-scale characteristics of mature hurricanes. Part I: General observations by aircraft. *J. Atmos. Sci.*, 41, 1268-1285.

Jorgensen, D. P., 1984b: Mesoscale and convective-scale characteristics of mature hurricanes. Part II: Inner core structure of Hurricane Allen (1980). *J. Atmos. Sci.*, 41, 1287-1311.

Jorgensen, D. P., E. J. Zipser, and M. A. LeMone, 1985: Vertical motions in intense hurricanes. *J. Atmos. Sci.*, 42, 839-856.

Jorgenson, D. P., and M. A. LeMone, 1989: Vertical velocity characteristics of oceanic convection. *J. Atmos. Sci.*, 46, 621-640.

Kinzer G. D., and R. Gunn, 1951: Evaporation, temperature, and thermal relaxation time of freely falling waterdrops. *J. Meteor.*, 8, 71-83.

Korolev, V. S. , S. A. Petrichenko, and V. D. Pudov, 1990: Heat and moisture exchange between the ocean and atmosphere in Tropical Storms Tess and Skip. *Soviet Meteor. Hydrol.*, 3, 92-94 (English translation).

Kossin, J. P., and M. D. Eastin, 1999: Observational evidence for turbulent exchange between the hurricane eye and eyewall. *J. Atmos. Sci.*, (Submitted).

Knollenberg, R. G., 1972: Comparative liquid water content measurements of conventional instruments and an optical array spectrometer. *J. Appl. Meteor.*, 11, 501-508.

Kuo, H.-L., 1959: Dynamics of convective vortices and eye formation. *The Atmosphere and Sea in Motion*, B. Bolin, Ed., Rockefeller Institute Press, 413-424.

Landsea, C. W., 1993: A climatology of intense (or major) Atlantic hurricanes. *Mon. Wea. Rev.*, 121, 1703-1713.

LaSeur, N. E., and H. F. Hawkins, 1963: An analysis of Hurricane Cleo (1958) based on data from research reconnaissance aircraft. *Mon. Wea. Rev.*, 91, 694-709.

Lawson, R. P., 1988: The measurement of temperature from an aircraft in cloud. Ph.D. dissertation. University of Wyoming, Laramie, Wyoming, 336 pp.

Lawson, R. P., and W. A. Cooper, 1990: Performance of some airborne thermometers in clouds. *J. Atmos. Oceanic Technol.*, 7, 480-494.

LeMone, M. A., 1980: On the difficulty of measuring temperature and humidity in clouds: Comments on "Shallow convection on Day 261 of GATE: Mesoscale arcs." *Mon. Wea. Rev.*, 108, 1702-1707.

Lenschow, D. H., and W. T. Pennell, 1974: On the measurement of in-cloud and wet-bulb temperatures from an aircraft. *Mon. Wea. Rev.*, 102, 447-454.

Liu, Y., D. Zhang, and M. K. Yau, 1997: A multiscale numerical study of Hurricane Andrew (1992). Part I: Explicit simulation and verification. *Mon. Wea. Rev.*, 125, 3073-3093.

Lord, S. J., H. E. Willoughby, and J. M. Piotrowicz, 1984: Role of parameterized ice-phase microphysics in an axisymmetric non-hydrostatic tropical cyclone model. *J. Atmos. Sci.*, 41, 2836-2848.

Lucas, C., E. J. Zipser, and M. A. LeMone, 1994: Vertical velocity in oceanic convection off tropical Australia. *J. Atmos. Sci.*, 51, 3183-3193.

Malkus, J. S., 1954: Some results of trade-cumulus cloud investigation. *J. Meteor.*, 11, 220-237.

Malkus, J. S., 1958: On the the structure and maintenance of the mature hurricane eye. *J. Meteor.*, 15, 337-349.

Malkus, J., and H. Riehl, 1960: On the dynamics and energy transformations in steady-state hurricanes. *Tellus*, 12, 1-20.

Marks, F. D. Jr., 1985: Evolution and structure of precipitation in Hurricane Allen (1980). *Mon. Wea. Rev.*, 113, 909-930.

Marks, F. D. Jr., and R. A. Houze Jr., 1987: Inner core structure of Hurricane Alicia from airborne Doppler radar observations. *J. Atmos. Sci.*, 44, 1296-1317.

Merceret, F. J., and H. W. Davis, 1981: The determination of navigational and meteorological variables measured by NOAA/RFC WP3D aircraft. NOAA Tech. Memo., ERL RFC-7, AOML, 4301 Rickenbacker Cswy., Miami, FL 33149, 47 pp.

Miller, B. I., 1958: On the maximum intensity of hurricanes. *J. Meteor.*, 15, 184-195.

Molinari, J., P. Moore, and V. Idone, 1999: Convective structure of hurricanes as revealed by lightning location. *Mon. Wea. Rev.*, 127, 520-534.

Montgomery, M. T., and J. Enagonio, 1998: Tropical cyclogenesis via convectively forced vortex Rossby waves in a three-dimensional quasigeostrophic model. *J. Atmos. Sci.*, 55, 3176–3207.

Neumann, C. J., B. R. Jarvinen, C. J. McAdie, and J. D. Elms, 1993: Tropical cyclones of the North Atlantic Ocean, 1871 - 1992. Fourth Revison. Nat. Cli. Data Center in cooperation with the Nat. Hur. Center, Coral Gables, FL, 193 pp.

Ooyama, K., 1969: Numerical simulation of the life cycle of tropical cyclones. *J. Atmos. Sci.*, 26, 3-39.

Ooyama, K. V., 1982: Conceptual evolution of the theory and modeling of the tropical cyclone. *J. Meteor. Soc. Japan*, **60**, 369-380.

Politovich, M. K., and W. A. Cooper, 1988: Variability of supersaturations in cumulus clouds. *J. Atmos. Sci.*, 45, 1651-1664.

Pruppacher, H. R., and J. D. Klett, 1997: *Microphysics of Clouds and Precipitation.* Kluwer Academic Publishers, 954 pp.

Powell, M. D., 1990: Boundary layer structure and dynamics in outer hurricane rainbands. Part II. Downdraft modification and mixed layer recovery. *Mon. Wea. Rev.*, 118, 918-938.

Powell, M. D., P. G. Black, S. H. Houston, and T. A. Reinhold, 1999: GPS sonde insights on boundary layer structure in hurricanes. Preprints, *23nd Conf. on Hurricanes and Tropical Meteorology*, Dallas, TX, Amer. Meteor. Soc., 881-884.

Pudov, V. D., 1992: The ocean response to the cyclones influence and its possible role in track formations. *ICSU/WMO International Symposium on Tropical Cyclone Disasters*, 367-376

Pyranometer Instrument Company Inc., 1980: Model PRT-5 precision radiometer instruction manual. Available from the Pyranometer Instrument Company Inc., Northvale, NJ, 07647.

Riehl, H., and J. Malkus, 1961: Some aspects of Hurricane Daisy (1958). *Tellus*, 13, 181-213.

Rodgers, E. B., and R. F. Adler, 1981: Tropical cyclone rainfall characteristics as determined from a satellite passive microwave radiometer. *Mon. Wea. Rev.*, 109, 506-521.

Ryan, B. F., G. M. Barnes, and E. J. Zipser, 1992: A wide rainband in a developing tropical cyclone. *Mon. Wea. Rev.*, 120, 431-447.

Samsury, C. E., and E. J. Zipser, 1995: Secondary wind maxima in hurricanes: Airflow and relationship to rainbands. *Mon. Wea. Rev.*, 123, 3502-3517.

Schubert, W. H., M. T. Montgomery, R. K. Taft, T. A. Guinn, S. R. Fulton, J. P. Kossin, and J. P. Edwards, 1999: Polygonal eyewalls, asymmetric eyewall contraction and potential vorticity mixing in hurricanes. *J. Atmos. Sci.*, 56, 1197-1223.

Shapiro, L. J., 1983: The asymmetric boundary layer flow under a translating hurricane. *J. Atmos. Sci.*, 40, 1984-1998.

Shapiro, L. J., and H. E. Willoughby, 1982: The response of balanced hurricanes to local sources of heat and momentum. *J. Atmos. Sci.*, 39, 378–394.

Shay, L. K., 1998: Role of warm ocean features on intensity change: Hurricane Opal. Proc. Tropical Cyclone Symp., AMS 78th Annual Mtg., Phoenix, AZ, 11-16 Jan, 1988.

Shay, L. K., R. L. Elsberry, and P. G. Black, 1989: Vertical structure of the ocean current response to hurricanes. *J. Phys. Oceanogr.*, 19, 649-669.

Shea, D. J., and W. M. Gray, 1973: The hurricane's inner core region: I. Symmetric and asymmetric structure. *J. Atmos. Sci.*, 30, 1544-1564.

Sheets, R. C., 1969: Some mean hurricane soundings. *J. Appl. Meteor.*, 8, 134-146.

Simpson, R. H., 1952: Exploring eye of Typhoon "Marge," 1951. *Bull. Amer. Metoer. Soc.*, 33, 286-298.

Smith, T. M., R. W. Reynolds, R. E. Livezey, and D. C. Stokes, 1996: Reconstruction of historical sea surface temperatures using empirical orthogonal functions. *J. Climate*, 9, 1403-1420.

Squires, P., 1958: The microstructure of colloidal stability of warm clouds. Part I: The relation between structure and stability. *Tellus*, 10, 256-261.

Staff, NHRP, 1956: Objectives and basic design of the National Hurricane Research Project. National Hurricane Research Project Report No. 1, U.S. Weather Bureau, 6 pp.

Stickney, T. M., M. W. Shedlov, and D. I. Thompson, 1990: Rosemount total temperature sensors. Technical Report 5755 Revision B. Rosemount Aerospace Division, Eagan, Minnesota, 27 pp.

Telford, J. W., and J. Warner, 1962: On the measurement from an aircraft of buoyancy and vertical air velocity in cloud. *J. Atmos. Sci.*, 19, 415-423.

Wei, D., A. M. Blyth, and D. J. Raymond, 1998: Buoyancy on convective clouds in TOGA COARE. *J. Atmos. Sci.*, 55, 3381-3391.

Willis, P. T., and P. Tattelman, 1989: Drop-size distributions associated with intense rainfall. *J. Appl. Meteor.*, 28, 3-15.

Willoughby, H. E., and M. B. Chelmow, 1982: Objective determination of hurricane tracks from aircraft observations. *Mon. Wea. Rev.*, 110, 1298-1305.

Willoughby, H. E., J. A. Clos, and M. G. Shoreibah, 1982: Concentric eyewalls, secondary wind maxima, and the evolution of the hurricane vortex. *J. Atmos. Sci.*, 39, 395-411.

Willoughby, H. E., 1995: Mature structure and evolution. *Global Perspectives on Tropical Cyclones*, R.L. Elsberry, ed., World Meteor. Organ. Geneva, Switzerland, pp. 21-62.

Willoughby, H. E., 1998: Tropical cyclone eye thermodynamics. *Mon. Wea. Rev.*, 126, 3053-3067.

Zehr, R., 1992: Tropical cyclogenesis in the Western North Pacific. NOAA Tech. Rep. NESDIS 61, 181 pp.

Zipser, E. J., and M. A. LeMone, 1980: Cumulonimbus vertical velocity events in GATE. Part II: Synthesis and model core structure. *J. Atmos. Sci.*, 37, 2458-2469.

Zipser, E. J., R. J. Meitin, and M. A. LeMone, 1981: Mesoscale motion fields associated with a slowly moving GATE convective band. *J. Atmos. Sci.*, 38, 1725-1750.

Appendix A

AIRCRAFT INSTRUMENTATION

The data used in this study was collected by two NOAA WP-3D research aircraft. Detailed documentation on the aircraft instrumentation has not appeared in formal literature as to date. Merceret and Davis (1981) and Jorgensen (1984a) provide a brief overview of a majority of the present instrumentation aboard the two aircrafts, including not only the flight level sensors, but also the navigation equipment, the cloud physics instrumentation, and the Doppler radars. Both aircraft have nearly identical flight-level instrumentation. Included in the following three sections are a description of the sensors primarily used in this study; the Rosemount Deiced 102a Total Temperature Sensor, the AOC modified Barnes PRT-5 CO_2 infrared radiometer, and the General Eastern Model 1011B dew point hygrometer. The majority of this material was taken from either the technical reports for each instrument provided by their respective manufacturers, or through personal communication with Richard McNamara (AOC) and Peter Black (HRD) in regards to the AOC modifications. For additional information on each instrument refer too Stickney et al. (1990), Pyronometer Instrument Company (1980), and General Eastern Instruments (1987).

A.1 Rosemount 102a Total Temperature Sensor

The total temperature immersion sensor is mounted on the external forward fuselage of the aircraft. The configuration and airflow patterns through the instrument housing for this model are shown in Figure A.1, and performance parameters for the sensor are given in

Table A.1. As shown in Figure A.1, the measured air flow enters the housing and is forced to take an abrupt turn just prior to the sensing element. This design is utilized to protect the sensing element from damage by solid particulates in the air, and to minimize the errors due to liquid drops. The design assumes solid and liquid airborne particles contain enough mass that their momentum will prevent them from turning toward the sensor, and thus, pass through the housing without effecting measurements. A hermetically sealed deicing heater is brazed integrally into the thermally conductive housing, directly heating the leading edges of the housing but maintaining ice-free conditions on all surfaces within the housing. Side ports (shown in Fig. A.1) are utilized to insure a high internal mass flow at normal flight speeds, thus, providing a regular replenishment of air to be sampled near the sensor, and preventing the adverse expansion of the heated housing boundary layer during periods when the deicing heater is in use.

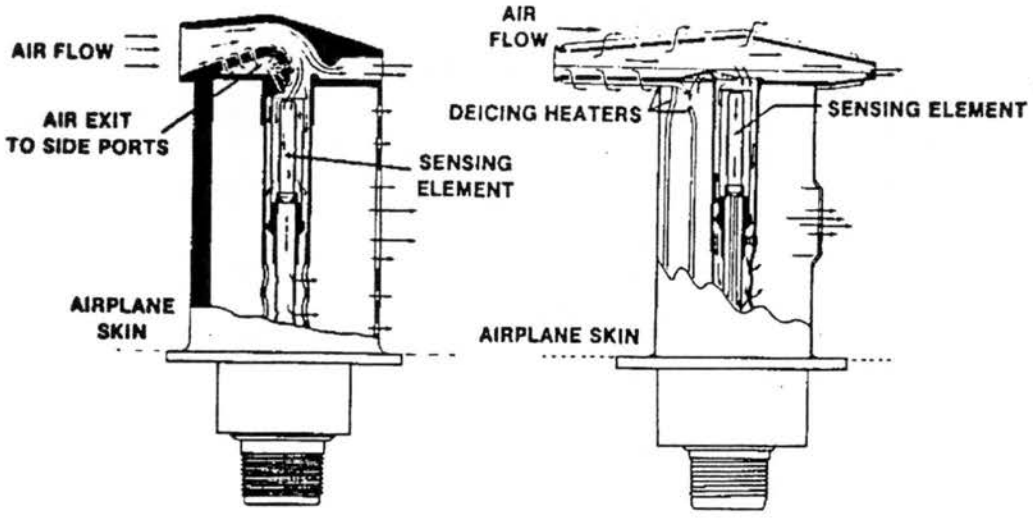

Figure A.1: Configuration and airflow patterns for the Rosemount 102a deiced total temperature sensor. Reprinted with permission from BF Goodrich Aircraft Sensors Division.

The sensor operates on the principle that the resistance in a 25 μm diameter platinum wire containing an electrical current is directly related to the temperature at the surface of the sensor. Thus, local sources of adverse thermal energy could effect the measurements. Self-heating and radiational errors are negligible. The sensor is designed with maximum

Table A.1: Performance parameters of WP-3D aircraft instrumentation primarily used in this study.

Variable	Instrument	Range	Resolution	Accuracy	Time Constant
Air Temperature	Rosemount Deiced 102a	-60°C to +60°C	0.03°C	±0.29°C	≈ 1.0 s
	AOC modified Barnes PRT-5 CO_2 Infrared Radiometer	-50°C to +30°C	0.05°C	±0.5°C	0.05 s
Dew point Temperature	General Eastern Hygrometer 1011B	-50 to°C +50°C	0.1°C	±0.25 °C (dew point) ±0.5°C (frost point)	≈ 5-20 s

thermal resistance between the housing and sensing element to prevent conduction errors from the aircraft fuselage or the deicing heater. Heating errors during flight operation can only occur during periods of low internal mass flow when the deicing heater is turned on. During such periods the heated boundary layer of the housing expands and contacts the sensing element producing an error on the order of 0.2±0.15 K. The instrument is also sensitive to the direction of the airflow entering the sensor housing and errors can occur if not from the forward direction. However, the mounting of the sensor along the aircraft fuselage, along with the high aircraft speeds compared to wind speeds, tends to locally straighten the flow prior to entering housing, and thus, producing a negligible error.

A.2 AOC Modified Barnes PRT-5 CO_2 Infrared Radiometer

The AOC modified Barnes PRT-5 radiometer unit is mounted inside the aircraft in the forward fuselage. The instrument "looks" horizontally through a hole in the fuselage on the right side of the aircraft, and is restricted to a 2° field of view. A block diagram of the instrument is shown in Figure A.2 and performance parameters are given in Table A.1. The instrument utilizes a bandpass filter centered on the 15 μm CO_2 absorption band, and operates under the principle that the observed radiance is proportional to a weighted average of the temperature in the sensed volume. Radiation emitted from the environment arrives in the optical unit at the optical chopper, which alternately blocks the radiation, or

allows it to pass to a detector in a temperature controlled chamber. The detector consists of a thermally, or radiatively, sensitive resistor coupled with an objective lens and an interference filter. The lens and filter permit only radiation in the optical CO_2 absorption band centered at 15 μm to reach the resistor. The detector and chopper are contained in a tightly controlled temperature environment so that when the chopper is blocking the incoming radiation the detector is essentially seeing the reference temperature of its own environment. Therefore, the detector constantly compares the equivalent blackbody temperature of the environmental target to the reference temperature, and the difference results in an a-c data signal. Data is sampled at a rate of 100 Hz, the optical chopping rate, and is amplified. The a-c signal is then synchronously demodulated to a d-c voltage which is related in magnitude and polarity to the temperature difference between the target and the internal cavity. The polarity assists in determining if the target is warmer or colder than the reference temperature (45°C). The d-c voltage is then related to a target temperature using a non-linear functional fit, and filtered to the desired sampling rate (1 Hz).

The original Barnes PRT-5 radiometers suffered from continuous calibration problems during flight. The optical unit was not sealed, and thus the internal reference temperature was affected by the non-regulated aircraft cabin temperature. In an attempt to correct this, AOC modified the instrument to maintain a more stable calibration. The optical unit was filled with nitrogen and pressure sealed in order to prevent any drift in the internal reference temperature. Furthermore, the objective lens and interference filter were originally composed of different materials. These were replaced with similar components composed of the same material. The modifications resulted in a more stable calibration, however, a time-dependent bias between the radiometer and Rosemount instrument still exists.

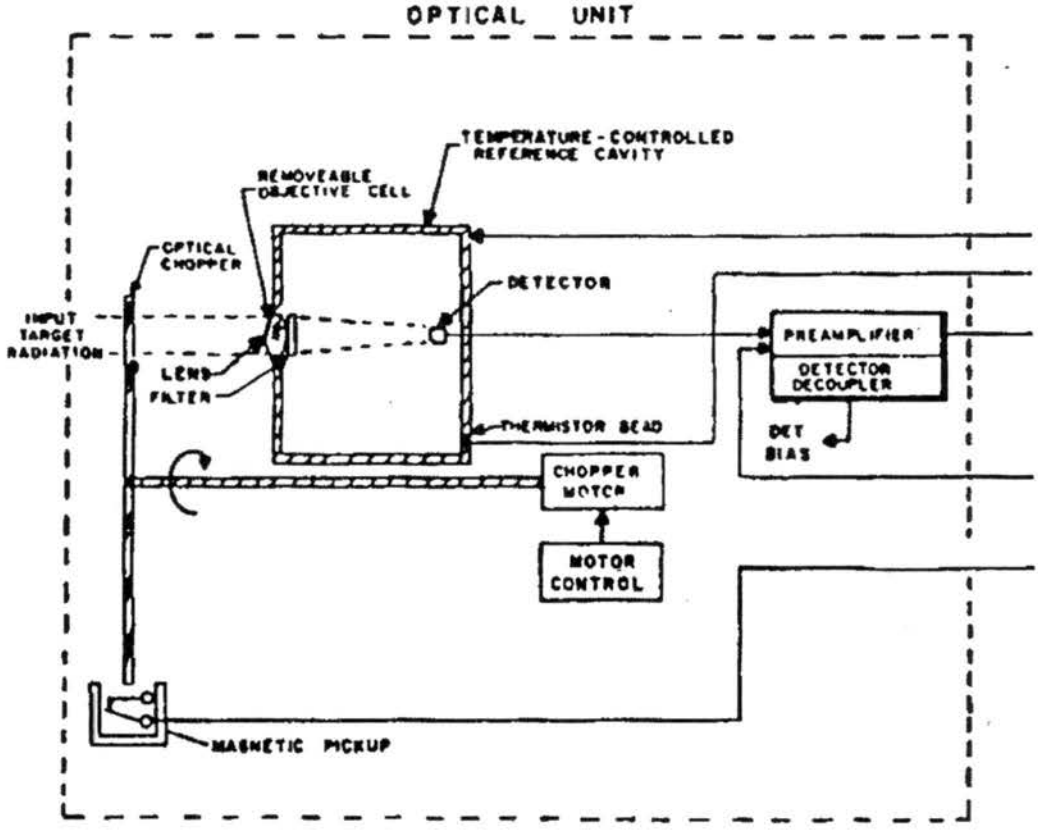

Figure A.2: Diagram of the optical unit of a Barnes PRT-5 CO_2 Infrared Radiometer. Reprinted with permission from The Pyrometer Instrument Company.

A.3 General Eastern Dew point Hygrometer 1011B

The General Eastern dew point hygrometer is mounted in the forward-side fuselage. Air must make a right-angled turn to be drawn into the instrument during flight, thus providing some protection from damage by solid particulates in the air and minimizing the impingment of liquid drops on the mirror. A block diagram of the instrument is shown in Figure A.3 and performance parameters are given in Table A.1. The instrument operates by stabilizing the temperature of a mirror at the point at which condensation begins to form on its surface, the dew point temperature of the ambient air. Embedded within the mirror is a platinum resistance temperature sensor that measures the temperature of the mirror. The mirror temperature is controlled by a thermoelectric cooler/heater. Condensation is optically detected when the original signal from the LED's becomes scattered and thus less energy is received by the phototransistor. Through continual heating and cooling of the mirror, the temperature of the mirror is maintained at the dew point.

The response time of the instrument varies as a function of whether the mirror is being heated or cooled to produce condensation. When the instrument enters a drier environment, the cooler is used to adjust the mirror temperature and the instrument has a fast response time ($\sim$ 5 s). When the instrument enters a more humid environment, the heater is used. The heater can not adjust the mirror temperature as fast as the cooler due to a possible overload of the electronic circuitry. Thus, in such cases the response time is slower ($\sim$ 10-20 s). On average the instrument can resolve dew point temperature gradients of 2° C s^{-1}. When excessive condensation occurs, or the mirror is wetted from hydrometeors, heat is supplied to the mirror to evaporate the excess. For this reason, and accuracy limits, the instrument is not capable of measuring the small supersaturations present in the environment, but rather only saturation and subsaturation.

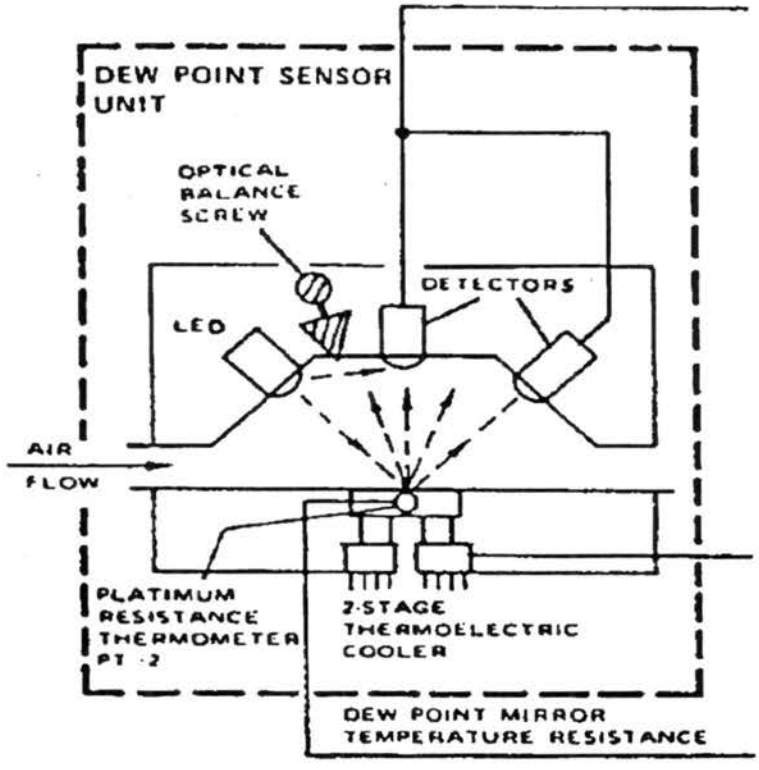

Figure A.3: Diagram of a General Eastern Dew point Hygrometer Model 1011B sensing unit. Reprinted with permission from Buck Research.

Appendix B

RADIAL COMPOSITES ABOUT THE EYEWALL RMU

Radial composites with respect to the eyewall RMU for minimal and intense hurricanes were presented in Chapter 6 from the reconstructed flight-level database used in this study. Presented here for completeness are similar composites of SR temperature, SR temperature anomaly from the mean hurricane season tropical atmosphere (Jordan 1958b), potential temperature (θ) calculated according to Bolton (1980), vertical mass flux, tangential velocity (V_θ), angular velocity (ω), relative vorticity (ζ), radial velocity (V_r), radial divergence (DIV), and pressure surface height. The vertical mass flux was evaluated for a unit strip of width 1 m across the flight as,

$$mass\ flux = \rho w dr \tag{B.1}$$

where ρ is the density determined from the equation of state, w is the vertical velocity, and dr is 0.5 km, or the radial width of each data bin. The axisymmetric vertical component of relative vorticity in cylindrical coordinates defined as,

$$\zeta = \frac{\partial V_\theta}{\partial r} + \frac{V_\theta}{r} \tag{B.2}$$

where the second term is the definition of angular velocity. Finally, the radial divergence is defined as,

$$DIV = \frac{\partial V_r}{\partial r} + \frac{V_r}{r} \tag{B.3}$$

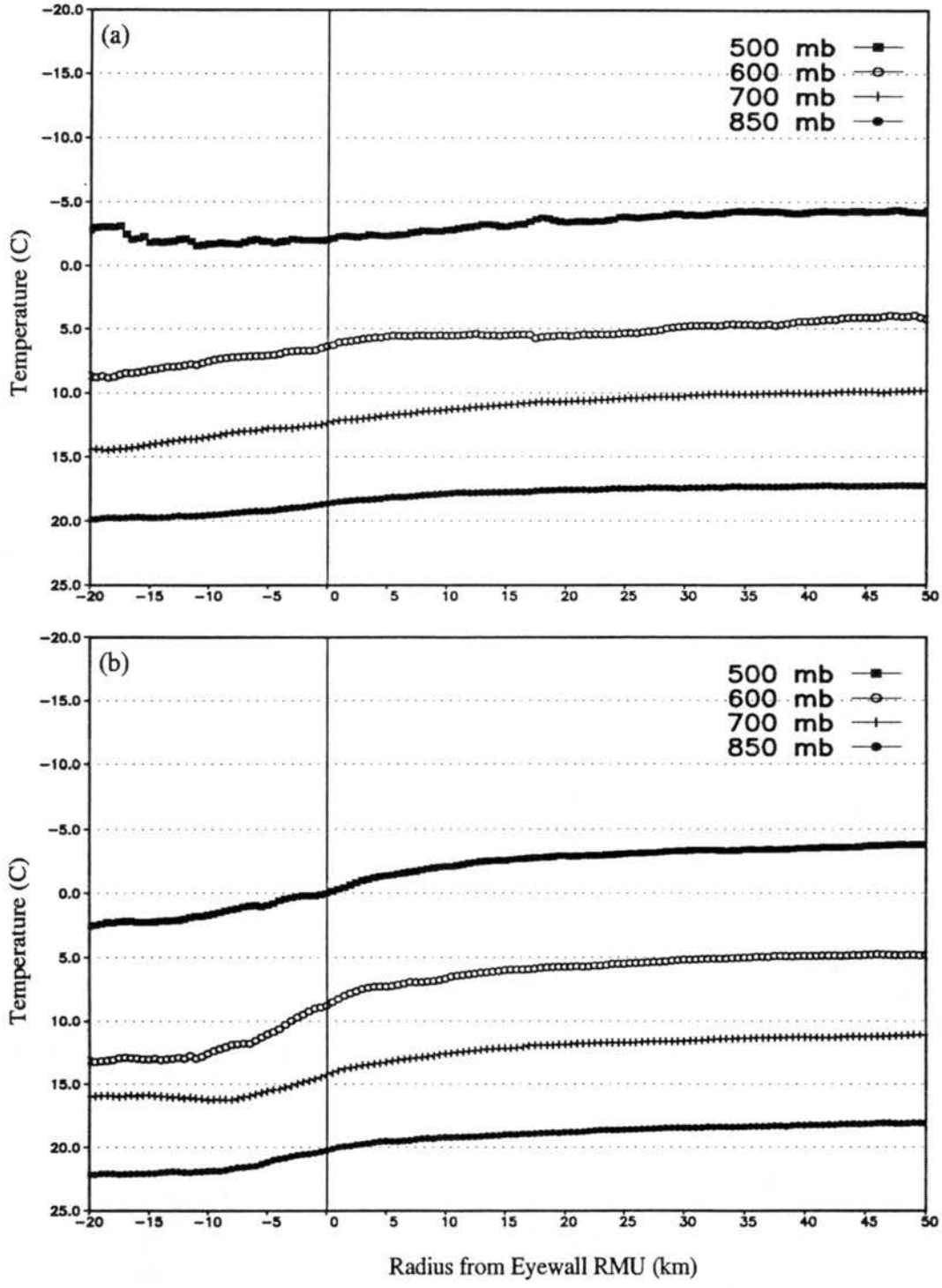

Figure B.1: Composite temperature derived from the side-looking radiometer (SR) for (a) minimal and (b) intense hurricanes at 850, 700, 600, and 500 mb about the eyewall RMU.

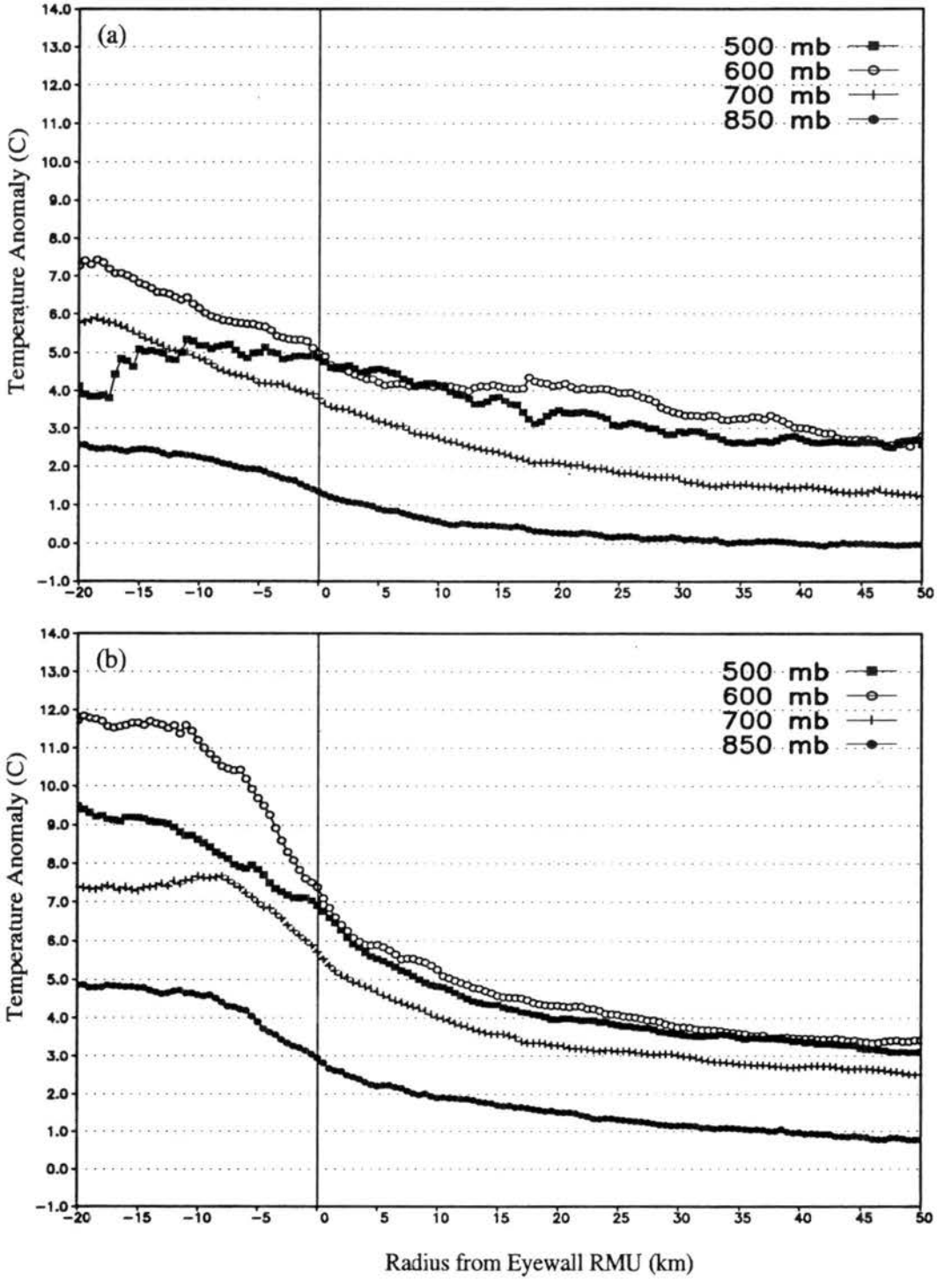

Figure B.2: Composite SR temperature anomaly from the mean hurricane season tropical atmosphere (Jordan 1958b) for (a) minimal and (b) intense hurricanes at 850, 700, 600, and 500 mb about the eyewall RMU. Mean hurricane season tropical atmosphere temperatures at these levels are 17.3°C, 8.6°C, 1.4°C, and -6.9°C respectively.

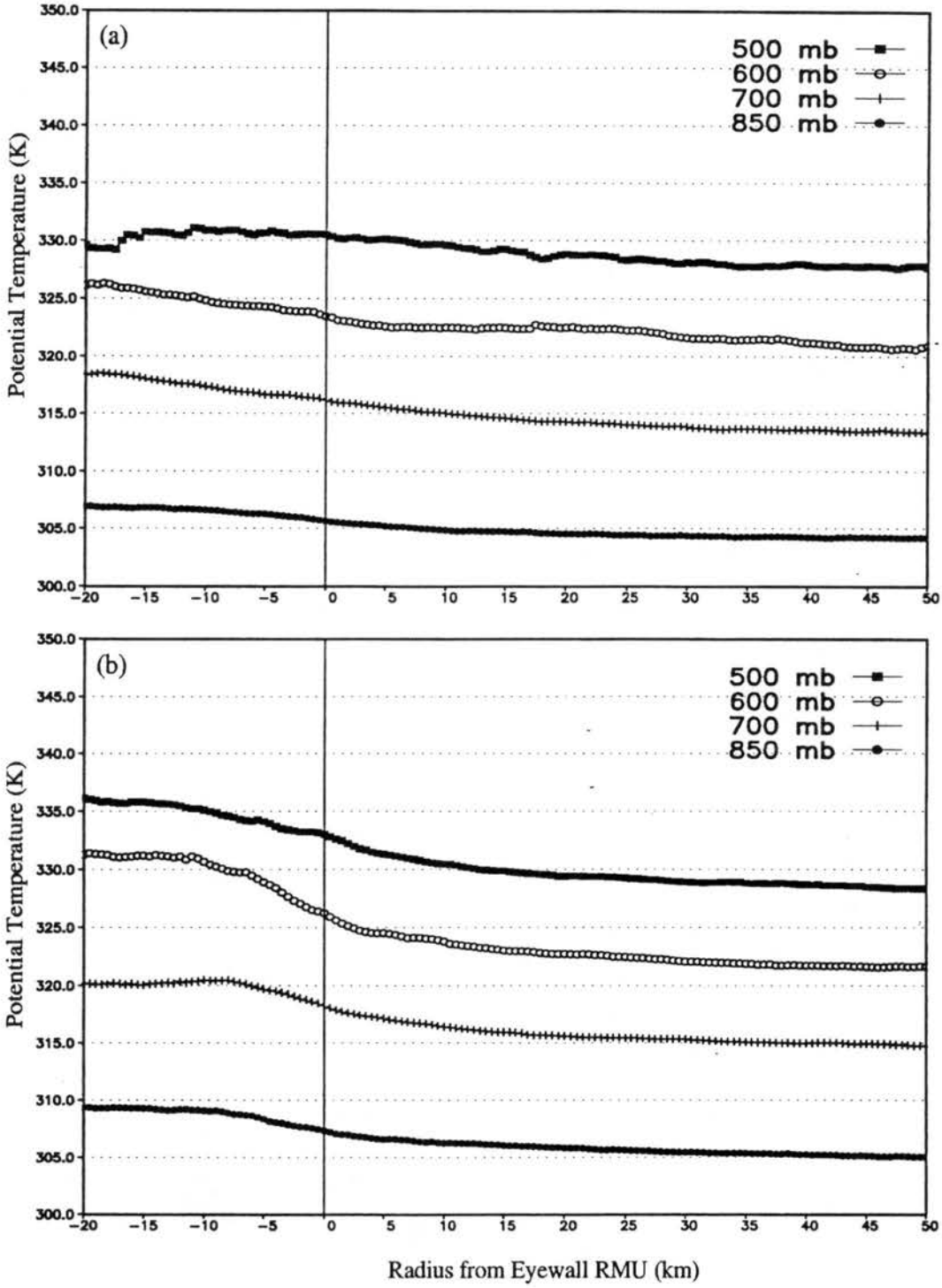

Figure B.3: Composite potential temperature for (a) minimal and (b) intense hurricanes at 850, 700, 600, and 500 mb about the eyewall RMU.

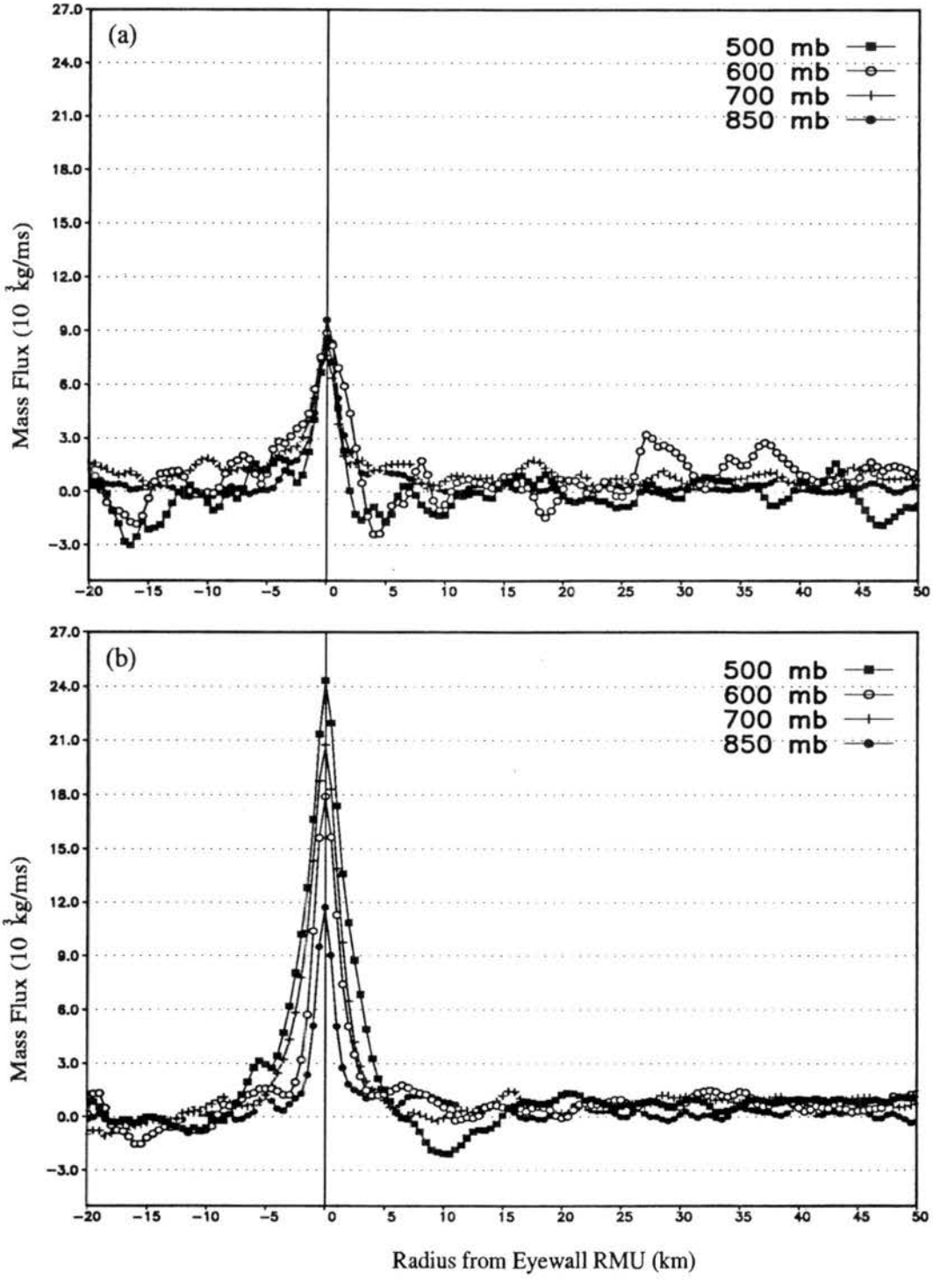

Figure B.4: Composite vertical mass flux for (a) minimal and (b) intense hurricanes at 850, 700, 600, and 500 mb about the eyewall RMU.

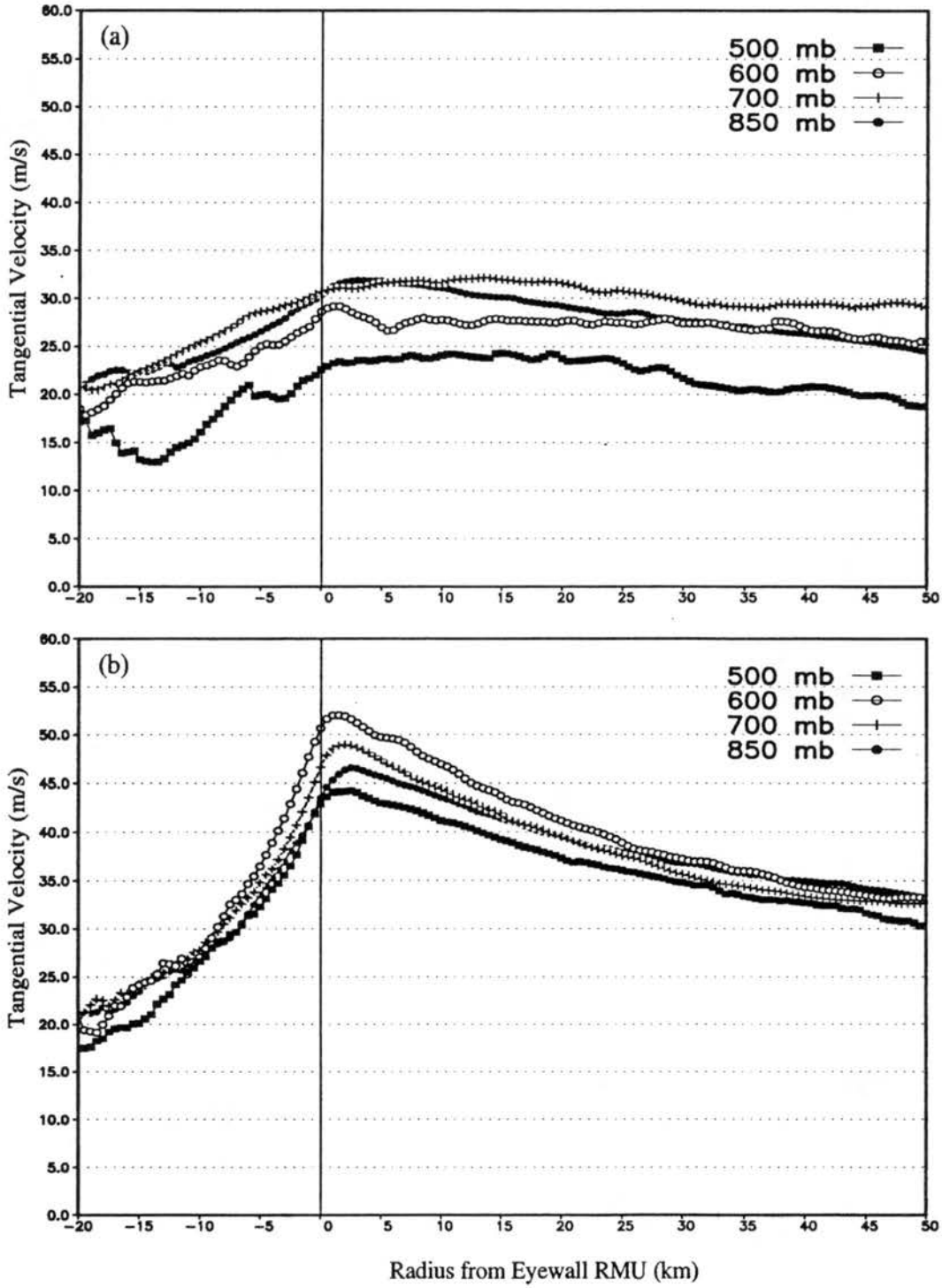

Figure B.5: Composite tangential velocity for (a) minimal and (b) intense hurricanes at 850, 700, 600, and 500 mb about the eyewall RMU.

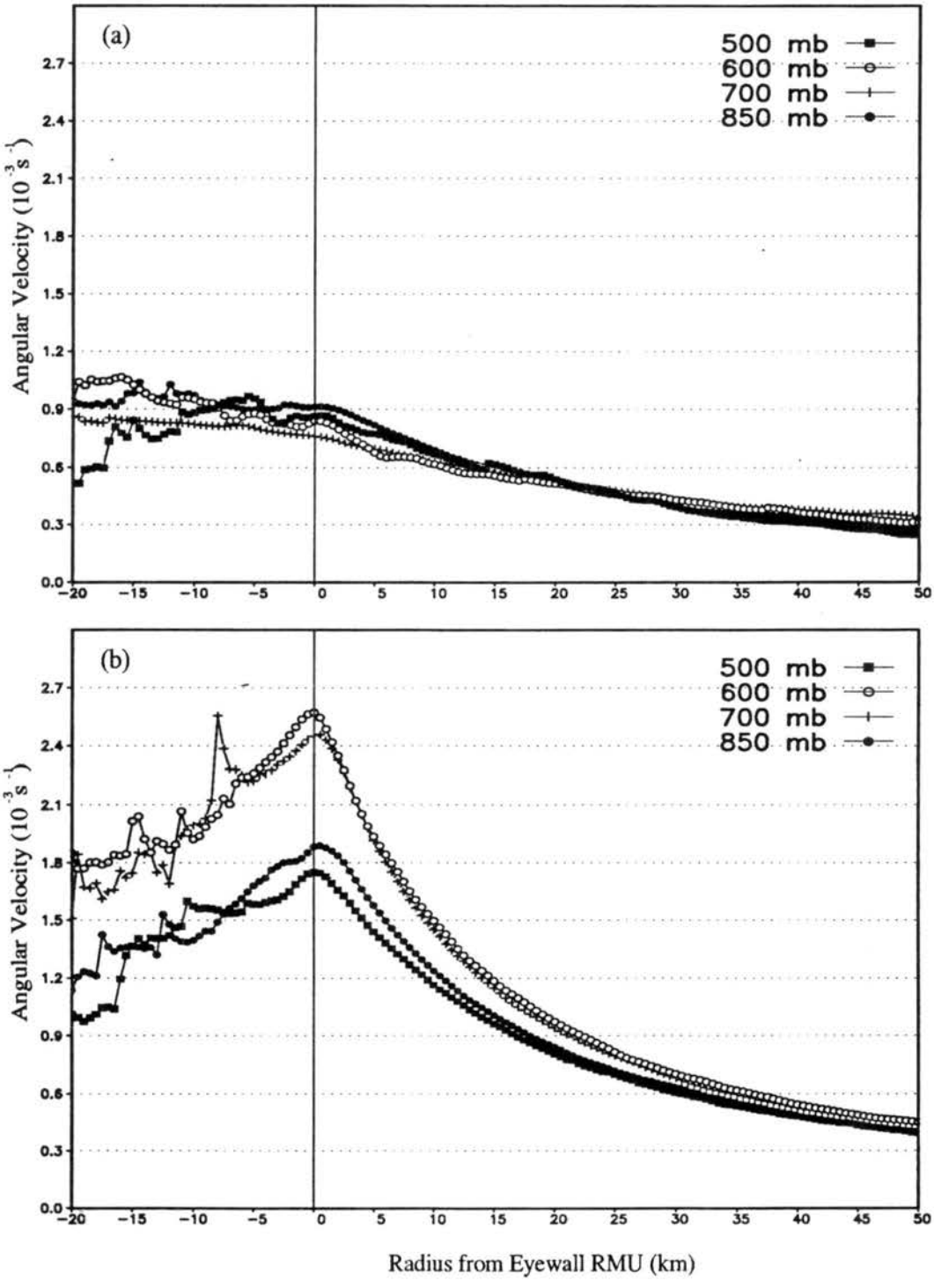

Figure B.6: Composite angular velocity for (a) minimal and (b) intense hurricanes at 850, 700, 600, and 500 mb about the eyewall RMU.

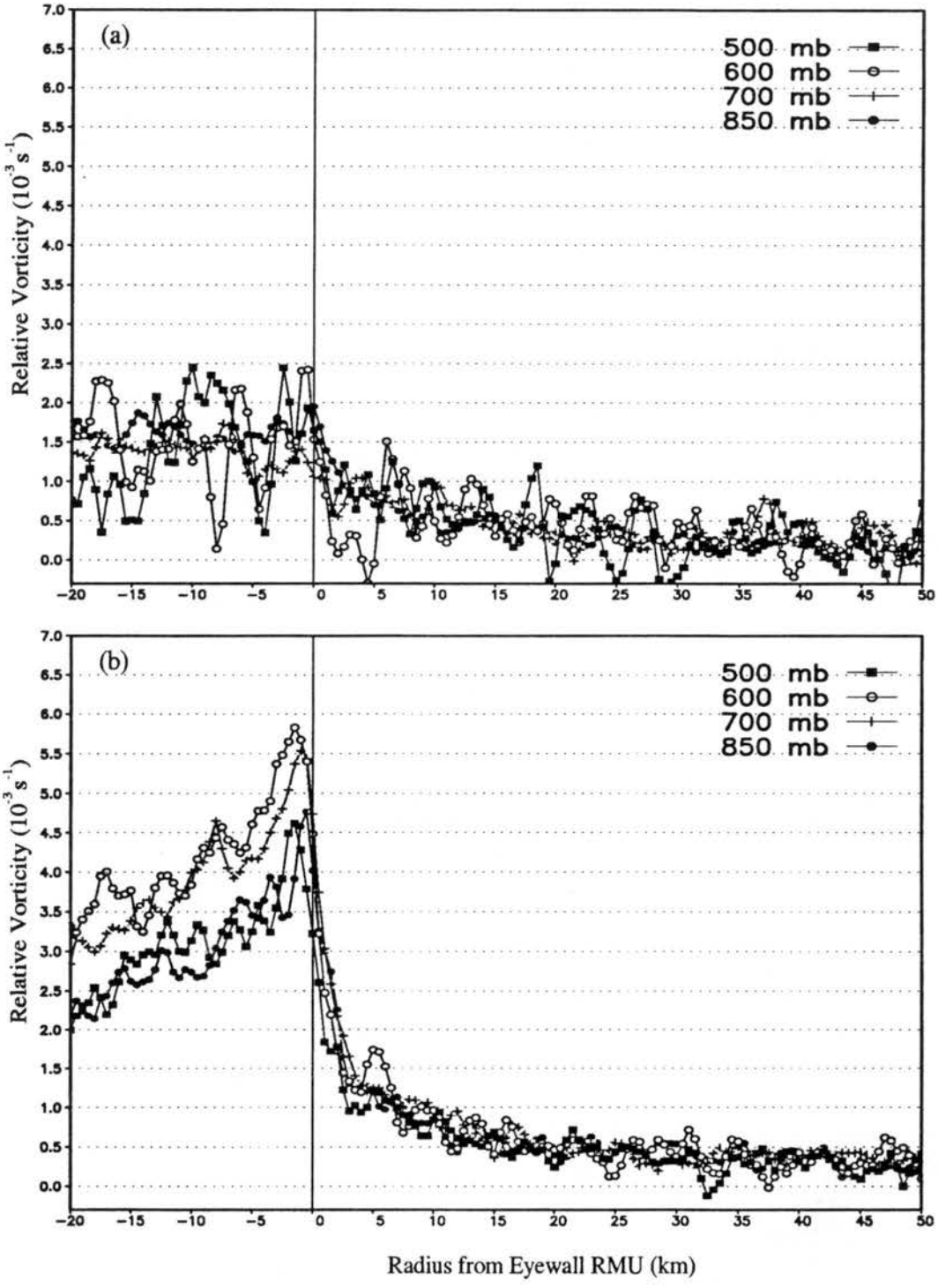

Figure B.7: Composite relative vorticity for (a) minimal and (b) intense hurricanes at 850, 700, 600, and 500 mb about the eyewall RMU.

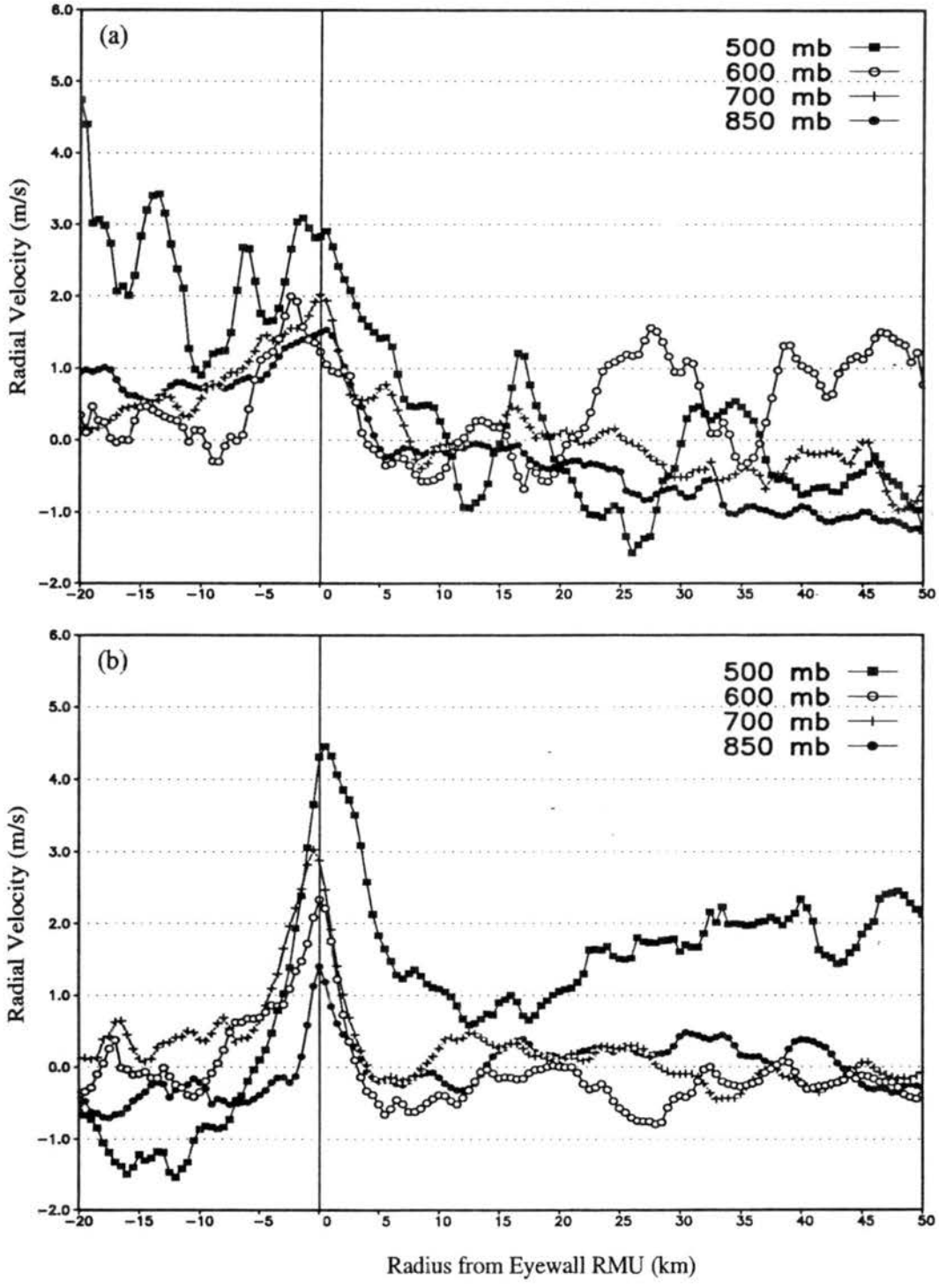

Figure B.8: Composite radial velocity for (a) minimal and (b) intense hurricanes at 850, 700, 600, and 500 mb about the eyewall RMU.

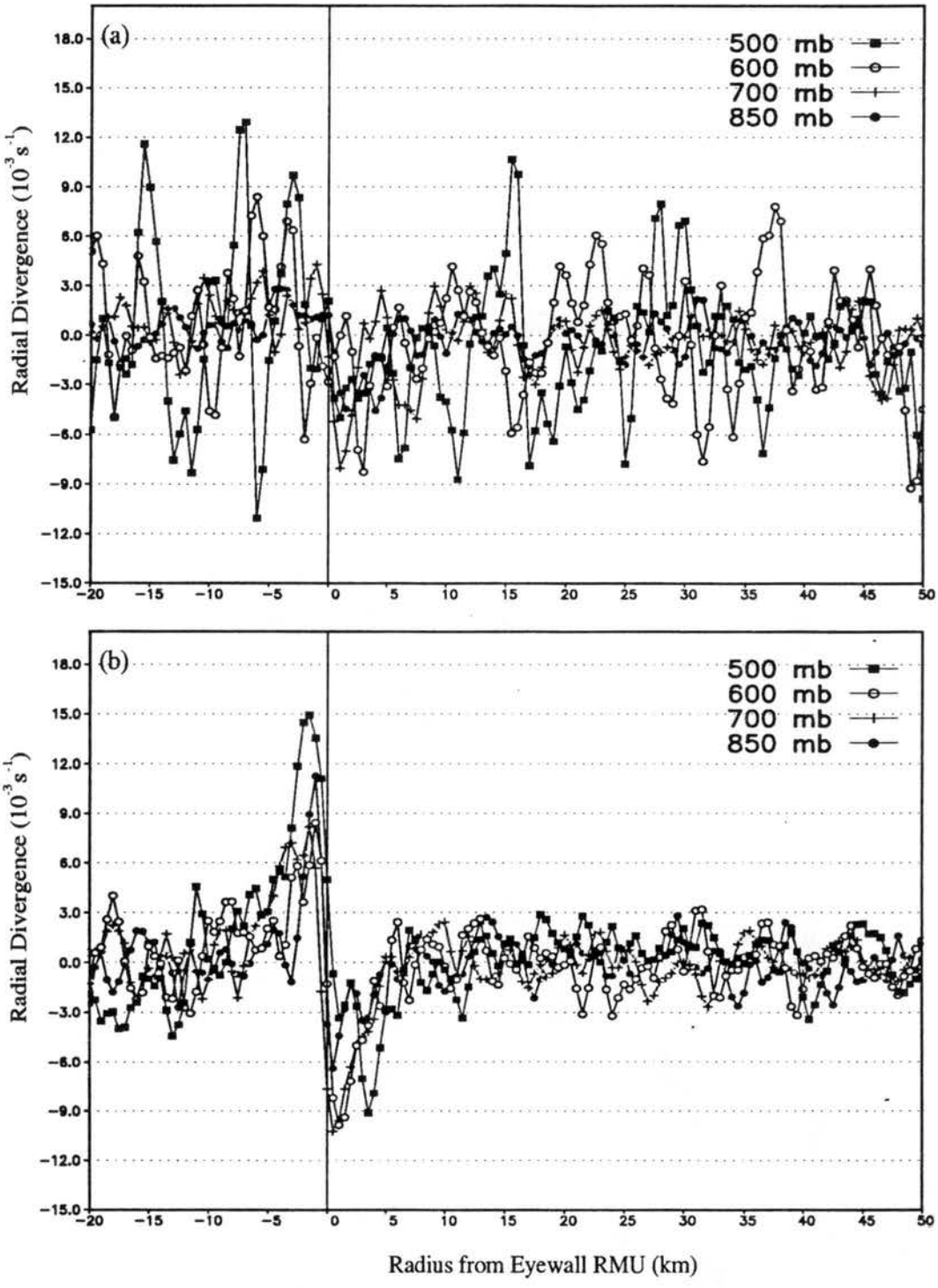

Figure B.9: Composite radial divergence for (a) minimal and (b) intense hurricanes at 850, 700, 600, and 500 mb about the eyewall RMU.

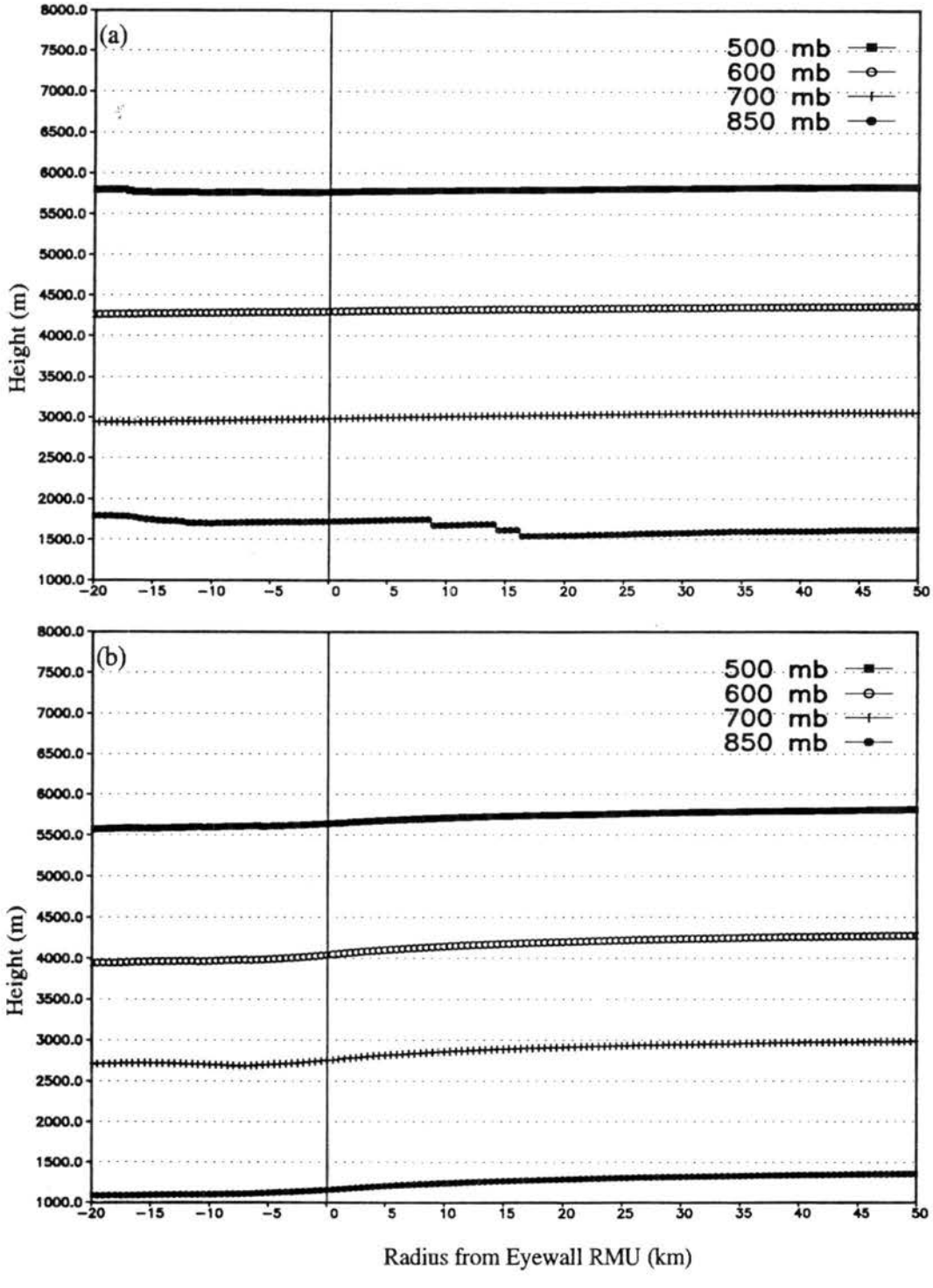

Figure B.10: Composite pressure surface heights for (a) minimal and (b) intense hurricanes at 850, 700, 600, and 500 mb about the eyewall RMU.

PROJECT REPORTS FROM W. M. GRAY'S FEDERALLY SUPPORTED RESEARCH
(SINCE 1967)

CSU Dept. of Atmos. Sci. Report No.	Report Title, Author, Date, Agency Support
104	The Mutual Variation of Wind, Shear and Baroclinicity in the Cumulus Convective Atmosphere of the Hurricane (69 pp.). W. M. Gray. February 1967. NSF Support.
114	Global View of the Origin of Tropical Disturbances and Storms (105 pp.). W. M. Gray. October 1967. NSF Support.
116	A Statistical Study of the Frictional Wind Veering in the Planetary Boundary Layer (57 pp.). B. Mendenhall. December 1967. NSF and ESSA Support.
124	Investigation of the Importance of Cumulus Convection and ventilation in Early Tropical Storm Development (88 pp.). R. Lopez. June 1968. ESSA Satellite Lab. Support.
Unnumbered	Role of Angular Momentum Transports in Tropical Storm Dissipation over Tropical Oceans (46 pp.). R. F. Wachtmann. December 1968. NSF and ESSA Support.
Unnumbered	Monthly Climatological Wind Fields Associated with Tropical Storm Genesis in the West Indies (34 pp.). J. W. Sartor. December 1968. NSF Support.
140	Characteristics of the Tornado Environment as Deduced from Proximity Soundings (55 pp.). T. G. Wills. June 1969. NOAA and NSF Support.
161	Statistical Analysis of Trade Wind Cloud Clusters in the Western North Pacific (80 pp.). K. Williams. June 1970. ESSA Satellite Lab. Support.
—	A Climatology of Tropical Cyclones and Disturbances of the Western Pacific with a Suggested Theory for Their Genesis/Maintenance (225 pp.). W. M. Gray. NAVWEARSCHFAC Tech. Paper No. 19-70. November 1970. (Available from US Navy, Monterey, CA). US Navy Support.
179	A diagnostic Study of the Planetary Boundary Layer over the Oceans (95 pp.). W. M. Gray. February 1972. Navy and NSF Support.
182	The Structure and Dynamics of the Hurricane's Inner Core Area (105 pp.). D. J. Shea. April 1972. NOAA and NSF Support.
188	Cumulus Convection and Larger-scale Circulations, Part I: A Parametric Model of Cumulus Convection (100 pp.). R. E. Lopez. June 1972. NSF Support.
189	Cumulus Convection and Larger-scale Circulations, Part II: Cumulus and Meso-scale Interactions (63 pp.). R. E. Lopez. June 1972. NSF Support.
190	Cumulus Convection and Larger-scale Circulations, Part III: Broadscale and Meso-scale Considerations (80 pp.). W. M. Gray. July 1972. NOAA-NESS Support.
195	Characteristics of Carbon Black Dust as a Tropospheric Heat Source for Weather Modification (55 pp.). W. M. Frank. January 1973. NSF Support.
196	Feasibility of Beneficial Hurricane Modification by Carbon Black Seeding (130 pp.). W. M. Gray. April 1973. NOAA Support.
199	Variability of Planetary Boundary Layer Winds (157 pp.). L. R. Hoxit. May 1973. NSF Support.
200	Hurricane Spawned Tornadoes (57 pp.). D. J. Novlan. May 1973. NOAA and NSF Support.

CSU Dept. of Atmos. Sci. Report No.	Report Title, Author, Date, Agency Support
212	A Study of Tornado Proximity Data and an Observationally Derived Model of Tornado Genesis (101 pp.). R. Maddox. November 1973. NOAA Support.
219	Analysis of Satellite Observed Tropical Cloud Clusters (91 pp.). E. Ruprecht and W. M. Gray. May 1974. NOAA/NESS Support.
224	Precipitation Characteristics in the Northeast Brazil Dry Region (56 pp.). R. P. L. Ramos. May 1974. NSF Support.
225	Weather Modification through Carbon Dust Absorption of Solar Energy (190 pp.). W. M. Gray, W. M. Frank, M. L. Corrin, and C. A. Stokes. July 1974.
234	Tropical Cyclone Genesis (121 pp.). W. M. Gray. March 1975. NSF Support.
—	Tropical Cyclone Genesis in the Western North Pacific (66 pp.). W. M. Gray. March 1975. US Navy Environmental Prediction Research Facility Report. Tech. Paper No. 16-75. (Available from the US Navy, Monterey, CA). Navy Support.
241	Tropical Cyclone Motion and Surrounding Parameter Relationships (105 pp.). J. E. George. December 1975. NOAA Support.
243	Diurnal Variation of Oceanic Deep Cumulus Convection. Paper I: Observational Evidence, Paper II: Physical Hypothesis (106 pp.). R. W. Jacobson, Jr. and W. M. Gray. February 1976. NOAA-NESS Support.
257	Data Summary of NOAA's Hurricanes Inner-Core Radial Leg Flight Penetrations 1957-1967, and 1969 (245 pp.). W. M. Gray and D. J. Shea. October 1976. NSF and NOAA Support.
258	The Structure and Energetics of the Tropical Cyclone (180 pp.). W. M. Frank. October 1976. NOAA-NHEML, NOAA-NESS and NSF Support.
259	Typhoon Genesis and Pre-typhoon Cloud Clusters (79 pp.). R. M. Zehr. November 1976. NSF Support.
Unnumbered	Severe Thunderstorm Wind Gusts (81 pp.). G. W. Walters. December 1976. NSF Support.
262	Diurnal Variation of the Tropospheric Energy Budget (141 pp.). G. S. Foltz. November 1976. NSF Support.
274	Comparison of Developing and Non-developing Tropical Disturbances (81 pp.). S. L. Erickson. July 1977. US Army Support.
—	Tropical Cyclone Research by Data Compositing (79 pp.). W. M. Gray and W. M. Frank. July 1977. US Navy Environmental Prediction Research Facility Report. Tech. Paper No. 77-01. (Available from the US Navy, Monterey, CA). Navy Support.
277	Tropical Cyclone Cloud and Intensity Relationships (154 pp.). C. P. Arnold. November 1977. US Army and NHEML Support.
297	Diagnostic Analyses of the GATE A/B-scale Area at Individual Time Periods (102 pp.). W. M. Frank. November 1978. NSF Support.
298	Diurnal Variability in the GATE Region (80 pp.). J. M. Dewart. November 1978. NSF Support.
299	Mass Divergence in Tropical Weather Systems, Paper I: Diurnal Variation; Paper II: Large-scale Controls on Convection (109 pp.). J. L. McBride and W. M. Gray. November 1978. NOAA-NHEML Support.

CSU Dept. of Atmos. Sci. Report No.	Report Title, Author, Date, Agency Support
—	New Results of Tropical Cyclone Research from Observational Analysis (108 pp.). W. M. Gray and W. M. Frank. June 1978. US Navy Environmental Prediction Research Facility Report. Tech. Paper No. 78-01. (Available from the US Navy, Monterey, CA). Navy Support.
305	Convection Induced Temperature Change in GATE (128 pp.). P. G. Grube. February 1979. NSF Support.
308	Observational Analysis of Tropical Cyclone Formation (230 pp.). J. L. McBride. April 1979. NOAA-NHEML, NSF and NEPRF Support.
—	Tropical Cyclone Origin, Movement and Intensity Characteristics Based on Data Compositing Techniques (124 pp.). W. M. Gray. August 1979. US Navy Environmental Prediction Research Facility Report. Tech. Paper No. CR-79-06. (Available from the US Navy, Monterey, CA). Navy Support.
—	Further Analysis of Tropical Cyclone Characteristics from Rawinsonde Compositing Techniques (129 pp.). W. M. Gray. March 1981. US Navy Environmental Prediction Research Facility Report. Tech. Paper No. CR-81-02. (Available from the US Navy, Monterey, CA). Navy Support.
333	Tropical Cyclone Intensity Change—A Quantitative Forecasting Scheme. K. M. Dropco. May 1981. NOAA Support.
—	Recent Advances in Tropical Cyclone Research from Rawinsonde Composite Analysis (407 pp.). WMO Publication. W. M. Gray. 1981.
340	The Role of the General Circulation in Tropical Cyclone Genesis (230 pp.). G. Love. April 1982. NSF Support.
341	Cumulus Momentum Transports in Tropical Cyclones (78 pp.). C. S. Lee. May 1982. ONR Support.
343	Tropical Cyclone Movement and Surrounding Flow Relationships (68 pp.). J. C. L. Chan and W. M. Gray. May 1982. ONR Support.
346	Environmental Circulations Associated with Tropical Cyclones Experiencing Fast, Slow and Looping Motions (273 pp.). J. Xu and W. M. Gray. May 1982. NOAA and NSF Support.
348	Tropical Cyclone Motion: Environmental Interaction Plus a Beta Effect (47 pp.). G. J. Holland. May 1982. ONR Support.
—	Tropical Cyclone and Related Meteorological Data Sets Available at CSU and Their Utilization (186 pp.). W. M. Gray, E. Buzzell, G. Burton and Other Project Personnel. February 1982. NSF, ONR, NOAA, and NEPRF Support.
352	A Comparison of Large and Small Tropical Cyclones (75 pp.). R. T. Merrill. July 1982. NOAA and NSF Support.
358	On the Physical Processes Responsible for Tropical Cyclone Motion (200 pp.). Johnny C. L. Chan. November 1982. NSF, NOAA/NHRL and NEPRF Support.
363	Tropical Cyclones in the Australian/Southwest Pacific Region (264 pp.). Greg J. Holland. March 1983. NSF, NOAA/NHRL and Australian Government Support.
370	Atlantic Seasonal Hurricane Frequency, Part I: El Nino and 30 mb QBO Influences; Part II: Forecasting Its Variability (105 pp.). W. M. Gray. July 1983. NSF Support.

CSU Dept. of Atmos. Sci. Report No.	Report Title, Author, Date, Agency Support
379	A Statistical Method for One- to Three-Day Tropical Cyclone Track Prediction (201 pp). Clifford R. Matsumoto. December, 1984. NSF/NOAA and NEPRF support.
—	Varying Structure and Intensity Change Characteristics of Four Western North Pacific Tropical Cyclones. (100 pp.). Cecilia A. Askue and W. M. Gray. October 1984. US Navy Environmental Prediction Research Facility Report No. CR 84-08. (Available from the US Navy, Monterey, CA). Navy Support
—	Characteristics of North Indian Ocean Tropical Cyclone Activity. (108 pp.). Cheng-Shang Lee and W. M. Gray. December 1984. US Navy Environmental Prediction Research Facility Report No. CR 84-11. (Available from the US Navy, Monterey, CA). Navy Support.
391	Typhoon Structural Variability. (77 pp.). Candis L. Weatherford. October, 1985. NSF/NOAA Support.
392	Global View of the Upper Level Outflow Patterns Associated with Tropical Cyclone Intensity Change During FGGE. (126 pp.). L. Chen and W. Gray. October, 1985. NASA support.
394	Environmental Influences on Hurricane Intensification. (156 pp.). Robert T. Merrill. December, 1985. NSF/NOAA Support.
403	An Observational Study of Tropical Cloud Cluster Evolution and Cyclogenesis in the Western North Pacific. (250 pp.). Cheng-Shang Lee. September, 1986. NSF/NOAA support.
—	Recent Colorado State University Tropical Cyclone Research of Interest to Forecasters. (115 pp.). William M. Gray. June, 1987. US Navy Environmental Prediction Research Facility Contractor Report CR 87-10. Available from US Navy, Monterey, CA. Navy support.
428	Tropical Cyclone Observation and Forecasting With and With and Without Aircraft Reconnaissance. (105 pp.) Joel D. Martin. May, 1988. USAF, NWS, ONR support.
429	Investigation of Tropical Cyclone Genesis and Development Using Low-level Aircraft Flight Data. (94 pp.) Michael G. Middlebrooke. May, 1988. USAF, NSF support.
436	Environmental and convective influence on tropical cyclone development vs. non–development. (105 pp.) Patrick A. Lunney. December, 1988.
446	The structural evolution of typhoons. (198 pp.). Candis Weatherford. September, 1989. NSF/NOAA and ONR Support
457	Relationships between tropical cyclone deep convection and the radial extent of damaging winds. (109 pp.) Daniel N. Shoemaker. October, 1989. AFGL Support.
468	Associations between West Pacific equatorial zonal winds and East Pacific SST anomalies. (103 pp.) Christopher C. Collimore. May, 1990. NSF Support.
480	An observational analysis of tropical cyclone recurvature. (124 pp.). Stephen J. Hodanish. May, 1991. ONR Support.
484	West African monsoonal rainfall and intense hurricane associations. (270 pp.). Christopher W. Landsea. October, 1991. NSF Support.

CSU Dept. of Atmos. Sci. Report No.	Report Title, Author, Date, Agency Support
508	Tropical cyclone motion and recurvature in TCM-90. (80 pp.). Michael E. Fitzpatrick. September, 1992. ONR Support.
520	Evidence of a stratospheric QBO modulation of tropical convection. (91 pp.). John A. Knaff. January, 1993. NSF and NOAA Support.
598	Understanding and forecasting tropical cyclone intensity change. (346 pp.). Patrick J. Fitzpatrick. March, 1996. AF Support.
—	The outer radius tangential winds of tropical cyclones. Stephen B. Cocks. MS Thesis. Spring 1998.
—	Multi-platform exploration of the inner-core intensity change for hurricane Marilyn (1995). Kelly Marie Carpenter. MS Thesis. August, 1999.